# Mechanical Adaptability in Fluidic Soft Robots

Sergio Picella





Ph.D. Thesis, Eindhoven University of Technology, March 2026

*Mechanical Adaptability in Fluidic Soft Robots*
Sergio Picella

ISBN: 978-90-386-6628-0

A digital version of this thesis can be downloaded from:
https://amolf.nl and https://research.tue.nl

The work described in this thesis was performed at AMOLF, Science Park 104, 1098 XG Amsterdam, The Netherlands, and the Mechanical Engineering department at Eindhoven University of Technology, Eindhoven, 5600 MB, The Netherlands.

This work is part of the Dutch Research Council (NWO).

Printing: Proefschriften

Cover art: Enrico Muzzin

# Mechanical Adaptability in Fluidic Soft Robots

Proefschrift

ter verkrijging van de graad van doctor aan de Technische Universiteit Eindhoven, op gezag van de rector magnificus prof. dr. S.K. Lenaerts, voor een commissie aangewezen door het College voor Promoties, in het openbaar te verdedigen op 4 maart 2026 om 16:00 uur

door

Sergio Picella

geboren te Putignano, Italië

Dit proefschrift is goedgekeurd door de promotoren en de samenstelling van de promotiecommissie is als volgt:

| | |
|---|---|
| Voorzitter: | prof.dr.ir. P.D. Anderson |
| Promotor: | dr.ir. J.T.B. Overvelde |
| Copromotor: | dr.ir. E. Steur |
| Leden: | prof.dr.ir. N. van de Wouw |
| | prof. dr. J. Rossiter (University of Bristol, School of Engineering Mathematics and Technology) |
| | dr. P. Maiolino (University of Oxford, Department of Engineering Sciences) |
| | prof. dr. ir F.T. Muijres (Wageningen University, Animal Sciences) |
| Adviseurs: | dr. A. Sadeghi (Universiteit Twente, Faculty of Engineering Technology) |

Het onderzoek of ontwerp dat in dit proefschrift wordt beschreven is uitgevoerd in overeenstemming met de TU/e Gedragscode Wetenschapsbeoefening.

# Contents

# Summary

The ability to integrate control, actuation, and sensing into devices has transformed how human tasks are automated and simplified. Necessities and efficiency requirements have reshaped how resources are used, to the point that entire eras have been named after the materials we manipulate, from Stone Age to today's Anthropocene and *Plastic Age*. To support this transformation, increasingly advanced tools have been created, evolving from simple hardware to systems capable of programmed responses to external stimuli. As these systems achieve greater complexity, so too have expectations grown for their capacity to operate independently of human input.

Long before the word *robot* was even coined (1920), literature explored the idea of creating human-like substitutes through characters like Frankenstein (1818) or Pinocchio (1883), challenging readers with the technological, philosophical, and ethical dilemmas of granting them autonomy. These narratives anticipated many of the debates we now face in the development of artificial intelligence and autonomous systems, leading to a central question: how can autonomy be designed into synthetic agents, and is it even possible? This thesis examines design strategies for fluidically powered devices capable of functioning without human oversight, with particular focus on the challenges of achieving mechanical adaptability in soft robotic systems.

To translate physical structure into behavior and reproduce levels of autonomy manifested throughout the Eukaryota, we explore soft robotics' compliant hardware as a platform for mechanical adaptability, demonstrating that complex behaviors can be encoded in hardware alone, using fluidics only. To materialize our approach, we use mechanical and fluidic non-linearities, such as buckling instabilities and phase transitions, that can express complex responses to simple external stimuli.

In the first part of this thesis, we address fundamental challenges concerning the control and energy autonomy of such devices. In Chapter 1, first, we introduce and review some motivating examples from biology, architecture and robotics that have contributed to the research of autonomous soft robots. Starting from this set of examples, we outline the scope of our research and formulate the research questions we use as a framework for the remainder of the thesis.

In Chapter 2, we focus on control strategies to allow (re)programmability of such compliant hardware. In particular, using an electronics-free approach, we develop a dictionary of pneumatic circuits that encodes coding variables' functionality and traditional coding statements, such as *If*, *If... else*, and *For* statements. We demonstrate that the high-level programmability we reproduce

using our hardware coding approach can mimic behavior typically observed in natural systems. We combine these *pneumatic coding blocks* to demonstrate programmability and automatic switching between behaviors in our soft robotic systems upon interactions with their environment.

Autonomous systems capable of unsupervised, long-term operation are intrinsically required to be energetically self-sufficient. To meet this purpose, in Chapter 3, we propose a strategy to enable energy autonomy in soft robots by taking advantage of phase transitions in a low-boiling-point fluid, combined with a fluidic control strategy. Our design results in a *thermopneumatic* strategy for powering electronics-free pneumatic soft robots through environmental circadian oscillations of temperature and sun intensity. Our design rules are inspired by the power-conversion capabilities and separation of time-scales often observed in natural systems. We base our design on a pneumatic logic strategy similar to the ones developed in Chapter 2 to demonstrate that environmentally available circadian oscillations are sufficient to power and control the operation of soft robots, with no need for human intervention or electronics on board. In particular, we demonstrate the validity and potential of our designs with indoor and outdoor demonstrators.

In Chapter 4, we approach the control of underactuated systems, central to soft robotics, through the lens of networked dynamical systems. Starting from the formalims of networked dynamical systems, often used in the context of central pattern generators, we examine how oscillatory patterns can emerge arise from the interplay of *excitability* and *frustration* in coupled oscillators. We specifically focus on the $N = 2$ case and to numerically and analytically study which conditions can lead to asymmetric spiking behavior. Furthermore, we develop a framework to relate high-level mathematical variables to physical magnitudes characterizing oscillatory phenomena in soft robots. Eventually, we study how our model can be used to investigate and predict synchronization thresholds in coupled mechanofluidic oscillators and discuss its potential in the broader context of artificial organs and soft robots.

However, while analyzing our work in the context of autonomous systems, it soon became clear that there is no agreed-upon definition that could encompass the diversity of examples available in the literature. This lack of consensus poses additional challenges that build on top of the technical ones while designing autonomous systems. Among these, we believe it particularly jeopardizes the possibility of interdisciplinary debate that inhibits efficient scientific communication, both within and outside academia. To tackle these issues, in Chapter 5 we inquire into the very definition of autonomy in artificial systems by focusing on high-level yet fundamental and more philosophical aspects in the context of (soft) robotics and discuss potential directions and strategies for designing synthetic agents. Starting from etymological considerations, we delve into both the

ethical and philosophical implications of integrating autonomous systems into our everyday lives. Based on these intuitions, we reconsider commonly agreed-upon ideas concerning robots and machines and identify key features of *automatic* and *autonomous* systems to eventually address challenges in definitions in the field of (soft) robotics. We use this discussion to suggest a different approach to robotic systems design, to motivate interdisciplinary debate about artificial systems, and eventually to discuss the potential for soft robotics to materialize the design of autonomous systems.

We conclude with Chapter 6, in which we summarize the main contributions of this thesis, focusing in particular on their potential for applications in real-world scenarios. By considering retrospectively the designs we proposed and their motivation in the context of machine autonomy, we leverage our results to emphasize the potential of hardware-encoded behaviors and soft robotics for applications to out-of-the-lab environments.

# Chapter 1
# Introduction



*"Beate le marionette su le cui teste di legno il finto cielo si conserva senza strappi! Non perplessità angosciose, né ritegni, né intoppi, né ombre, né pietà: nulla! E possono attendere bravamente e prender gusto alla loro commedia e amare e tener se stesse in considerazione e in pregio, senza soffrir mai vertigini o capogiri, poiché per la loro statura e per le loro azioni quel cielo è un tetto proporzionato"*

—L. Pirandello,
*Il fu Mattia Pascal*, 1904

*"Blessed are the puppets upon whose wooden heads the mock sky remains unbroken! No anguished bewilderments, no hesitations, no setbacks, no shadows, no pity: nothing at all! They may wait with fearless composure, take delight in their little drama, love themselves and hold themselves in high esteem, yet never suffer dizziness or faintness, for by virtue of their stature and deeds that sky is a perfectly fitting canopy."*

—L. Pirandello,
*The Late Mattia Pascal*, 1904

1

## 1.1 Mechanical adaptability

The possibility of implementing sensing, control, and actuation in devices has enabled the automation and simplification of human tasks. Requirements of necessity and efficiency have driven us to reshape available resources in order to meet our production goals. This trend is so central to human history that entire ages, from the Stone Age to today's Anthropocene and *Plastic Age* [1], are defined after the materials we manipulated.

To simplify such resource transformation, increasingly advanced tools are being designed. From passive hardware devices, such as hand tools, to more articulated systems, these devices are designed to automatically respond to external stimuli to execute well-defined, preprogrammed operations. At the same time, the possibility of designing *autonomous* systems, able to operate as unsupervised and trustworthy human substitutes, motivated research into what we now identify as *robotics*. The idea of designing synthetic human replacements has long been a source of inspiration in literature, dating back to before the industrial and robotic revolutions. Notable literary examples, from Frankenstein (1818) to Pinocchio (1883), have challenged readers with technological questions and philosophical and ethical dilemmas, anticipating many of the debates about artificial intelligence and autonomous systems. But how can we design autonomy in synthetic agents, and is it possible in the first place to do so?

In this thesis, we explore design approaches for fluidically controlling and powering devices that can operate independently of human input. We focus on *mechanical* adaptability in artificial systems and address some foundational challenges when designing robotic systems. The mechanical adaptability we refer to here hints at the possibility of encoding robot's behavior directly in mechanical responses by designing trajectories in its energy landscape. This workflow allows to design responses that we identify as behavior in robotic systems that can be manifested with no need for electronics. This additional constraint of electronics-free systems is justified by the challenge and choice to rely on mechanical properties to manifest behaviors in our designs. As a result, we will demonstrate that behaviors will emerge as a result of trajectories we design in the energy landscape of our systems, rather than being artificially dictated by a controller. The design of mechanical adaptability lies at the foundation of the content of this thesis.

## 1.2 System and ecosystem

In the same way that no living being is required to, nor can likely, survive outside its habitat, no robotic system is built to operate successfully outside its intended

environment. The way robots interact with the world, not solely their ability to engage in abstract reasoning, defines their prowess in operation. Therefore, reconsidering system boundaries becomes fundamental, not only to define how devices are supposed to operate, but also to provide valuable resources to leverage for enhancing their operation. In the next section, we support this statement by reporting examples from both robotics and biology, and their relevance to the design rules we outline in our work.

## The role of environment

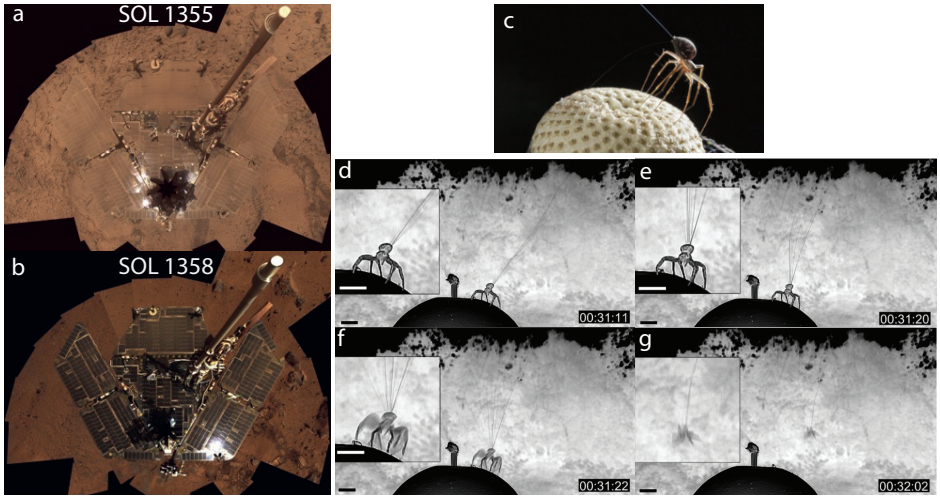


Figure 1.1: **Examples of bodyware in synthetic and natural agents. (a)-(b)** Reconstructed self portrait from the panoramic cameras of NASA's Spirit rover before (SOL 1355, October 26$^{th}$, 2007) and after a *cleaning event* (SOL 1358, October 29$^{th}$, 2007) Credits: NASA/JPL-Caltech/Cornell. **(c)** Crab spider dispersing silk to start the kiting phase and travel airborne. Credits: Michael Hutchinson. **(d)-(g)** Snapshots of kiting behavior snapshots in a crab spider. Scale bar is 5mm. Adapted from [2].

Among the great variety of examples in engineering and biology that can serve as motivating examples to blur the boundaries between (synthetic) agents and their environment, we focus on two particular cases. Devices meant to operate in space exploration often use solar power to harvest energy from their environment and amplify the reach for long-term, energy-independent operation. NASA's Spirit rover (2004-2010) could recharge its battery using solar panels that were supposed

to power the rover for about 90 days before sand covered them, compromising their operation (Figure 1.1**a**). However, surprisingly and unexpectedly, after the solar panels got covered in martian sand, periodic *cleaning events* started to occur. These cleaning events allowed the solar panels to recover their recharging potential, thus extending the operational time of the rover twenty times longer than the originally designed. It was later discovered that these cleaning events were caused by strong winds in Martian atmosphere that cleaned sand off the panels (Figure 1.1**b**)[3]. Using given environmental factors to enhance the range of operation is also a technique followed in nature in different systems. Among the many, e.g., in aerial dispersal of silks in spiders manifesting *kiting* behavior [2] and dandelion seed being carried by winds [4], air currents help these systems to traverse distances about 2-4 orders of magnitude larger than their body sizes.

From these examples, we understand that it is convenient (and oftentimes required) to consider the environment as a part of the system we design. Taking advantage, sometimes unexpectedly, of these expanded boundaries and how they change in time, designs can benefit from the interaction with their surroundings by blurring the line between the system and its environment. For this purpose, an inspirational design principle we try to bring forward is that the integration of hardware and software components in the same *bodyware* [5] should be equally expanded to also integrate the environment and its changes while designing or describing a robot. By doing so, we design systems capable of drawing operational cues and energy from variations in their environment to move towards mechanical adaptability in soft, electronics-free systems. The design, characterization, and integration of such compliant hardware then lie at the foundation of our quest to enable mechanical adaptability in electronics-free soft robotic systems.

## Energy harvesting

Similar investigations in the context of combining energy harvesting and actuation capabilities have been developed to allow long-term, unsupervised operation of artificial systems. For the purpose of this thesis, it is worth mentioning two examples in biobased self-burrowing mechanisms and shape-morphing façades in architecture that take advantage of environmental changes to enable unsupervised, long-lasting operation. In both these scenarios, mimicking the behavior of biological systems has been of great inspiration for taking advantage of naturally occurring gradients throughout, e.g., circadian cycles, to sufficient to control and power electronics-free systems.

In the first example, biobased materials are designed in such a way that moisture gradients in time can cause swelling of cellulose layers [6]. This swelling is designed to generate a drilling motion of the system, thus allowing it to burrow into the ground. The tip of the structure can be functionalized by including a

seed and can enhance its germination chances. The second example we report is artificial and focuses on using electronics-free energy-harvesting solutions for architectural purposes. In particular, we have demonstrated that temperature and sun intensity circadian oscillations can pressurize pouch motors [7] connected between a rigid, pneumatically insulated aluminum frame and movable panels. As temperature increases, the pressure in the frame rises and actuates the pouch motors, causing the spring-loaded panels in Figure 1.2**d-e** to move and shade the area underneath the aluminum dome. As temperature decreases and pressure drops accordingly, the panels recover their initial configuration [8][1].

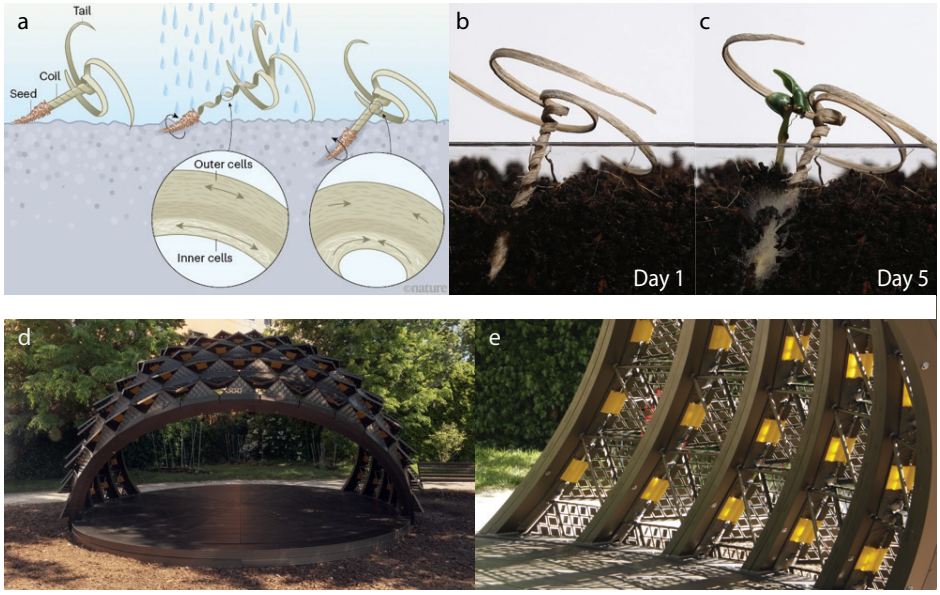


Figure 1.2: **Examples of *wired-intelligence* systems in the context of electronics-free soft robotics and *bodyware* (a)** *E-seeds*: self-burrowing behavior of *Erodium* seeds induced by naturally occurring oscillations in environmental moisture levels. **(b)-(c)** Snapshot of system's germination state and position in time. Adapted from [6]. **(d)** *Sombra* pavillon for the Biennale di Architettura 2025 in Venice [8]. **(e)** Detail of linear pouch motors (in yellow) actuating the triangular panels. This work is the result of our collaboration as Soft Robotic Matter group at AMOLF with architecture companies Airshade, MVRDV, Metadecor et al. Credits: Jaap Heemskerk.

[1]This work is the result of our collaboration as Soft Robotic Matter group at AMOLF with architecture companies Airshade, MVRDV, Metadecor et al.

1

## 1.3 From energy landscapes to behavior

To translate design intuition into mechanical adaptability, we draw inspiration from the following abstraction. In robotics, programmed responses emerge from the interplay between inputs and control policies that stabilize or reshape the system's state. As an example, a system can be intentionally pushed away from equilibrium by external inputs, and it can respond by either attempting to resist this perturbation or allowing the transition to a new configuration. Understanding how stable equilibria are distributed across a system's energy landscape becomes fundamental knowledge to determine its behavior. Such an understanding not only informs the choice and arrangement of physical components required to generate specific behaviors (e.g., bistability, oscillations, and damped responses) but also unveils knowledge about the relation between its components. We define the mechanical adaptability as the ability to reshape and traverse such energy landscapes to manifest control and actuation that we identify as behavior in synthetic agents. The design of mechanical adaptability lies at the foundation of the content of this thesis.

To better exemplify these statements, we report a conceptual example of the design of energy landscapes in Figure 1.3 based on the von Mises truss. In particular, we consider the energy landscape $E$ associated with the horizontal displacement $x$ of the point connecting the two beams under different configurations. We start by considering the system in the idealized 1-dimensional case in Figure 1.3**a** with infinitely stiff beams and its corresponding energy landscape. Based on this idealized example, we then build up different energy landscapes through different variations of this design. For this case, the energy landscape corresponds to two isolated equilibria, that are not connected by any trajectory in the corresponding energy landscape. However, as we consider systems closer and closer to real-case scenarios, material elasticity must be taken into account, and different energy landscapes, thus different mechanical behaviors, emerge. Having introduced linear springs in Figure 1.3**b** allows bistability to arise, so that the system has two connected, stable, and energetically equivalent configurations. On top of that, an unstable equilibrium sets at $x = 0$. This energy landscape lies at the foundation of several strategies to allow mechanical computation, [9], memory capabilities [10], and actuation pathways [11]. Moreover, bistability allows the system, e.g., to withstand mechanical perturbations lower in magnitude than the energy barrier separating the two energy minima. This energy barrier can be increased or reduced in magnitude, e.g., by changing the position of its boundary conditions (Figure 1.3**c**). If we modify further this structure by including a rotational spring between the linear springs (Figure 1.3**d**), we can reshape the bistable energy landscape into a monostable one, with a non-linear response when the system is out of its equilibrium configuration. This energy landscape can be

used to represent snap-through instabilities and more complex case studies, such as the one in Figure 1.4**c**, and allows the system to transition back to its unique stable configuration whenever a perturbation occurs. From this fundamental example in Figure 1.4, we observe that non-monotonic energy landscapes can be obtained using linear springs when geometrical constraints and relative position of the nodes in space is taken into account during the design phase. On top of that, non-linear responses are intrinsically embedded in the material responses in large deformation regimes. The platform we use for translating design intuitions into experimental realization of mechanically autonomous devices is based on compliant materials often used in the context of soft robotics.

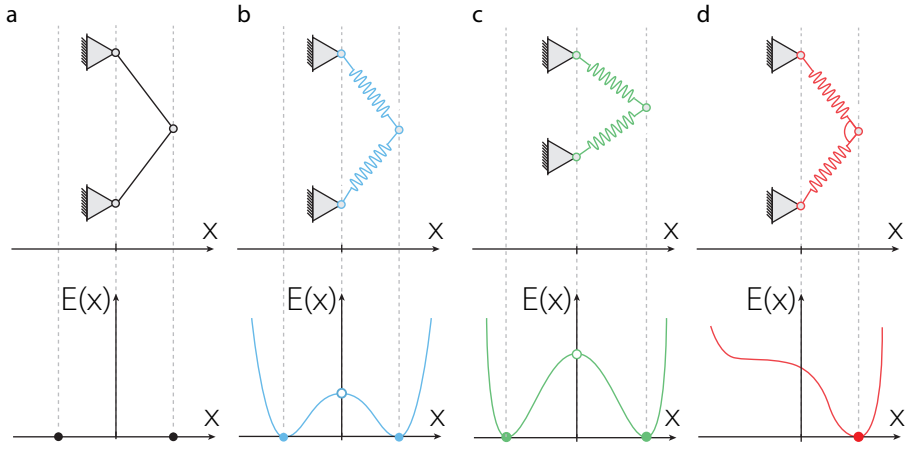


Figure 1.3: **Examples of *mechanical adaptability* design in von Mises truss systems with their energy landscapes. (a)** Ideal case with stiff beams. **(b)** Bistability obtained by including elasticity in the beams. **(c)** Tuning of the energy barrier by changing the relative position of the boundary conditions. **(d)** Monostable energy landscape obtained by adding a rotational spring between the linear springs. We represent stable and unstable equilibria with full and empty dots, respectively.

### 1.3.1 Why using *soft* robotics?

To materialize mechanical adaptability, we make use of the framework and platforms developed within the context of soft robotics. Soft robots are robots that rely on compliant materials, rather than rigid joints and hard frames. They are typically based on flexible, deformable materials, such as silicone elastomers, or

gels, that can mimic the adaptability and compliance observed in living organisms. In particular in the context of electronics-free systems, the materials typically used in the context of soft robotics lend themselves well for implementing hardware solutions to design and access energy landscapes such as the ones we represented in Figure 1.4 at scales going from millimiter [12] to meter [13]. Furthermore, among the advantages of soft robotic systems and soft hardware in general, we mention that compliant hardware is intrinsically able to comply with unstructured environments [14, 15]. Although the use of compliant materials for individual components is popular and well studied in the soft robotics community, it is not always the case that research efforts are directed towards overall electronics-free systems. This, in turn, means that often design efforts are required to embed electronic components inside compliant hardware, compromising its overall resilience to environmental conditions [16, 17]. Alternatively, material science-oriented efforts are required in order to integrate electrically responsive material in compliant hardware, complicating the design and fabrication of such devices [18, 19].

Moreover, the integration of soft materials to encode behaviors that can be expressed by the robotic system as a whole also suggests a different perspective on the role of hardware and software in artificial systems. In this thesis, we focus on electronics-free robotic system designs where the soft hardware itself plays the role of computing and software capabilities generally delegated to electronic components and software.

One of our arguments in support of using soft materials stems from the capability to mechanically program and reprogram these energy landscapes, to shape the robotic behavior based on the state of the system, without relying on an electronic controller. Moreover, using soft hardware can allow us to take advantage of both linear and non-linear mechanical responses reversibly [20, 21]. This framework is universal and finds applications and approximations across various scales and physical implementations: elastic forces can be used to model electron-electron repulsion, as well as to optimize load-bearing elements in engineering and architecture, as in the case in Figure 1.3. Nevertheless, at the centimeter scale we explore, soft materials provide additional features that we leverage for designing our systems. In particular, they enable the exploration of mechanical regimes that extend beyond linear elastic behavior, allowing for the repeated access to large-deformation regimes, e.g., through ballooning or buckling instability, without material failure. Thus, the possibility of operating in both linear and non-linear elastic regimes simultaneously through soft materials enables the direct encoding of rich mechanical responses into the material and geometry, rather than relying on a electronic controller that could be prone to hacking or failure in unsupervised environments.

However, the cost of introducing non-linearities to shape the behavior of robotic systems is that we shift the burden of dictating operating policies from

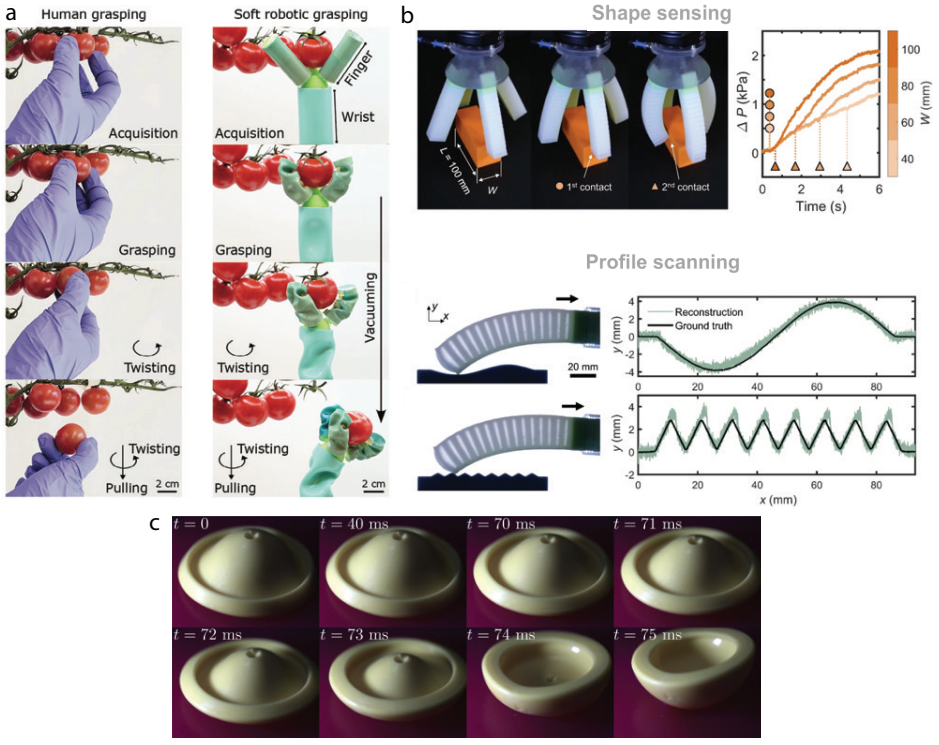


Figure 1.4: **Embodying mechanical adaptability and behavior in soft hardware. (a)** Soft manipulator created using programmable instabilities sequences of soft cylindrical structures under negative pressure. Adapted from [22]. **(b)** Proprioperception mechanism enabling shape sensing and profile scanning in electronics-free actuators. This work is the result of a collaboration with S. Zou, J. de Vries, V. Kortman, A. Sakes and J.T.B. Overvelde published in *Nature Communication*. Adapted from [23]. **(c)** Snapshots of viscoelastic effects driving a snap-through instability in a jumping popper toy. Adapted from [24].

controllers to material and structural design. While this trajectory increases the efforts of the design phase, it also reduces the complexity and power requirements of the controller, as illustrated in the manipulation demonstrator in Figure 1.4**a** [22]. For this case study, the understanding and design of buckling instabilities in cylindrical elastomer shells is used to program deformation upon decreasing pressures and mimic the complex motion of human grasping. At the same time, studying the non-linear relation between pressure and volumes in soft actuators

has allowed the integration of sensing capabilities in actuators that can safely interact with their environment, as in Figure 1.4**b** [23]. Furthermore, soft materials can take advantage of viscoelastic effects to program the time response of, e.g., a monostable jumping popper toy undergoing a snap-through instability as reported in [24] and Figure 1.4**c**. As a result, soft robotic systems are not only inherently safe and compliant to environment variability, but also allow for rich mechanical programmability, leveraging the (non)linear nature of elasticity to manifest a rich zoo of adaptive behaviors.

### 1.3.2 Electronics-free approach

Prior to the advent of electronic transistors, electronics-free solutions were the only viable strategy for technological implementation of actuation, energy harvesting, and control devices. Fundamental computational capabilities, power amplification, and memory capacity in these early designs were implemented through hardware-based solutions based on mechanical and fluidic non-linearities, such as the siphon effect and mechanical multistability. Examples of these designs range from continuous time-keeping mechanisms (Figure 1.5**a**) up to more recent mechanical calculators (Figure 1.5**b**) and pneumatic self-playing musical instruments (Figure 1.5**c**). Such and similar systems demonstrated that automatic, reliable systems could be based solely on mechanical and physical principles.

It is relevant to clarify, since the beginning of this thesis, that our inquiry into electronics-free approach in the era of software and AI is certainly not an attempt to overrule electronics, nor to dictate strict boundaries of what we believe design rules for robotics should be. On the contrary, we believe that this design constraint and research direction can represent a valuable asset for efficient design solutions that can emerge from design rules. Our intuition of design rules for robotic systems is modeled after strategies formalized within the context of the so-called *wired intelligence*. According to this design approach, the relations between the individual components of a given design, rather than the complexity of its individual components, can drive the emergence of well-defined reactions[2] we identify as *behaviors*[26].

Early robotics research in this direction were performed in the context of neurobiology and cybernetics [27] in the 1940s and were more systematically categorized by Valentino Braitenberg [28] and critically discussed in robotic contexts, among others, by Rodney Brooks [29, 30]. Such an approach to behavior-focused robotics shifted from the need for abstract internal representations of

[2] *Reflexive* in ethology and *reactive* robotics both indicate stimulus-response direct relation between output of a sensor and actuator, with no intermediary control policy. Similarly, *reactive* in ethology and *responsive* in robotics both refer to consolidated through learning outputs that can be changed by a control policy. Examples in the context of electronics-free sytems can be found in [25].

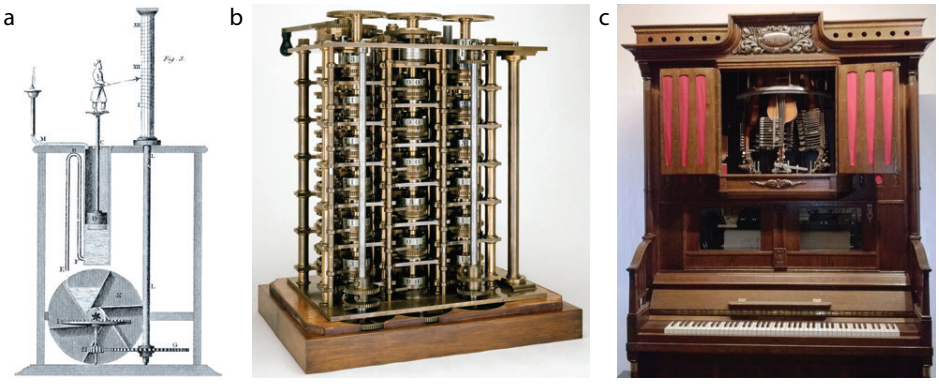


Figure 1.5: **Examples of automatic, electronics-free devices (a)** Ctesibius water clock (∼250BCE) was used up as a continuous time keeping device until Huygens perfected pendulum clocks in the 17$^{\text{th}}$ century. **(b)** *Pascaline* mechanical calculator from 1642 could perform addition, subtraction, multiplication, and division. **(c)** *Hupfeld Phonoliszt-Violina* in Speelklok Museum, Utrecht. Under constant air input flow, this automatic instrument could simultaneously play three violins and a piano.

control devices to the design of real-world physical interaction. By doing so, Brooks suggests that using wired intelligence to build reactive instead of overcomplicated responsive ones could help leverage the environment itself rather than constructing unnecessary internal representations [31]. Furthermore, we believe that focusing on electronics-free solutions can help unveil and explore physical principles that can be implemented in robotic designs and enhance their robustness in out-of-the-lab environments. We will demonstrate that such principles show the potential for programming robotic behavior while outlining strategies to control and power electronics-free pneumatic soft robotic systems.

### 1.3.3 Actuators and sensors

At the same time, it is often the case in biological systems that actuators rely on local sensing capabilities to stabilize or fine-tune their position in real-time. Examples of this *proprioperception* mechanism have been found across scales of living systems, from plants [32] to insects and human joints and muscles [33]. It is observed that proprioception capabilities can colocalize functionality and enhance the applicability potential of combined hybrid soft and stiff robotics systems. Examples in this context have been recently demonstrated, e.g., in the context

of sensing in gripping applications as Figure 1.4**b** and [23][3]. In this thesis, we leverage this principle to reduce the number of components while broadening their functionality.

## 1.4 *Looking past the paper sky*

In the aforementioned case studies, the operating policy is directly and univocally determined by the state of the environment around it, with the system directly reacting to its environment. On the contrary, while thinking in terms of robotic systems, we often picture more convoluted features, such as memory, decision-making, and autonomy, to be addressed. Nevertheless, designing such and similar solutions that could address a great variety of applications remains a daunting challenge.

Aware that no single solution could address the plethora of scenarios available, irrespective of the compliance of its hardware or the use of electronics, it is crucial to remind ourselves that, in Rodney Brook's words:

> *We do not usually complain that a medical expert system, or an analogy program cannot climb real mountains. It is clear that their domain of expertise is somewhat more limited and that their designers were careful to pick a well-circumscribed domain in which to work. Likewise, it is unfair to claim that an elephant has no intelligence worth studying just because it does not play chess.*

- Elephants don't play chess, 1990

### 1.4.1 Mechanically adaptable *marionettes*

It took 66 years from the first heavier-than-air flight in 1903 to moon landing in 1969, more than 180 years from the first general-purpose computation machine (Charles Babbage's Analytical Engine, 1837) to the first release of ChatGPT (2022). Still, the quest for autonomous systems remains an open challenge, not only from a technological point of view, but also in terms of ethical and societal implications [34]. This trend becomes even more apparent when we focus on the design of humanoid automata for demonstrating cutting-edge technologies [35], from ancient times up to modern days. The *Servant of Phylo* in Figure 1.6**a** was an automaton designed during 3$^{rd}$ century BCE as a machine to pour wine and water into serving cups [36]. Its working principles were based on pneumatic and fluidic control to automatically start serving wine whenever a cup was placed in

[3]This work is the result of a collaboration with S. Zou, J. de Vries, V. Kortman, A. Sakes and J.T.B. Overvelde published in *Nature Communication*

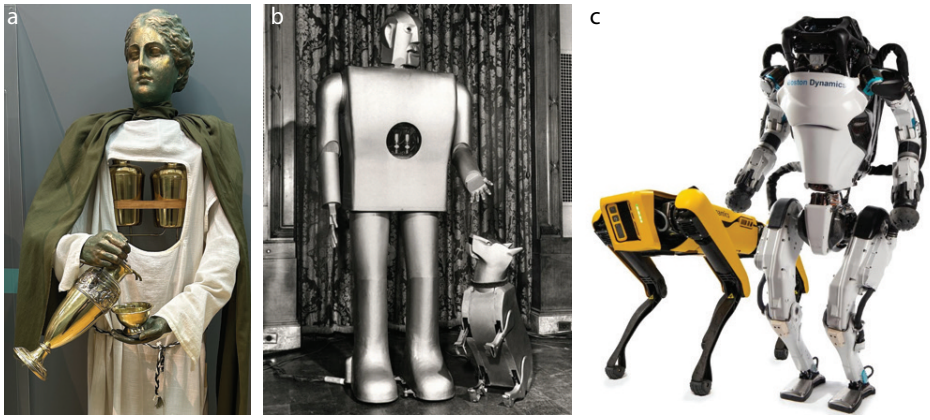


Figure 1.6: **Evolution of *marionette* automata (a)** Servant of Phylon (∼250BCE). Credits: Rhodes Museum of Ancient Greek Technology. **(b)** *Elektro and Sparko* (1939) automata. Credits: Bettmann's Archive. **(c)** *Atlas and Spot* (2020). Credits: Boston Dynamics.

its hands and stop whenever the desired proportion of water and wine was poured. Following the trend in recreational purposes, Elektro (humanoid automaton) and Sparko (dog-like automaton) in Figure 1.6**b** [37] were designed for the World Fair 1939 in New York. Elektro executed a series of preprogrammed audience interactions, including basic arm movements, cigarette smoking, balloon inflation, and speech, with a system comprising 48 relays, 11 DC motors, an air compressor, and 33 RPM records. A more recent, electronics-based example that follows and expands the principles demonstrated in the aforementioned examples is the 2020 Atlas [38] and Spot [39] robots from Boston Dynamics in Figure 1.6**c**. Atlas and Spot, in particular, have demonstrated to have the potential to outperform human precision and accuracy in dedicated tasks while adapting to unstructured environments and real-world conditions during operation.

These and other examples from robotics and pre-robotics have clarified the feasibility of designing reactive machines capable of replacing humans in various operations, thereby enhancing our capabilities in resource transformation or entertainment. However, these systems are frequently (tele)operated automatic input-output machines that adhere to operational principles that have been injected into the system. Even neural networks, after their training phase, are supposed to operate as what we define as *marionette* systems, input-output devices that, with a different degree of determinism, can automatically react to a given set of inputs. If training is online during operation, then extra precautions need to be taken into account to prevent critical events, e.g., in the case of a self-driving car or

for *intelligent* prosthetic organs. Defining accountability and ethical implications becomes then a challenge as crucial as the technical implementation of a particular *autonomous* solution.

Everyday life experience indicates that we tend to overlook many of these marionette systems that consistently enhance our living standards. Furthermore, technological advancements are continuously developing more effective methods to benefit from such systems, while also striving for the autonomy of these artificial agents.

## 1.5 Objectives

The focus of this thesis is to design marionettes that minimize the amount of *strings* required to control and power them, tackling both technical and conceptual points of view. Electronics-free systems are significant not only as a technological challenge, but also as a means of showing that behaviors can be hardwired in material properties and unfold through interactions with the environment, without the aid of electronic controllers. To move towards more and more mechanically adaptable systems, we summarize the key points concerning design rules and principles that have guided us through our work.

The first design question concerns control challenges and the use of non-linearities and soft materials to implement fundamental coding statements in electronics-free hardware. Several strategies to encode, e.g., binary logic and electronics component equivalents in fluidic soft robots have been implemented [40, 41]. However, to enable higher-level programming capabilities based on coding statements, rather than binary logic, while taking advantage of analog and parallel computation from hardware-based devices, we focus on the following research objective.

> *Objective 1. Defining a vocabulary of electronics-free circuits to materialize coding statements and embed fluidic programs in the components and their interconnection.*

To materialize the vision of having autonomous soft robots operating without *human-in-the-loop*, we must envision systems in which the environment itself, rather than a dedicated supervising agent, can provide cues for operation, as well as an accessible energy source to execute such programs. For this reason, we focus on energy autonomy aspects, with a particular emphasis on the thermodynamics of energy harvesting.

> *Objective 2. Design an energy harvesting approach for energy autonomy in electronics-free soft robotics and pave the way towards unsupervised, continuous operation.*

When designing actuation policies, e.g., for locomotion of soft robots, often two approaches are followed. In the first one, the actuation policy is fully dictated by a (external) controller that impose actuation sequences. Examples of this approach can involve electronic controllers [42], as well as well-defined patterns induced by specific networks of oscillators topologies, such as electronics-free ring oscillators [43, 44]. The second approach, more aligned with the field of active matter and complex systems, is to study and design emergence in networked systems. Oscillating patterns that emerge as a result of coupling between oscillators can, e.g., be used to control the actuation pattern of end effectors for locomotion [45] as well as programming material responses [46, 47]. This approach has proven to be beneficial, among others, in the context of central pattern generators in synthetic agents, as well as having the potential to emulate stable gait dynamics in natural systems from insects' [48] to mammals' locomotion gaits [49]. We follow this second approach to study how oscillation patterns can emerge in such and similar systems and relate high-level mathematical models to physical systems. Therefore, in this thesis, we approach the study of such networked dynamical systems by addressing the following research question.

> *Objective 3. Study analytical and numerical tools to design and interpret pattern emergence in coupled oscillators, with a particular focus on soft robotic applications.*

As we design devices less and less dependent on human supervision, addressing such systems as "intelligent" or "smart" can inflate expectations about the potential for computation and actuation capabilities that are often not met. To ideally create *robotic* systems (able to autonomously operate as human substitutes) rather than machines (automatic *extension* of human actuation, powering, and sensing capabilities), there is a deeper conceptual step that is often overlooked.

Therefore, we outline such a definition framework for *automatic* and *autonomous* systems to address practical implications and challenges for design, control theory, and safety assurance. We summarize our research direction to cope with this challenge by formulating the following research objective.

> *Objective 4. Reflect on the difference between automatic and autonomous systems, and identify fundamental requirements for autonomy in artificial systems.*

By focusing on this aspect, we mean to address societal, more than technological, challenges that often arise while having different scientific endeavors communicating with each other or presenting such systems to the general public.

1

## 1.6 Thesis structure

We reflect our contributions to the research objectives in the chapters organized as follows.

In Chapter 2, we address Objective 1, and introduce a pneumatic programming language for electronics-free soft robots, implementing analog mechanical equivalents of logical constructs like *If*, *If... break*, and *For* statements using non-linear pneumatic components. By combining these modular blocks, we demonstrate programmable behavior in a self-contained soft gripper, enabling it to alter its operating policy in response to environmental inputs without the need for electronic controllers. Following our use of soft hardware alone, we implement *pneumatic coding blocks* that mimic computation (sequencing, conditional branching and loops), grounded in the Böhm-Jacopini theorem for developing a structured coding language.

We tackle Objective 2 and the challenge of energy harvesting to enable energy autonomy in soft robotic systems in Chapter 3. Our approach is based on taking advantage of temperature gradients in the electronics-free, pneumatic soft robot environment, and harnessing thermopneumatic effects. We use a low-boiling-point fluid, combined with non-linear pneumatic components, to design a thermodynamic cycle based on naturally occurring oscillations of temperature and light intensity.

In Chapter 4, we draw inspiration from methodologies associated with central pattern generators to study the interplay of excitability and frustration in coupled oscillators. For this work, we target Objective 3 use the framework of networked dynamical systems, and more specifically Kuramoto-like oscillators. By focusing on the simplest case of two interacting oscillators, we introduce analytical tools that help reveal and interpret the range of possible behaviors such systems can display. Our broader aim is to connect these theoretical insights to practical directions, particularly the design of networked systems in the context of soft robotics.

To clarify the design purpose and scope of marionette and robotic systems, i.e. Objective 4, we engage in a detailed discussion of the definitions of automatic and autonomous systems in Chapter 5. Starting from considerations regarding critical applications such as autonomous vehicles and implantable medical devices, we examine the underlying implications of such definitions in artificial agents. We address the dichotomy between performance and risk when using automatic control loops rather than potentially autonomous designs that can encourage unexpected emergent behaviors.

In Chapter 6, we conclude by retrospectively analyzing how our work is related to automatic and autonomous systems. We propose that mechanical adaptability serves as a stepping stone towards the creation and development of autonomous artificial agents.

This thesis is structured according to a paper-based format. Chapters 2–5 are based on journal articles that have been published, submitted, or are currently in preparation, and present the core concepts, methods, and results relevant to addressing our research objectives.

The chapters of this thesis are organized according to structures appropriate to their respective aims and methodologies. Chapters 2 and 3 follow the format commonly used in experimental science publications, with results presented before methods. Chapter 4 adopts a more theoretical organization, in which the modelling framework and analytical methods are introduced prior to the presentation of results. Chapters 5 and 6 depart from the conventional scientific paper structure and adopt a more conceptual and reflective organization, allowing for a broader discussion of underlying ideas related to adaptability and autonomy.

Although the chapters differ in purpose and format, they are unified by a common research goal of investigating strategies to enable adaptability in fluidic soft robots. Each chapter approaches this theme from a different perspective, and together they form a coherent narrative that explores adaptability from experimental, theoretical, and conceptual angles.

To preserve clarity and continuity in the main text, only material essential to the central narrative of each chapter is included. At the end of Chapters 2, 3, and 4 we provide an additional justification to link together the different content under one narrative flow.

Supplementary figures, extended derivations, and methodological details specific to each chapter are provided separately in the corresponding supplementary material at the end of each chapter. Several chapters refer to supplementary video material that illustrates experimental setups and system's behavior. Readers consulting the electronic version of this thesis may access all videos referenced in the following chapters via this link. For the printed version, access is provided through the accompanying QR code.

1

# Chapter 2

# Pneumatic coding blocks enable programmability of electronics-free fluidic soft robots

2


Abstract

Decision-making based on environmental cues is a crucial feature of autonomous systems. Embodying this feature in soft robots poses non-trivial challenges on both hardware and software that can undermine the simplicity and autonomy of such devices.

Existing pneumatic electronics-free soft robots have so far mostly been approached by using system fluidic circuit architectures analogous to digital electronics. Instead, here we design dedicated *pneumatic coding blocks* equivalent to *If*, *If... break* and *For* software control statements, which are based on the analogue nature of non-linear mechanical components. We demonstrate that we can combine these coding blocks into programs to implement sequences and to control an electronics-free autonomous soft gripper that switches between behaviors based on interactions with the environment. As such, our strategy provides an alternative approach to designing complex behavior in soft robotics that is more reminiscent of how functionalities are also encoded in the body of living systems.



Published as: Pneumatic coding blocks enable programmability of electronics-free fluidic soft robots, Sergio Picella, Catharina M. van Riet, and Johannes T. B. Overvelde, *Science Advances* 2024

## 2.1 Introduction

2

Soft robotics branches off more traditional robotics and offers a hardware platform for diverse contexts where adaptivity and sensitivity are important, ranging from agriculture to medicine and human interaction [50–53]. In particular, compliant hardware enhances robustness to unstructured and unknown tasks by embodying mechanical behavior that responds directly to external stimuli [15, 54]. Nevertheless, many soft robotic systems still rely on electronic sensors and controllers that, although potentially accurate, cheap and precise, impose additional fabrication challenges for the integration into the soft hardware. Furthermore, integration of electronics also limits the potential broad application perspective of soft robotics in domains where electronics would fail, including high radiation environments [55, 56], implantable medical devices [57], de-mining applications [58], or explosive environments in general [59].

As such, a recent trend in soft robotics points towards reproducing the response of electronic components using a pneumatic electronics-free approach [60, 61]. Several studies have focused on the development of components with logic-port functionalities [40, 62], which often depend on mechanical non-linearities and instabilities to generate complex behavior [44, 63–66]. Based on these components, a few robots have been built with programmed functionalities that arise when combining multiple components [43, 67]. However, although these components and circuits share similar features with their electronic counterparts, a more general approach for achieving high-level programmability to build pneumatic circuits is still missing. A strategy to effectively convert preferred behavior to a pneumatic circuit design would make electronics-free soft robots even more appealing, as it would simplify and allow the embodiment of more complex programs in the soft robots that can interact with the environment directly.

We enable the design of electronics-free soft robots that can autonomously make decisions (i.e. switch between different behaviors or programs) based on interactions with the environment, by drawing inspiration from mechanical programming. Machines and robots designed prior to the advent of software had to rely exclusively on hardware programming, thus basing their working principles on interactions of mechanical and pneumatic components with themselves and operators. The schematics of these robots and automated machines were often based on the intuition of so-called wired intelligence. According to this design principle, different behaviors from the machines can be obtained by directly connecting actuators and sensors, with no need for dedicated controllers [28]. In our case study, we design our systems to follow similar design rules and constraints to avoid the use of external electronic controllers in pneumatic circuits.

To achieve mechanical programming, we take inspiration from the modularity of coding statements used in software programs. We aim to design a general

library of pneumatic circuit blocks that enable the programmability of pneumatic soft robots and allow them to run versatile pseudocodes that can be designed following our circuit design approach. We set the basis for a structured coding language by identifying the minimal requirements for our pneumatic equivalent coding language to comply with the hypotheses of the Böhm-Jacopini theorem[68]. According to this programming language theorem, a program has the potential to execute any task if the control system has the following capabilities: *i)* executing commands in sequence, *ii)* conditionally going to subprograms through selection statements, and *iii)* repeating subprograms as long as a boolean condition is met. Therefore, we focus on prototyping statement-equivalent circuits that can manifest these functionalities to write and run pneumatic electronics-free programs for soft robots.

We introduce pneumatic circuits for *If*, *If... break* and *For*, and demonstrate the sequential execution of instructions. We then introduce the designs for both continuous and boolean variables that can be used in our fully pneumatic programming environment. Finally, we demonstrate that our modular approach enables more complex programming, where we focus on a soft gripper that changes its behavior when detecting an object, as we schematically represent in Figure 2.1. Through our demonstrator, we show that our modular coding approach allows the integration of actuation, sensing and feedback within the same pneumatic platform.

## 2.2 Results

### 2.2.1 Programming environment

To introduce our soft pneumatic programming environment, in the following section, we present our statement equivalent coding blocks for the *If*, *If... break*, and *For* control flow statements and show their operation in Video 1 (Section 2.5). Furthermore, we demonstrate that our soft pneumatic coding approach allows for introducing variables that can be written, read and used through mechanical interaction with the pneumatic system. Analogous to coding, we give the equivalent pseudocodes of the soft pneumatic programs we introduce in this section. We include additional examples of control statements and circuit designs implemented through our electronics-free strategy in Supplementary Material.

### 2.2.2 Fluidic *If* implementation

The first fluidic circuit we design reproduces the functionality of an *If* statement. To design our fluidic circuit, we make use of a soft hysteretic valve that was previously developed by our group [69]. The hysteretic valve is based on an

2

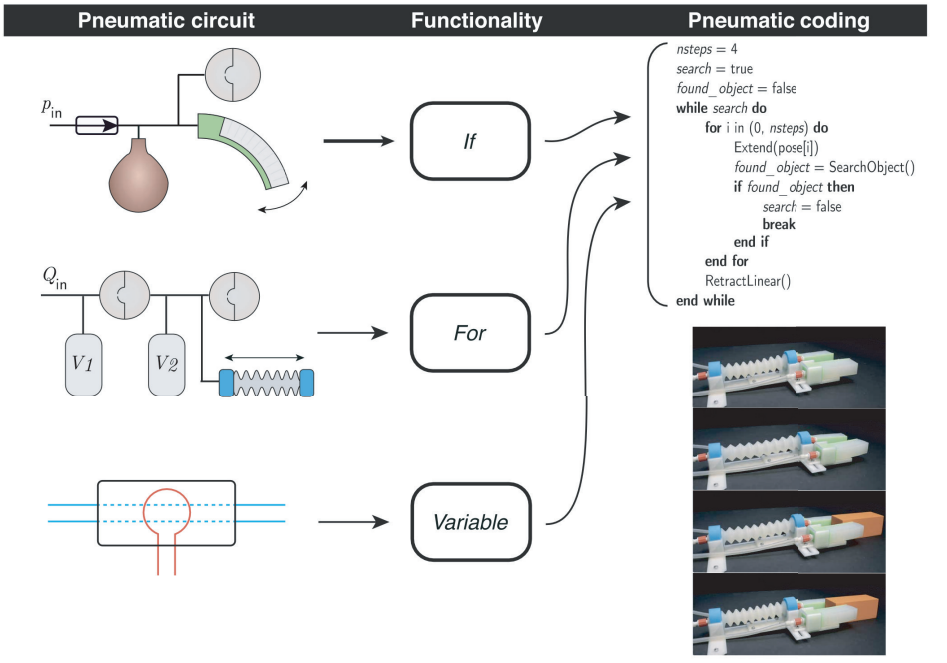


Figure 2.1: **Overview of our design approach to enable pneumatic coding.** Our approach is based on a library of dedicated pneumatic circuits that represent specific coding statements. These statements can be combined to develop pneumatic programs that can respond to the environment.

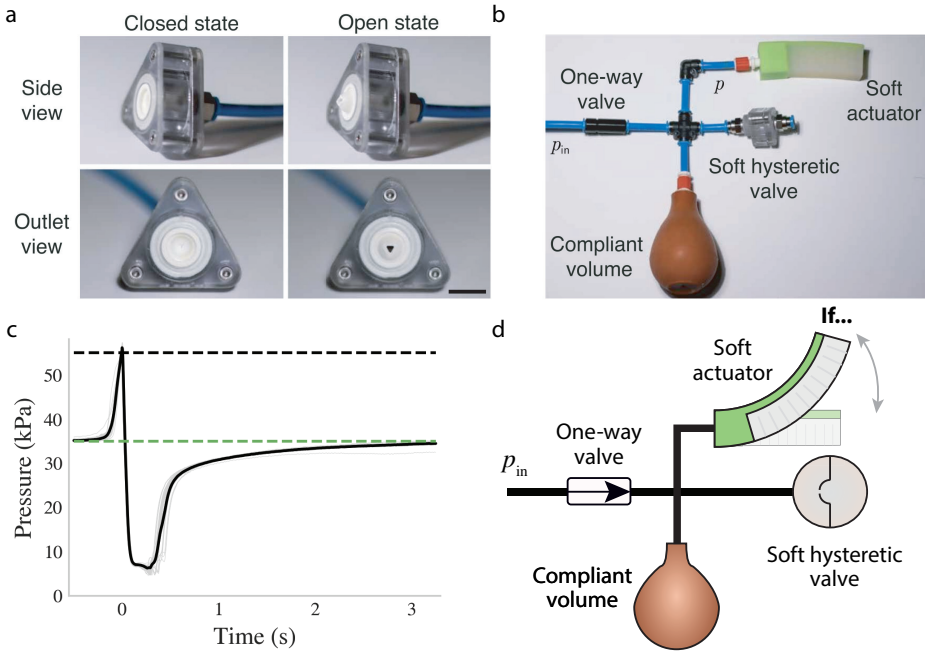


Figure 2.2: **Pneumatic equivalent of an *If* statement.** (**a**) Experimental realization of a soft hysteretic valve in its holder in its closed and open states. Scale bar = 12mm. (**b**) Experimental realization of the *If* pneumatic circuit. (**c**) Measurement of the pressure $p$ upon interacting with (squeezing) the compliant volume. The interaction occurs at $t = 0$s. The dashed green and black lines indicate $p_{\text{in}} = 35$kPa and $\Delta p_{\text{open}} = 55$kPa of the hysteretic valve, respectively. The grey solid lines are individual pressure measurements at ten different interaction events, and the black solid line indicates their average. The inset photos represent the state of the soft actuator at the specific moment in time. (**d**) Schematic of pneumatic circuit used for the *If* functionality in **b**.

elastomeric dome with three cuts at its apex. When the $\Delta p$ pressure difference between the pressure upstream and downstream of the valve is below a critical value $\Delta p_{\text{open}}$, the valve remains in a *closed* state. When the pressure on the initially closed valve reaches a critical value $\Delta p > \Delta p_{\text{open}}$, the dome snaps and the valve transitions to its *open* state in which air can flow through the valve. Upon reducing the pressure, the dome snaps back to its closed state when the upstream pressure drops below a $\Delta p_{\text{close}}$ value. We report examples of the open and closed state of the soft hysteretic valve in Figure 2.2**a**.

To enable the *If* functionality using this hysteretic valve, we make use of the critical opening pressure of the valve, combined with pressure fluctuations that can trigger the opening. We demonstrate the functionality in a fluidic circuit in Figure 2.2**b**, where we show both the experimental realization and a schematic. Additional setup parameters are reported in Table S2.17. We connect a compliant volume that we can interact with before the soft hysteretic valve and pressurize it to $p_{\text{in}}$ so that the pressure difference across the valve is $\Delta p_{\text{if}}$, being lower than the critical value $\Delta p_{\text{if}} < \Delta p_{\text{open}}$. In addition, we connect a one-way valve to prevent backflow upon interaction with the compliant volume. Now, when we squeeze the compliant volume, the increase in pressure causes the soft hysteretic valve to snap open, triggering the *If* statement (Figure 2.2**b**). Note that in the circuit in Figure 2.2**b-d**, we use a soft actuator to indicate the pressure when the *If* condition is met and after it when pressure equilibrates back to $p_{\text{in}}$.

As the whole circuit is pressure controlled, the pressure automatically resets to $\Delta p_{\text{if}}$ after an opening event as long as the pressure difference dips below the closing pressure $\Delta p_{\text{close}}$ of the valve (Figure 2.2**c**). The time scale of the reset can be controlled by including additional fluidic resistances in series with a one-way valve. Moreover, the sensitivity of the *If* condition can be increased or decreased by varying $\Delta p_{\text{if}}$ to be closer or further from $\Delta p_{\text{open}}$, respectively (Figure S2.1). Using this principle, soft hysteretic valves can be used to detect interaction with the environment as we show in Figure 2.2.

This circuit can be regarded as an *If* statement that is triggered by a mechanical interaction and that automatically resets afterwards. The equivalent pseudocode for this specific configuration is shown in Algorithm 1. Through our fluidic implementation of the *If* pneumatic coding block, we materialize the selection control statement required to meet the selection hypothesis of Böhm-Jacopini theorem.

**Algorithm 1** Pseudocode for the *If* circuit in Figure 2.2

```
Pressurize(actuator)
if interaction then
    Deflate(actuator)
end if
```

### 2.2.3 Fluidic *If... break* implementation

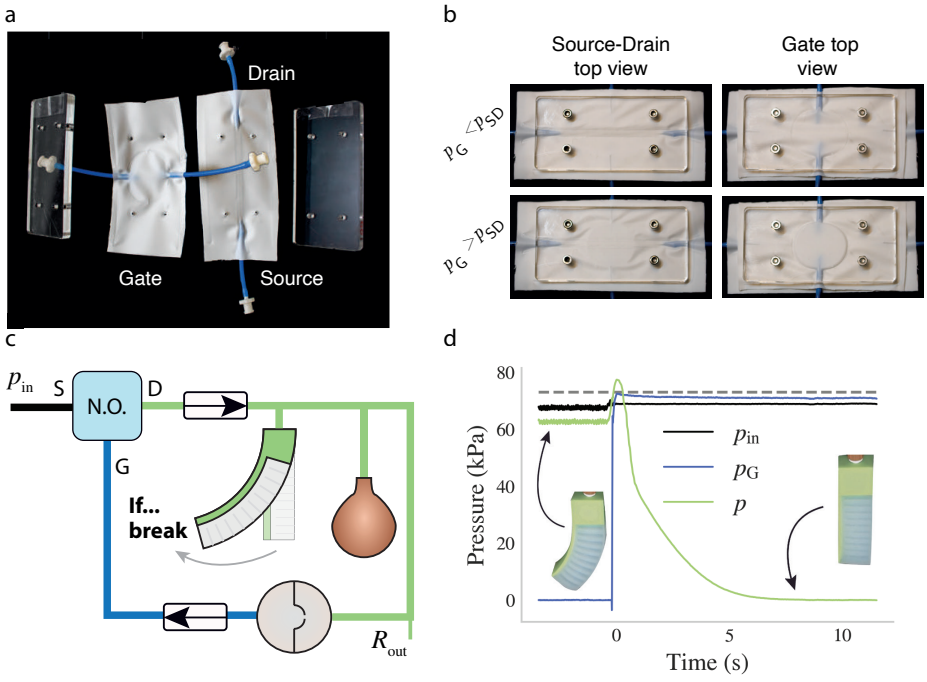


Figure 2.3: **Pneumatic equivalent of an *If... break* statement.** (**a**) Schematic of the components used to assemble a pneumatic N.O. valve. (**b**) Assembled N.O. valve, for different gate pressures. (**c**) Schematic of the *If... break*. **d** Experimental measurement for a pneumatic circuit based on the schematic in **c**, for an interaction event with the compliant volume that occurs at $t = 0$s. The black, blue, and green solid lines represent the approximately constant input pressure $p_{in} \approx 68$kPa, the pressure at the gate $p_G$ of the N.O. valve, and the actuator pressure $p$, respectively. The dashed line represents the opening pressure $\Delta p_{open} = 70$kPa of the hysteretic valve. Snapshots of the actuator's state are taken from the experimental realization of the setup at the corresponding moments in time.

The *If* condition alone serves the purpose of a trigger event for which input signals must overcome a certain programmable threshold to activate the conditional statement. In order to harness the analogy with coding statements further, we next design an *If... break* statement. To achieve this, we introduce a pneumatic

Normally Open (N.O.) valve that draws inspiration from microfluidic valves [70]. Our valve is shown in Figure 2.3**a** and is fabricated by heat sealing two pairs of Thermoplastic Polyurethane (TPU) sheets together (Figure S2.5). The channels and pouches that reproduce the N.O. valve functionality are reported in Figure 2.3**b**, as also indicated by the *source-drain* and *gate* channels. We stack the TPU sheets and confine them between two acrylic sheets (Figure 2.3**b**) to guarantee the mutual influence of the channels on one another when they are pressurized. If the gate channel is not pressurized, air can freely flow between the input (source) and output (drain) ports. When the gate channel is pressurized at a sufficiently high pressure, it will close the channel connecting the source to the drain.

To achieve the *If... break* functionality, we place the source and drain of the N.O. valve in series with the pressure input of the *If* circuit. We make use of the triggered output pressures from the hysteretic valve to control the gate pressure of the N.O. valve. Note that we include an $R_{\text{out}}$ fluidic resistance in parallel with the actuator that is venting to the atmosphere. This ensures that, once the gate is pressurized, the soft actuator can deflate. With this setup, it is possible to control pressures and flows in other parts of the circuit as we demonstrate through the circuit in Figure 2.3**c**. Additional setup details in Table S2.17. Similar to the *If* circuit, we first pressurize $\Delta p_{\text{if}} < \Delta p_{\text{open}}$, which results in the bending of the soft actuator. When we now interact with the compliant volume, the valve opens, deflating the actuator and pressurizing the gate of the N.O. valve. As a result, the actuator does not repressurize because the gate pressure prevents airflow through the source-drain channel (Figure 2.3**d**).

The functionality of this pneumatic circuit is described by the pseudocode in Algorithm 2, which is characteristic of an *If... break* statement. Note that larger (or smaller) $R_{\text{out}}$ values result in slower (or faster) deflation times as well as in higher (or lower) actuator pressures when the N.O. valve is in the open state, similarly to what previously has been demonstrated [71]. Moreover, note that by adding different fluidic resistors venting to the atmosphere in the gate branch (Figure S2.6), we find different timescales for automatic reset of $p_{\text{G}}$. Thus, both long-term and short-term memory of the triggered state can be achieved. On top of that, if no fluidic resistor is used in the gate branch, $p_{\text{G}}$ is held indefinitely, as we show in Figure S2.7.

### 2.2.4 Fluidic *For* implementation

The ability to iteratively perform a task is a key feature for designing compact and versatile software. To obtain a fluidic implementation of the iterations needed to meet the requirements of Böhm-Jacopini theorem, we implement a pneumatic circuit representative of the *For* control statement in our electronics-free environment. Similar to the *If* statement, we base the *For* functionality on

**Algorithm 2** Pseudocode for the *If... break* circuit in Figure 2.3**c**

```
while true do
    Pressurize(actuator)
    if interaction then
        Deflate(actuator)
        break
    end if
end while
```



circuits containing hysteretic valves. Previous work from our group demonstrated that when a hysteretic valve is supplied with a continuous flow $Q_{\text{in}}$, it starts to act as a relaxation oscillator by opening and closing cyclically at a fixed frequency [69]. The frequency can be tuned by varying a volume $V_1$ placed before the valve or by controlling the inflow $Q_{\text{in}}$ of air. Therefore, this device converts a continuous input flow into a pulsatile output flow, so that, at each snapping event, a finite amount of air traverses the orifice of the valve.

The pneumatic *For* circuit we design is based on two hysteretic valves connected in series, using only a single constant flow $Q_{\text{in}}$ as input (Figure 2.4**a** and Table S2.17). We found that, when connecting the output of a first hysteretic valve with the input of a second hysteretic valve, the air released from the first valve pressurizes a volume $V_2$ placed between both valves in discrete steps (Figure 2.4**b**). This step-wise increase in pressure occurs until the buckling pressure $\Delta p_{\text{open},2}$ of the second valve is reached. At that moment, the trigger event of the first valve also triggers the opening of the second hysteretic valve, hence automatically resetting the whole system. We demonstrate the potential for applications with the example in Figure 2.4**a-c**, in which we inflate a soft actuator in discrete steps, after which the position of the linear actuator resets before the cycle starts (Figure 2.4**b**). Through the nomenclature "Extend($pose[i]$)" in Algorithm 3, we refer to the linear extention of the bellow actuator to these discrete positions.

From a functionality point of view, we obtain a step-wise increase in pressure that automatically resets after a number of discrete steps, hence mimicking the *For* control statement functionality. The functionality of this fluidic circuit is indicated in the pseudocode in Algorithm 3. Moreover, besides a *For* loop, the introduced pneumatic coding block can also be employed as a time trigger or internal clock for pneumatic soft robots. In our fluidic circuit, note that the $V_1$ and $V_2$ volumes dictate both the number of iterations before the reset mechanism is triggered and the duration in time of the *For* loop. In Figure 2.4**d**, we report the different number of steps in the *For* loop and the duration of the loop for different combinations of $V_1$ and $V_2$. More details about design rules for the number of iterations timing are given in Figure S2.9. We separately highlight

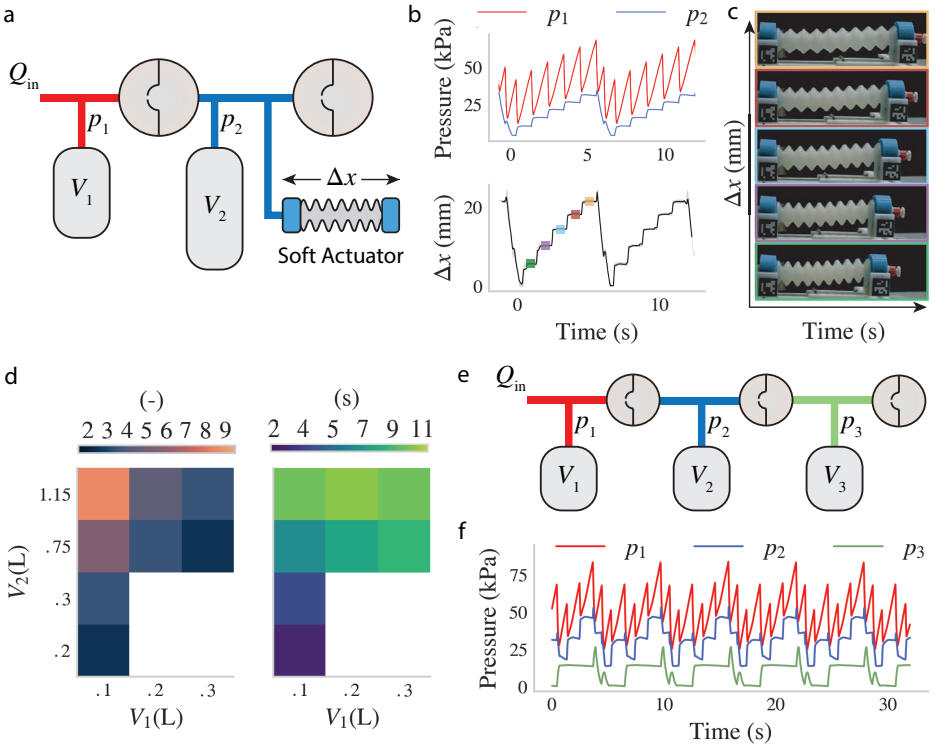


Figure 2.4: **Pneumatic equivalent of a *For* statement.** (**a**) Schematic of the pneumatic *For* circuit. $x$ indicates the linear extension of the soft actuator. (**b**) Experimental measurement of the averaged pressure in volumes $V_1$ and $V_2$, and tracking of the extension $\Delta x$ of the linear actuator with respect to its resting position over 20 different repetitions of the *For* loop. (**c**) Snapshots of the linear actuator used for the corresponding highlighted positions as indicated by the colored dots in **b**. (**d**) Different number of iterations (left) and periods (right) of the *For* loop for different volume combinations of $V_1$ and $V_2$.The black entries on the heatmaps represent $V_1$ and $V_2$ combinations for which the *For* behaviour in **b** was not observed. Note that for this experiment the soft actuator was removed from the setup. (**e**) Schematic and (**f**) experimental data of the nested *For* loop.

three cases in our experiment in Figure S2.10**b**.

**Algorithm 3** Pseudocode for the *For* circuit in Figure 2.4**a**

```
nsteps = 5
while true do
    for i in (0,nsteps) do
        Extend(pose[i])
    end for
end while
```



Importantly, the connection in series of multiple soft hysteretic valves can be further exploited to obtain nested *For* loops. We report an example case in Figure 2.4**e-f** where we connect three valves in series to obtain two nested, step-wise increasing pressures with two distinct states for $p_2$ and three for $p_3$, being able to describe overall six distinct states. Note that pressure is not only the actuating medium but also encodes the state of the system. Thus, pressure can be directly used by the circuit itself with no need for an external processor or transducer. Yet, this also puts constraints on the number of nested loops that can be achieved.

### 2.2.5 Sequential execution of instructions using the *For* statement

Before continuing with our fluidic implementation and representation of variables, we demonstrate the potential for application of the *For* pneumatic circuit by using it as a clocking device to enable simultaneous readout and execution of sequential instructions. With this demonstration we show that we meet the first requirement for the Böhm-Jacopini theorem. We materialize this functionality by introducing the design of a demultiplexer in Figure 2.5. The demultiplexer device we design is based on the working principles of cardboard punched cards, particularly popular in traditional book organs, automatic looms and early computers. The demultiplexer strategy works by sliding a PVC punched card through a slot, which, based on the positions of holes, connecting $p_{\text{in}}$ to four different outputs. To address the pressure outputs in sequence and execute instructions sequentially, we drive a punch card with several holes using the pneumatic *For* coding block that generates the step-wise inflation of a linear extension of the bellow actuator as we demonstrated in Figure 2.4**b**. Note that to reach larger extensions of $\sim$ 10cm we used a hysteretic valve with an opening pressure of 55kPa, which is higher than the one we used in Figure 2.4**b**. As a result, using the pneumatic circuit in Figure 2.5**a**, the punched card is fed into the readout device shown in Figure 2.5**b** at well-defined positions in time.

Using this demultiplexer, we can implement sequences and sequential execution

of coding statements such as selection (*If*, *If... break* and *If... else*) and iteration (*For*) statements. Specifically, we aim to use this component to implement a device that can execute the pseudocode in Algorithm 4. As we highlight in this algorithm, the strategy implemented for executing the sequences of instructions can be rewritten in terms of *For* and *If* statements.

**Algorithm 4** Pseudocode for the execution of sequential instructions as represented in Figure 2.5**b** and Video 1 (Section 2.5). *StepTime* variable can be modified by operating on the frequency of the *For* loop feeding the instructions into the decoder.

```
while true do
    for i in (0,8) do
        if i in [0,1] then
            Pressurize(p1)
        end if
        if i∈[2,3] then
            Pressurize(p2,p3)
        end if
        if i∈[4,5] then
            Pressurize(p3)
        end if
        if i∈[6,7] then
            Pressurize(p4)
        end if
        Wait(StepTime)
        Depressurize(p1,p2,p3,p4)
    end for
end while
```

To design a pneumatic circuit to run this code, and to demonstrate the workings of the demultiplexer, we connect its output channels to four bellow actuators as shown in Figure 2.5**b** and use a specific design of a punch card that addresses all of the four output channels that are connected to the bellows. The resulting response when providing an input of $p_{\text{in}} = 367\text{kPa}$ is visually shown in Figure 2.5**c** and Video 1 (Section 2.5), while we report the data for this experiment in Figure S2.11. As expected, instructions that originate from the design of the punched card are executed sequentially in time at the frequency dictated by the fluidic *clock* mechanism enabled by the *For* loop (Figure S2.11**a-c** and Video 1 (Section 2.5)).

Note that in our design, the number of instructions that can be read in time mostly depends on the number of extension steps executed by the *For* loop.

Instead, the number of channels (different sets of instructions to be executed) is determined by the design of the demultiplexer and depends on the number of output channels of the readout device. Moreover, note that as the position of the punched card is determined by the extension of the linear actuator, once the *For* loop restarts, the punched-hole card also resets to initial conditions. During this retraction phase, all the instructions are sequentially re-executed in reverse order when the linear actuator retracts. However, the retraction occurs relatively quickly, limiting the time that each channel is addressed as can also be seen in Figure S2.11. Additionally, by using internal delays and resistances, the input pressure can potentially effectively be disconnected during the retraction phase. Design parameters for the experimental realization of this experiment are reported in Figures S2.12-S2.13 and Table S2.17.

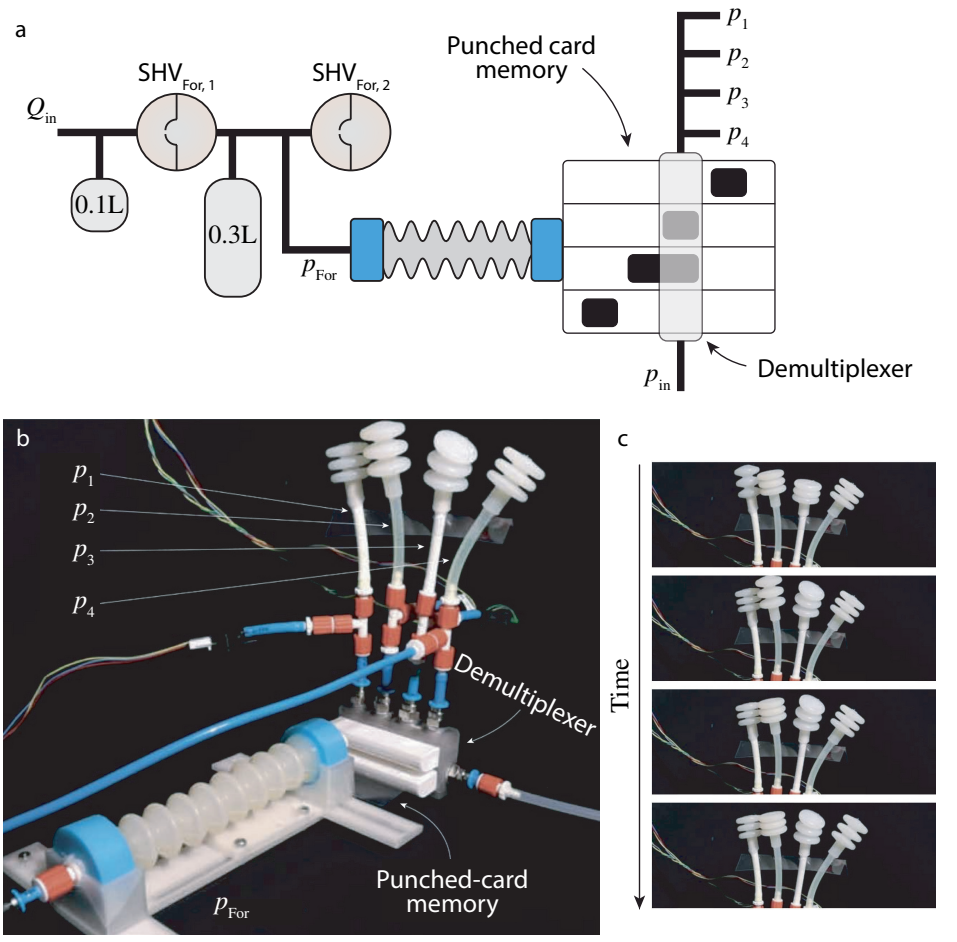


Figure 2.5: **Schematic of a pneumatic circuit and component to obtain sequential execution of instructions.** The *For* loop enables clocking capabilities and feeds a 0.1mm PVC punched card that encodes the instructions to be executed. By connecting an input pressure $p_{in} = 367$kPa, the four different output channels can be pressurized following the sequence of instructions in the physical support memory. **(a)** Circuit design and physical support memory. In black, the punched holes provide the change of fluidic resistance required to pressurize a specific channel. The duration of operation can be encoded in the different lengths of each aperture. **(b)** Experimental realization of the setup. **(c)** Highlight of bellow deformation as a consequence of the sequential readout of instructions in time. We report the data from this experiment in Figure S2.11 and its realization in Video 1 (Section 2.5).

### 2.2.6 Fluidic implementation of variables

Variables are fundamental building blocks of any program as they allow encoding of both the results of internal memory and external inputs. In fact, we can already identify the use of variables in previously introduced coding statements. For example, for the *If... break* statement, the N.O. valve describes a discrete variable as it can be in an open or closed state, analogous to a *true* or *false* state. Interestingly, by setting the gate pressure $p_G$ of the N.O. valve to intermediate levels between the fully open and fully closed states, we can regulate the flow from source to drain, therefore encoding non-binary information through the pressure at the gate branch. To demonstrate this, we leverage this approach to write continuous pneumatic variables to control both the amplitude and frequency of oscillation in a pneumatic soft actuator. In our demonstrator in Figure 2.6**a**

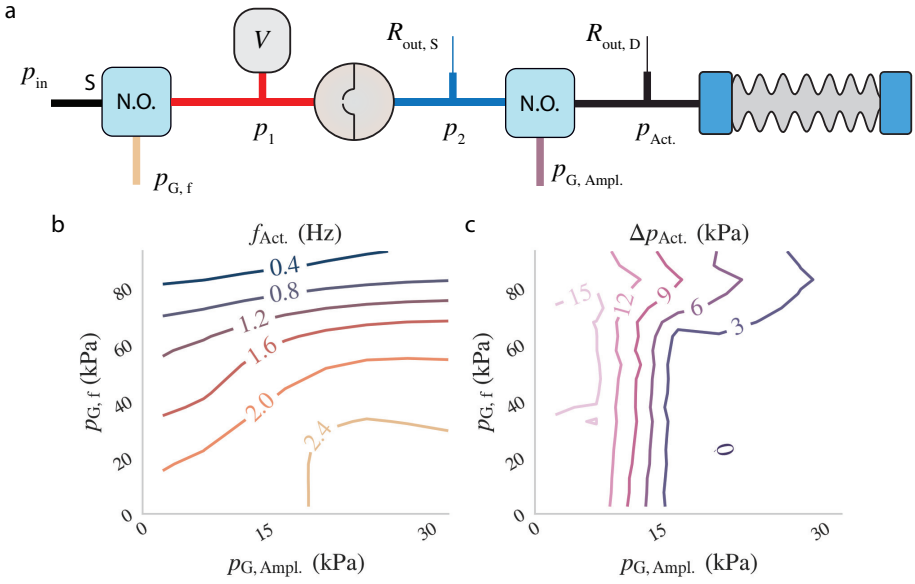


Figure 2.6: **Encoding pneumatic continuous variables using N.O. valves.** (**a**) Schematic of the pneumatic circuit. (**b**) Iso-frequency $f_{Act}$ and (**c**) iso-amplitude of oscillations $\Delta p_{Act}$ curves as a function of the control parameters $p_{G,\,Ampl.}$ and $p_{G,\,f}$.

and Video 4 (Section 2.5), we tune the gate pressures for the frequency control $p_{G,\,f}$ and for the amplitude control $p_{G,\,Ampl.}$ of two different N.O. valves. Here, $p_{G,f}$ dictates the fluidic resistance of the first N.O. valve that converts an input pressure $p_{in}$ coming from a pressure regulator into a tunable, continuous input

flow for the downstream branch. The resulting flow feeds a soft hysteretic valve that converts the continuous input flow into a pulsatile one. Moreover, we use $p_{\mathrm{G,\ Ampl.}}$ to isolate the actuator branch from the remainder of the circuit, therefore controlling the amplitude of the oscillations of the linear actuator. Note that we connect the output of the soft hysteretic valve in parallel to a fixed fluidic resistor $R_{\mathrm{out,\ S}}$. Moreover, the drain of the second N.O. valve is connected in parallel with a second fixed resistor $R_{\mathrm{out,\ D}}$ and the soft actuator. The role of $R_{\mathrm{out,\ S}}$ and $R_{\mathrm{out,\ D}}$ are to vent to the atmosphere after each oscillation, allowing pressure to automatically reset after each snapping event of the soft hysteretic valve. With this demonstrator, we have therefore introduced the notion of continuous variables in our pseudocode, as described in Algorithm 5.

**Algorithm 5** Pseudocode for the circuit using continuous variables in Figure 2.6**a**

```
while true do
    Extend(amplitude(p_{G,Ampl.}),frequency(p_{G, f}))
end while
```

We demonstrate in Figure 2.6**b-c** that it is possible to control the frequency, amplitude and absolute pressures of oscillations. Our circuit characterization shows that it is possible in the parameter design space to tune frequencies between .1Hz and 5Hz while controlling the amplitude of the oscillation at the same time. We report extended data on this experiment in Figure S2.8. Moreover, we push further the parallelism between traditional programming and our hardware fluidic coding by introducing boolean variables in Figure S2.23.

## 2.3 Programming behavior and feedback in a soft gripper

To demonstrate the applicability of our approach towards designing fluidic programs using the previously introduced fluidic coding blocks, we next combine our statement-equivalent circuits to assemble a soft fluidic demonstrator that runs a basic program. This program focuses on enabling an independent interaction with the environment. Our aim is to integrate embedded sensing in the gripper so that it is able to detect an object and change behavior accordingly. Specifically, we aim to develop a program for a single pneumatic soft robotic gripper with two pneumatic degrees of freedom. One degree of freedom activates two bending actuators that can grip an object, while the second degree of freedom controls a soft extension actuator that is used to extend and retract the gripper. These soft actuators are assembled on a **P**oly**L**actic **A**cid (PLA) 3D-printed frame (Figure

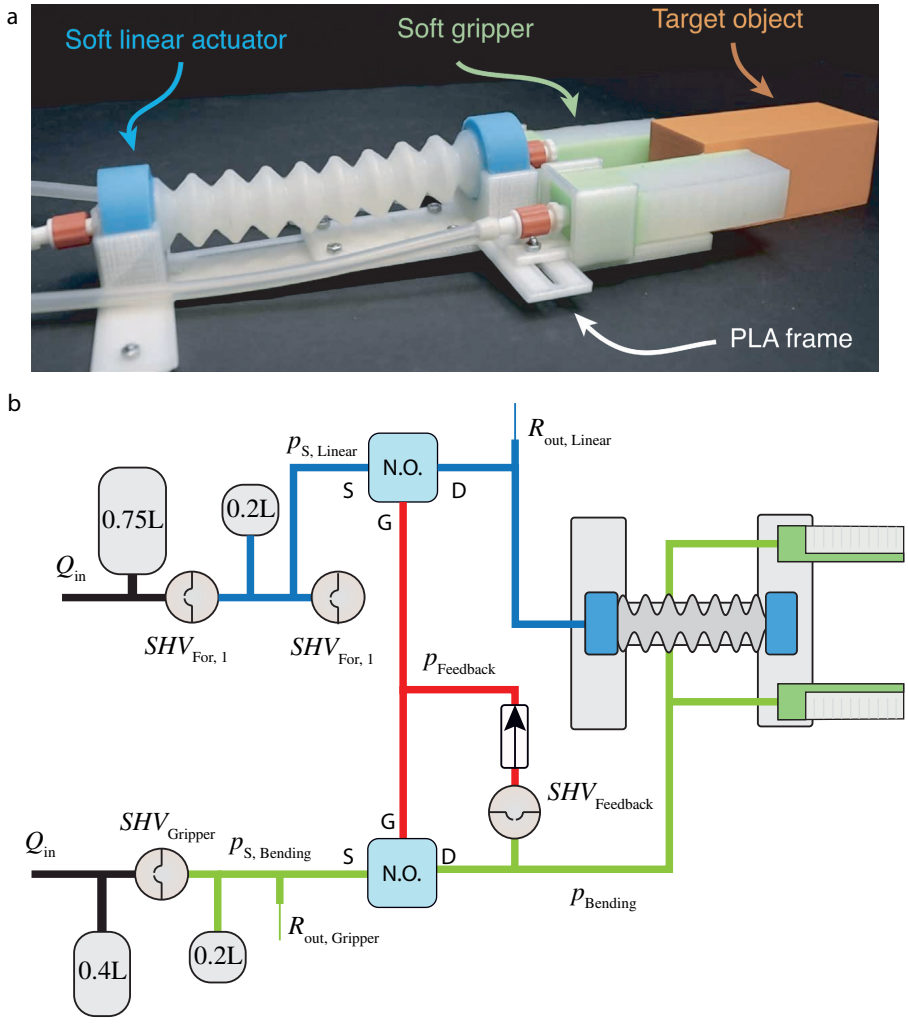


Figure 2.7: **Assembly of pneumatic coding blocks to design a circuit for a soft robotic retriever demonstrator.** (**a**) Highlight of the hardware components. We assemble a soft linear actuator with two bending actuators through a PLA frame. This allows us to obtain a pneumatic soft robot that can elongate as well as grab target objects. (**b**) We combine the *For* (blue) and *If... break* (red) pneumatic coding blocks to functionalize the actuators so that the pneumatic soft retriever executes the program in Algorithm 6.

2.7**a**).

To design our demonstrator, we start by writing the pseudocode as given in Algorithm 6. This pseudocode describes the behaviour of a soft gripper that is searching for an object by extending along a line in multiple steps. If an object is detected, the object is grasped, after which the gripper retrieves the object by moving back to its initial position.



**Algorithm 6** Pseudocode for the pneumatic soft retriever in Figure 2.7

```
nsteps = 4
search = true
found_object = false
while search do
    for i in (0,nsteps) do
        Extend(pose[i])
        found_object = SearchObject()
        if found_object then
            search = false
            break
        end if
    end for
    RetractLinear()
end while
```

Next, we transform the pseudocode into a fluidic circuit as shown in Figure 2.7**b**, for which we combine the previously developed fluidic coding statements. We combine the pneumatic coding blocks representative of the *For* and *If... break* statements. Note that we only need a constant power input to the system, and no control is further needed. This power is provided by two flow sources as shown in Figure 2.7**b**, which feed into the two separate branches of our fluidic program that run in parallel. One of the branches incrementally extends the position of the gripper by pressurizing the linear actuator similar to the example in Figure 2.4**b**. The second branch periodically inflates and deflates the soft gripper, similar to the overall behavior explained in the *For* coding block, but with only one iteration before reset. The range of motion of the gripper can be tuned by changing the $R_{\text{out, Gripper}}$, following the same approach we presented while studying pneumatic variables in Figure 2.6.

Moreover, we use the *If... break* circuit to embed sensing in the soft gripper. This feature can be achieved by harnessing the fact most soft actuators can also directly be used as a sensor [23]. As an example, when the deformation of the soft gripper is constrained, pressure will (slightly) increase as internal volumetric changes are now limited by the interaction with the environment. Comparing this

observation with the examples we provided in the *If... break* circuit, this means we do not need the additional bulb. Instead, we can use the increase in pressure in the soft actuator due to interactions with the environment as the trigger event for the hysteretic valve used in the *If... break* statement.

At the same time, the trigger signal from the *If... break* can be used to isolate the linear actuator following the example circuit we demonstrated in Figure 2.6, preventing it from oscillating once the object is detected. As a result, when the *If... break* statement is triggered, the feedback loop should change the preprogrammed response of the soft robotic unit.

From a functionality point of view, the states of the boolean variables we report in the pseudocode Algorithm 6 are encoded in the pressure at the gates of the N.O. valves. By using a fluidic resistance $R_{\text{out, Linear}}$ in parallel with the linear actuator, once it is isolated from the *For* branch, it deflates through $R_{\text{out, Linear}}$ and thus retracts. Note that we do not employ this strategy in the gripper branch so that the pressure inside the gripper is retained once the *If... break* condition is triggered. By doing so, the retriever keeps on gripping the target object while retracting instead of scanning the environment.

The fully measured behavior of the soft gripper with embedded sensing is shown in Figure 2.8. When the program is initialized, the inflow at the gripper is regulated to match the actuation frequency of the linear actuator. This subprogram loops until the *If... break* condition is triggered by the presence of the target object, which we place after the eighteen loops of the full program, and occurs after approximately 370s in Figure 2.8**a-c**. At this point, we see a clear change in behavior, as the N.O. gates in the fluidic circuit are triggered. This caused the soft extension actuator to retract, and the soft gripper to remain closed. It is important to note that we still observe some pressure oscillations in the linear actuator and soft gripper branch of the program. In Video 2 (Section 2.5) we report the execution of this experiment together with the autonomous switch from the *scan & search* (Figure 2.8**d-f**) to the *grip & retrieve* behaviours Figure 2.8**e-g**. We do note that during the operation of the gripper, the operator is manually touching the soft gripper, which could aid the detection of the object by increasing the deformation of the gripper and, thus, the internal pressure.To demonstrate that the gripper can autonomously detect an object, we performed an additional run of this experiment with a slightly modified circuit design in the *For* pneumatic coding block (Figure S2.14 and Video 2 (Section 2.5)).

Although not directly implemented in the demonstrator of the retriever in Figure 2.7, we can devise additional strategies to increase the complexity of the task performed, for example to release the object after a certain time. These strategies can remain relatively straightforward: already including a fluidic resistance in parallel with the gripper and venting to the atmosphere could be an effective way to incorporate such timing. Such timing is also shown in Figure S2.6-S2.7,

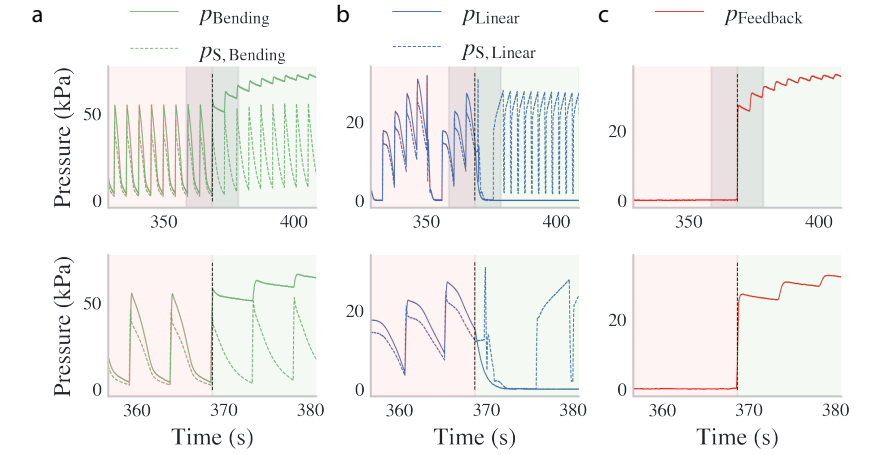


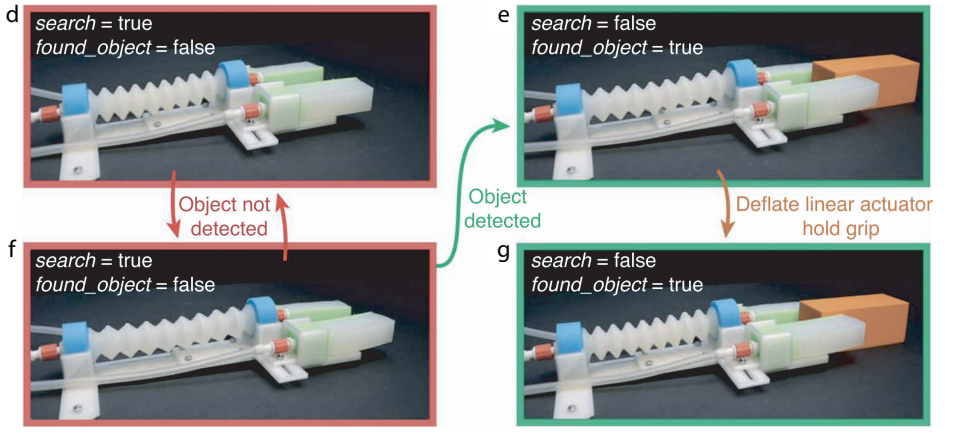


Figure 2.8: **Experimental data and schematic representation of the obtained behavior of the soft robotic retriever demonstrator.** (**a-c**) Pneumatic responses of the circuit before and after the *If* condition is triggered upon gripping the orange object, respectively for the bending actuator branch (green), the linear actuator branch (blue) and the feedback branch (red). In the top row we report an overview of the two different pneumatic responses before and after the *If... break* condition is triggered, with the successful gripping event occurring at $t^* = 368$s. The shaded time window of the interaction event is shown in more detail in the bottom row. (**d-g**) Schematic representation of the behaviour of the pneumatic soft retriever unit running Algorithm 6. Highlights of behaviour before and after the *If... break* condition is triggered are highlighted respectively in red and green.

Figure S2.25 and Video 3 (Section 2.5), where we demonstrate that by including increasingly larger fluidic resistances in parallel with the gate branch of the N.O. valve and venting to the atmosphere, we can retain pressure for increasingly longer times. Through this approach, the pressure in the gripper branch could be retained long enough to allow the full retrieving of the target object before releasing the grip by lowering the pressure in the gripper branch.



## 2.4 Discussion

Inspired by traditional coding statements, we introduce a strategy to materialize algorithms using electronics-free pneumatics circuits. Through our design rules, we program responses and switch between responses in soft robotic systems. Furthermore, from a functionality point of view, the pneumatic circuits we propose fulfil the requirements for the Böhm–Jacopini theorem[68]. For each of our designs, we illustrate the potential for applications in soft robotics, highlighting features in the parameter space useful to encode complex responses in pneumatic soft robots. The pneumatic coding blocks we introduce can perform operations in series (as in the case of the nested *For* loop in Figure 2.4**f**) as well as in parallel (Algorithm 6 and Figure 2.7 for the retriever demonstrator). This last feature lends itself well to further investigation of computational interest, as well as the possibility of introducing sensory feedback to different branches of the pneumatic branches, similar to biological processes that can be executed and triggered in parallel.

Through our design choice of working in an electronics-free environment, we ensure that pressurized air volumes work both as an actuating medium and state control variables of the system. This represents a valuable asset, e.g., in scenarios where electrostatic discharges can compromise the operation of robotic systems. Drawing inspiration from the self-sensing strategy in pneumatic grippers [23], we introduce sensing through the actuators themselves, lifting the requirement for dedicated external (electronic) sensors to achieve feedback. Therefore, we embed actuation, sensing and control within the same pneumatic, electronics-free platform, with no need for signal transducing.

Nevertheless, the design choice to not use signal transduction to control the pneumatic circuits imposes some limitations in the context of the scalability of our designs. As each component in a given branch of the circuit causes a pressure drop, it reduces the expendable energy to actuate and control the branches both downstream and in parallel to it. We report that this is not an issue at the scale of component types and numbers we investigated. A potential solution to overcome this potential limitation is to provide separate pressure inputs for different branches or decouple parallel branches using the temporary switches such as the N.O. valve we presented.

Although the individual pneumatic coding blocks we design can reproduce

high-level functionalities of control statements in a coding language, combining such circuits does not directly translate into traditional programming. On the one hand, the analog and continuous nature of the pneumatic medium can impose some limitations while combining pneumatic circuits to achieve the desired functionalities. As an example, the physical properties of the hysteretic valves and actuators in the example in Figure 2.7 must be simultaneously taken into account while designing the pneumatic circuit able to execute Algorithm 6 for the soft retriever. Such fundamental differences with traditional programming require an alternative approach to directly build a compiler able to return the optimal circuit design starting from a preferred high-level functionality. On the other hand, while combining subprograms in the very same example, the possibility to run programs in parallel and let them affect one another emerges from the design of the pneumatic circuits itself. Through this modular approach, we were able to build a soft gripper demonstrator that was able to run a program that we would not have been able to develop without insights gained from each coding block.

Using the design of the fluidic demultiplexer we introduced in Figure 2.5**a**, we materialize flash memory-like properties in our demultiplexer that uses punched cards. Such physical memory can relatively easily be implemented with off-the-shelf components and can address (re)programmability of sequential instructions through a different design of the punched holes. Furthermore, it is worth highlighting that our strategy can be used to extend the execution of instructions past the pure *digital* output signal, e.g., by designing slots with variable width or shape in the punched cards. However, it is technically not feasible with such punched-hole memory to reach the same order of magnitude of instruction density of SRAM, DRAM and flash memory that exists in more general-purpose computers today. Still, we expect that our electronics-free approach can still be useful to integrate redundancy and simple autonomous responses through hardware solutions.

In our study, we did not investigate whether we used the minimal required number and type of components for our designs. We opted instead to focus on the general hardware programming strategies rather than the specific circuit optimization. Efforts have been made in the community to tackle circuit optimization and create compilers to map specific actuator outputs to given pneumatic inputs. However, the programmability of pneumatic responses is generally addressed within the context of binary logic [72]. Such an approach can be useful in many other studies both at macrofluidic [41, 71] and at microfluidic scale [40, 73]. To our knowledge, only a few studies [74, 75] have focused on non-binary logic to program the behavior of soft robots so far.

Even though in current work we only focused on showing the use of the fluidic coding blocks in a gripper demonstrator, other applications should be in reach. For example, the ability to exhibit locomotion patterns, as well as the capability to switch between them under given environmental cues, is a crucial feature for

control and actuation autonomy in soft robots. We expect that our control strategy lends itself well to both programming such patterns and changing behavior as a response to environmental changes. This capability could be beneficial while designing locomotion patterns in (soft) robotic walkers. The pneumatic circuits we design could be used as a passive, redundant system to, e.g. detect impacts or sense the strength of interaction between the (soft) robotic system and its environment. Moreover, the control and design strategy we propose could be used, e.g., to obtain (re)programmability of the position of an actuator for rehabilitation devices [76] and wearable smart textiles [77, 78].

We envision it would be possible to reproduce at least some of the pneumatic coding blocks that we presented in our work at smaller and larger scales, provided that different components with a similar non-linear response in the pressure-flow diagram can be developed. Nevertheless, fabrication limitations and experimental setups constraints often set the pressure and dimensions to be in the same range we investigated. This is particularly true when zooming in on the pneumatic soft robotics community we address in our work, with only relatively few examples exploring other high-pressure [79], larger [13, 80] or smaller [70, 81] size scales. In order to scale down our control strategies into the domain of microfluidic valves and actuators compatible to similar works [82, 83], we believe that other non-linearities and hysteresis could be used to obtain similar functionalities. As an example of such functionalities, microfluidic bistable and differential amplifiers, and delay and signal generation capabilities [84, 85] could be used as foundations for microfluidic coding blocks.

Despite our approach not being straightforward to implement for complex algorithms, it is often true that it is a small set of basic instructions that drives the actuation and life cycle of living beings in elementary, yet complex scenarios. This is particularly true when considering systems that can navigate natural environments by means of simple interactions with their ecosystems. As a well-known example from literature, we mention the case of the Venus Flytrap plant. This carnivorous plant stays in an idle state until a prey triggers its sensory hairs more than once within a pre-defined time window. When these conditions are met, its leaves snap shut, thus trapping the prey [86, 87]. From a coding perspective, the plant is idle until the input signal overcomes a certain threshold twice, a behaviour we can physically represent using the pneumatic *For* and *If* coding blocks. We replicate functionality similar to the Venus Flytrap case study in Figure S2.24. Such a fundamental capability gives the Venus Flytrap the capability to survive and grow in natural environments by manifesting autonomous behavior in actuation, sensing and feedback from its environment. Similarly, we also believe that the responsiveness we implemented in pneumatic, electronics-free soft robots can help move towards autonomous, soft robots capable of decision-making while maintaining a limited number of components [88].

The aforementioned studies focus on how to use the response of individual non-linear components to obtain programmable behaviors. Conversely, our efforts are instead aimed at defining a library of circuits to be used and combined in both binary and non-binary logic. We believe such an approach can encourage the opportunity to intuitively design responses in pneumatic soft robots starting from a desired pseudocode, in a modular electronics-free environment, even starting from different hardware solutions. Therefore, our approach paves the way to the realization of pneumatic coding blocks to be used for programming responses in soft robots that are meant to interact with their environment and manifest decision-making capabilities.

### 2.4.1 Link to the following chapter

In this chapter, we examined how control strategies can be embodied in the interactions among nonlinear, electronics-free components. However, the pneumatic coding blocks presented here remain inherently dependent on external energy sources for their operation, e.g., through flow regulators and pressurized air sources. Although these blocks can facilitate the control of soft robots through hardware programmability, such reliance constrains the ability of these systems to operate indefinitely without human supervision. This observation underscores that, in order to obtain machines capable of operating as human substitutes, control alone is insufficient in the absence of an appropriate energy supply.

While the combined consideration of control versatility and long-term powering strategies is often overlooked in the literature, the following chapter builds on the knowledge of pneumatic coding blocks to address this limitation. In the next chapter, we explore energy-harvesting strategies for powering electronics-free soft robotic systems and investigate how the environment itself can be exploited both as an energy source and as a cue for triggering functional responses.

## 2.5 Videos

- **Video 1** We present the bare minimum example circuits for the *If*, *If*... *break* and *For* pneumatic coding blocks. The pseudocode representative of the pneumatic circuit is highlighted, together with changes in the circuit's state that occur upon interaction.

- **Video 2** Two different executions of the soft robotic retriever program obtained by combining the *For* and *If*... *break* pneumatic coding blocks. Extended data for this run and pneumatic circuit design are represented in Figure 2.8.

- **Video 3** Example of a pneumatic circuit for boolean variables, AND and OR logic gates, and *If*... *else* pneumatic circuit. Further examples of tunability of the *For* pneumatic circuit and examples of fluidic circuits encoding continuous variables through the control of the N.O. valve.



All the movies related to this chapter are available at this link. If you are holding a paper version, you can scan this QR code:

Videos - Chapter 2

## 2.6 Materials & Methods

### 2.6.1 Fabrication of the N.O. valve

To assemble the N.O. valve, we use two plexiglass plates that enclose two pairs of TPU sheets (ECL000009 Ecoseal® Film T150 85A), heat sealed together at 240°C. We heat seal the TPU to obtain the source-drain channel (Figure S2.15**a**) and gate channel (Figure S2.15**b**). The heat sealing procedure is executed using a modified 3D printer (Felix Tec 4 3D printer), of which we use the heat generated from a custom-modified printhead to heat seal two sheets of TPU following the designed patterns [89]. We highlight fabrication details in Figure S2.16.

We fabricate the plexiglass plates by laser cutting (Speedy 300, Trotec®) an 8mm thick plexiglass following the design in Figure S2.15**c**. Once the two identical plexiglass sheets have been laser cut and the TPU sheets heat sealed, the individual pieces are assembled together. We follow the step-by-step protocol in Figure S2.17. To be able to fluidically control the channels, we use a FESTO® tube with an outer diameter of 4mm with a 4cm length, and we slide it inside the TPU channels as in Figure S2.17**d**. The TPU channel size is chosen so that the TPU channels always compress the FESTO® tube, forming an airtight connection without additional elements required. We then connect a 2.25mm Luer Lock at the free end of the FESTO® tubes to connect each channel to our pneumatic circuits.

### 2.6.2 Fabrication of the interacting volumes

The heat sealing procedure we use to fabricate enclosed volumes is closely related to procedure we reported in Figure S2.16, the difference being the material employed. The pattern we heat seal is shown in Figure S2.18**a**. To fabricate these TPU-coated nylon fabric pouches, we use a nylon-coated TPU (Nylon, 70den, TPU-coated one side, sealing temperature 270°C). We connect the heat-sealed pouch to a FESTO® 6mm tube to connect it to our pneumatic circuits as we show in Figure S2.18**b-d**. As both our pouch design and the FESTO® tube are made of TPU, we can heat seal the two elements together using a custom design heat sealer made up of a circular heater, controlled at 190°C. The design of the custom heat sealer is reported in Figure S2.18**g-i**. After placing a heat-resistant layer (commercial baking paper) between the circular heating element and the connection point of the TPU pouch with the FESTO® tube (Figure S2.18**e**), we wait about 15s to obtain an airtight connection. The resulting component can withstand pressures higher than 2bar without leakages.

### 2.6.3 Fabrication of the soft actuators

**Linear Actuator** The design of the linear actuator is based on the schematics of bellow actuators [90] and reported in Figure S2.19. To fabricate this component, we use outer molds in VeroClear on a PolyJet 3D printer (Eden260VS, Stratasys®) and a BVOH water-soluble inner mold. We assemble the inner and outer mold together and align the two using a metal rod that fits the inner diameter of the inner mold. After assembling the molds as in Figure S2.19**a**, we inject Smooth-On® Dragon Skin (DS) 20. We inject this two-components silicon using a cartridge (AF 400-01-10-01, Sulzer®) after the two components have been degassed. Before casting silicones, we spray the surface of the molds with Ease release 200, Smooth-On®. We use a static mixing nozzle (MFQ 05-24L) using a pneumatic extrusion gun to inject the DS20 silicon through the injection hole highlighted in Figure S2.19**a**. After this step, we use a cartridge filled with Elite Double (ED) 32 Fast silicone (Zhermack®) to fill the outer molds of the end-caps as in Figure S2.19**b**. When the ED32 silicon is fully cured, we remove the inside rod used for the alignment and use a water pump in parallel with a tunable flow resistor for venting to flush the water-soluble support material from inside the actuator. We report the dimensions of the linear actuator in Figure S2.19**c-d**

**Bending Actuator** We fabricate the bending actuators following a procedure similar to the one already developed within our group [23]. We report fabrication details and dimensions respectively in Figure S2.20-S2.21. For the fabrication of the air chambers we highlight in Figure S2.21**b**, we use a sacrificial inner mold in BVOH, highlighted in Figure S2.20. We fabricate this actuator using of two

different silicones (ED32 and DS20). Therefore a two-steps procedure is required for allowing two different silicones to bond together. First we assemble the molds as in Figure S2.20**a** using M6 screws to guarantee alignment. We position the inner mold in the slot of the bottom mold. We inject the DS20 silicone after spaying mold release and the same equipment as described in the fabrication of the linear actuator. We wait 3.5 hours out of the 5 hours required for the DS to cure and we disassemble the top and bottom molds of the first step (Figure S2.20**a**) to substitute them respectively with the top and bottom molds of the second step (Figure S2.20**b**) onto which we apply mold release. Casting the ED32 on the DS20 after this time guarantees a solid interface between the two materials. We insert the plug to obtain an entry point to pneumatically actuate the resulting actuator. We then inject the ED32 and wait the for the DS20 to be fully cured. We then use a water pump in parallel with a tunable flow resistor for venting to flush the water soluble support material from inside the actuator. We report the geometrical parameters of our design in Figure S2.21.

## 2.7 Supplementary Materials

S2

We report extended data and further investigations to support the claims in the main text. Furthermore, we include additional circuit designs and videos to better highlight the features of our systems and suggest further functionalities that can be embedded in fluidic circuits using our approach. The Supplementary Material is organized as follows:

- i) Description of additional experiments and characterization of custom components.
- ii) Figures for additional material.
- iii) Tables with extended details of components and experiment details.
- iv) Additional pneumatic circuit designs.

## i) Description of additional measurements and characterization of custom components

- Proving tunability of *If* pneumatic coding block (Figure S2.1-S2.2)
- Force, displacement, pressure measurements to measure the sensitivity Pneunet actuator (Figure S2.3-S2.4)
- Characterization of N.O. valve fluidic properties (Figure S2.5)
- Short-term and long-term memory in N.O. valve (Figure S2.6-S2.7)
- Extended data on continuous variables pneumatic circuit (Figure S2.8)
- Model of the *For* pneumatic coding block (Figure S2.9-S2.10)
- Measuring the position of the linear actuator in time (Figure 2.4**c**)
- Design of demultiplexer and physical memory support (Figure S2.11-S2.12-S2.13)

**Proving tunability of *If* pneumatic coding block (Figure S2.1-S2.2)**

**Changing input pressure** We demonstrate that the pressure difference $\Delta p$ necessary to trigger the *If* condition in the design we propose can be tuned by controlling the input pressure $p_{\text{in}}$ in the pneumatic circuit. We make use of a soft hysteretic valve with $\Delta p_{\text{open}} = 70\text{kPa}$ and assemble a pneumatic circuit as

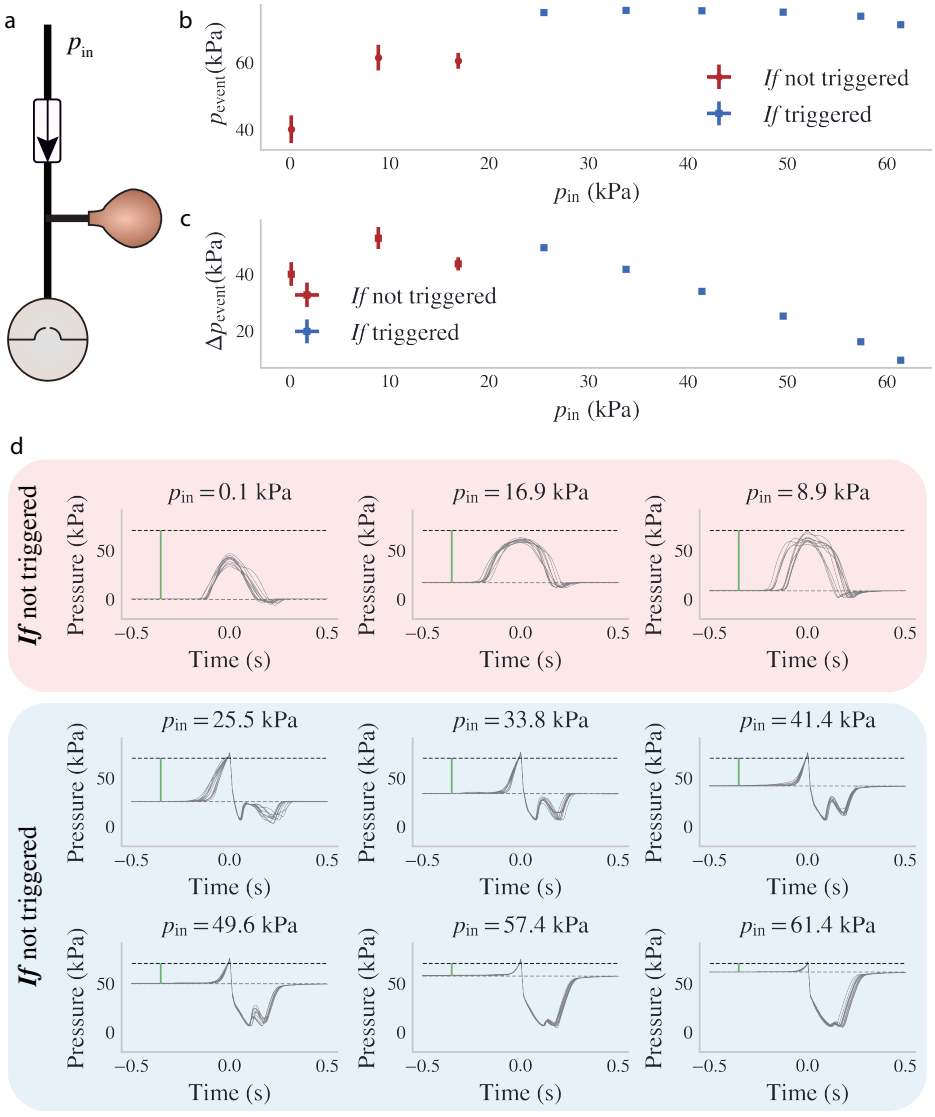


Figure S2.1: **Sensitivity of the *If* circuit to external mechanical inputs.** A VWR® 60mL bulb was used as compliant volume. (**a**) Circuit schematics. (**b**) Average maximum peak pressure and (**c**) average pressure increment resulting from an interaction event $p_{\text{peak, event}}$ for different input pressures $p_{\text{in}}$. (**d**) Data for the 10 individual runs. The grey solid line represents the ten different runs performed. The black dashed line represents the opening pressure of the soft hysteretic valve $\Delta p_{\text{open}} = 70\text{kPa}$. The grey dashed line indicates $p_{\text{in}}$.

S2

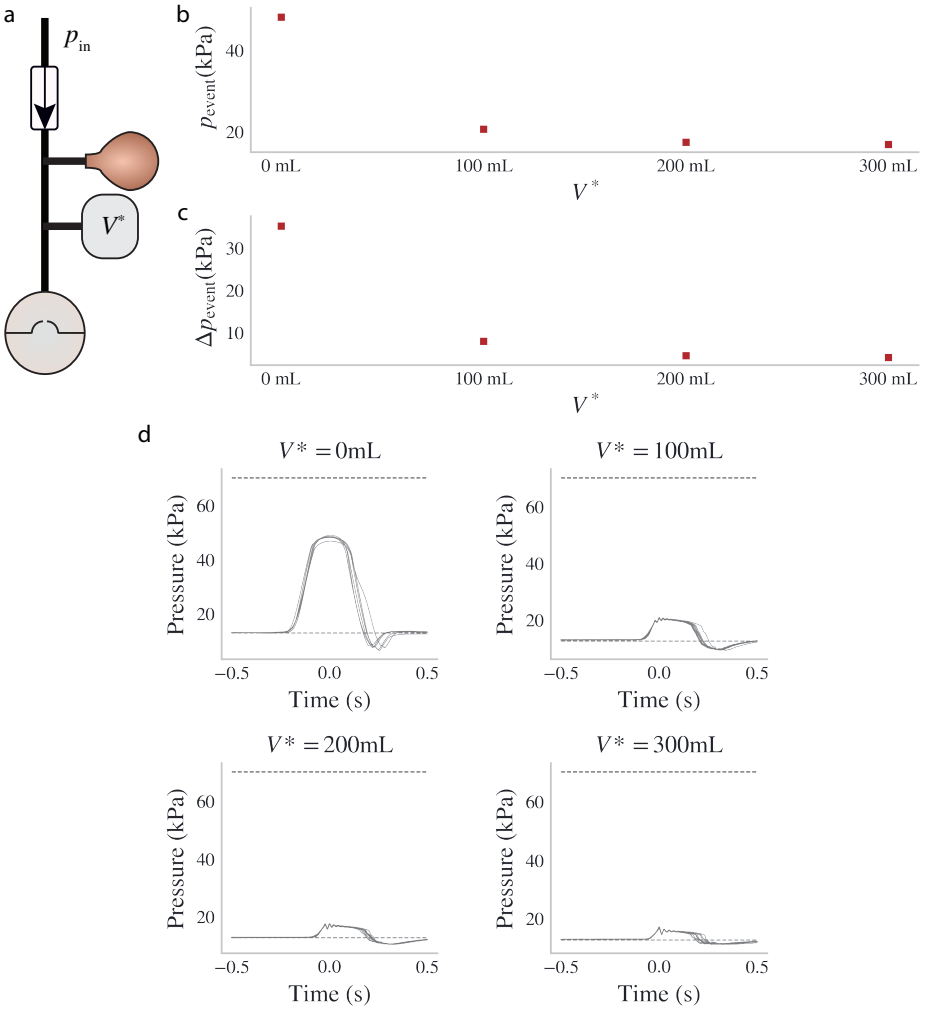


Figure S2.2: **Sensitivity analysis of the *If* circuit to external mechanical inputs with different stiff volumes in parallel to the compliant VWR® bulb of 60mL.** (**a**) Circuit schematics. (**b-c**) Experimental data of the average of ten iterations per configuration, with reported, but not visible, error bars. **b** $p_{\text{event}}$ maximum peak pressure and $\Delta p_{\text{event}}$ pressure increase **c** reached. The circuit design, except for the $V^*$, and parameters are the same as the circuit presented in Figure S2.1. (**d**) The grey solid lines represent the pressures of ten different runs of the same experiment, the grey dashed line and black dashed line represent the input pressure at the pressure regulator $p_{\text{in}}$ and $\Delta p_{\text{open}}$ of the soft hysteretic valve, respectively. In this experiment $p_{\text{in}} = 13$kPa and $\Delta p_{\text{open}} = 70$kPa.

in Figure S2.1**a**. As anticipated when introducing the *If* pneumatic circuit, the role of the one-way valve is to prevent the pressure controller from regulating the changing pressure downstream of the pneumatic circuit by preventing backflows. In Figure S2.1 we report the peak pressure (**b**) and differential pressure increase obtained upon interaction with the compliant volume (**c**). While performing these experiments, a compliant volume $V_{compliant}$ was used (VWR®, 15mL bulb ) and fully compressed following the same time span and intensity protocol. This resulted in a similar differential increase in pressure as an outcome of the interaction with the compliant volume. For each $p_{\text{in}}$ pressure probed, ten interactions with the soft volume were performed to demonstrate the repeatability of this circuit design. Data from the pressures for each execution of the experiment is reported in Figure S2.1. In Figure S2.1**b-c**, we highlight in red the cases in which the *If* condition was not triggered. Conversely, we indicate in blue the cases in which the pneumatic *If* condition was met.

**Including additional stiff volumes before the soft hysteretic valve** If on the one hand, the pressure difference $\Delta p$ activation threshold can be determined through $p_{\text{in}}$, adding an additional fixed volume $V$ in parallel with the compliant volume affects the sensitivity to the interaction with the compliant volume. We support this last statement with the following set of experiments, in which we modify the very same circuit as in Figure S2.1 with different $V^*$ stiff volumes that are placed in parallel with $V_{\text{compliant}}$. We report the resulting schematics of the circuit and data in Figure S2.2. The decreasing $\Delta p$ resulting from an interaction event when $V^*$ can be intuitively explained by looking at a simplified model for interaction with a compliant volume using the ideal gas law. By assuming the *If* condition is not triggered by a compression of the compliant volume, we consider a given $V_0$ of connectors and tubing in the circuit (in our experimental study, $V_0 \simeq 45\text{mL}$) and $V_{\text{stiff}} = V_0 + V^*$. The $p_{\text{event}}$ peak pressure achieved upon full compression of the compliant volume reads

$$p_{\text{event}} = p_{\text{in}} \frac{V_{\text{stiff}} + V_{\text{compliant}}}{V_{\text{stiff}}}$$

Therefore, the larger $V_{\text{stiff}}$, the smaller the influence of the compliant balloon being fully compressed upon one interaction event. Such a model does not take into account the dynamic effects present in the physical system as we are using an equation of state to model transient phenomena. Nevertheless, such a simplified model still gives an idea of the scaling law of $p_{\text{event}}$ with increasing stiff volumes in parallel to the inlet of the soft hysteretic valve.

We repeat the same experiment as in Figure S2.1, adding a $V^*$ stiff volume in parallel to the compliant volume and using a $p_{\text{in}} = 13\text{kPa}$ at which the *If* condition is not triggered when the compliant volume is manually fully compressed.

S2

Our study demonstrates that it is possible to decrease or increase the $\Delta p_{\text{event}}$ needed for the pneumatic *If* coding block to be triggered by increasing or decreasing the $p_{\text{in}}$ and equivalently, by decreasing and increasing $V_{\text{stiff}}$.

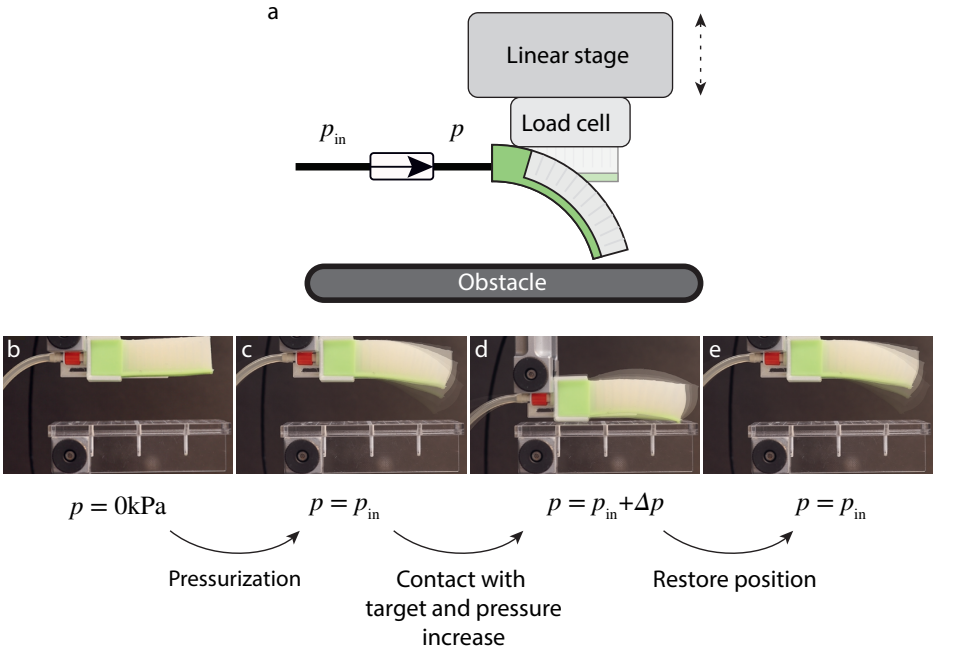


Figure S2.3: **Sensitivity characterization of the Pneunet actuator. (a)** Diagram of the experimental setup. **(b-e)** Operating procedure for measuring the pressure increase $\Delta p$ when a pressurized actuator is deformed upon contact as a function of the initial pressure $p_{\text{in}}$. The overlayed photos are representative of the different pressures $p_{\text{in}} \in$ [21.7kPa , 27.9kPa , 37.2kPa , 43.3kPa , 47.5kPa] to better highlight differences in deformation. **b** The actuator is initialized at $p = 0$kPa, then is pressurized at $p_{\text{in}}$ and deforms as in **c**. We wait 10s before moving the linear stage down 30mm at $60\frac{\text{mm}}{\text{s}}$ and achieve the geometrical deformations in **d**. Finally, we move the linear stage to recover the initial position while moving at the same speed in **e**.

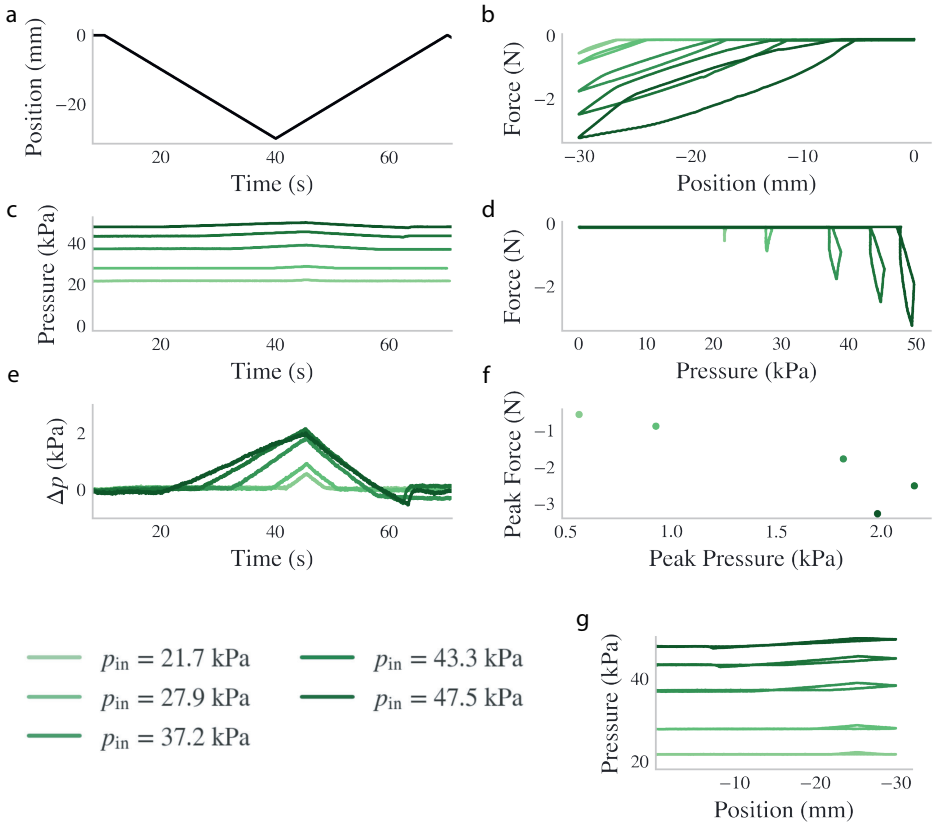


Figure S2.4: **Combined data from tensile test and fluidic measurements collected for the experiments performed in Figure S2.3. (a)** Imposed position in time. **(b)** Measured force in time. **(c)** Pressure inside the actuator in time. **(d)** Measured force as a function of the pressure inside the actuator. **(e)** pressure excess $\Delta p = p - p_{\text{in}}$ in time. **(f)** Extracted plot of peak force as a function of the peak pressure measured while performing the same experiment at different input pressures $p_{\text{in}}$. **(g)** Pressure as a function of position.

**Force, displacement, pressure measurements to measure the sensitivity Pneunet actuator (Figure S2.3-S2.4)**

To have a quantitative understanding of the forces at play during the demonstrator experiment in Figure 2.7, we perform additional experiments where we characterize both the grasping force of the Pneunet actuator and the resulting sensing resolution

that can be obtained using these actuators. We used the setup as shown in Figure S2.3**a**, where we attach one Pneunet actuator to a ± 100 N Instron 132151 load cell. By connecting a one-way valve in series with a pressure regulator, we can measure the $\Delta p$ pressure increase upon contact with a plexiglass plate (Figure S2.3**b-e**). The role of the one-way valve is to prevent the $p$ pressure in the actuator from being regulated once the additional $\Delta p$ is generated by contact with the target object. To perform the measurement, we initialize the system by pressurizing the Pneunet actuator to $p_{\text{in}}$. We wait 10s to let the pressure equilibrate in the actuator. We then emulate the contact with a target object by displacing the linear stage by −30mm and then 30mm at 60mm/s.

We report the measured data of position, force and pressure in Figure S2.4. To understand how the geometrical deformation affects the increase in pressure, we repeat this experiment for different input pressures $p_{\text{in}}$. From these results we observe that, within the working operating pressures of the Pneunet actuator ($p_{\text{in}} \sim$ 20kPa $\boldsymbol{\nabla\cdot} \sim$ 50kPa), we measure forces ranging from $\sim$ 1N to $\sim$ 3N, as we report in Figure S2.4**b**,**d**. As expected, for fixed displacement increasing the pressure will also increase the maximum peak force (Figure S2.4**f**).
Moreover, we can extract further data to quantify the sensitivity of our system for object detection. From Figure S2.4**e** we infer that the $\Delta p$ resulting from mechanical deformation ranges from .6kPa to 2kPa, which corresponds to a senstivity of 2.76% to 4.25% with respsect to the applied pressure, respectively. These values are in the same order of magnitude as the ones measured for a Pneunet actuator we fabricated for similar work but with different geometrical parameters [23]. While these pressure differences are relatively small, we were able to correctly identify them using or fluidic approach.

### Characterization of N.O. valve fluidic properties (Figure S2.5)

To study and characterize how the fluidic resistance of our design of the N.O. valve changes with different input and gating pressures, we connect this component to two different pressure regulators as in Figure S2.5**a**. In Figure S2.5**b-e** we report the experimental data from our experiment. With the goal to evaluate how the fluidic resistance across the source-drain channel $R_{\text{SD}}$ changes for different combinations of $p_{\text{SD}}$ and $p_{\text{G}}$, we impose a given $p_{\text{SD}}$ at the first pressure regulator. We then change the $p_{\text{G}}$ at the gate of the N.O. (dashed line in **b**.) by linearly increasing it in one minute, keeping it constant for twenty seconds, and bringing it down to ambient pressure $p_{\text{amb}}$.

Through the flow measurement at the drain channel $Q_{\text{SD}}$ (S2.5**d**) and the pressure measured at the source pin, we derive the fluidic resistance across the source and drain $R_{\text{SD}} = \frac{p_{\text{SD}}}{Q_{\text{SD}}}$ (S2.5**c**). To better investigate the hysteresis in the opening and closing of our design of the valve, we identify the closing pressure $p_{\text{G,close}(SD)}$ as the $p_{\text{G}}$ that causes $Q_{\text{SD}}$ to drop to .005SLPM starting from the

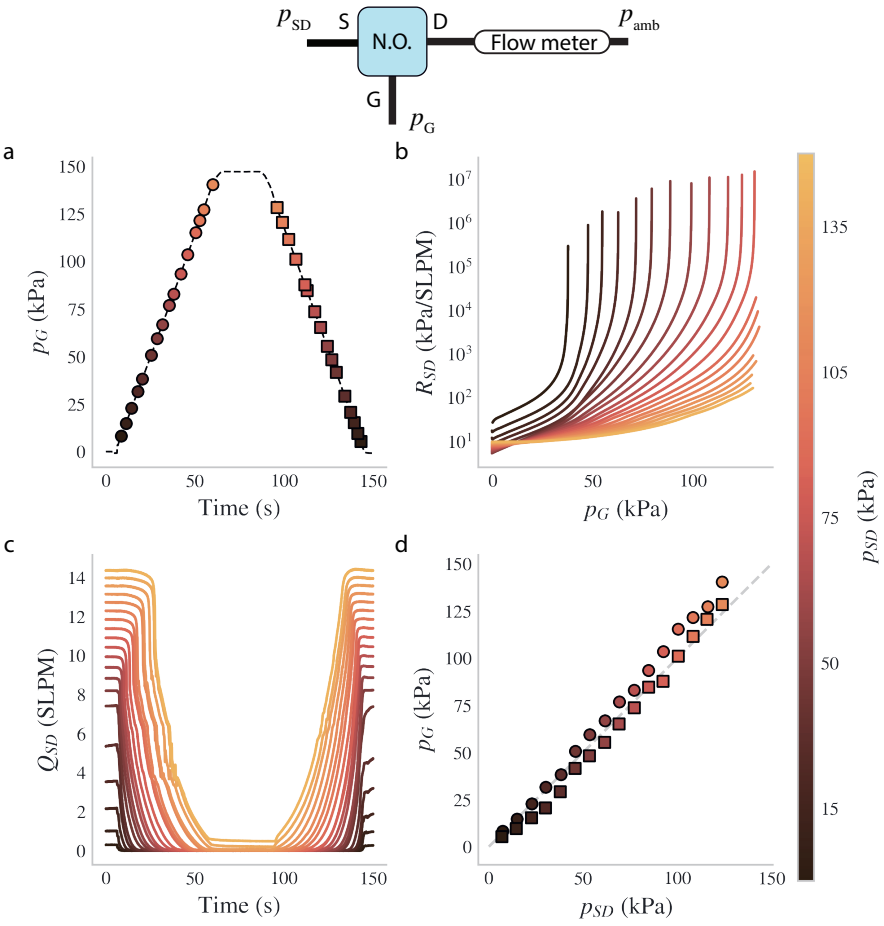


Figure S2.5: **N.O. valve characterization of fluidic resistance as a function of both pressure at the source $p_{SD}$ and pressure at the gate $p_G$.** (**a**) Circuit schematics for the characterization. For each experimental realization, $p_{SD}$ was set at different values represented through different colours in the colorbar. We modified the setpoint of the $p_G$ pressure regulator in time following the shape in the dashed black line in (**b**). Circles and square represent respectively $p_{G,\,close}(SD)$ and $p_{G,\,open}(SD)$. (**c**) $R_{SD}$ fluidic resistance measured as a function of $p_G$ for different $p_{SD}$. (**d**) Flow $Q_{SD}$ measured in time for different $p_{SD}$ and fixed profile of $p_G$ in time as in **b**. (**e**) Plot of the $p_{G,\,close}(SD)$ and $p_{G,\,open}(SD)$ in **b** as a function of $p_{SD}$. The dashed gray line represent the condition $p_{SD} = p_G$.

open state of the N.O valve. Conversely, we define $p_{\mathrm{G,open}(SD)}$ as the $p_{\mathrm{G}}$ value at which, once the N.O. is in the closed state, it reopens upon a decrease of $p_{\mathrm{G}}$ so that $Q_{\mathrm{SD}} > .005\mathrm{SLPM}$. As both opening and closing pressures depend on $p_{\mathrm{SD}}$, we repeat this measurement for different $p_{\mathrm{SD}}$ indicated by the color bar in Figure S2.5. We report the opening and closing pressures of the N.O. valve using circles and squares respectively, with colours corresponding to the $p_{\mathrm{SD}}$ imposed at the source of the N.O. valve. Through this characterization of fluidic properties of the N.O. valve, we can outline the response of our design to different $p_{\mathrm{SD}}$ and $p_{\mathrm{G}}$ combinations. Our results in Figure S2.5 show that we can access not only the open and closed states for this valve, but also intermediate states that we can use for additional designs of pneumatic circuits. To better picture and investigate this phenomenon, we report in Figure S2.5**e**. the opening and closing pressures from Figure S2.5**b**. and compare them to the corresponding $p_{\mathrm{SD}}$ used in the experiment. From this visualization, it is possible to appreciate that both $p_{\mathrm{G,close}}(SD)$ and $p_{\mathrm{G,\ open}}(SD)$ almost match the $p_{\mathrm{SD}}$ values, with a deviation in the order of a few kPa within the investigated range. This suggests that our design of the N.O. valve manifests only negligible hysteresis. However, the $p_{\mathrm{G,close}}(SD)$ required to close the source-drain channel for a given $p_{\mathrm{SD}}$ is consistently slightly higher than its correspondent opening pressure. Such a response can be due to the differences in surface area between the source-drain and gate channels in our design but this difference has not compromised the performance nor the realization of the experiments we report in our study.

### Short-term and long-term memory in N.O. valve (Figure S2.6-S2.7)

**Short-term memory** With the following experiments, we support the statement in the main text concerning the potential for the N.O. valve to operate as a temporary switch. We achieve such a result by designing a circuit shown in Figure S2.6**a**. In this experiment, we set a $p_{\mathrm{SD}}$ pressure and initial gate pressure $p_{\mathrm{G,0}}$. Moreover, we use a one-way valve and a flow constrictor $R_{\mathrm{out}}$ connected to the gate branch as in our schematics.

In our experiments, we first initialize $p_{\mathrm{G,\ 0}}$, let the system equilibrate and then switch off $p_{\mathrm{G,\ 0}}$ by changing its setpoint to ambient pressure. Our schematic guarantees that the excess pressure in the gate branch can vent to the atmosphere only through $R_{\mathrm{out}}$ when the pressure regulator controlling $p_{\mathrm{G,0}}$ is switched off.

As $p_{\mathrm{G}}$ drops from $p_{\mathrm{G,0}}$ to ambient pressure $p_{\mathrm{amb}}$, the gate pressure will cross the $p_{\mathrm{G,open}(SD)}$ we highlighted in Figure S2.5. When this condition is met after $t_{\mathrm{memory}}$ seconds after $p_{\mathrm{G,0}}$ has been switched off at time $t = 0\mathrm{s}$, the $Q_{\mathrm{SD}}$ flow between source and drain will rise until reaching its saturation level. We define this saturation air flow to be $.99\% \cdot \max(Q_{\mathrm{SD}})$ and $t_{\mathrm{memory}}$ the time at which this flow value is met. The $t_{\mathrm{memory}}$ value therefore depends on $p_{\mathrm{G,0}}$, $p_{\mathrm{SD}}$ and $R_{\mathrm{out}}$. In this experiment, we fix the first two parameters and investigate the

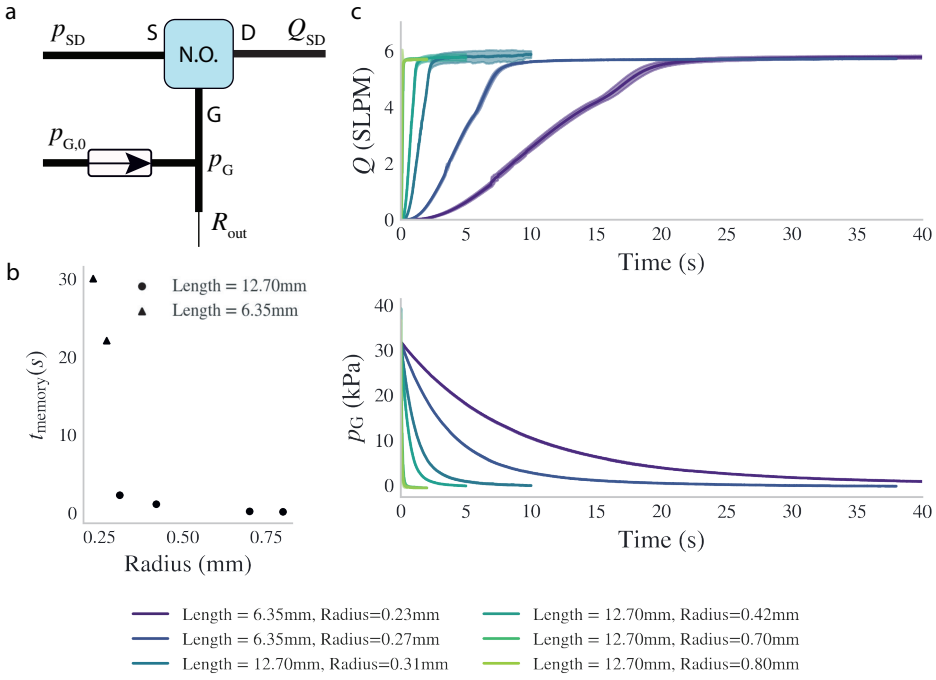


Figure S2.6: **Circuit design and measurement to characterize the memory effect of a N.O. valve.** We initialize the pressures at $p_{SD} = 30$kPa and $p_{G,0} = 40$kPa. (**a**) Circuit design At $t = 0$s the input branch of the pressure regulator at the gate is switched off so the gate branch releases pressure through the flow restrictor $R_{out}$ of different radii and lengths. Experiments were repeated five times for each of the $R_{out}$ studied. The $t_{memory}$ time before the full depressurization of the gate is calculated as the difference in time between $t = 0$s and the $t_{memory}$ at which $Q_{SD}(t_{memory}) = .99 \cdot \max(Q_{SD})$. (**b**) Measured $t_{memory}$ for different $R_{out}$ (SMD® medical needles with different radii and lengths) for five repetitions of the same experiment, error bar not visible. **c** Comparison of $p_{SD}$ and $Q_{SD}$ in time for different $R_{out}$ fluidic resistors.

S2

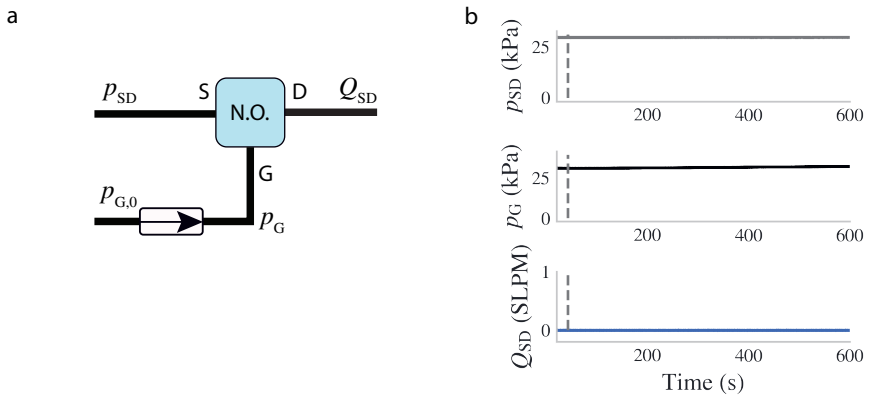


Figure S2.7: **Pressure and flow measured for confirming the capability of the N.O. valve to retain pressure indefinitely at the gate branch over one experiment realization.** The initial conditions for the experiment are the same as the ones used in Figure S2.6. (**a**) Circuit design. (**b**) Measured pressures at source, gate and flow across the source and drain. The dashed vertical grey line in **b** indicates the time at which $p_{G,0}$ is brought to $p_{amb}$.

effect of different $R_{out}$ on $t_{memory}$. We report the result of this investigation in Figure S2.6**b** and Figure S2.6**c**. We note that in this experiment the N.O. valve behaves as a **N**ormally **C**losed valve (N.C.) for $t < 0$s. The transition from N.C. to N.O. can be controlled by controlling the pressure in the gate branch.

**Long-term memory** In Figure S2.7 we repeat the same experiment in the limit case in which there is no flow constrictor to vent pressure in the gate branch to the atmosphere. By doing so, we demonstrate that the N.O. valve we designed is able to retain gate pressure for timescales long enough for our experiments. Thus, the N.O. valve can be used both as volatile and non-volatile memory.

**Extended data on continuous variables pneumatic circuit (Figure S2.8)**

We report in Figure S2.8 representative data for pressure in time in the experimental setup we presented in Figure 2.6**a**. In addition to the data previously presented, we include the extended heatmaps and peak pressure achieved for the different combinations of $p_{G,\,Ampl.}$ and $p_{G,\,f}$.

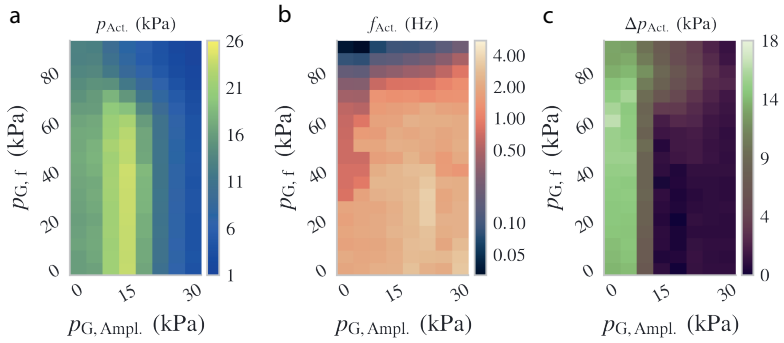


Figure S2.8: **Extended data of results reported in Figure 2.6 as a function of $p_{G,\,Ampl.}$ and $p_{G,\,f}$.** We report the heatmaps for maximum peak pressure **a**, frequency of actuation **b** and pressure amplitude of oscillations $\Delta p_{Act.}$ **c**. To better highlight the change in frequency of the oscillations in the actuator, we use a logarithmic colormap in **b**.

### Model of the *For* pneumatic coding block (Figure S2.9-S2.10)

We outline a simplified model to elucidate the design rule for the number of iterations $N$ and $\Delta T$ time interval between iterations in the *For* pneumatic coding block. The goal of this investigation is to define a set of design rules to approximate the expected response of this pneumatic circuit. We use data in Figure 2.4**d** to validate our modelling method. In Video 4, we report an example in which we modify the fluidic properties of the circuit to change the frequency of actuation. The experimental data was collected using sensors and regulators specified in the Materials & Methods section for what concerns the experiment in Figure 2.4**d**.

**Model for $N$ number of steps in the pneumatic *For* coding block** We consider the pneumatic circuit in Figure S2.9**a** and work under the hypothesis of the ideal gas law. Although the ideal gas law is an equation of state, we prove that this hypothesis is still useful in making predictions of the $N$. This is mostly because of the timescale of opening-closing of the soft hysteretic valve being $\mathcal{O}(.01s)$, therefore much faster than the other time scales in our system. As a result, we can assume that the opening of a soft hysteretic valve transfers air molecules almost adiabatically, thus making the ideal gas law approximation valid for our modeling purposes. Moreover, the pneumatic regimes we investigate throughout our work are in the range of compressibility factor $Z = \frac{pV}{nRT} \simeq 1$, in which the ideal gas hypothesis holds true.

S2

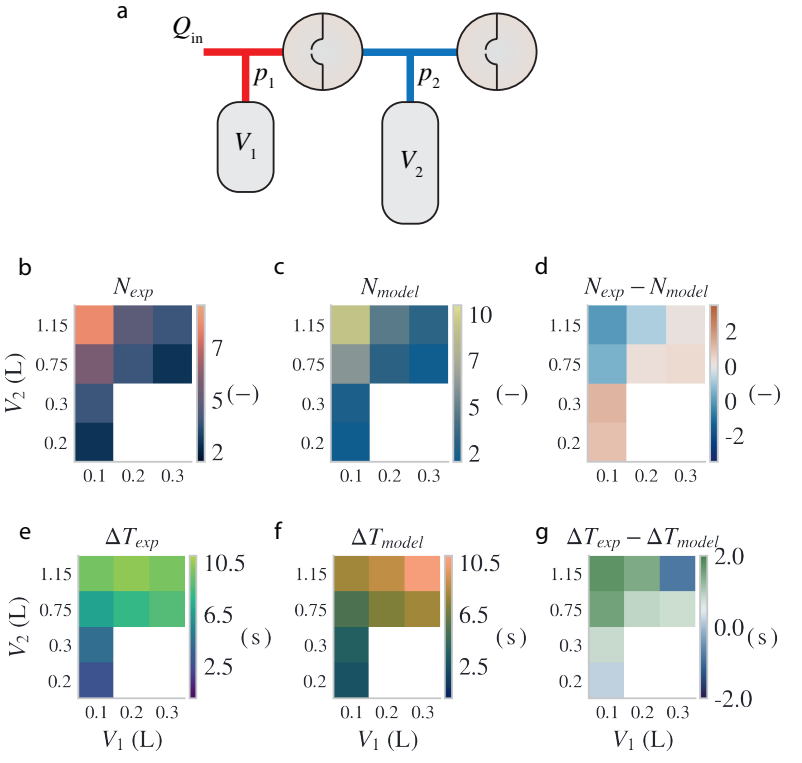


Figure S2.9: **Pneumatic circuit of the experiment in Figure 2.4d that we use to model the behavior of the pneumatic *For* loop.** The circuit is composed of two soft hysteretic valves in series. We connect stiff pre-capacitances $V_1$ and $V_2$ before each soft hysteretic valve and provide a flow input of $Q_{\text{in}}$=2SLPM. (**b-d**) Comparison between the experimental data **b**, the model from Equation (S2.5) **c** for the $N$ number of iterations in the pneumatic *For* coding block as a function of the stiff capacitances $V_1$ and $V_2$ in the schematic in **a**. **d** Discrepancy between experimental data and the model. (**e-g**)Comparison between the experimental data **e**, the model **f** for the $\Delta T$ number of iterations in the pneumatic *For* coding block as a function of the stiff capacitances $V_1$ and $V_2$ in the schematic in **a**. **g** Discrepancy between experimental data and the model. The empty entries in **b-g** represent combinations of $V_1$ and $V_2$ for which the *For* pneumatic behavior was not observed.

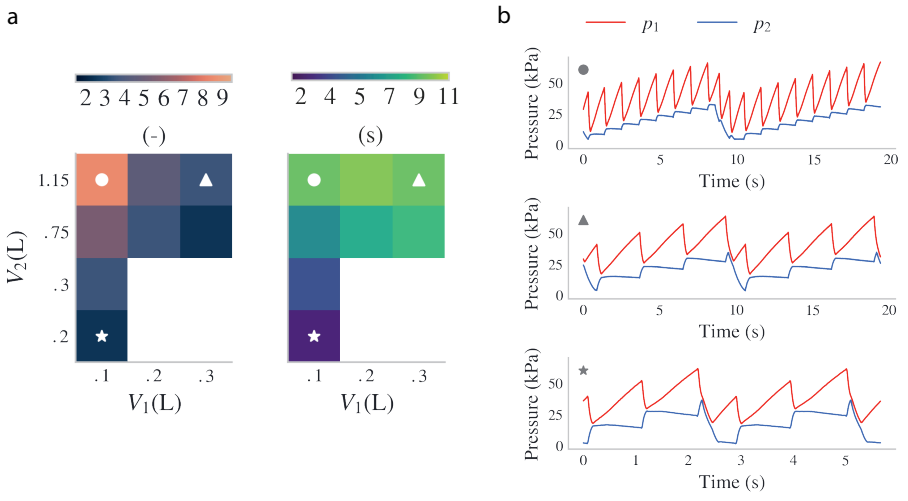


Figure S2.10: **Parameter exploration of the tunability properties of the *For* pneumatic coding block.** (**a**) Heatmaps for tunability of the number of iterations in the *For* loop and frequency of actuation as a function of $V_1$ and $V_2$. (**b**) Example of limit cases pressures in time.

In our analysis, we consider the two soft hysteretic valves having $\Delta p_{\text{open},1}$, $\Delta p_{\text{close},1}$ and $\Delta p_{\text{open},2}$, $\Delta p_{\text{close},2}$ connected in series. Additionally, we connect the stiff volumes $V_1$ and $V_2$ in parallel to the inlet of the first and second soft hysteretic valve, respectively.

At each opening event of the first soft hysteretic valve, $\Delta n_1$ of air molecules will traverse the orifice of the first valve so that

$$\Delta n_1 = \frac{(\Delta p_{\text{open},1} - \Delta p_{\text{close},1})\, V_1}{R\, T_{\text{amb}}} \tag{S2.1}$$

where $R$ is the gas constant and $T_{amb}$ is the temperature at which the experiment is performed, assumed to be constant within the timescales of the experiment. At the same time, the $n_{2,0}$ number of molecules initially in the branch downstream of the first soft hysteretic valve can be derived from the ideal gas law.

$$n_{2,0} = \frac{p_{2,0}\, V_2}{R T_{amb}} \tag{S2.2}$$

In Equation (S2.2), $p_{2,0}$ is the pressure initially present in the branch downstream

to the first soft hysteretic valve. As a consequence of the opening of the first soft hysteretic valve, the number of molecules in the $V_2$ branch will increase from $n_{2,0}$ to $n_{2,0} + \Delta n_1$. The increase in the number of molecules in this branch will in turn result in a new equilibrium pressure

$$p_2 = p_{2,0} + \frac{V_1}{V_2} \left( \Delta p_{\text{ open},1} - \Delta p_{\text{close},1} \right) \tag{S2.3}$$

Therefore, the pressure in the branch upstream from the second soft hysteretic valve will increase at each opening event of the first soft hysteretic valve by an amount

$$\Delta p_2 = \frac{V_1}{V_2} \left( \Delta p_{\text{open},1} - \Delta p_{\text{close},1} \right) \tag{S2.4}$$

As $p_2$ drops every time it reaches $\Delta p_{2,\text{ open}}$ and to a minimum value of $\Delta p_{2,\text{ close}}$, we can derive the expected number of iterations in the *For* pneumatic coding block circuit by

$$N_{\text{model}} = \lfloor \frac{\Delta p_{\text{open},2} - \Delta p_{\text{close},2}}{\Delta p_{\text{open},1} - \Delta p_{\text{close},1}} \frac{V_1}{V_2} \rfloor \tag{S2.5}$$

where $\lfloor \ \rfloor$ indicates the floor operation.

We compare our model to the experimental data we show in Figure S2.9**d**, **g**.

**Model for ΔT time interval between steps in the pneumatic *For* coding block** To estimate the $\Delta T$, we consider only the case of stiff volumes for simplicity. An iteration in our pneumatic *For* loop is obtained at each opening event of the first soft hysteretic valve. We consider $Q_{\text{in}}$ input flow in our circuit and the assumption that the opening and closing dynamic of the soft hysteretic valve is faster compared to the $\Delta T$ time scale.

The pressure interval $\Delta p_{\text{open},1} - \Delta p_{\text{close},1}$ necessary to get an opening event will therefore be covered in a $\Delta t$. We start with the differential equation for pressure

$$\dot{p}_1 = \frac{\rho R T}{M V_1} Q_{\text{in}} \tag{S2.6}$$

given $\rho = 1.125 \frac{\text{kg}}{\text{m}^3}$ air density, $M = 0.029 \frac{\text{kg}}{\text{mol}}$ molar mass of air, $R = 8.3145 \frac{\text{J}}{\text{mol} \cdot \text{K}}$ and $T_{\text{amb}}$ in Kelvin. By integrating in time, considering that all the parameters

on the right-hand side of Equation (S2.6) are constants, we first obtain the $\Delta t$ time of a single step within the *For* loop by evaluating

$$\Delta p_{\text{open},1} - \Delta p_{\text{close},1} = \int_0^{\Delta t} \frac{\rho R T_{\text{amb}}}{M V_1} Q_{\text{in}} dt \tag{S2.7}$$

$$= \Delta t \, \frac{\rho R T_{\text{amb}}}{M V_1} Q_{\text{in}} \tag{S2.8}$$

assuming the first valve closes at time $t = 0$s. Thus, from Equation (S2.8) we derive:

$$\Delta T = \Delta t \cdot N_{\text{model}} \tag{S2.9}$$

From the comparison between the experimental data and the model from Equation (S2.9) in Figure S2.9, it seems that the simplified model we propose can predict the high-level response of the *For* pneumatic circuit for given circuit parameters. This is particularly true for small $N$. We speculate that for increasing $N$, other effects, such as the leakage of the soft hysteretic valves with varying upstream pressures, must be taken into account to obtain a more reliable approximation.

A similar approach can be used to extend this model for the case of non-stiff volumes, although, in that case, the dependency of the geometrical volume in the ideal gas law from pressure $V(p)$ makes it unfeasible to perform such straightforward calculations. In that case, only a coupled fluido-mechanical model can help make accurate predictions on the behavior of the pneumatic circuit we presented.

We report additional data concerning the tunability of both the number of iterations and frequency of execution of the *For* pneumatic coding block. Reported data are the averages over 20 full loops of actuation for each configuration in Figure S2.10.

### Measuring the position of the linear actuator in time (Figure 2.4c)

We tracked the distance travelled in time by the linear actuator by making use of ARTag ArUco fiducial markers. Two markers were fixed respectively on the fixed end and on the moving end of the sliding PLA frame we used in Figure 2.4**c**. The tracking in time was performed using a video recorded at 50fps on a Canon 850D camera. The visual data was processed using a Python script and the `open-cv` package to correct objective lens distortion. The same package was used to track the ArUco markers in time.

S2

**Design of demutiplexer and physical memory support (Figure S2.11-S2.12-S2.13)**

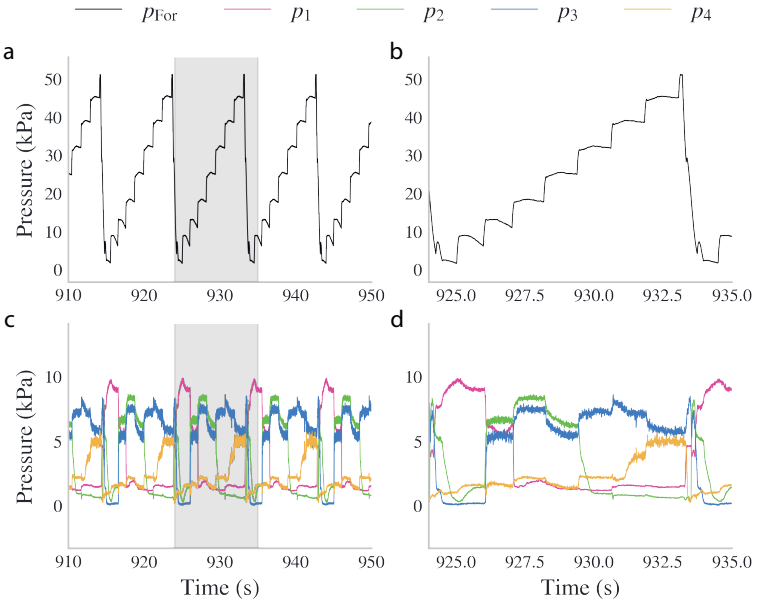


Figure S2.11: **Experimental data for demonstrating the sequencing capabilities of the device in Figure 2.5. (a)-(b)** Pressure on the linear actuator controlled using the pneumatic *For* coding block. **(c)-(d)** Pressure at the output channels. In **b** and **d** we report the highlight of measured pressures during one actuation cycle that is shaded in **a** and **c**. The data represented in this experiment was collected while performing the experiment in Video 1.

We report the demultiplexer design and section view in Figure S2.12. As the punched card with instruction is subject to the $p_{in}$ pressure, it is pushed against the separating pins in the cross-section view in Figure S2.12**b**. This mechanism, together with the large change in fluidic resistance provided by the opening on the punched card, prevents leakages between channels while guaranteeing the execution of instructions in time. Still, just like in a book organ when no note is played, the system is based on continuous leakages. Therefore, a high input pressure is needed to drive its operation as a program counter. The .1mm PVC sheet is attached to the free end of the PLA slider of the linear actuator controlled by the clocking mechanism of the *For* loop using double-sided tape. Its design and dimensions are reported in Figure S2.13. To facilitate the feeding mechanism

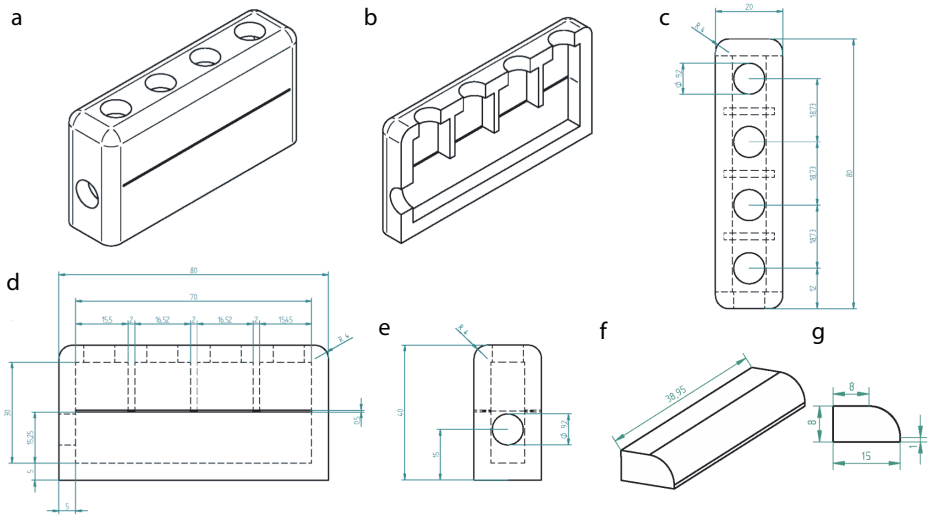


Figure S2.12: **Demultiplexer design.** To fabricate this component, we use outer molds in VeroClear on a PolyJet 3D printer (Eden260VS, Stratasys®). **(a)** Perspective view of the demultiplexer. **(b)**-**(e)** Details of views and dimension. **(f)**-**(g)** Design and dimensions used for the white PLA elements to feed the PVC punched card in Figure S2.11. **(f)** Perspective view. **(g)** Side view. Sizes are in mm.

and prevent out-of-plane deformation of the punched card, we assembled on the demultiplexer two PLA elements of which we specify the design in Figure S2.12**f-g**.

The height of the slot opening through which the punched card slides, together with its material properties, have been designed to guarantee minimal friction while maintaining enough stiffness to prevent the PVC sheet from deforming out of plane when the linear bellow pushes it into the feeder. As a result of its operation, we measure and report the data for multiple loops of actuation in Figure S2.11.

We envision different strategies to guarantee an increasing number of different instructions to be executed. Among these, it would be possible to increase the overall length of the physical support memory together with the extension range of the linear actuator. Alternatively, by decreasing the step size of the extension and length of the apertures in the PVC sheet while increasing the number of steps from the clocking mechanism, the number of instructions density could be

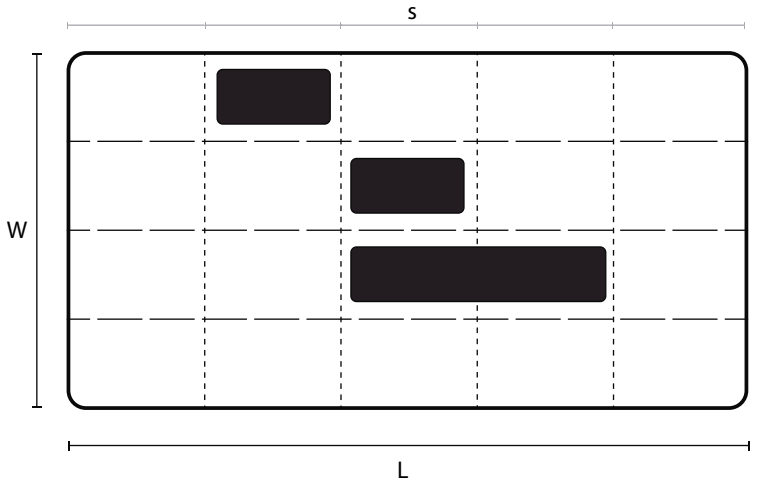


Figure S2.13: **Design and dimensions used for the 0.1mm thick PVC punched card used in the experiment in Figure S2.11.** Width $W = 69.5$mm, total length $L = 80$mm. The length of a punched hole corresponds to a single instruction, which is $s = 14$mm and is equal to its width.

increased without changing the dimensions of the current apparatus.

**Additional experiment for the pneumatic retriever program (Algorithm 6 and Figure S2.14)**

To demonstrate that the gripper can also detect an object without manually interacting with it, we performed an additional experiment. First, we slightly modify the circuit in Figure 2.7**c** only in the *For* loop branch controlling the position of the linear actuator, to increase the timing of the linear extension steps. We put the N.O. valve on the linear actuator branch (in blue) before the hysteretic valves controlling the pneumatic *For* loop and change the size of the fixed volumes on the same branch. To allow deflation of the linear actuator once the *If... break* condition is triggered, we include an additional tunable fluidic resistance venting to atmosphere $R_{\text{out, Linear 1}}$, while keeping the fluidic resistance in parallel with the linear actuator the same as in Figure 2.7**b**. The resulting pneumatic circuit and measured response is shown in Figure S2.14 and Video 2.

Differently from what we show in the first experiment where we manually interact with the gripper when placing the object in between, in this additional run the soft gripper actuators return a lower increase of $p_{\text{S, Bending}}$ pressure in the *If... break* branch, likely due to the reduced deformation that occurs when gripping the object. Nevertheless, the increase in pressure in the gripper as a consequence of the contact with the target object is still able to trigger the *If... break* statement in Algorithm 5 and thus guarantees the successful operation of the pneumatic program. It is worth mentioning that the dynamic response to inflation of the actuator, together with other circuit properties such as parasitic impedances, can affect the operation of the program. As an example, the presence of excessive tubing length can hinder the operation and dampen the overall sensitivity of the *If... break* circuit, as we also observed when setting up the demonstrator.

S2

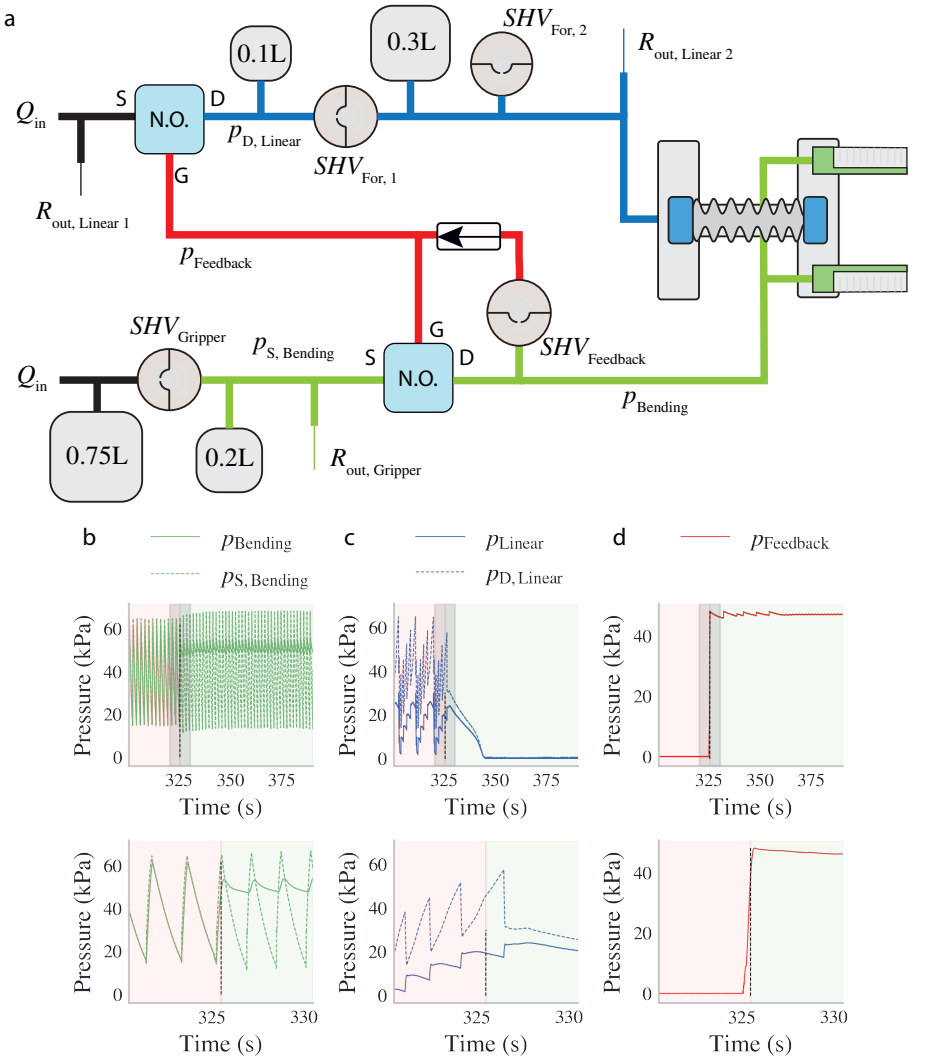


Figure S2.14: **Schematics and experimental data of the retriever demonstrator.** Values of the individual components are the same we reported in Table S16. **(a)** Circuit schematics. **(b-d)** Experimental data from the circuit before and after the *If... break* condition is triggered upon gripping the object, respectively for the bending actuator branch (green), the linear actuator branch (blue), and the feedback branch (red). In the top row, we report an overview of the two different pneumatic responses before and after the *If... break* condition is triggered, with the successful gripping event. The shaded time window of the interaction event is shown in more detail in the bottom row.

## ii) Additional fabrication details and data for supplementary material



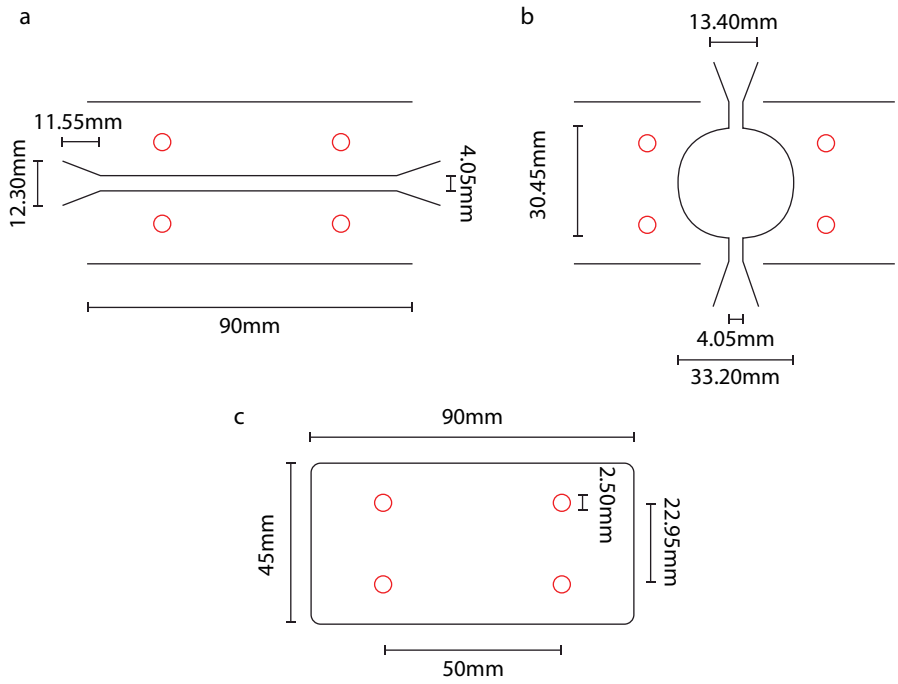


Figure S2.15: **Diagram of the files used to fabricate the N.O. valve.** (**a**) TPU source-drain channel. (**b**) TPU gate channel. (**c**) Single plexiglass plate enclosure. We use the red circular elements in **a**, **b** and **c** to facilitate the alignment in the assembly of the N.O. valve as we highlight in Figure S2.17 using M4 screws and nuts.

S2

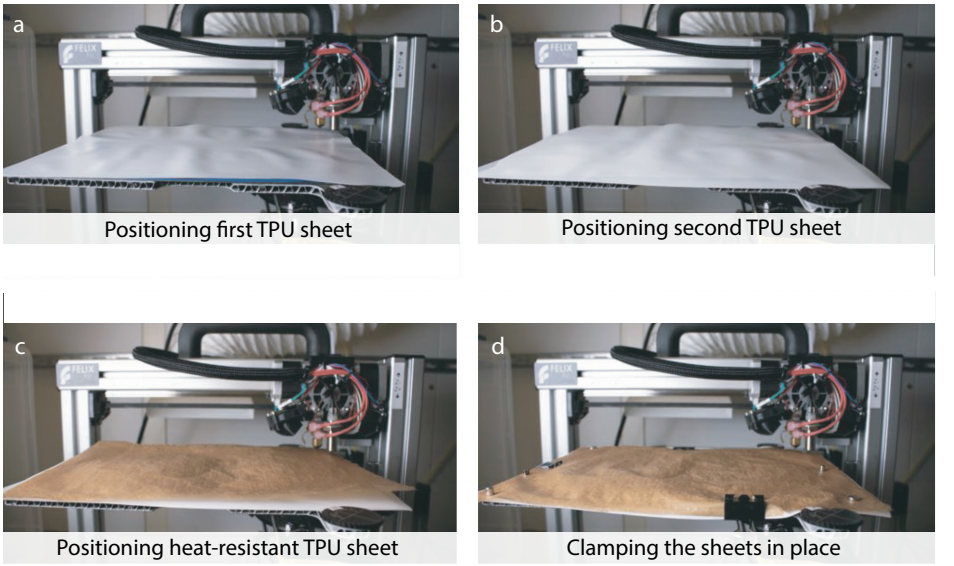


Figure S2.16: **Fabrication details for the heat sealing procedure of the TPU sheets used in the N.O. valve.** (**a**-**b**) The TPU sheets are first cut and positioned on the print bed of the modified 3D printer. A heat-resistant sheet (commercial baking paper) is then positioned (**c**) and fixed (**d**) on top of the TPU sheets using clamps and magnets.

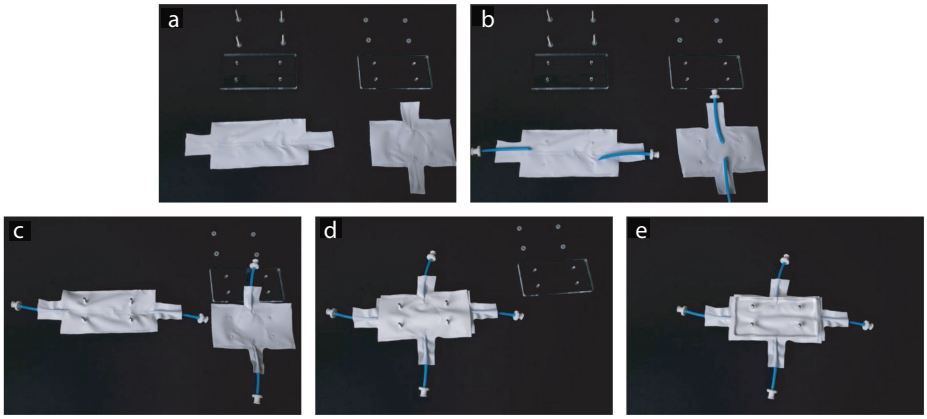


Figure S2.17: **Assembly procedure of the two plexiglass plates and two pairs of heat sealed TPU sheets for our design of the N.O. valve.** (**a-b**) The FESTO® outer diameter 4mm tubes with the Luer connectors are prepared. (**c-d**) The prepared FESTO® tubes are inserted into each of the ports in the N.O. valve design and aligned on top of the first plexiglass. The alignment of the resulting multilayer structure is guided with four M4 screws. (**e**) The second plexiglass is then positioned on top and secured with M4 screws and nuts so that the distance between the two plexiglass plates is 4mm.

S2

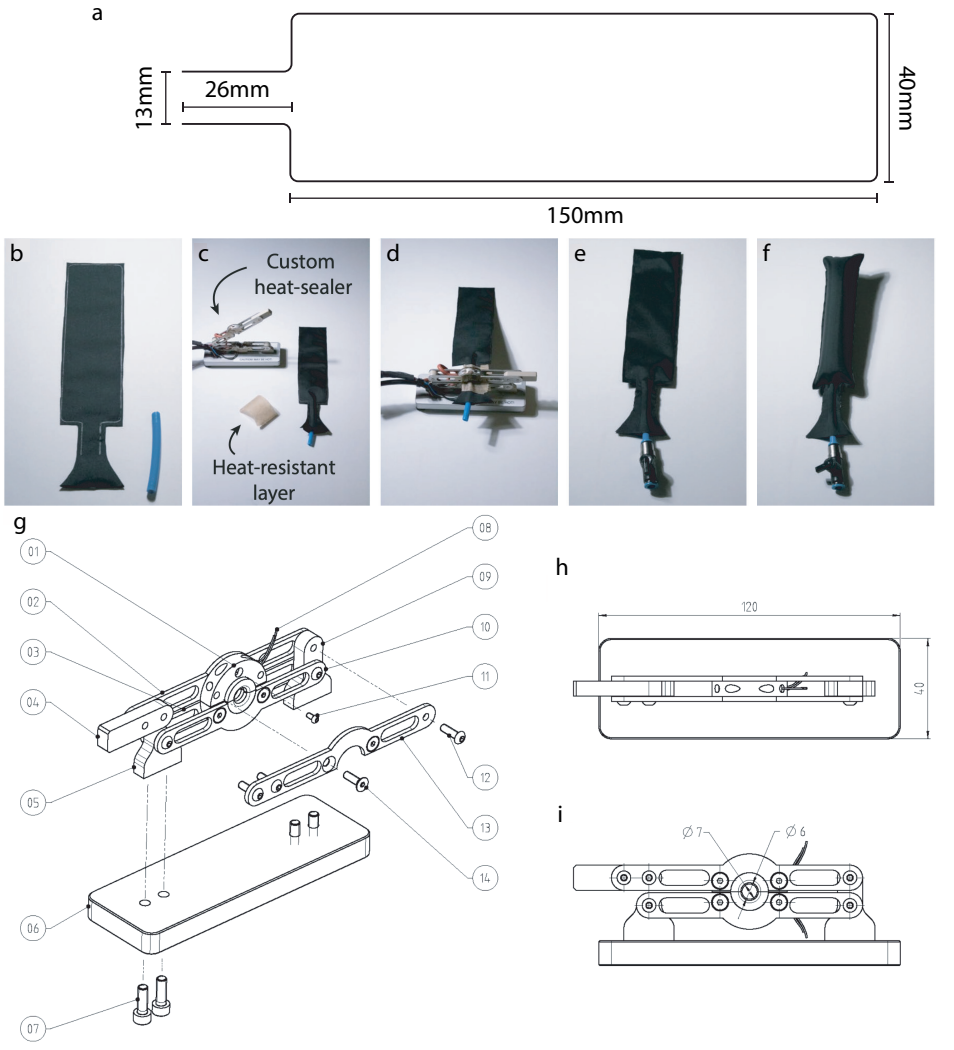


Figure S2.18: **Fabrication of nylon-coated TPU pouches.** (**a**) Drawing of the pouch outline. (**b-f**) Heat sealing process needed to connect the TPU pouch with the FESTO® tube in **a**. **b** Nylon-coated TPU after heat-sealing. **c-f** Highlights of the custom circular heat sealer and heat resistant layer that are then used **c**. The configuration in (**d**) is maintained for 15s at 200°C. The procedure in **d** can be repeated until the connection is airtight.(**e-f**) Deflated ($p_{\text{TPU pouch}} = p_{\text{amb}}$) and inflated ($p_{\text{TPU pouch}} = 5\text{bar}$) state of the TPU pouch. (**g-i**) Assembly of the custom circular heat sealer. Numbered components in **g** are reported in Table S2.16. **h-i** Top and side view, dimensions are in mm.

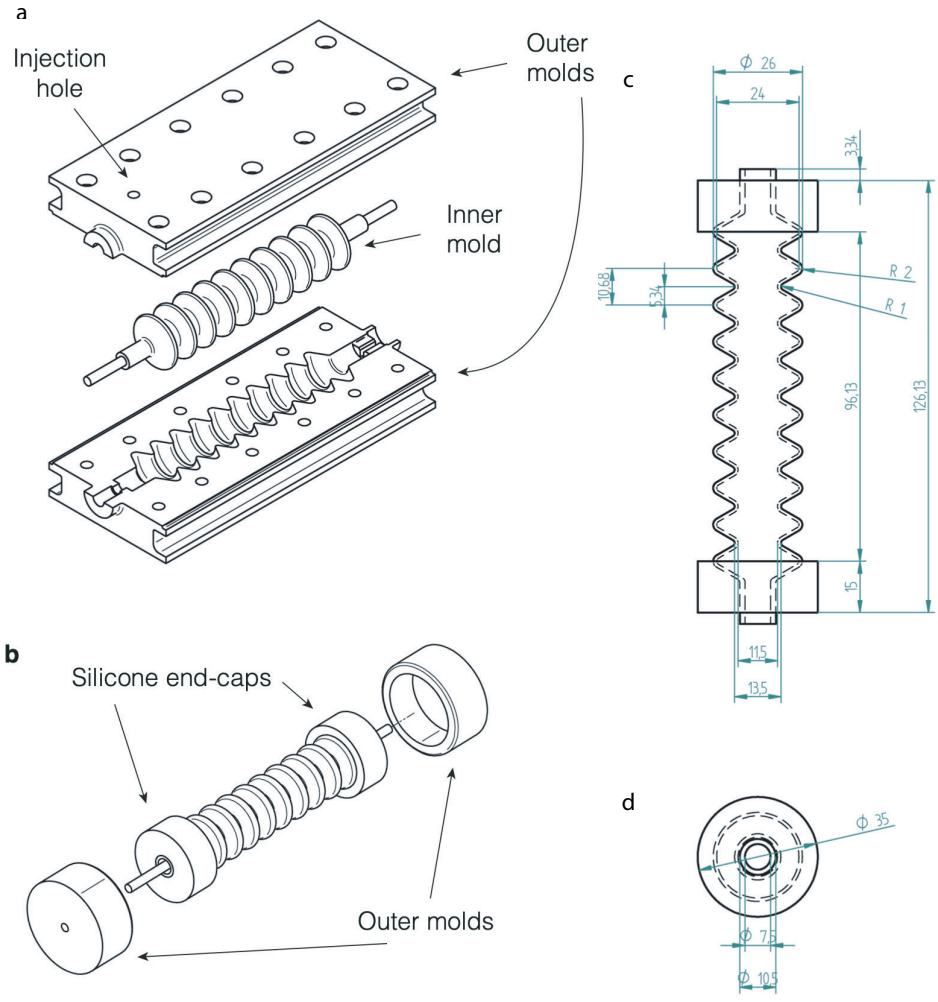


Figure S2.19: **Details of fabrication process of the linear soft actuator used in Figure 2.4c, Figure 2.5 and Figure 2.7.** (**a**) The inner mold of BVOH support material is assembled inside the outer mold. DS 20 silicone is then injected to fill the space between inner and outer molds. (**b**) Fabrication detail of the ED32 fast end-caps of the actuator. (**c-d**) Specifics of actuator's dimensions, R1 and R2 in **c** refer to the radii of curvature. All dimensions are in mm.

S2

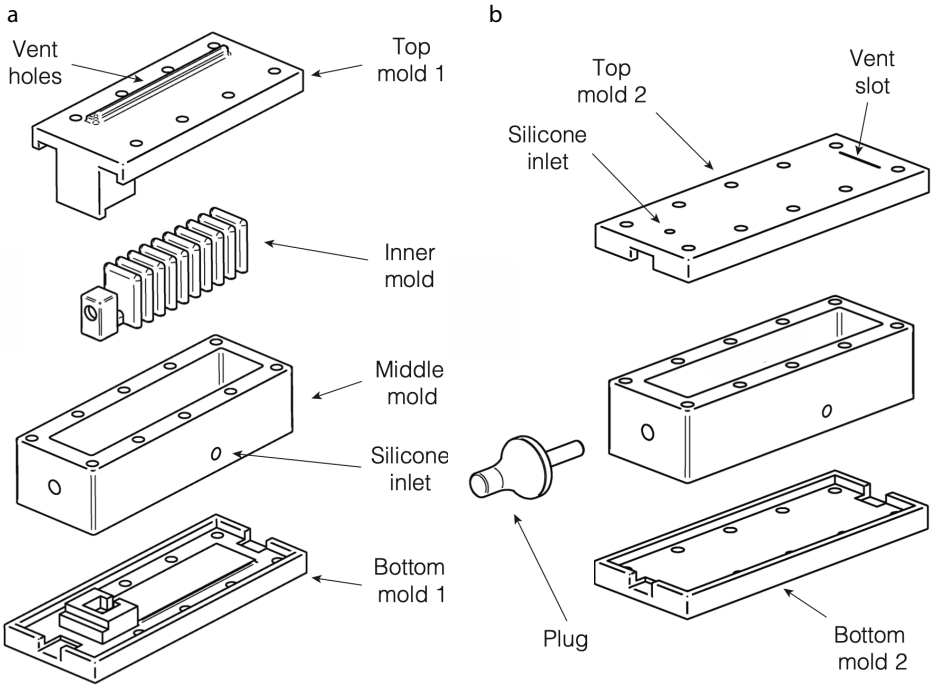


Figure S2.20: **Two-steps procedure fabrication of the soft bending actuators. (a)** In the first step we insert the inner mold on Bottom mold 1 and inject DS 20 from the silicone inlet. **(b)** After waiting 2.5h, we substitute Top Mold 1 and Bottom Mold 1 with Top Mold 2 and Bottom Mold 2 respectively, before inserting the Plug and injecting ED 32.

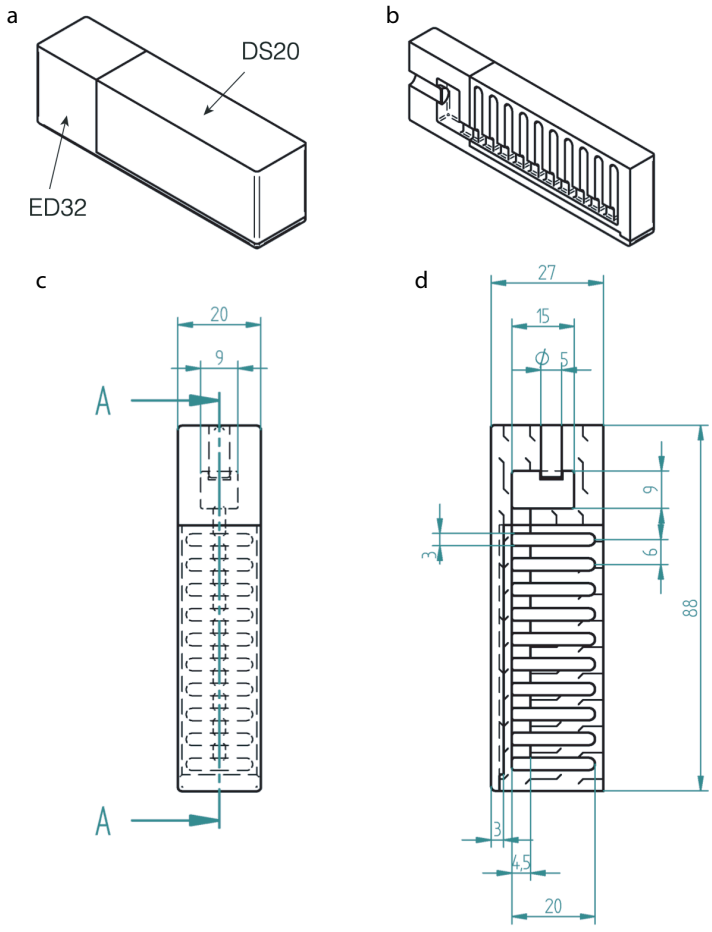


Figure S2.21: **Geometrical parameters of the soft bending actuators.** (**a**) Highlight of the resulting actuator with the two different silicone materials (ED32 and DS20). (**b**) Cross section view to highlight the array of internal air chambers resulting after the support material has been removed from inside the soft actuator. (**c**) Top view. (**d**) Side view. Dimensions are in mm.

S2

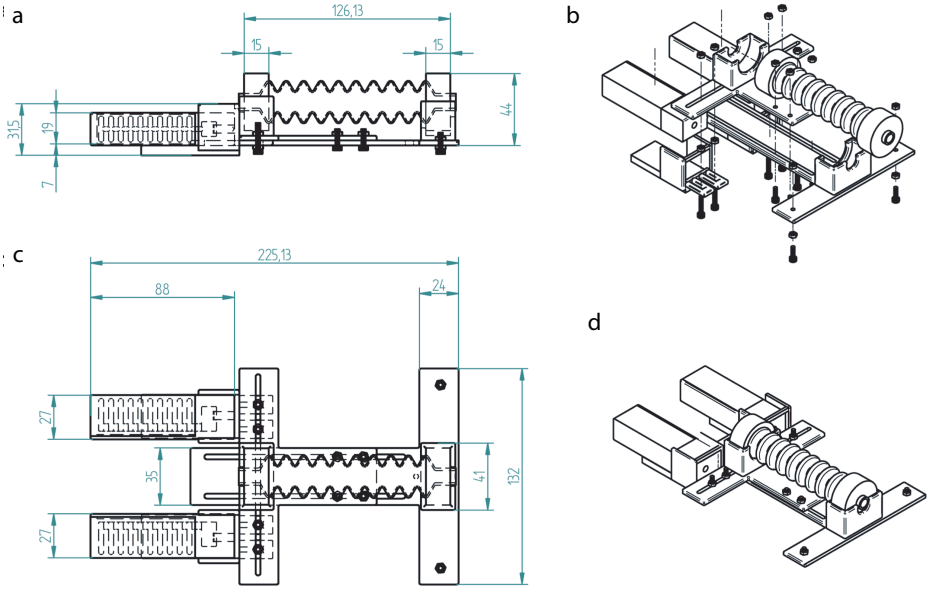


Figure S2.22: **Schematics of the assembly we use in Figure 2.4b, Figure 2.5, and Figure 2.7.** We fabricate a 3D-printed PLA frame to accommodate the soft linear actuator and the two bending actuators. We assemble the individual parts together using M2 screws. To reduce friction with the ground, we also use the M4 screw heads as contact points to the surface on which the assembly sits. **(a)-(c)** Geometry and dimensions of the assembly. **(b)-(d)** Assembly with highlighted screw positions and completed assembly. For the demonstrators in Figure 2.4**b**, Figure 2.5, we do not include in the assembly the two supports for the Pneunet actuators.

# iii) Tables with extended details of components and experiment details



### Fluidic regulators and sensors

Air pressure and airflow data measured throughout our work were collected using analog sensors using a data acquisition card NI-DAQ USB-6212, National Instruments® with custom software developed at AMOLF. All experiments were initialized with 10s blank measurements to calibrate the offsets in the sensors. Data collected from each experiment was analysed using a custom Python script.

In the following tables, we report the details of the components used in our experiments.

| Variable | Component |
|---|---|
| $p_{\text{in}}$ | VEAB-L-26-D13-Q4-V1-1R1 8046307, FESTO® |
| $p$ | SSCDRRN015PDAA5, Honeywell® |

Table S2.1: **Sensors and regulators for experiment in Figure 2.2.** Sampling frequency = 1kHz

| Variable | Component |
|---|---|
| $p_{\text{ in}}$ | VEAB-L-26-D13-Q4-V1-1R1 8046307, FESTO® |
| $p$ | SSCDRRN015PDAA5, Honeywell® |
| $p_{\text{G}}$ | SSCDRRN015PDAA5, Honeywell® |

Table S2.2: **Sensors and regulators for experiment in Figure 2.3.** Sampling frequency = 1kHz

| Variable | Component |
|---|---|
| $Q_{\text{in}}$ | SLA5850, , Brooks Instrument® |
| $p_{\text{A}}$ | MPX5100DP, NXP® |
| $p_{\text{B}}$ | MPX5100DP, NXP® |

Table S2.3: **Sensors and regulators for experiment in Figure 2.4a.** Sampling frequency = 500Hz

S2

| Variable | Component |
|---|---|
| $Q_{\text{in}}$ | SLA5850, , Brooks Instrument® |
| $p_{\text{A}}$ | MPX5700DP, NXP® |
| $p_{\text{B}}$ | MPX5700DP, NXP® |

Table S2.4: **Sensors and regulators for experiment in Figure 2.4d.** Sampling frequency = 500Hz

| Variable | Component |
|---|---|
| $Q_{\text{in}}$ | SLA5850, , Brooks Instrument® |
| $p_{\text{A}}$ | MPX5100DP, NXP® |
| $p_{\text{B}}$ | MPX5100DP, NXP® |
| $p_{\text{C}}$ | SSCDRRN015PDAA5, Honeywell® |

Table S2.5: **Sensors and regulators for experiment in Figure 2.4g.** Sampling frequency = 500Hz

| Variable | Component |
|---|---|
| $Q_{\text{in}}$ | SLA5850, , Brooks Instrument® |
| $p_{\text{A}}$ | MPX5100DP, NXP® |
| $p_{\text{B}}$ | MPX5100DP, NXP® |

Table S2.6: **Sensors and regulators for experiment in Figure 2.5.** Sampling frequency = 500Hz

| Variable | Component |
|---|---|
| $p_{\text{in}}$ | VEAB-L-26-D13-Q4-V1-1R1 8046307, FESTO® |
| $p_1$ | SSCDRRN015PDAA5, Honeywell® |

Table S2.7: **Sensors and regulators for experiment in Figure S2.1-S2.2.** Sampling frequency = 1kHz

| Variable | Component |
|---|---|
| $p_{\text{G}}$ | SSCDRRN015PDAA5, Honeywell® |
| $p_{\text{SD}}$ | SSCDRRN015PDAA5, Honeywell® |
| $Q_{\text{SD}}$ | AWM5104, Honeywell® |

Table S2.8: **Sensors and regulators for experiment in Figure S2.5.** Sampling frequency = 250Hz

| Variable | Component |
|---|---|
| $p_{G,0}$ | SSCDRRN015PDAA5, Honeywell® |
| $p_G$ | SSCDRRN015PDAA5, Honeywell® |
| $p_{SD}$ | SSCDRRN015PDAA5, Honeywell® |
| $p_{in}$ | VEAB-L-26-D13-Q4-V1-1R1 8046307, FESTO® |
| $Q_{SD}$ | AWM5104, Honeywell® |

Table S2.9: **Sensors and regulators for experiment in Figure S2.6-S2.7.** Sampling frequency = 250Hz

| Variable | Component |
|---|---|
| $p_{in}$ | VEAB-L-26-D13-Q4-V1-1R1 8046307, FESTO® |
| $p_{out}$ | SSCDRRN015PDAA5, Honeywell® |
| $p_G$ | MPX5700DP, NXP® |

Table S2.10: **Sensors and regulators for experiment in Figure S2.23c.** Sampling frequency = 500Hz

| Variable | Component |
|---|---|
| $p_{in}$ | VEAB-L-26-D13-Q4-V1-1R1 8046307, FESTO® |
| $p_{out}$ | SSCDRRN015PDAA5, Honeywell® |
| $p_{G,1}$ | MPX5700DP, NXP® |
| $p_{G,2}$ | MPX5700DP, NXP® |

Table S2.11: **Sensors and regulators for experiment in Figure S2.23d-e.** Sampling frequency = 500Hz

| Variable | Component |
|---|---|
| $p_{in}$ | VEAB-L-26-D13-Q4-V1-1R1 8046307, FESTO® |
| $p_1$ | SSCDRRN015PDAA5, Honeywell® |
| $p_2$ | MPX5100DP, NXP® |
| $p_{Act.}$ | SSCDRRN015PDAA5, Honeywell® |
| $p_{G,\,f}$ | MPX5700DP, NXP® |
| $p_{G,\,Ampl}$ | SSCDRRN015PDAA5, Honeywell® |

Table S2.12: **Sensors and regulators for experiment in Figure 2.6** Sampling frequency = 1kHz

S2

| Variable | Component |
|---|---|
| $Q_{\text{in, Linear}}$ | SLA5850, , Brooks Instrument® |
| $Q_{\text{in, Gripper}}$ | SLA5850, , Brooks Instrument® |
| $p_{\text{S, Linear}}$ | SSCDRRN015PDAA5, Honeywell® |
| $p_{\text{Linear}}$ | MPX5100DP, NXP® |
| $p_{\text{S, Bending}}$ | MPX5100DP, NXP® |
| $p_{\text{Bending}}$ | SSCDRRN015PDAA5, Honeywell® |
| $p_{\text{Feedback}}$ | SSCDRRN015PDAA5, Honeywell® |

Table S2.13: **Sensors and regulators for experiment in Figure 2.7-2.8.** Sampling frequency = 1kHz

| Variable | Component |
|---|---|
| $p_{\text{in}}$ | VEAB-L-26-D13-Q4-V1-1R1 8046307, FESTO® |
| $p_{\text{in}}$ | SSCDRRN015PDAA5, Honeywell® |
| $p_{\text{Gripper}}$ | MPX5100DP, NXP® |
| $p_{\text{G}}$ | SSCDRRN015PDAA5, Honeywell® |

Table S2.14: **Sensors and regulators for experiment in Figure S2.24.** Sampling frequency = 1kHz

| Variable | Component |
|---|---|
| $p_{\text{in}}$ | SSCDRRN015PDAA5, Honeywell® |
| $p_{\text{A}}$ | SSCDRRN015PDAA5, Honeywell® |
| $p_{\text{B}}$ | SSCDRRN015PDAA5, Honeywell® |

Table S2.15: **Sensors and regulators for experiment in Figure S2.26.** Sampling frequency = 1kHz

**Highlights of fabrication**

| Number | Component | Quantity |
|---|---|---|
| 1 | Sealblock 6mm tubes (AL6082, anodized white) | 1 |
| 2 | Arm top left | 1 |
| 3 | Arm bottom left | 1 |
| 4 | Handle (PEEK) | 1 |
| 5 | Fixture (PEEK) | 1 |
| 6 | Base (AL6082, anodized white) | 1 |
| 7 | Hexagon socket cap screw M4x12 | 4 |
| 8 | Watlow heater CIA 9604 | 1 |
| 9 | Hinge post | 1 |
| 10 | Arm bottom right | 1 |
| 11 | Round head low screw M2x4 | 2 |
| 12 | Round head low screw M3x10 | 5 |
| 13 | Arm top right | 1 |
| 14 | Hexagon socket cap screw M3x10 | 4 |

Table S2.16: **Description of the components in Figure S2.18g.**

S2

| Reference Figure | Component | Details |
|---|---|---|
| Figure 2.2 | Compliant volume | VWR®, 60mL bulb |
| Figure 2.3**c** | Compliant volume | VWR®, 60mL bulb |
| | $R_{\text{out}}$ | SMD® 21 gauge 6.35mm length needle |
| Figure 2.4**a** | $V_1$ | FESTO® 100mL air reservoir |
| | $V_2$ | FESTO® 750mL air reservoir |
| | $\Delta p_{\text{open},1}$ | 38kPa |
| | $\Delta p_{\text{open},2}$ | 32kPa |
| | $Q_{\text{in}}$ | 2SLPM |
| Figure 2.4**f** | $V_1$ | FESTO® 100mL air reservoir |
| | $V_2$ | FESTO® 750mL air reservoir |
| | $V_3$ | FESTO® 500mL air reservoir |
| | $\Delta p_{\text{open},1}$ | 38kPa |
| | $\Delta p_{\text{open},2}$ | 32kPa |
| | $\Delta p_{\text{open},3}$ | 23kPa |
| | $Q_{\text{in}}$ | 2SLPM |
| Figure 2.5 | $\Delta p_{\text{open},1}$ | 20kPa |
| | $\Delta p_{\text{open},2}$ | 55kPa |
| | $Q_{\text{in}}$ | 1SLPM |
| Figure 2.6 | $R_{\text{out, S}}$ | SMD® 18 gauge 12.7mm length needle |
| | $R_{\text{out, D}}$ | SMD® 20 gauge 12.7mm length needle |
| | $V$ | FESTO® 100mL air reservoir |
| | $\Delta p_{\text{open}}$ | 55kPa |
| | $p_{\text{in}}$ | 110kPa |

*(Continues on the following page)*

| Reference Figure | Component | Details |
|---|---|---|
| Figure 2.8 | $R_{\text{out, Linear}}$ | SMD® 25 gauge 6.35mm length needle |
| | $R_{\text{out, Gripper}}$ | SMD® 25 gauge 6.35mm length needle |
| | $SHV_{\text{Gripper}}$ $\Delta p_{\text{open}}$ | 70kPa |
| | $SHV_{\text{Feedback}}$ $\Delta p_{\text{open}}$ | 55kPa |
| | $SHV_{\text{For, 1}}$ $\Delta p_{\text{open}}$ | 20kPa |
| | $SHV_{\text{For, 2}}$ $\Delta p_{\text{open}}$ | 28kPa |
| | $Q_{\text{in, Linear}}$ | 1.2SLPM |
| | $Q_{\text{in, Gripper}}$ | 1.2SLPM |
| FigureS2.23 **c** | $R_{\text{out}}$ | SMD® 25 gauge 6.35mm length needle |
| | $\Delta p_{\text{open}}$ | 38kPa |
| | $p_{\text{in}}$ | 25kPa |
| FigureS2.23 **d-e** | $R_{\text{out}}$ | SMD® 25 gauge 6.35mm length needle |
| | $\Delta p_{\text{open,blue}}$ | 32kPa |
| | $\Delta p_{\text{open,ochre}}$ | 38kPa |
| | $p_{\text{in}}$ | 25kPa |

Table S2.17: **Extended details of parameters and components not described in the main text.** *SHV* refers to the **S**oft **H**ysteretic **V**alves that were fabricated following the procedure in [69]. The one-way valves used in our work are the FESTO® H-QS-61.

S2

# iv) Additional pneumatic circuits design

- Encoding variables using the N.O. valve (Figure S2.23)
- Single use *If* pneumatic coding block (Figure S2.24)
- *If* pneumatic coding block (Figure S2.25)
- Venus flytrap inspired pneumatic circuit (Figure S2.26)

### Encoding variables using the N.O. valve (Figure S2.23)

To obtain boolean non-volatile memory in our circuits, we make use of one soft hysteretic valve, the N.O. valve, two one-way valves, and two TPU heat-sealed pouches that we use as interacting volumes as shown in Figure S2.23**a**. Through the one-way valves, we create an oriented-ring network for airflow, and we connect one branch of this network to the gate of the N.O. valve. We functionalize this circuit by injecting a finite volume of air in the ring network so that the gate of the N.O. valve reaches a pressure $p_G < \Delta p_{\text{open}}$, $\Delta p_{\text{open}}$ being the opening pressure of the hysteretic valve. In this configuration, if the source is pressurized at $p_{\text{S}}$ so that $p_{\text{S}} < p_{\text{G}}$, it results in the N.O. valve being in the closed state, which we show in Figure S2.23**a**. To change the state of the N.O. valve, representative of the boolean state of our pneumatic variable, we reduce the volume of the pressurized TPU pouch by interacting with it so that $p_{\text{G}} > \Delta p_{\text{open}}$ and the hysteretic valve opens. The air volume inside the ring circuit is therefore forced to follow the path dictated by the one-way valves. Therefore, as $p_{\text{G}}$ drops to $p_{\text{amb}}$, the gate of the N.O. valve opens, and the output pressure $p_{\text{out}}$ increases, which we schematically represent in Figure S2.23**b**. In order to close the N.O. valve again, it is sufficient to interact with the TPU pouch not connected to the gate, so that the air volume can be moved back into the gate branch to and increase $p_{\text{G}}$ again. We report the pressure in time at the output of the circuit and at the gate branch in Figure S2.23**c** upon multiple interaction events. We highlight that the underlying idea behind the change of state of the boolean variable is still based on the intuition of the triggerable signal we introduced in the *If* coding block. In this configuration, the role of the soft hysteretic valve is to determine a certain critical pressure that must be reached in order for the gate to change its state. Moreover, a second hysteretic valve can be connected in series to the one-way valve in the gate branch to tune different activation/deactivation thresholds for the pressure inputs to trigger the switch of the boolean variable. Differently from before, we can now use the same volume of air through the oriented ring configuration, so that once the first pressurization of the gate has occurred, the system can be controlled and modified with no need for pressure or flow regulators. On top of that, similarly to what we discussed for the *If* case, we can tune the sensitivity of the ring network

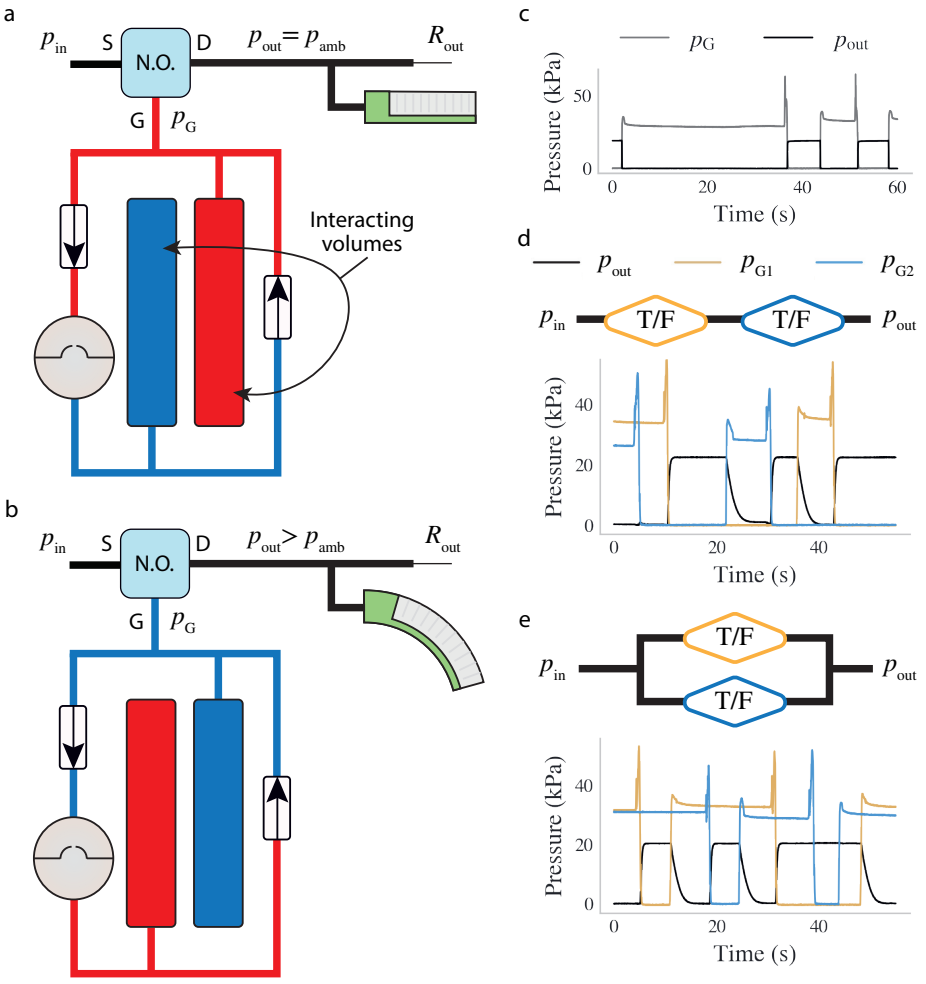


Figure S2.23: **Schematics and experimental data for the boolean variable circuit.** (**a-b**) Circuit diagram for the different states of the boolean variable. Red and blue indicate the high-pressure and low-pressure branches, respectively. When $p_G > p_{p_{in}}$, the N.O. valve is closed, as in **a**. Conversely, when $p_{in} > p_{p_G}$ as in **b**, $p_{out} > p_{amb}$. (**c**) Pressures in time for the schematics in **a** upon different activations and deactivations of the boolean variable. (**d-e**) Pressures in time at the gates and at the output for the connections of two boolean variables respectively in series and in parallel. For these experiments, we connect $p_{out}$ to the same soft actuator and $R_{out}$ as in **a** and **c**. We report the parameters of this pneumatic circuit in Table S2.17.

to mechanical interactions with the pouch by controlling the initial pressurization of the gate. This means that the closer $p_G$ is to the $\Delta p_{\text{open}}$, the smaller the increase in pressure upon interactions that will be needed for the transition of the state of the gate to take place.

TPU pouches lend themselves well to be used in the pneumatic ring network we investigate here when compared to other compliant volumes. We support this argument by stressing that once a TPU pouch is deformed to have almost negligible geometrical internal volume, it has low stiffness and, therefore, generates only negligible negative pressure in the same branch. This last feature, in particular, prevents unwanted airflow inside the pneumatic ring network, increasing the overall repeatability and tunability of the circuit. On top of that, as the ring circuit is pneumatically isolated from the environment and the soft hysteretic valve has negligible leaking, both the total volume of air as well as its distribution in the circuit stay fixed over time. Thus, this circuit shows long-term memory effects, as we show in Figure S2.18**a-f**.

Using the pneumatic ring network circuit, it is possible to change the state of the N.O. valve and let it transition from an open to closed state (and vice-versa) with no need for it to be connected to an external source of pressure or flow. From a functionality point of view, we observe that the individual N.O. valve can be considered as a boolean logic gate. This also means that two boolean variable circuits connected in series must behave as an *AND* port and as an *OR* gate when connected in parallel. We prove this last statement by connecting two boolean variable circuits in series (Figure S2.23**d**) and parallel (Figure S2.23**e**) and in Video 3. For these experiments, we control the gate pressures $p_{\text{G},1}$ and $p_{\text{G},2}$ to pressurize or depressurize the shared output branch according to the state of the individual logic gates.

We highlight that, for the gate mechanism to work, it is necessary for $p_{\text{S}}$ to be lower than $p_{\text{G}}$ as, otherwise, the N.O. valve operates as a tunable flow restrictor.

### Single use *If* (Figure S2.24)

We further demonstrate the capability of our system to reproduce high-level functionalities using the circuit design in Figure S2.24. Compared to what we presented in Figure 2.3, with this pneumatic circuit, we let the actuators transition from a non-pressurized to a pressurized state. By modifying the circuit design compared to the aforementioned ones for the *If* pneumatic circuits, we enable single-use sensing capabilities that can be used, e.g., permanently changing the state of a fluidic variable in our pneumatic coding blocks dictionary. With this pneumatic circuit, we mean to reproduce a single-use triggerable behavior of the *If* pneumatic coding block to let the state of a soft gripper transition from the non-actuated to the actuated state upon interaction with a compliant volume (VWR® bulb of 150mL) taking place at $t = 0$s.

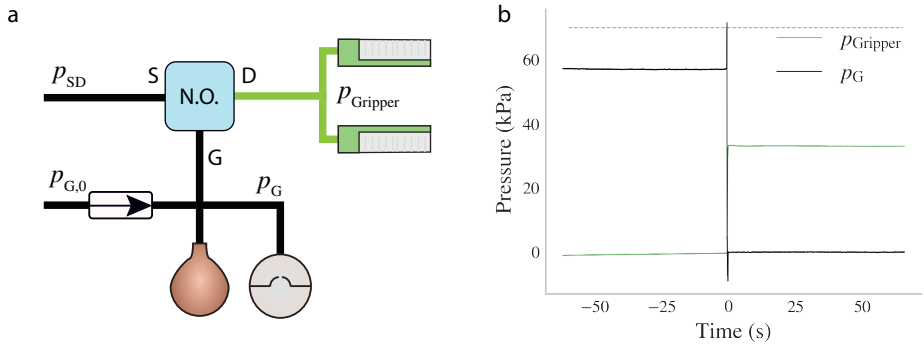


Figure S2.24: **Exploring single-use sensing capabilities in pneumatic soft robots using the *If* pneumatic coding block.** (**a**) Circuit design. (**b**) Experimental data from the execution of the experiment as described in the main text. The dashed gray line represents $\Delta p_{\text{open}} = 70\text{kPa}$, the activation threshold of the pneumatic *If* condition. The compliant volume is a VWR®, 15mL bulb. The green and black data represent respectively the pressure in the gripper and at the gate of the N.O. valve.

We connect two bending actuators similar to the ones used in Figure 2.7 to the drain of a N.O. valve. We set a $p_{\text{in}} = 30\text{kPa}$ pressure at the source of the N.O. valve. The gate of the N.O. valve is here connected to a pressure source controlled at $p_{\text{G},0}$ through a one-way valve and in parallel with the compliant volume and a soft hysteretic valve with $\Delta p_{\text{open}} = 70\text{kPa}$.

This initialization protocol takes inspiration from the one we explored in Figure S2.6. While initializing the system, $p_{\text{in}} < p_{\text{G},0} = 55\text{kPa}$, the gripper is at $p_{\text{amb}}$ and therefore not inflated. We then set the pressure regulator at the gate to ambient $p_{\text{amb}}$ and observe that, in this configuration, the soft hysteretic valve is able to retain pressure. This is due to the fact that in this experiment the initial pressure in the gate branch is closer to the $\Delta p_{\text{open}}$ of the soft hysteretic valve and therefore the soft hysteretic valve has only negligible to no leakages as studied more in detail in [91]. Thus, $p_{\text{G}}$ is retained at $p_{\text{G},0}$ and the pneumatic circuit is now able to execute the pseudocode in Algorithm 7.

Moreover, we highlight that in the circuit design we propose in Figure S2.24, the control system to execute the pseudocode in Algorithm 7 does not require to be constantly connected to a power source for the pneumatic *If* condition to operate.

**Algorithm 7** Pseudocode for single-use *If* circuit in Figure S2.24

```
DeflatedActuator = true
while DeflatedActuator do
    if interaction then
        Inflate(actuator)
        DeflatedActuator = false
    end if
end while
```

### *If*... *else* pneumatic circuit (Figure S2.25)

The pneumatic coding block equivalent to an *If*... *else* statement can be obtained by using the circuit in Figure S2.25**a** that we use to materialize the functionality of the pseudocode in Algorithm 8. Starting from the *If* pneumatic coding block schematics in Figure 2.2, the conceptual step to enable the *If* ... *else* functionality is to enable feedback to the system that can create a boolean switch from one state to another while pressurizing the desired ... *else* channel. To meet this purpose, we use a constant pressure input at $p_{\text{in}} = 60\text{kPa}$ connected in parallel to the source of a N.O. valve and the inlet of a soft hysteretic valve with opening pressure $\Delta p_{\text{open}} = 68\text{kPa}$ through a one-way valve. To provide the required feedback once the *If* condition is triggered, we connect the outlet of the hysteretic valve to the gate port of the N.O. valve. While performing our experiment with this circuit design, we measure the pressures before the soft hysteretic valve $p_{\text{SHV}}$, at the drain of the N.O. valve $p_{\text{If}}$, and at its gate $p_{\text{Else}}$.

**Algorithm 8** Pseudocode for the *If*... *else* circuit in Figure S2.25. *Interaction*, *Threshold* and *ResetTime* are variables dictated by the specific sizing of the components in the fluidic circuit.

```
while true do
    if Interaction<Threshold then
        Pressurize(p_If)
    else
        Pressurize(p_Else)
        Depressurize(p_If)
        Wait(ResetTime)
        Depressurize(p_Else)
    end if
end while
```

To integrate an automatic reset with the initial conditions, we include in our design $R_{\text{If}}$ and $R_{\text{Else}}$ fluidic resistances venting to the atmosphere at the drain

and gate port of the N.O. valve respectively. As a result, when the *If* condition is triggered, the air pressure will reach the drain port of the N.O. valve while the gate branch is not pressurized. Therefore, this part of the Algorithm 8 is executed

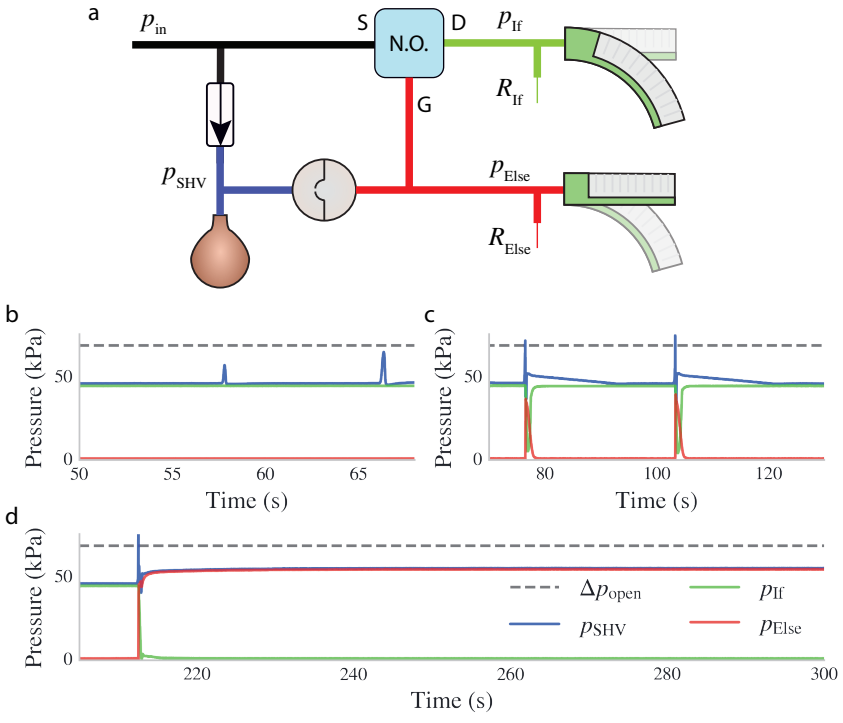


Figure S2.25: **Schematics and data for the *If... else circuit.*** **(a)** Circuit design. **(b-d)** Experimental data representative of the pseudocode in Algorithm 8. **b** When the strength of the interaction does not exceed the set threshold pressure, the *... else* condition is not triggered and the *If* branch (green) stays pressurized. **c** When the pressure before the soft hysteretic valve (blue) exceeds the opening pressure of $\Delta p_{open} = 68$kPa (dashed gray), the *... else* condition is met, and the corresponding branch in red gets pressurized. We enable short-term memory in this circuit by using fluidic resistances $R_{If}$ (18G SMD®) and $R_{Else}$ (22G SMD®). **d** By substituting $R_{Else}$ with a Luer® cap, pressure in the *... else* branch is retained indefinitely, thus allowing long-term memory of the interaction. We show the operation of this pneumatic circuit both in its short-term and long-term memory configuration in Video 3.

both in the idle state and when the interaction does not overcome the desired threshold as we show in Figure S2.25**b**. Conversely, whenever an interaction with the compliant volume causes a large enough pressure increase, the opening of the soft hysteretic valve is triggered. Once the gate branch is pressurized, $p_{\text{Else}}$ increases, and it isolates the source of the N.O. from the drain so that $p_{\text{If}}$ drops while pressure is retained at the gate branch. The role of $R_{\text{Else}}$ is to enable a reset time for the whole *If... else* functionality as we demonstrate in Figure S2.25**c**. We highlight that the *ResetTime* in Algorithm 8 can be increased (decreased) by choosing larger (smaller) $R_{\text{Else}}$ values. At the same time, the variables *Interaction* and *Threshold* can be tuned by changing the volume before the soft hysteretic valve and/or $p_{\text{in}}$, as we show in Figure S2.1-S2.2.

This pneumatic coding block can also be turned into a single-use *If... else* by not venting the pressure at the gate of the N.O. valve. We obtained this result by exchanging the fluidic resistance with a Luer® cap as we show Video 3 and Figure S2.25**c**. Furthermore, we envision that obtaining nested *If... elif... else* pneumatic coding block is indeed possible by expanding on the design in Figure S2.25**a** and adding additional *If... else* conditions in parallel with the gate of the N.O. valve.

### Counting interactions within a given time span using the *If* pneumatic coding block (Figure S2.26)

An interesting feature arises from the design of the pneumatic *If* circuit when considering the case in which the threshold condition is not met with a single interaction event. We investigate this case study by realizing a circuit as in Figure S2.26, without using a pressure or flow regulator. Instead, we use one-way valves and a compliant volume we mechanically interact with. Through this configuration, we force an oriented path for airflow at each interaction with the compliant volume. After the interacting volume, we connect a first soft hysteretic valve in series with a one-way valve. After this second one-way valve, we connect a parallel of a soft bending actuator and a soft hysteretic valve.

As a result of this circuit design, at each interaction with the compliant volume, air is forced through the first soft hysteretic valve and then, through the second one-way valve, pressurizes the branch downstream to it. The role of the first hysteretic valve is to provide a discrete number of air molecules to be flowing to the downstream branch of the circuit only if the $p_A$ in the branch upstream the first hysteretic valve is higher than $\Delta p_{\text{open, 1}}$ of the first soft hysteretic valve. The second one-way valve prevents back-flow of air upon pressurization of the downstream branch, and we make use of the second hysteretic valve to vent to atmosphere $p_B$ with a fast discharge of air molecules only if $p_B > \Delta p_{\text{open, 2}}$. The resulting fluidic circuit is, therefore, able to materialize the functionalities in Algorithm 9. The overall response of the proposed pneumatic circuit can be

S2

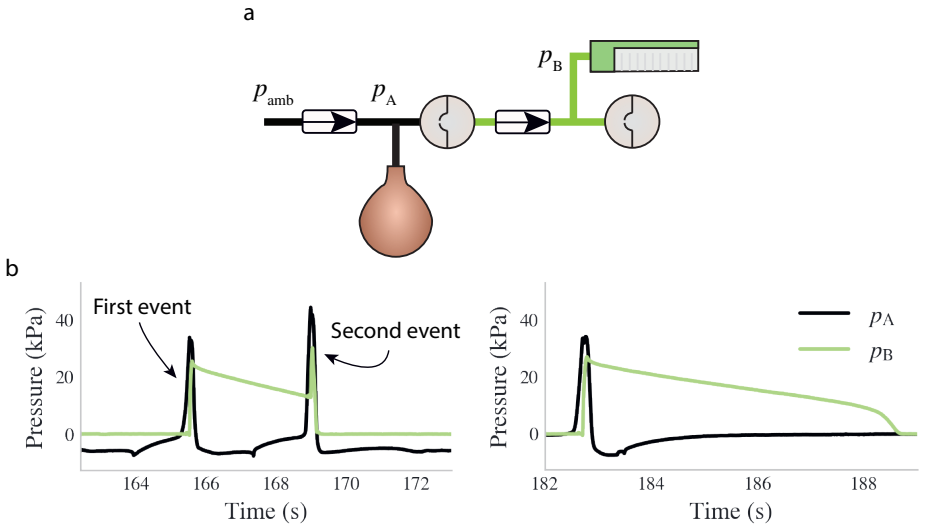


Figure S2.26: **Schematics and experimental data for the pneumatic circuit meant to count the number of interactions with a compliant volume.** (**a**) Circuit design. The interaction volume is a VWR® 150mL bulb. The hysteretic valves have $\Delta p_{\text{open},1} = 24\text{kPa}$ and $\Delta p_{\text{open},2} = 32\text{kPa}$ respectively. (**b**) Example of experimental results for two consecutive interactions that trigger the fast discharge dynamic of pressure before the downstream soft hysteretic valve (top) and a single interaction that results in a slow discharge of pressure (bottom).

related to the *leaky-integrate and fire* response often studied and characterized in biological neuron models. Importantly for our purposes in this demonstrator,



**Algorithm 9** Pseudocode for emulating the response of Venus-Flytrap plants to external stimuli following the circuit design in Figure S2.26.

```
FirstInteraction = false
SecondInteraction = false
if FirstInteraction then
    Inflate(Actuator)
    SlowDeflation(Actuator)
    if SecondInteraction then
        FastDeflation(Actuator)
        SecondInteraction = false
    end if
    FirstInteraction = false
end if
```

as the opening in the soft hysteretic valves is fabricated through laser cutting, these components do not retain pressure once pressurized but allow for leakages. This behavior is particularly evident when a soft hysteretic valve is pressurized at a pressure much lower than the opening pressure [69, 91]. We leverage this feature to automatically reset the pressure in the downstream branch $p_B$ with a slow venting of air molecules whenever $p_B < \Delta p_{open,2}$.

In this configuration, increasing the magnitude of the stiff volume in parallel with the soft actuator will result in a reduced influence in $p_B$ of each interaction with the compliant balloon. This design strategy, similar to the one we introduced in Figure S2.2, results in an increasing number of interactions needed to trigger the fast discharge dynamics of the second soft hysteretic valve. Differently from the previous case where the circuit was controlled using a pressure regulator, now the interactions must occur within a certain time frame in order to trigger the *If* condition from the downstream soft hysteretic valve.

# Chapter 3
# Harvesting environmental circadian oscillations for energy autonomy of soft robots

3

Abstract

Energy autonomy remains elusive in soft robotic devices, yet it is an essential requirement for their real-world application outside lab environments. Some strategies to place an energy source on-board have been proposed for air-powered soft robots, which all require manual intervention for long-term use. We propose a thermopneumatic strategy that takes advantage of circadian thermal oscillations and a pneumatic control circuit to move towards energy autonomy in (soft) robotic systems. The thermodynamic cycle we develop harvests thermal energy from the environment and stores it as pneumatic pressure, after which it is autonomously discharged to power soft pneumatic devices. Our approach uses a low-boiling-point fluid that allows us to repeatedly obtain sufficient energy for the operation of pneumatic soft robotic systems. A developed model shows that our proposed strategy can be used around the world, given sufficient light intensity and ambient temperature. To illustrate the potential of our thermopneumatic concept, we demonstrate that in a single real-world thermal cycle it can trigger 142 activations of a self-oscillating actuator, and that a soft pneumatic robot with two self-oscillating limbs can harvest energy from a thermal source to achieve locomotion. This study proposes a long-term energy harvesting strategy to achieve energy autonomy in soft electronic-free robots.

Based on: *Harvesting environmental circadian oscillations for energy autonomy of soft robots*, Sergio Picella, Alberto Comoretto, Olivier Vaarkamp, and Johannes T. B. Overvelde, *submitted*

## 3.1 Introduction



Soft robots have gained popularity as a result of their intrinsically adaptable interaction with their environment [92, 93]. This feature has motivated the widespread exploration to use soft robotics in, e.g. medicine [78], chemically or mechanically hazardous environments [59, 94], and in the food industry [95, 96]. Their application in these often unstructured and unknown environments can become even more appealing when these soft systems can manifest increasing levels of control and energy autonomy, to reduce the need for human intervention and (tele)operated supervision. While recent studies have shown that soft robots can navigate complex environments or change their actuation pattern based on external stimuli [43, 97, 98] with no need for humans in the control loop [99, 100], solutions to combine the harvesting, storing and control of the energy necessary to power these systems are lacking.

Most soft robots depend on the use of tethers to provide electrical or pneumatic power[101–103], use wirelessly provided electromagnetic [104, 105], acoustic [106] or thermal [107] fields, or harness embedded single-use energy reservoirs (chemical or pneumatic) [108–111]. Such powering strategies often require external human interaction with the robotic system or limit their application to specifically controlled environments, thus preventing them from achieving operational autonomy [112]. To obtain autonomous systems capable of continuous operation, the idea of harvesting energy from naturally occurring environmental changes, e.g., in light intensity and temperatures, to power responsive machines has been explored [113–119], with only a few examples working on strategies to enable energy autonomy [77, 120, 121]. Similar principles have recently been investigated in the context of architectures with embedded electronics-free control, actuation, and powering for smart building façades [122]. However, for these and similar studies, the incoming energy is directly used by the actuators to power automatic responses, rather than a more versatile strategy in which harvesting, storing, and controlling the use of the gathered energy can be separated in time.

In the present work, we propose a strategy to achieve energy autonomy in pneumatic soft robots. Inspired by the view of Mazzolai et al. [5], our approach aims towards the integration of control, power, and actuation components within the same *bodyware* of soft robots intrinsically designed to operate in natural environments. Here, we design a thermopneumatic cycle that can slowly harvest thermal energy from the environment and store it as pneumatic pressure, after which it can be discharged more quickly to power and control soft pneumatic devices. The heat engine cycle is designed around naturally occurring environmental oscillations of temperature and light intensity during the day-night cycle, to enable autonomous energy harvesting during multiple cycles. The term *circadian* in the title and throughout this work indicates that the system can be powered

and actuated by day-night oscillations in temperature and daylight, rather than implying a once-per-day operation. Our approach is based on the pressure generated by the evaporation of a Low-Boiling-point Fluid (LBF), which we couple to a hysteretic valve for controlled pressure release. Compared to previous work that mainly achieved direct responsive systems [120, 123–128], the use of such a hysteretic component is essential to decouple harvesting and release of energy.

We first present our concept for a thermopneumatic cell that can repeatedly harvest, store and release energy obtained from the environment. We evaluate the performance of our system using experiments performed in a controlled lab environment. Secondly, and based on our experimental observations and thermodynamic understanding, we develop a lumped thermodynamic model to simulate the pneumatic response and energy harvesting capabilities of our approach in different locations worldwide. Finally, we show the potential for applications in the context of pneumatic soft robots by demonstrating the operation of our energy-harvesting cell in an outdoor environment. Moreover, we embed our thermopneumatic circuit in a locomoting soft robot to show that our design can be integrated and used as an on-board energy-harvesting element.

## 3.2 Results

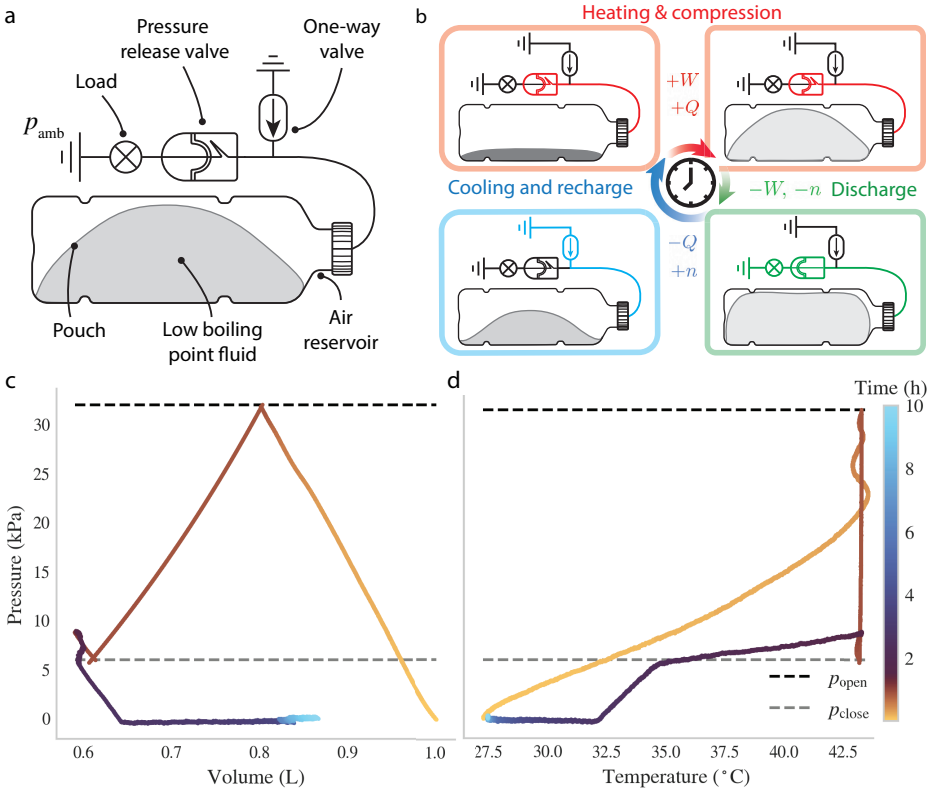


Figure 3.1: **Overview of the thermopneumatic harvesting cell and experimental data of energy harvesting cycle**. **(a)** Thermopneumatic circuit design. **(b)** Working principle of a single energy harvesting cycle. We distinguish between the *compression*, *discharge* and *recharge* phases (respectively in red, green and blue), where we highlight the branch of the pneumatic circuit that is involved in each of the processes together with the state of the pneumatic valves. (**c-d**) Experimental data from the thermopneumatic cell during one thermal cycle from $T_{\text{lab}} = 27°\text{C}$ to $43°\text{C}$ in 2 hours before thermalizing back to $T_{\text{lab}}$ in 8 hours.

### 3.2.1 Thermopneumatic design concept

We extract thermal energy from the environment through a thermopneumatic cell that is driven by the evaporation and condensation of an LBF (Novec 7000® , $T_{\text{boil}}(p_{\text{amb}})$=34°C). Evaporation of Novec 7000® has been successfully used in other soft robotics studies, where actuation is achieved by artificially controlling the temperature using heat sources from resistive heating elements to acoustic waves [127, 129–131]. Here, our goal is to use naturally occurring temperature and solar intensity oscillations during the day-night cycle to harvest, store, and use energy from the environment. The thermopneumatic design concept we use to materialize these functionalities is shown in Figure 3.1**a**, where we distinguish between *(i)* the component to harvest and store pneumatic energy, *(ii)* the component to control the pressure release, and *(iii)* the component that uses the pressure to perform some function and to do work.



#### Harvesting and storing pneumatic energy

To harvest thermal energy from the environment and store pneumatic pressure, we insert a pouch of 15cm by 19cm of heat-sealed nylon coated with TPU containing 5g of LBF inside a 1L plastic bottle that operates as a stiff air reservoir. We provide more details of fabrication in the Methods section. If we close the container and increase the temperature of the LBF-pouch above its boiling temperature $T_{\text{boil}}$, the LBF undergoes evaporation. As a result, the LBF-pouch expands, compressing the air inside the reservoir. The more thermal energy is added to the system, the larger the volume change of the LBF-pouch as a consequence of the vaporization, resulting in a higher internal air pressure in the container.

Note that the use of the LBF-pouch is essential to reach sufficient pressure in the container. While the thermal expansion of the air inside the container also contributes to an increase in pressure, we show through a comparative experiment (S3 section A.2) that the maximum pressure reached at a temperature increase of 30°C differs between $\simeq$ 18kPa for only air, and $\simeq$ 90kPa when including the LBF-pouch. This is mostly due to the fact that, as the fluid evaporates, it undergoes a density change of about three orders of magnitude, whereas, in the ideal-gas law regimes we investigate here, the same temperature increases of the air volume alone causes a pressure increase about five times lower. Practically, the use of an LBF-pouch allows us to localize energy harvesting and storage, while the air inside the air reservoir can be exchanged with the outside environment.

#### Regulating the pressure inside the container

Although we could directly connect the air reservoir to a soft actuator for activation, this directly connects the environmental conditions to the actuator state. This

limits the power conversion capabilities as seen in natural systems, which we wish to reproduce[132, 133].

Instead, to decouple the timescales of charging and actuation, we connect a custom-made pressure relief valve to the air reservoir as shown in the schematics in Figure 3.1**a**. By decoupling of timescales we mean that, unlike approaches where harvested energy is converted into actuation as it becomes available [114, 134], our system stores incoming energy during a slow compression (charging) phase and releases it only after reaching a threshold via a much faster discharge, followed by a distinct recharge process.The working principle of the pressure relief valve is based on a previously proposed - but not yet implemented - design [62], and is based on a monostable elastomeric dome with a silicone tube that passes through the pole of the dome. We provide additional information about the valve design and fluidic properties in the Methods sections and in S3 section A.5.



This valve has two inlets connected in parallel, one connected to the silicone tube and the other connected to the chamber enclosed by the dome itself. The opposite end of the silicone tube is used as the valve outlet. In the resting (normally closed) state, the input pressure $p$ is lower than the activation pressure $p_{\text{open}}$, and the dome kinks the silicone tube preventing the flow of air. When $p > p_{\text{open}}$, the elastomeric dome snaps and unkinks the silicone tube that passes through its pole, allowing the air to flow through the tube. The valve remains in the open state until $p$ drops below $p_{\text{close}}$, the pressure at which the dome transitions back to its monostable state. When this condition is met, the silicone tube kinks again and the valve transitions back to the closed state. Note that given the relatively long time scales involved in the thermopneumatic cycle, it is essential that the valve does not leak. We found that similar valves often show leakage that, although typically relatively small, makes them unsuitable for this specific application [91].

In our thermopneumatic design, the amount of LBF, together with the pressure-release valve critical pressures, fully determines the kind of load that can operate downstream to the energy harvesting cell. As we measure in a comparative experiment in S3 section A.2, by increasing the amount of LBF, it is possible to achieve higher pressures upon vaporization. At the same time, by modifying the geometry of the pressure-release valve and thus its opening pressure (S3 section A.5), we can achieve a greater energy buildup in the energy harvesting cell.

In addition to the pressure relief valve, we also add a commercial one-way valve in parallel to the pressure relief valve (Figure 3.1**a**). This one-way valve ensures that outside air can flow back into the container when the pressure inside the container drops below the atmospheric pressure. This is essential to refill and restore the system to the initial conditions after every activation cycle.

### Thermopneumatic cycles: harvesting thermal energy to perform work

Now that we have a way to harvest thermal energy, store pressure, and control the release, we focus on the resulting thermopneumatic cycle that the system undergoes to perform work when subjected to an increase and decrease of temperature. Before connecting more complex fluidic circuits or actuators after the pressure relief valve that can power soft devices and robots, we first connect a resistive load to gain more insight into the behavior of the developed thermopneumatic system.

The thermopneumatic cycle for our system can be defined in three phases as indicated in Figure 3.1**b**: the *heating & compression phase*, *discharge phase*, and *cooling & recharge phase*. We can observe these phases experimentally when connecting our device to the resistive load (Figure 3.1**a**) and placing it in an oven (Memmert® UF30plus) that regulates the temperature from $T_{\text{lab}} = 27°\text{C}$ to 43°C for 2 hours, before letting it cool back to $T_{\text{lab}}$ for 8 hours. Without loss of generality, when discussing the temperature $T$ in our experiments, we refer to the temperature of the air inside the air reservoir as in Figure S3.18**a**, unless stated otherwise.

Figure 3.1**c-d** reports the pressure, volume, and temperature of the air inside the air reservoir resulting from a single thermal load cycle. The *heating & compression phase* is defined as the period during which pressure builds up as a result of increasing temperature and evaporation of the LBF. As the internal pressure increases from 0 to 32kPa, the LBF-pouch expands, causing the geometric volume of air in the container to decrease. Note that if no LBF-pouch had been present, the geometric volume $V$ of the container would not change, and the volume $V$ would remain 1L. Therefore, we can infer the geometric volume of the LBF-pouch from Figure 3.1**c**, which equals approximately 0.2L at the end of the heating & compression phase.

This phase transitions into the *discharge phase*, which is initiated by the opening of the pressure relief valve when $p > p_{\text{open}}$, and results in the release of air from the container through the pressure relief valve. As a result of the discharge, the pressure of the air inside the container drops, causing the LBF-pouch to further expand and act as a pump to drive additional air out of the container. This process occurs until $p < p_{\text{close}}$ and the TPU pouch occupies about 0.4L of the geometrical volume inside the rigid container. Note that after the valve closes, the pressure inside the container can increase again if more heat is provided to the system, as can be seen by the small increase in pressure at the end of the discharge phase. This is a result of the decoupling of time scales.

Finally, the *cooling & recharge phase* is initiated when the applied temperature starts to decrease, resulting in the condensation of the LBF that leads to a decrease in the LBF-pouch volume. This effectively generates a negative pressure in the air container when reaching 32.5°C (Figure 3.1**d**), which initiates air flow through the one-way valve to (slowly) restore the air volume in the reservoir. As such, the

environment around the energy harvesting unit operates as a pressure regulator at ambient pressure during this phase.

Note that in Figure 3.1**c** we do not measure a full reset to the initial conditions of the thermopneumatic loop after a single controlled thermal oscillation. Conversely, in a comparative experiment (S3 section A.3), we show that our system has the potential to recover its initial conditions and that the discrepancy between the initial and final geometrical volume of air lies mostly in the non-zero closing pressure of the commercial pressure-release valve. Although we acknowledge the possibility of leakages of LBF through the TPU pouch, we do not reckon leakages of powering fluid to be pronounced enough during the time scale of a single thermopneumatic cycle to prevent the full recovery of the initial conditions.



### 3.2.2 Performance of our thermopneumatic cycle

From a single thermopneumatic cycle, we can extract the energy output harvested from the environment. Integrating the pressure-volume data in Figure 3.1**c**, we obtain that a single thermal cycle has approximately dissipated 6J of energy through the resistive load. This energy can be defined as the work done by the system in this specific scenario. Assuming that the system is back to its initial state at the end of the cycle, the same amount of thermal energy has thus been harvested from the environment. While this number seems relatively low, we will show later that it is sufficient to power an untethered robot. Moreover, the harvested energy is significant compared to the maximum energy stored in the system at any time, which we estimate to be close to $\Delta p \cdot V \approx 30\text{kPa}{\cdot}1\text{L} = 30\text{J}$. Specifically, if we assume an ideal case where all the air molecules inside the air reservoir are expelled throughout the discharge phase and by using an ideal pressure-release valve with the same $\Delta p_{\text{open}}$ but a $\Delta p_{\text{close}} = 0\text{kPa}$, a maximum value of about 15J could be harvested.

We can furthermore derive the efficiency of transforming thermal energy (heat) into mechanical energy (pressure) to be equal to $\eta = 0.87\%$, which can be compared to an ideal Carnot cycle that would give an efficiency of $\eta_{\text{Carnot}} = 5.06\%$ (see S3 section A.6 for details). For a better comparison, we consider engines that rely on phase transitions like the ones we base our energy harvesting device on, such as Organic Rankine (OR) engines, rather than on chemical reactions such as Otto or Diesel engines. In the case of OR engines, we observe an efficiency of $\eta_{\text{OR}} \simeq 10\%$ [135] and $\eta_{\text{Carnot, OR}} \in [50\%\boldsymbol{\nabla} \cdot 80\%]$ depending on the specific technology considered. When we take into account already optimized technologies such as OR engines as a reference, it seems that for the thermopneumatic cell we reach $\eta/\eta_{\text{Carnot}}$ in the same order of magnitude as OR engines. In addition, for our case study, we measure a specific energy density of $\approx 112.6\frac{\text{J}}{\text{kg}}$ and a specific power density of $\approx 2.7\frac{\text{W}}{\text{kg}}$.

It should be noted that when we compare the performances of the thermopneumatic device over other commonly investigated methods for energy autonomy in terms of specific energy density, specific power density and efficiency (Figure S3.7), we find that our approach offers comparable quantities compared to previous work based on chemical reactors. Yet, it is important to mention that previous research investigating energy autonomy focuses primarily on energy regulation rather than energy harvesting [112], and therefore needs to be (manually) refilled after every use. The fact that our system can harvest energy from circadian cycles is a characteristic feature of energy-autonomous systems. Therefore, when comparing our specific energy and power density to other systems, the numerical values must be interpreted carefully by also considering the fundamental differences, capabilities, and purposes between our system and those referenced in the literature.



### 3.2.3 Repeated energy harvesting cycles

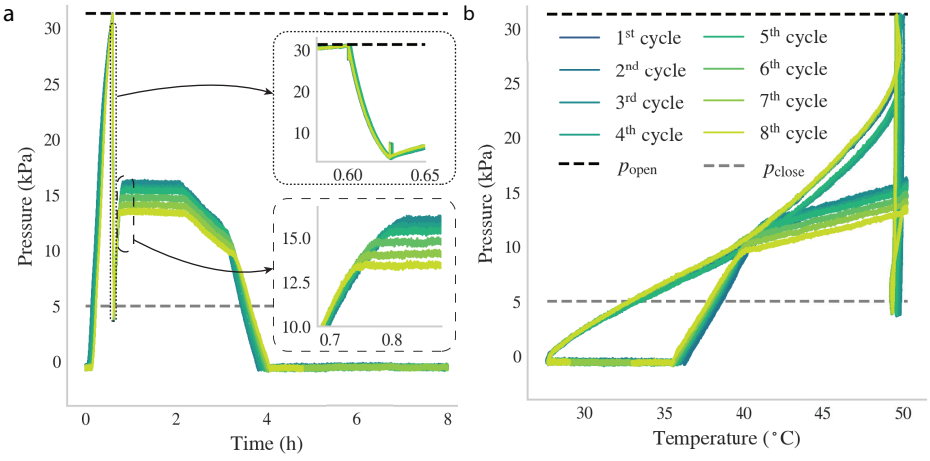


Figure 3.2: **Experimental data for continuous repeated charging and discharging of the energy harvesting cell.** We place the thermopneumatic cell in an environment where we control the temperature. We obtain eight continuous loops of thermal oscillation, in which we bring the temperature from $T_{\text{lab}}$ to 50°C in 2 hours, before letting the system thermalize back to $T_{\text{lab}}$ in 6 hours. **(a)** Pressure in time during to the discharge phase (dotted) and saturation after the discharge phase of the heating provided to the system. **(b)** Pressure-temperature plot of the same data as in **a** for the repeated cycles.

One crucial feature of our energy harvesting approach is that it allows for

several cycles of energy harvesting, provided that the temperature oscillations have a sufficiently large amplitude and period. Therefore, we experimentally measure the response of our energy harvesting unit for eight consecutive temperature oscillation cycles. For each thermal oscillation, we increase the temperature from $T_{\text{lab}} \approx$27 to 50°C for two hours, before letting the system cool down back to $T_{\text{lab}}$ during another six hours. While a temperature of 43°C should be sufficient to trigger the discharge phase, to ensure that the valve would open up several times during our longer continuous experiment, we imposed a maximum temperature of 50°C. The results of this cyclic experiment are reported in Figure 3.2, where we show the response in the pressure-time and pressure-temperature space.



We find that for all eight cycles, our proposed system is capable of harvesting energy from the environment, and every cycle is approximately identical. Nevertheless, we do measure a non-negligible drift between each cycle, which can be seen by the reduction of the pressure after the discharge phase when the temperature is still at 50°C. We hypothesize that this drift upon repeated actuation could be caused partly by potential leakages of LBF through the nylon-coated TPU, but, predominantly by the non-zero closing pressure of the commercial one-way valve. These two experimental limitations, combined, could cause a decrease in both the powering and actuating fluid that generates the pressure shift after the discharge phase. This statement is supported by analyzing the data further, where the results in S3 section A.4 show that the decrease in pressure after every cycle stabilizes at $\approx -.6$kPa after the fifth cycle.

### 3.2.4 Modeling the harvesting response to real-world conditions

The experiments and resulting analysis we performed so far took place in lab conditions, only taking into account changes in ambient temperature. Therefore, in this section, we model the response of the design of the energy harvesting unit under more realistic real-world conditions. We start by leveraging the previous experimental results to build a model, after which we inform it with historical data from weather stations.



#### Modeling the temperature in the reservoir

Phase transitions with simultaneous changes of volume, temperature, and pressures results in polytropic non-quasistatic thermodynamic processes that are non-trivial to model. Furthermore, a thermopneumatic model capable of predicting the response of the energy harvesting cell should also be able to account for different slow time scales (compression and recharge phases) as well as the fast time scale (discharge phase) simultaneously. As we want our model to predict the response of our thermopneumatic cell in real-life conditions, we should not only consider the thermal response as observed in the previous experiments performed in lab conditions but also incorporate contributions from light intensity and radiative heat transfer.

Combining these considerations while keeping the focus on the energy harvesting applications for pneumatic soft robots, we derive a physics-based lumped model starting from fundamental thermodynamic heat exchange rates $\dot{Q}$ as shown in Figure 3.3**a**, and described in detail in the S3 section B. We assume that the temperature $T(t)$ in the reservoir and pouch are identical, where the temperature change depends on contributions from radiation, convection and absorption. Moreover, as a first approximation and to simplify the model we assume that the pressure inside the reservoir does not influence the thermal properties of the cell.

The result is a model where the temperature evolution can be determined by specifying the initial temperature $T(0)$, the ambient temperature $T_{\text{amb}}$ and incoming sun radiation $I(t)$. All other parameters can be derived from existing literature, with the only exception being the geometrical coefficient $\alpha$ that accounts for the effect the position of the sun has on absorption. We describe in the S3 section B how we used experiments to fit this quantity.

#### Modeling the pressure in the reservoir

Although the introduced model allows us to determine the temperature, predicting the pressure $p(t)$ in the reservoir of the pneumatic cell requires us to know the current state of the system. We define a boolean variable $F$ that best indicates the

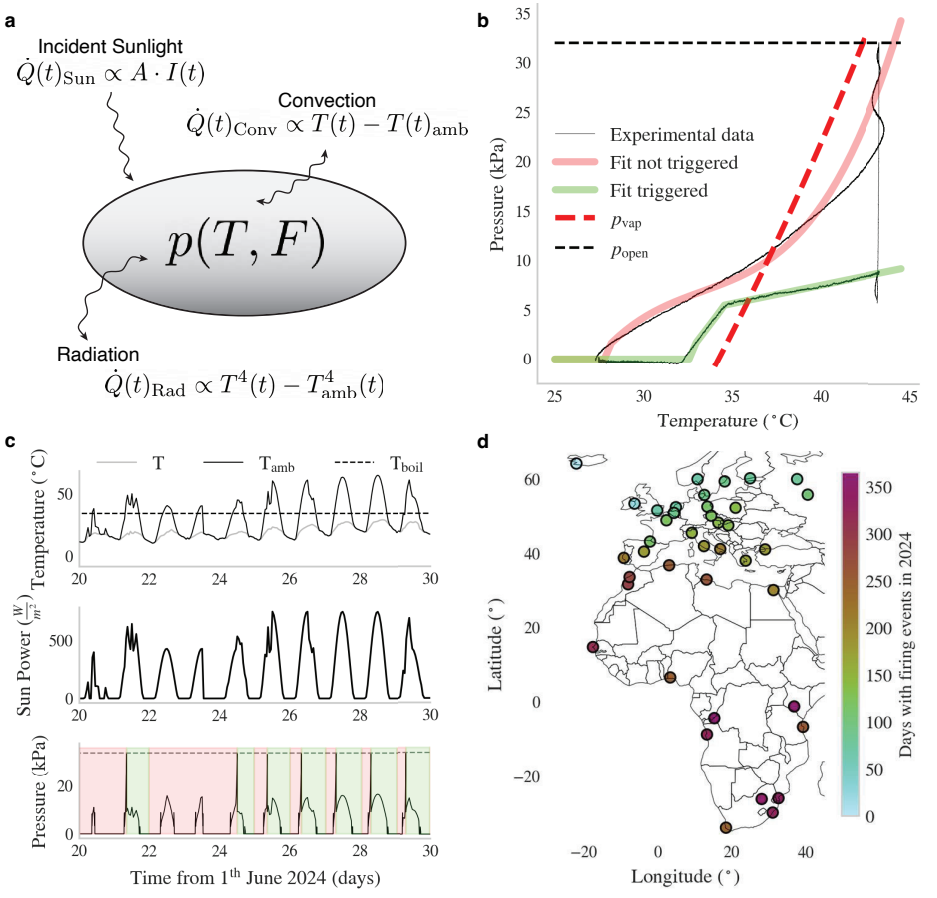


Figure 3.3: **Results for modeling the behavior of the energy harvesting cell. (a)** Gray-box model of the thermopneumatic cell of heat transfer including convection, radiation, and incident sunlight. **(b)** Fits of experimental data in the pressure-temperature space when the pressure-release valve has (in red) and has not (in green) been triggered. We report the vapor pressure of the LBF with the dashed red line. **(c)** Ambient (gray) and simulated air (black) temperature, simulated absorbed sun power on the thermopneumatic unit area, and simulated pressure inside the unit throughout the first two weeks of June 2024 in Amsterdam. We highlight whether a firing event occurs during the specified time window in green and red, respectively. **(d)** Simulated number of days with a firing event for 2024 in different locations between -20° and 50° longitude.

current state of the system. When $F$ is *False* the system has been fully recharged to ambient conditions and is ready to harvest energy from its environment. In contrast, when $F$ is *True* the system has reached the critical pressure to open the pressure relief valve, discharged its pressure, and should be recharged. Based on the state the system is in, the pressure in the energy harvesting cell can follow two different paths in the pressure-temperature plane, as observed in our experimental data from Figure 3.1**d**.

Let us first focus on the case for which $F$ is *False*. For $T > 27°C$, we measure a continuous increase in air pressure as indicated by the fit in Figure 3.3**b**. Considering the boiling temperature of the LBF at a given pressure $T_{\text{vap}}(p)$ and the scaling of vapor pressure $p_{\text{vap}}(T)$ of the LBF with changing temperature, as $T$ increases, we assume the vapor pressure increases following the Clausius-Clapeyron equation (Equation (S3.1) in S3 section A.1). This also accounts for an increasing boiling temperature as a result of increasing pressure, which is more significant when pressures inside the air reservoir are higher.

Next, we consider the case for which $F$ is *True*. After a firing event of the valve, we observe a discontinuous $p(T)$ with three distinct linear regimes. When $T > T_{\text{vap}}(p)$, variations in environmental temperature cause linear changes in pressure that we explain by considering the ideal gas law on both the remainder of the air inside the air reservoir after the discharge phase, as well as the LBF in the gas phase. Instead, when the $T \simeq T_{\text{vap}}(p)$, condensation of the LBF occurs. Consequently, we observe a sudden change in slope in the pressure-temperature plane due to the reducing volume of the TPU pouch, up until most of the LBF transitions back to its liquid phase. This decrease in pressure continues until reaching pressures close to the ambient pressure, where it is mainted at $p_{\text{amb}} - \Delta p_{\text{open, 1way}}$ as a result of the slow recharging of the reservoir through the one-way valve.

For completeness, we report $p_{\text{vap}}(T)$ using the fit suggested from the technical datasheet of the LBF (Equation (S3.2) from S3 section A.2) in Figure 3.3**b**. The small deviation we observe between the $p_{\text{vap}}(T)$ curve and experimental data can be explained by considering that the vapor pressure is measured with LBF alone, while we measure the response of the whole thermopneumatic system.

Finally, we consider when the system changes the state $F$. In our model, we switch $F$ from False to True whenever $p \geq \Delta p_{\text{open}}$. Moreover, based on preliminary experimental trials, we observe that it takes about 6 hours to complete the recharge phase. Thus, we assume the recharge phase to be fully completed if the temperature drops below 27°C for at least 6 hours, switching back $F$ from True to False. Although this approximation is quite conservative in terms of the modeling of the recharge capabilities of the energy harvesting cell, directly modeling the amount of change in the number of air molecules in the air reservoir during the recharge phase proves to be a non-trivial task.

Note that during recharging we observe that when the temperature inside the air reservoir $T$ is lower than 27°C, the air pressure inside the air reservoir is $p(T \leq 27°\text{C}) = p_{\text{amb}} - \Delta p_{\text{open, 1way}}$. Here, $\Delta p_{\text{open, 1way}} \simeq$1kPa is the opening pressure of the one-way valve triggered during the recharge phase. When the air reservoir has completed the recharge phase, we measure $p = p_{\text{amb}} - \Delta p_{\text{close, 1way}}$ with $\Delta p_{\text{close, 1way}} \simeq$1kPa is the opening pressure of the one-way valve.



**Simulating real-world conditions**

The lumped model now allows us to coarsely predict the behavior of the thermopneumatic cell under real-world conditions. To do so, we use weather station data for different coordinates to simulate the pressure $p(T, F)$ in the reservoir, as a function of ambient temperature and sun intensity at different locations and times around the world. First, in Figure 3.3**c** we show an example output of the pressure $p(T, F)$ in our simulated environment for the last days of June 2024 in Amsterdam. Based on the ambient temperature $T_{\text{amb}}$ and sun power intensity $I$ gathered from weather station data, we simulated the air temperature $T_{\text{air}}$ inside the energy harvesting cell.

From our simulated data, it is apparent that a firing event can occur even if the ambient temperature $\text{T}_{\text{amb}}$ is lower than $\text{T}_{boil}$. This is mostly due to the presence of sunlight intensity and indicates the importance of sunlight in the heat transfer balance. From the same data, we also observe abrupt changes in incoming solar power resulting from the presence of cloud coverage. We observe that even if $\text{T}_{\text{amb}}$ does not dramatically change between the days in Figure 3.3**c**, cloud coverage can hinder heat transfer contributions from solar radiation and prevent firing events. Our model also includes the effects of air moisture on specific heat capacity, although we observe that air moisture has only a marginal effect on the results. We report an extended explanation of our model in Supplementary Material B and Equation (S3.15).

We next simulate the response of the energy harvesting cell using data from 2024 at different locations. In Figure 3.3**d** we report the predicted total number of days during 2024 for which the cell would have fired, for different locations in Europe and Africa. It is apparent that there is a correlation between latitude and the total number of observed firing events during the year. Yet, we do observe variations for locations with similar latitudes, which are mostly due to the local orography and nearby water masses, as also demonstrated in Figure 3.3**d** when comparing, e.g., Bilbao to Rome. We interpret the number of firing events during a full year as a quality factor for the simulated performance of our thermopneumatic energy harvesting strategy, aware that the representation in our lumped model of the recharge phase is highly simplified.

### 3.2.5 Demonstrators

With the goal in mind to probe the potential for applications of our energy harvesting cell, we target soft robotics applications by testing the capability of our thermopneumatic approach in two separate settings. In the first demonstrator, we evaluate if real-world conditions can be sufficient to trigger the compression and discharge phases in our thermopneumatic strategy by leaving our electronics-free design in real-world conditions outside of the lab. In addition, we aim to use the released pressure to power a self-oscillating soft actuator. In the second demonstrator, we aim to evaluate if the thermopneumatic cycle generates sufficient energy to power the locomotion of an untethered walking soft robot that uses two self-oscillating limbs to propel itself forward.



**Compression and discharge phases in a real-world environment** In the first demonstrator, we place the energy harvesting cell from Figure 3.1**a** in an outdoor environment for 2.5 hours, while measuring its pressure in time as the system is subjected to both temperature increase and incident sun radiation (on June 27$^{\text{th}}$ 2024 in Amsterdam). To demonstrate the advantages of decoupling the charging and discharging time-scales of our thermopneumatic cell, in this experiment, we replace the fluidic resistor with a self-oscillating tube actuator [136]. The tube actuator manifests self-oscillating behavior (at frequencies $\in [1, 4]$Hz) when subjected to an inflow greater than 0.1SLPM and a pressure greater than 10kPa. By separating the timescales between energy harversting and actuation, combined with a relative low pressure and air flow activation thresholds for the self-oscillating actuator, the setup should guarantee that a single energy harvesting event can return a relatively large number of activations of the actuator (see Methods sections).

To perform our experiment, we first initialize the system at laboratory conditions of $p = p_{\text{amb}}$ and $T_{\text{lab}} = 27°$C and then bring it to the outside environment, exposed to sunlight as in Video 1 (Section 3.4) and Figure 3.4**a**. During this experiment, as expected we observe a gradual increase in pressure during the compression phase up until the discharge phase occurs at $p \simeq 33$kPa (Figure 3.4**b**), as indicated by the analog pressure sensors.

Throughout the discharge phase, the pressure triggers the self-oscillating actuator to start oscillating, which causes the pressure to decrease slightly after every activation cycle (Figure 3.4**c**). This discharge phase lasts for about 15 minutes, where we observe a total of 142 oscillations of the actuator, after which the pressure-release valve automatically transitions back to its closed state once the air reservoir hits the closing pressure of the valve at $p \simeq 11$kPa (Figure 3.4**d**). During this experiment, we observe that actuation frequencies range from 5Hz, at the beginning of the discharge phase up to 0.1Hz at the end of the discharge phase. Such a frequency shift is a direct consequence of the drop in driving pressure and

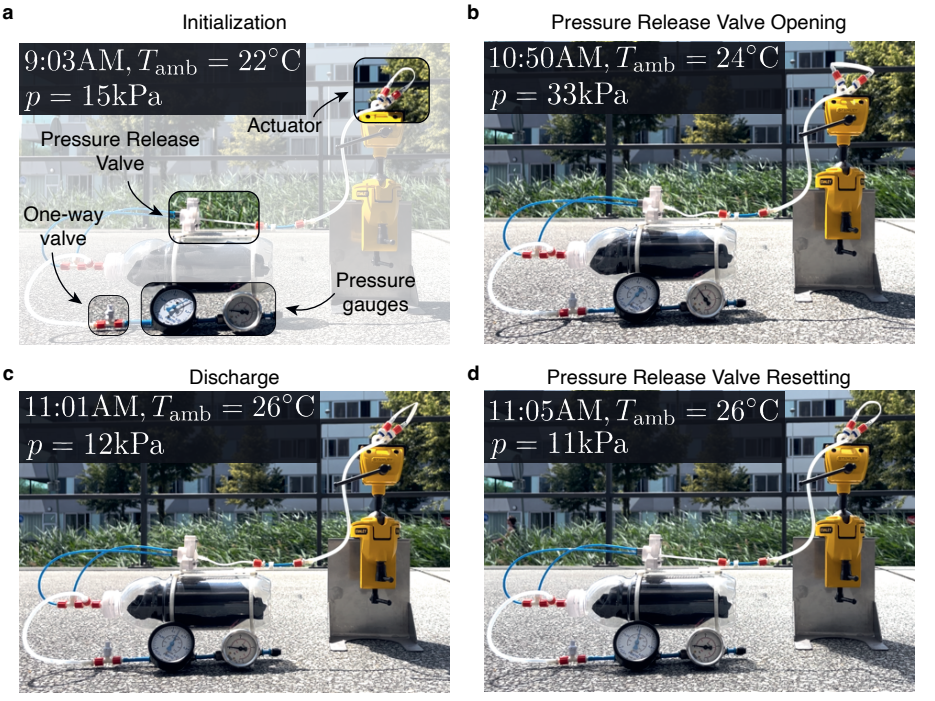


Figure 3.4: **Snapshots of an outdoor experiment where we harvest thermal energy to power a self-oscillating actuator. (a)** Initialization of the system with highlights of the main components. **(b)** When $p = \Delta p_{\text{open}} =$ 33kPa, the pressure-release valve opens, and the self-oscillating tube actuator starts to perform its motion. **(c)** The actuation lasts throughout most of the discharge phase, while the total pressure inside the air reservoir drops. **(d)** As $p = \Delta p_{\text{close}} = 11$kPa, the valve transitions back to its closing state. The pneumatic circuit of this demonstrator is the same as in Figure 3.1**a**, and for comparison also shown in Figure S3.18**a**.

flow as the self-oscillating actuator operates as a resistive load.

By comparing the approximate energy cost for a single oscillations in the self-oscillating tube actuator of 0.06J [136] to the energy that we harvest from a single circadian oscillation (≃6J) from the pressure-volume curve in Figure 3.1**c**, we can derive that a single energy harvesting cycle should generate approximately 120 activations of our actuator. This prediction is close to the observed 142 oscillations, suggesting that our approximation of the harvested energy from our thermopneumatic device is in the same order of magnitude as the one we

observed. In particular, with this demonstrator, we show that the separation of time scales, combined with the relatively low amount of energy required for each activation of the self-oscillating actuator, is sufficient to repeatedly generate motion with a single discharge phase from the energy harvesting unit. Moreover, although not directly evaluated here, we mention that under sufficiently high environmental temperature and solar irradiance, the system may undergo multiple actuations within a single day, with successive compression–discharge events occurring without an intervening recharge phase. Continued heat influx has potential for triggering a secondary firing, which can enhance vacuum generation during recharge but yields reduced mechanical work due to the smaller displaced air volume.



**Harnessing heat from the environment to generate locomotion** In the second demonstrator, we aim to show the potential for energy, control, and actuation autonomy through our thermopneumatic approach. To that end, we design an untethered walker powered by our energy harvesting cell. Based on a similar soft-legged robot design that we introduced while developing control-autonomous walkers using self-oscillating tube actuators[136], we 3D print PETG hardware components to connect all parts of the soft-legged robot. In this demonstrator, we assemble the same thermopneumatic circuit schematic as the one we investigated in Figure 3.1**a** and Figure 3.4, but use a PET bottle with 0.5L volume, while keeping 5g of LBF inside the same TPU volume. This choice was made to make the size, mass, and moment of inertia of this walker more compatible with the forces expressed by the actuators. The final soft-legged robots weighs 154g (out of which 82g for the pressure-release valve) and we report the schematics of the walker design in Figure 3.5**a**, together with further details on the specific pneumatic circuit in the Methods section.

As the oven previously used is too small for the soft-legged robot, we instead use a heat gun set to 220°C, positioned at about 30cm from our demonstrator, to simulate incoming environmental heat and provide sufficient heat to drive the thermopneumatic cycle. We found that this relatively high temperature is necessary for the system to stabilize at about 50°C for long enough to evaporate the LBF and pressurize the air past $\Delta p_{\text{open}}$, given the temperature ($T_{\text{lab}} = 27°\text{C}$) and volume of the room ($12\text{m}^3$) where the experiment was performed. After heating the system for ≈18 minutes, the pressure-release valve opens, and the pressurized air discharges through the actuators. The force exerted by the pressurized air causes the self-oscillating actuators to activate synchronously, pivoting the robot on its rigid front legs, and allowing it to progress forward, as we show in Video 2 (Section 3.4) and Figure 3.5**b**. Even though the experiment successfully demonstrates eight activation cycles, the locomotion phase takes place only during the first part of the discharge phase. This is likely because there is a threshold force needed to be

exerted by the actuators to tilt the body of the walker and initiate locomotion.

During this experiment, we measure the robot's position using an ArUco fiducial marker as shown in Figure 3.5**c**, indicating that the robot moved a total of 2 body lengths (i.e. 40cm) during the activation event. At the same time, we visualize the temperature of the walking unit using an infrared camera to get better insights into the heating and cooling time scales given the imposed environmental conditions. We estimate the cost of transport (COT) of the walking demonstrator from the cycle energy $E = 6$ J, system mass $m = 0.154$ kg,

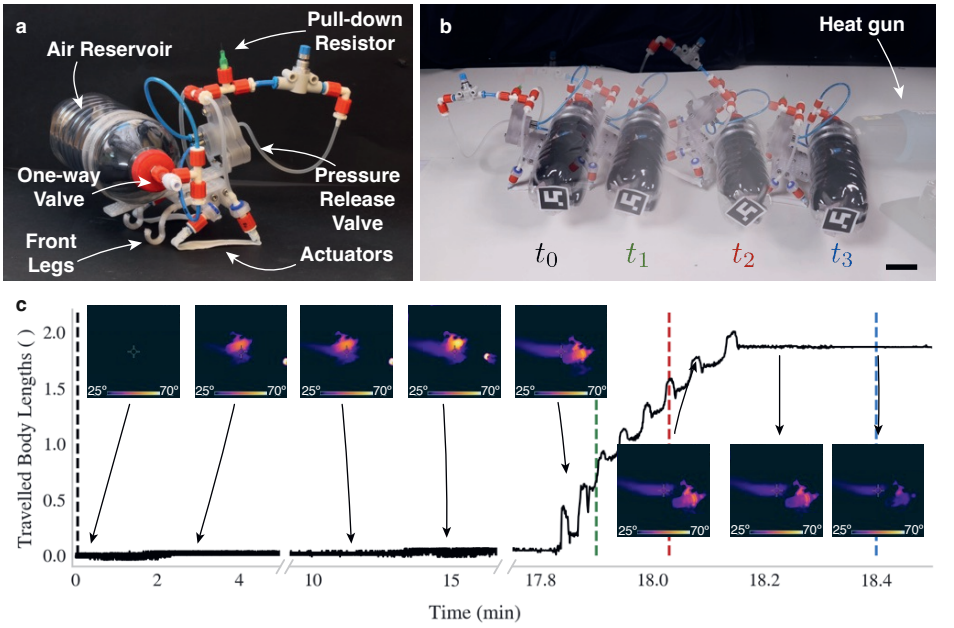


Figure 3.5: **Energy autonomy of a soft walker demonstrated in laboratory environment. (a)** Schematics of the main hardware components of an untethered walker powered by an energy harvesting cell. **(b)** Overlay of snapshots during the locomotion phase. Once the unit starts to locomote, the thermal source (heat gun) is moved away from the walker's trajectory to avoid heat damage to its components. The scale bar represents 5cm length. **(c)** We track the walker's position using a fiducial marker on the side of the air reservoir and plot the unit position in time. At the same time, we gather information about the walker's temperature using an IR camera in the insets at the corresponding highlighted timestamps. We report the pneumatic circuits of this demonstrator in Figure S3.18**b**.

gravitational acceleration $g = 9.81$ m/s$^{-2}$, and travelled distance $d = 0.4$m. Based on these values, we obtain a COT $= E/mgd \approx 10$. This value is comparable to a previous walker using the same actuators (COT $\simeq 11$ in [136]) and falls within the range reported in locomotion-focused studies (COT $\simeq 4.8$ in [137] and COT $\simeq$ 30–67 in [138]). Although our locomotion duration is shorter and has a lower speed as a result of the design, our approach demonstrates that one important avenue to increase the cost of transport is by harvesting energy directly from the environment as we do not have to consider conversions from, e.g., battery to pumps.

To further illustrate that environmental conditions can cause the soft-legged robot to trigger multiple times, in Video 2 (Section 3.4), we report the same experimental setup as the one in Figure 3.5 with the system experiencing two consecutive cycles of compression, discharge (locomotion), and recharge phases.



## 3.3 Discussion

In this work, we proposed and investigated a strategy to materialize energy harvesting capabilities in soft pneumatic systems. By leveraging fluidic and mechanical nonlinearities, we demonstrated that thermopneumatic cycles can decouple the time scales of energy harvesting and storage. As a result, our approach enables the accumulation of sufficient environmental energy to generate the air flows and pressures compatible with the operation of soft robotic systems.

Our results highlight two key features for materializing energy harvesting in soft robotic systems, with no human-in-the-loop required for their autonomous operation. First, the system must return to the same state at the beginning of each circadian cycle, specifically in terms of thermodynamic variables and mass of powering and actuating fluids, to guarantee repeated, unsupervised operation. At the same time, the energy harvesting unit we design should be able to release the accumulated energy to enable operation on a timescale quicker than the circadian oscillations instead of providing a slow continuous response throughout the single harvesting cycle. Moreover, we demonstrate that our proposed system operates simultaneously as an energy harvesting and energy storage unit. Autonomous entities in nature also often implement both requirements [139], from the ballistic ejection of spores and seeds in fungi [140], plants [141], and prey capture in both terrestrial and marine animals [142, 143]. Similarly, we require that such energy autonomous systems should be capable of decoupling of power conversion, with a slow time scale for energy harvesting and a faster one for operation in their environment.

While we focused on the design of a thermodynamic process for the energy harvesting unit and its potential use for soft robotics, further optimization should be done to be able to implement our approach reliably in real-world applications.

For example, we observe a slow, yet consistent, decrease in energy being harvested for repeated cycles. Still, our measured efficiency lies within the same order of magnitude as the Carnot efficiency for our system and is comparable with the efficiency of technologies known in literature, such as Rankine engines.

We believe that our strategy can add an increased level of programmability to early examples working in this direction such as temperature-responsive shape morphing systems [144], smart façades [145], and biobased, stimuli-responsive robots [6]. We envision potential improvements to our thermopneumatic strategy that can pave the way toward outdoor applications. For example, working with lower threshold opening pressures on the pressure-release valve or multiple buffer volumes as an air reservoir could allow, e.g. multiple firing events during a single day, or not waste the work done to pressurize air inside the air reservoir even if a firing event is not triggered. Furthermore, using the combined effect of temperature differences and incident sunlight could be more beneficial than relying exclusively on solar or thermal energy-based systems alone.
On top of that, while a more absorbing pouch material would likely increase light-to-heat conversion, we did not yet consider alternatives that are compatible with our fabrication constraints and required material properties. Beyond material changes, we envision the integration of passive self-oscillatory mechanisms (e.g., self-shadowing and self-focusing [146–148]) as a strategy to enhance heating during compression while reducing exposure during discharge/recharge, thereby accelerating recovery and potentially increasing cycle frequency.

In addition to soft robotics applications, we foresee our approach could facilitating tasks of already existing technologies by introducing a redundant, electronics-free, and reliable hardware-based solutions for sustainable energy harvesting. Although locomotion and manipulation remain common benchmarks in soft robotics, we believe our thermopneumatic approach can be used in different endeavors, e.g., where daily cycles of actuation can be driven by environmental conditions. For example, we believe that the thermopneumatic strategies we presented here can be integrated into architectural applications, such as in passive, energy autonomous structures for moving façade in the architecture domain [8, 149]. The model we developed can be leveraged to quantify the potential for applications in such and similar case studies in different locations.

### 3.3.1 Link to the following chapter

In the previous chapters, we developed methods for explicitly controlling and powering electronics-free soft robots. The fundamental control strategies introduced in Chapter 2 informed the design of the energy-harvesting cell presented in this chapter. In Chapters 2 and 3, the core building blocks employed in the fluidic valves are based on the snap-through instability of monostable dome-like

structures. These valves can serve both as control elements and as actuators in electronics-free soft robotic systems [69], and it has been argued in the literature that these devices can be modeled as relaxation oscillators [91, 136]. Thus, this class of oscillators represents a promising platform for the emergence of collective behavior, which we aim to investigate and exploit for controlling and actuating fluidic networks in soft robotics. To this end, the following chapter examines the underlying design principles governing pattern emergence and maps the behavior of idealized oscillators onto experimental soft robotic platforms.

To investigate pattern emergence in these and related systems, as well as their potential as controllers and actuators in fluidic networks, we investigate the dynamics and pattern formation of coupled fluidic relaxation oscillators using mathematical tools from dynamical systems theory.



## 3.4 Videos

- **Video 1: Outdoor demonstrator** Video of experimental execution of experiments presented for outdoor motion in Figure 3.4. At 9.15AM June 27$^{\text{th}}$ 2024, we brought the system outside the AMOLF building in Amsterdam and then connected it following the schematics in Figure S3.18**a**.

- **Video 2: Indoor locomotion demonstrators in laboratory environment** We assemble two self-oscillating actuators on the thermopneumatic cell as in Figure 3.5**a** and follow the pneumatic connections as in Figure S3.18**b**. To drive the temperature oscillations in our indoor locomotion demonstrators, we use a heat gun regulated at 220°C and progressively bring it closer to the setup to simulate an increase in temperature. In the first part of the video, we report the experimental realization from which the data in Figure 3.5 has been extracted. In the second part of the video, we repeat the indoor locomotion test controlling two consecutive thermopneumatic cycles and showing the potential for repeatability of the thermopneumatic loop for locomotion. After heating the system using the same protocol as in the first locomotion experiment in Figure 3.5, we wait 6 hours to let the system undergo its recharge phase before repeating the same heating procedure.

All the movies related to this chapter are available at this link. If you are holding a paper version, you can scan this QR code:

Videos - Chapter 3

3

## 3.5 Materials & Methods

### TPU pouch fabrication

To make pouches containing LBF fluid, we heat-seal two sheets of nylon (70den, one side coated with TPU, 170g/sqm), sealing them at 270°C using a custom modified 3D printer [150]. The pouch design is based on the sketch in Figure S3.11. After trimming the remainder of the material from the heat-sealed pouch, we place a FESTO® 6 tube in the opening and heat-sealing it to the TPU pouch [150]. This allows an effective interface to vacuum air and fill the pouch with the LBF before sealing the connection point using a Luer® stopper.

To evaluate the sizing of the pouch, we consider that, within the ranges of pressures investigated in our work, we observe only limited elastic deformation from the nylon-coated TPU, and thus it can be considered as an inextensible textile. As we expect, the maximum geometrical volume that the pouch can occupy is directly related to the 1L plastic volume bottle. To obtain an ideal volume of the pouch $V_{\text{pouch, max}}$, we use Equation (3.1) developed by Robin [151], using for the width $w = 160\text{mm}$ and height $h = 190\text{mm}$:

$$V_{\text{pouch, max}} = w^3 \left( \frac{h}{\pi w} - 0.142 \cdot \left(1 - 10^{-h/w}\right) \right) \tag{3.1}$$

As we show in Figure S3.11, we include a 13mm heat-sealed channel in our design to fit a FESTO® 6mm tube. Moreover, to reduce local stresses along the heat-sealed corners, we replace all sharp corners with a radius of 10mm.

### Pressure-release valve fabrication

The custom pressure-release valve we use in our work is based on a design previously suggested [62], yet it has so far not been experimentally evaluated. Its operating

mechanism is based on the kinking instability of a silicone tube passing through the pole of a silicone monostable dome (Figure S3.12). To fabricate this design, we cast the silicone dome in a 3D printed mold, and directly 3D print the holder to obtain the components with parameters as in Figure S3.13. We print the holder and the molds using Veroclear on an Eden260VS, Stratasys® printer. The silicone dome is made made by injection molding Dragon Skin® 30 (Smooth-On® ) in the mold, following the steps in Figure S3.14. Before injecting the two-component silicone, we spray Mann Ease Release 200® on the molds in Figure S3.14**a** to guarantee a smooth and easy removal of the silicone once it is cured. We apply a first layer of mold release and then wait five minutes before applying a second layer so that the mold release can settle uniformly before starting the injection molding (Figure S3.14**b**). During this step, we inject silicone from one end of the top injection mold while holding the 3D-printed molds vertically to favor the escape of air bubbles from the opposite side. Once the injection step is completed, we rotate the component horizontally so that the silicone inlet and outlet lay at the same height while the silicone cures.

We wait for the silicone to cure for 16h to obtain the dome as in Figure S3.14**c**. We then post-process the silicone dome by heating it to 60°C for 2h. After this step, we proceed by cleaning the tube and dome with isopropanol, and sliding the silicone tube (2.6mm outer diameter, 0.3mm wall thickness) inside the opening in the silicone dome. We leave 1cm tube protruding from the dome opening on the pole end. On the opposite side of the dome, we make sure to use more than 10cm of silicone tube to allow a versatile interface with the connectors downstream to the pressure-release valve. To bind and seal the connection between the tube and the dome, we apply SilPoxy® on the concave side of the pole of the dome.

Once we obtain the component as shown in Figure S3.14**d**, we assemble it with the Veroclear valve molds (Figure S3.13). We slide 2mm of FESTO® 4 tube at the end of the silicone tube on the concave side of the dome as in Figure S3.15**a**, and slide it on the pin of the holder as in Figure S3.15**b**. This step guarantees a firm connection between the silicone tube and the holder while allowing the silicone tube to be fully kinked when the valve is in the closed state. We then connect the top side and bottom holders using three M4 screws and obtain the pressure-release valve as in Figure S3.15**c-d**. We complete the assembly by using FESTO® 4 QS fittings on the inlet side to allow a pneumatic interface to the inlet of the valve.

Before using the valve in our experiments, we validate that the valve does not leak in its closed state by performing the tests illustrated in Figure S3.16.

#### Protocol to check leakage-free behavior of the pressure-release valve

To validate that our experimental implementation of the pressure-release valve [62] materializes the leakage-free properties we desire for our design, we perform

the following measurements. We connect the pressure-release valve to a pressure regulator to impose a linear increase in input pressure $p_{\text{in}}$ from 0 to 45kPa in 20 minutes before bringing the $p_{\text{in}}$ to 0kPa in another 20 minutes. We continuously repeat these pressurization and depressurization cycles five times and report the output data for pressure and flow in Figure S3.16. We report with the black think lines the individual realization of the pressurization and depressurization cycles. At the same time, in the scatter plot, we report the average values of flow as a function of pressure in time. In the inset, we zoom close to the region of low flows to better highlight that, when the valve is in the closed state and pressurized at $p < \Delta p_{\text{open}}$, no airflow is measured until the opening pressure is reached.



**Measurement of thermodynamics variables**

To measure and infer the thermodynamic variables in our experiments, we use an NI-DAQ USB-6212, National Instruments® board for all the measurements, with sampling rates specified as in Table S3.1. We use an SSCDRRN015PDAA5, Honeywell® as pressure sensor (±100kPa range), and a HAFBLF0750C4AX5 (±0.75SLPM) to measure air flow. We connect the sensor following the schematics in Figure S3.17**a**, with the air pressure and airflow measured in parallel and in series with the air reservoir inlet, respectively. Throughout our experiments with controlled temperature, we enclose the air reservoir inside the Memmert® UF30plus oven. While performing our experiments using the oven, we keep the pneumatic circuit and sensors outside the oven at $T_{\text{lab}} = 27°\text{C}$ and use FESTO® 4 tube to connect them to the air reservoir.

To gather information on the air temperature inside the bottle while connecting the pneumatic circuit to the air reservoir, we pierce the cap of the plastic bottle we use as air reservoir to obtain two separate openings. We then insert the thermal probe (PT100) inside a FESTO® 6 tube and slide it inside one of the openings. At the other opening, we insert a Luer® connector to create a pneumatic interface between the inside and outside of the bottle cap. We then seal the two openings of the cap using SilPoxy® , and wait 12 minutes for it to cure. The last step in our protocol is to pressurize the closed bottle with the modified cap and validate that we obtained no leakage at the connection.

While performing experiments with temperature regulation, we use a secondary PT100 probe to measure the temperature inside the oven while regulating it to the desired temperatures. By doing so, we obtain simultaneous measurements of air temperature inside and outside the air bottle to calibrate our heat transfer model. Experimentally, we observe only a limited delay between the two measured temperatures. We speculate that this is due to the low mass of the fluids involved and the thin walls of the PET bottle. As an example of data output, in Figure S3.17**b** we report the measured data for pressure and temperature, together with the inferred air volume using Equations (3.4)-(3.7) for the experiment in Figure

3.1**c-d**. To infer the volume of enclosed air, we perform our calculations using absolute pressures and $K$.

**Inferring air geometrical volume with pneumatically insulated air reservoir** To infer the air volume when the system is pneumatically insulated from the environment, we start from the assumption that during the corresponding thermodynamic process, the number of air molecules in the air reservoir is constant. We consider this assumption to be valid as we measure zero flow at the outlet of the air reservoir, and we preliminarily check for leakages in our setup. Considering the configuration in Figure 3.1**a**, we define $n$ to be the number of air molecules in the system, $R$ as the gas constant, and $T_0$ and $V_{0,\text{ air}}$ as temperatures and volumes at the beginning of the thermodynamic process. By applying the ideal gas law, we derive:

$$nRT_0 = p_0 V_{0,\text{ air}} \tag{3.2}$$

When the system reaches a pressure, temperature $p$, $T$, we obtain

$$nRT = pV_{\text{air}} \tag{3.3}$$

Thus, as $n$ is conserved, we infer the correspondent geometrical air volume $V_{\text{air}}$

$$V_{\text{air}} = \frac{p_0}{p}\frac{T}{T_0}V_0 \tag{3.4}$$

We consider this first-order approximation to be valid as, at the thermodynamic ranges we investigate, the compressibility factor $Z = \frac{pV}{nRT} \simeq 1$. At the same time, as we know that within our operating pressure regimes, we observe no deformation of the air reservoir, we can approximate $V_{\text{LBF}}$ volume of the pouch containing the LBF

$$V_{\text{LBF}} = (p, T, n_{\text{LBF}}) = V_{\text{reservoir}} - V_{\text{air}}(p, T, n) \tag{3.5}$$

While performing our analyses, we considered these equations to be valid whenever the system is pneumatically isolated from the environment. Therefore, we take as starting conditions $(p_0, T_0, n)$ corresponding to the instances where the pressure release (one-way) valve transitions from the open to the closed state up until the one-way (pressure release) valve opens. In particular, this occurs between the recharge and discharge phases and between the discharge and recharge phases.

Although the ideal gas law is meant to be valid on quasistatic processes, we deem Equation (3.4) valid under the hypothesis of slow heating and cooling before and after the discharge phase.

**Measuring air volume during discharge and recharge processes** We monitor the amount of air molecules and their volume during the discharge and recharge processes using flow sensors. For our experimental investigation, we use a bidirectional flow meter with a maximum range of 0.75SLPM connected in series with the air reservoir inlet. While performing our experiments, we make sure to include a flow constrictor after the output of the pressure-release valve to guarantee that the peak values we register are within the sensor's range. This requirement is not needed on the input of the air reservoir (output of the one-way valve), as the flow during the recharge phase is already within the sensing range, whereas it helps measure the airflow during the discharge phase by reducing its peak value. In the experiments in Figure 3.1 and Figure 3.2, we use a 22G, 12.7mm SMD® needle.

To infer volume changes starting from flow values, we first convert the SLPM values into the corresponding number of moles per second $\Delta n$, knowing that 1SLPM= .00073386$\frac{mol}{s}$. We start by assuming the conditions at $t_0$ reference start time, thermodynamic variables are pressure $p_0$, temperature $T_0$ and volume $V_0$. Thus, we can derive the initial amount of air molecules in the system $n_0$

$$n_0 = \frac{p_0 V_0}{R T_0} \tag{3.6}$$

To infer $V(t)$ geometrical volume of air at a given time $t$, we consider measured input (outlet) flow during the recharge (discharge) phases, with the corresponding air temperature and pressure to rewrite the ideal gas law under changing number of molecules

$$V(t) = \frac{\left(n_0 + \int_{t_0}^{t} \Delta n(\tau) d\tau\right) R T(t)}{p(t)} \tag{3.7}$$

Eventually, we integrate this equation in time to infer the air volume inside the air reservoir at any given time, with known temperature and pressure during the processes with non-zero net airflow.

**Details of pneumatic circuits used in the demonstrators** Based on the pneumatic circuit design in Figure 3.1**a**, we include self-oscillating tube actuators [136] as a load in the thermopneumatic circuit to demonstrate the potential for motion and locomotion. In Figure S3.18**a**, we include a single self-oscillating tube actuator in series with the outlet of the pressure-release valve. For demonstrating locomotion capabilities instead, we include two self-oscillating tube actuators in parallel with a pull-down resistor at the outlet of the pressure-release valve as shown in Figure S3.18**b**.

## 3.6 Supplementary Materials

We provide additional data and specifications that we use to support the statements in the main text.

The Supplementary Material is organized as follows:

- **A: Description of additional experiments**
- **B: Heat transfer model**
- **C: Figures for Methods**
- **D: Description of videos**
- **E: Table of fluidic setup details**

S3

### A: Description of additional experiments and characterizations

This section contains the description of additional experiments and characterizations peformed to support the results in the main text, and is divided in the following sections:

1. **Evaluating vapor pressure of the LBF**
2. **Dependency of maximum pressure on the amount of Novec 7000©**
3. **Ideal thermopneumatic cycle using manual valves**
4. **Accuracy of air volumes and the recovery of initial condition during consecutive thermopneumatic loops**
5. **Characterization of pressure-release valve opening pressures with varying thickness**
6. **Efficiency calculations**
7. **Energy density, power density, and efficiency comparison**
8. **Comparison with other LBF candidates**
9. **Strategies to reduce potential leakages of LBF**

S3

### A.1: Evaluating vapor pressure of the LBF

Given the interest in working with temperatures in the range compatible with real-world external temperatures and meaningful pressures in the context of soft robotics, we use the Clausius-Clapeyron relation for vapor pressure of the LBF. We show that this relation sets a theoretical constraint on the potential in energy harvesting for our thermopneumatic unit.

First, we consider the LBF undergoing a phase transition and assume that the LBF is at its vapor pressure $p_{\text{vap, A}}$ when at boiling temperature $T_{\text{boil, A}}$. Through the Clausius-Clapeyron equation, we derive the boiling temperature $T_{\text{boil, B}}$ for another corresponding vapor pressure $p_{\text{vap, B}}$ when the latent heat of vaporization of the fluid $L$ is known

$$p_{\text{vap, B}}(T_{\text{boil, B}}) = p_{\text{vap, A}} \cdot \exp\left[ -\frac{L}{R}\left(\frac{1}{T_{\text{boil, B}}} - \frac{1}{T_{\text{boil, A}}}\right)\right] \tag{S3.1}$$

with $R$ the gas constant. Through Equation S3.1, it is possible to infer the vapor pressure $p_{\text{vap}}$, namely the maximum pressure that an evaporating fluid can reach at a given temperature before the coexistence of fluid and gas phase at thermal equilibrium. Once the vapor pressure is reached and the system is at equilibrium with its environment, no further increase in pressure can occur.

For our application, this means that once the LBF has reached its vapor pressure, a pressure increase can occur only if the temperature is further increased, consequently increasing the vapor pressure according to Equation S3.1. We overlay the results from Clausius Clapeyron equation with experimental data in Figure 3.3**b**. Equation S3.1 returns the ideal behaviour of the LBF of our choice, whereas our experimental data encloses the response of the different subsystems in our design. Deviations between experimental data and the results of Equation S3.1 can be justified by the presence of air inside the air reservoir that causes an increase in pressure upon heating up, even before the evaporation of the LBF.

### A.2: Dependency of maximum pressure on the amount of Novec 7000©

To better understand how a different amount of LBF (Novec 7000© ) in the TPU pouch affects the scaling of maximum pressure for a given air reservoir volume and maximum temperature in the system, we perform a comparative experiment in Figure S3.1. We consider the same plastic bottle as an air reservoir as the one we used to perform our experiments in Figures 3.1-3.2, with no valves connected to it and place the system in the oven while controlling its air pressure and temperature. We increase the temperature from $T_{\text{lab}} = 27°\text{C}$ to $T_{\text{max}} = 55°\text{C}$ before letting the system thermalize back to $T_{\text{lab}}$. In Figure S3.1**a**, we report the measured pressure as a function of the oven temperature in time for different amounts of LBF, compared with the case with no LBF-pouch inside the bottle. At the same

time, we plot the vapor pressure $p_{\text{vap}}$ of the Novec 7000® LBF to compare our experimental results with data from the technical datasheet of the LBF.

$$p_{\text{vap}}(T) = e^{\frac{-3548.6}{T}+22.978} \tag{S3.2}$$

This visualization suggests that, although there is a small discrepancy of the temperatures of maximum pressures between experimental data and $p_{\text{vap}}$ fit from the datasheet (Equation S3.2), the evaporation of the LBF returns maximum pressures comparable with the ones indicated on the datasheet for given maximum temperatures. We justify deviations between the two by considering that the expression in Equation S3.2 suggested by the datasheet of Novec 7000® is a fit performed on the LBF alone, whereas we consider temperature sweeps happening in the isolated bottle with LBF-pouch inside and at steady state. We expect the presence of air inside the air reservoir to cause deviations from the ideal LBF thermopneumatic response. Following the method we described in Equation 3.4, in Figure S3.1**b** we report the value of the pressure against $V(p)$ for the different realizations of our experiment with different LBF and observe that the compression ratio we obtain increases with higher peak pressures, i.e. amount of LBF fluid in the compliant pouch.



We report the time response of the pressure to the temperature cycle for the different amounts of LBF fluid in Figure S3.1**c**. For these experiments, as well as for the ones performed while gathering the data for Figure 3.1-3.2, the oscillations in temperature happening close to the target $T_{\text{max}}$ value are the result of the PID controller of the oven as the temperature inside the oven chamber approaches the desired end value. We do not observe these oscillations during the cooling down process as, to allow gradual decrease in temperatures, we switch off the oven while leaving its door closed. This means that, during the cooling down, the PID controller of the oven cannot intervene in regulating the temperature and we use the oven hardware to passively regulate the temperature back to $T_{\text{lab}}$ slowly.

This experimental realization clearly shows that using the LBF-pouch inside the air reservoir can increase the maximum pressure reached by the system upon pressurization by more than 500% by increasing the amount of LBF. However, a limiting factor for the maximum pressure that the system can reach, besides mechanical failures that might occur at higher pressure, is the $p_{\text{vap}}$ vapor pressure of LBF. As we explained while describing our model in Figure 3.3, vapor pressure sets a thermodynamic boundary for further evaporation of the LBF once evaporation of the LBF occurs, thus limiting the potential for reaching higher pressure for a set maximum temperature.

S3

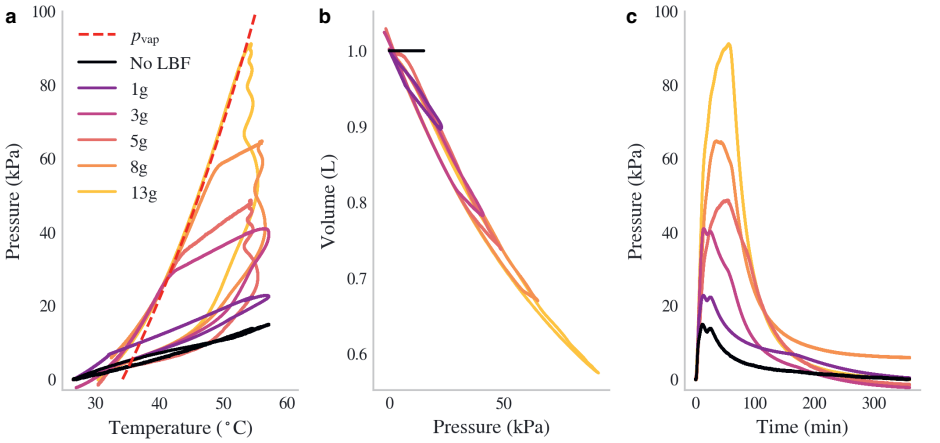


Figure S3.1: **Characterization of the thermopneumatic pressure response as a function of the LBF mass in the pouch.** We consider different LBF amounts and compare the thermopneumatic response of the system with the case where no LBF fluid is used inside the pouch (black solid lines). **(a)** Pressure as a function of air temperature. We report the vapor pressure $p_{vap}$ using the red dashed line. **(b)** Volume as a function of pressure, evaluated using Equation 3.4. For the case with no LBF in the pouch, we assume that the geometrical deformation of the air reservoir is negligible so that air molecules fully occupy the air reservoir volume of 1L. **(c)** Pressure in time for the different scenarios investigated.

### A.3: Ideal thermopneumatic cycle using manual valves

Our data in Figure 3.1 suggests that the non-zero closing pressures, both of our pressure-release valve and of the one-way valve, limit the pneumatic response of our thermopneumatic approach. At the same time, this feature hinders both the efficiency and the recharging dynamic of the energy-harvesting cell. To better explore the differences between our experimental realization of our thermopneumatic strategy with an ideal experimental setup with zero closing pressure, we perform a comparative experiment by using the same TPU pouch with LBF as in Figure 3.1, but replacing the commercial one-way and custom pressure-release valves in Figure S3.17**a** with manual FESTO valves.

With this experiment, we mean to emulate experimentally the thermopneumatic response of our system under the hypothesis of ideal (with zero closing pressure) one-way and pressure-release valves. While performing this experiment, we regulate the oven to the same maximum temperature as the one we used

in Figure 3.1**b-d**. At the same time, for a better comparison, we use the same equations and protocols to infer the change in volumes inside the air reservoir as in Equations 3.4-3.7.

To perform this experiment, we initialize the system at temperature $T_{\text{lab}} = 27°\text{C}$ and place the air reservoir in the oven before initializing the same temperature profile for the oven we used in Figure 3.1. When the pressure reaches approximately the opening pressure of the pressure-release valve, we emulate the opening of the pressure-release valve by opening the manual valve at the outlet. Similarly, after the discharge phase, we close the manual valve at the outlet before switching off the heating from the oven (2 hours after the beginning of the experiment) while opening the manual valve at the inlet of the energy-harvesting cell. We then let the experiment run for the remaining 8 hours during which the temperature slowly drops up until $T_{\text{lab}}$, just like in Figure 3.1**c-d**.

Data from this experiment is shown in Figure S3.2, and indicates two main features of such an ideal system. First, the LBF in the TPU pouch can expel air volume up to the point where the air pressure equals ambient pressure, thus producing a larger hysteresis in the pressure-volume plane and yielding more work and higher efficiency. Secondly, we observe that by integrating the airflow during the recharge phase, we fully recover the initial state of this experimental realization.

In conclusion, this comparative experiment that emulates the thermopneumatic response in the case of ideal valves with zero closing pressures serves two purposes. First, it indicates that the data processing method we use is able to grasp the expected behavior of an ideal system, showing also that the integration technique we used and the workflow are reliable enough. Secondly, it suggests that the initial state of pressure and volume in the system is not fully recovered due to the non-zero closing pressure of the one-way valve, predominantly. This also means that, upon consecutive thermopneumatic cycles, slightly fewer air molecules are reinjected in the air reservoir during the recharge phase.

### A.4: Accuracy of air volumes and the recovery of initial condition during consecutive thermopneumatic loops

Especially while considering the experiments in Figure 3.2, it is worth mentioning that there is a significant difference between the discharge (10 minutes) and recharge (3 hours) times. This places notable challenges on the precision and comparison between some of the measurements. We show details of the raw data from the new flow sensors in Figure S3.3. This difference in time scales introduces non-trivial challenges while collecting the voltage readings of the flow sensor and performing the time integration of the SLPM to infer the geometrical volume of air in time using Equation 3.7. However, our protocol for executing the experiments

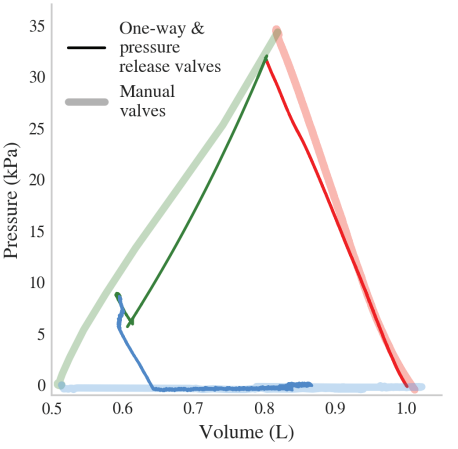


Figure S3.2: **Comparison of the heat cycle using valves and manual control**. The thin line shows the heat cycle obtained from the experiment performed using the combination of pressure release and one-way valve as in our thermopneumatic cell from Figure 3.1**c**. The thicker line indicates results from the experiment performed using manually operated valves, to simulate zero closing pressures both on the pressure-release and one-way valve. We highlight in red, green, and blue the compression, discharge, and recharge phases respectively for the two cases.

and processing sensor data seems to be sufficiently accurate to represent an ideal thermopneumatic cycle as shown in previous section.

We believe that the mismatch in air volumes measured at the beginning and at the end of an energy harvesting cycle is not caused by measurement-related errors. In particular, we do not deem systematic integration error to dramatically affect our results, as we do not observe a drift in flow data over time, and it appears the flow sensor recovers its offset zero value at the beginning of each new thermal cycle. On top of that, we report that the commercial Luer® one-way valves we performed our experiments with have low but non-zero opening and closing pressures that could prevent the full recovery of air volume after the recharge phase. We highlight that our pressure measurements indicate that the opening and closing pressures do not drift in time, suggesting that the pneumatic behavior of our custom-made component is stable upon repeated energy harvesting cycles. As a one-way valve, we use a commercial Luer® duckbill check valve.

At the same time, we observe a slight pressure drop just after each of the discharge phases, as we observe in the insets of Figure 3.2**a**. We further investigate

these pressure drops in Figure S3.4. In Figure S3.4**a**, we report the average value and standard deviation of the equilibration pressure measured for the end of the discharge phase up until the oven is switched off. In Figure S3.4**b**, we show the deviation of the average equilibration pressures after the firing event measured in Figure S3.4**a** from the first thermopneumatic cycle. We evaluate the difference in average equilibration pressure between consecutive thermopneumatic loops in Figure S3.4**c**. From this data, we observe a loss in pressure after the firing event that stabilizes at about 0.5kPa/cycle after five thermopneumatic cycles. Although we acknowledge the potential leakage of LBF from the TPU pouch as a potential cause for this slight drop in equilibration pressure through loss of powering fluid over time, we believe a more realistic explanation lies in the non-zero closing pressure of the one-way valve. While reproducing our energy harvesting approach using manual valves instead of the custom pressure-release valve, we observe that the system is indeed able to recover its initial state.



In conclusion, even though the volume measurements might not be accurate due to the experimental challenges, experimental data suggest that our protocol to infer air volumes is still accurate enough to grasp the slight variation in performance of the energy harvesting unit over time.

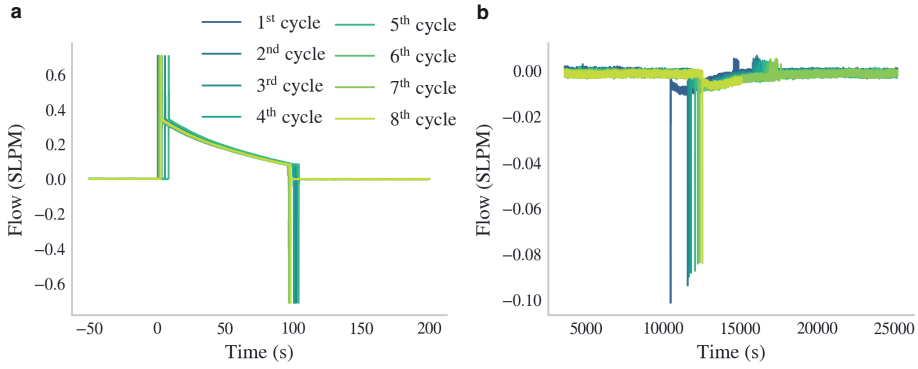


Figure S3.3: **Additional data for the flow measurements performed during the experiment in Figure 3.2 on repeated energy harvesting cycles. (a)** Flow data for the discharge phase. We overlay the different thermopneumatic cycles in time to highlight that the discharge phases we measured always follow the same trend in time and have well-determined duration. **(b)** Highlight of the incoming net flow during the recharge phase.

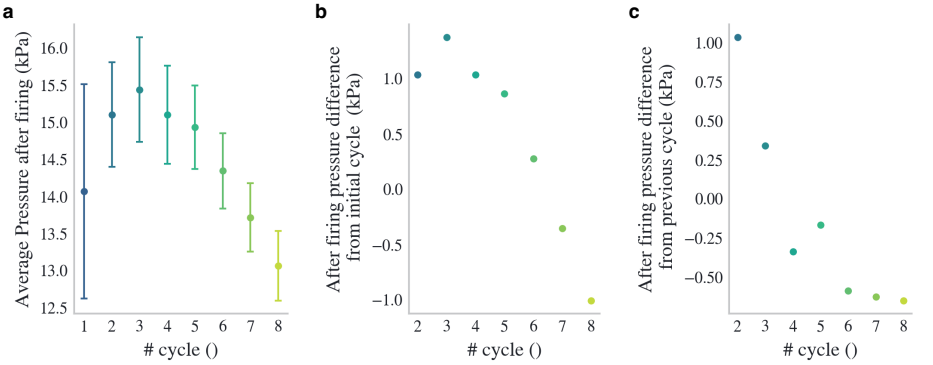


Figure S3.4: **Characterization of pressure losses upon repeated thermopneumatic cycles.** We characterize the pressure losses from the time instance where the pressure-release valve closes up to when we switch off the heating in the controlled oven environment and consider its average and standard deviation value for the different thermopneumatic cycles in Figure 3.2. **(a)** Equilibration pressure per cycle. **(b)** Difference of average equilibration pressures with the first thermopneumatic cycle. **(c)** Difference between the average equilibration pressures of consecutive thermopneumatic cycles.

### A.5: Characterization of pressure-release valve opening pressures with varying thickness

We investigate how the silicone dome geometry affects the critical pressure of the pressure-release valve, particularly focusing on its thickness. We fabricate different silicone domes and report their fluidic properties in Figure S3.5. We fabricate domes with different thicknesses $t = [0.75, 1, 1.25, 1.5, 1.9]$mm and sweep input air pressure from $p_{\text{amb}}$ to $p_{\text{max}} = [5, 10, 15, 30, 50]$kPa while measuring the airflow. We then measure $\Delta p_{\text{open}}$ ($\Delta p_{\text{close}}$) the pressure at which the valve transitions from 0 to 0.05SLPM (0.05 to 0.0SLPM).

For each dome thickness, we pressurize the valves 30 times and report the average and standard deviation of the opening and closing pressures from the last 15 pressurization and depressurization cycles. From our experiments, we observe a non-linear increase of the opening pressures with increasing dome thickness of the dome structure, the closing pressures follow a mostly linear trend. Therefore, for what concerns our purposes, we observe that the dome thickness can be used as a control parameter to embed different pneumatic behaviors in fluidic, electronics-free circuits.

To maximize the volume spanned by the thermodynamic state of the energy harvesting unit in the pressure-volume space, it is crucial to use a pressure-release

valve with the largest discrepancy between opening and closing pressures that can be triggered using real-world conditions. Therefore, in our study, we focused on the silicone dome design with thickness $t = 1.90$mm.

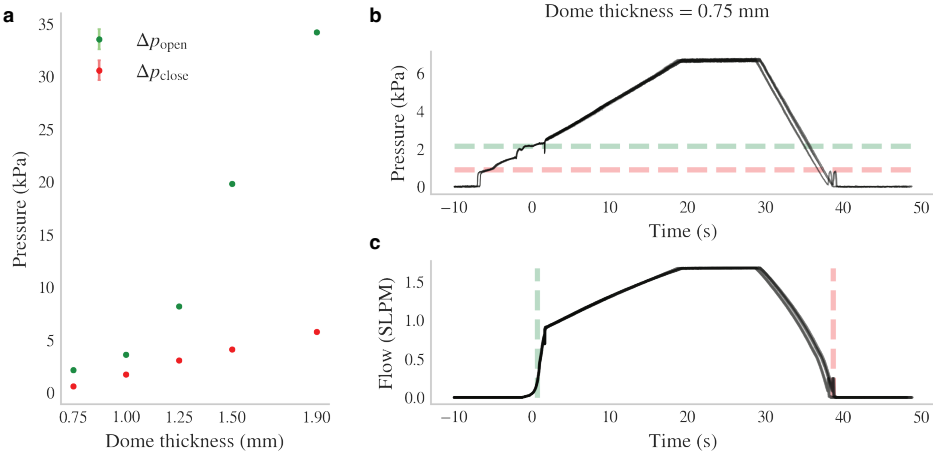


Figure S3.5: **Effect of dome thickness on opening and closing pressures of the pressure-release valve. (a)** Opening and closing pressures for different thicknesses tested. Error bars (standard deviation) are reported but not visible. **(b-c)** Example of characterization data through overlay of **b** pressure and flow **c** in time for 15 consecutive pressurization and depressurization cycles for $t = 0.75$mm. We highlight the measured opening and closing pressure values with the corresponding flow measured with the green and red dashed lines, respectively.

### A.6: Efficiency calculations

With the goal in mind to evaluate the efficiency of our thermopneumatic approach and quantify the performance of our energy harvesting cell compared to already developed technologies, we consider the following hypotheses. We particularly focus on the experimental results from Figure 3.1, thus we perform our analysis considering that the energy harvesting cell operates between $T_{\text{lab}} = 27°\text{C}$ and $T_{\text{max}} = 43°\text{C}$.

For our analysis, we can consider that the TPU pouch containing the LBF operates as a thermally activated piston that compresses and pressurizes the air volume inside the air reservoir upon evaporation of the LBF. We focus on the efficiency of one full thermopneumatic cycle. This hypothesis allows us to approximate, over one thermopneumatic cycle, the change in internal energy is neglible, that is $\Delta U = 0$. This means that we can evaluate the efficiency $\eta$ of our

thermopneumatic approach by considering

$$\eta = \frac{|W|}{Q_{\text{in}}} = \frac{Q_{\text{in}} - |Q_{\text{out}}|}{Q_{\text{in}}} = 1 - \frac{|Q_{\text{out}}|}{Q_{\text{in}}} \tag{S3.3}$$

We consider this approximation realistic in the first-order approximation and evaluate the work $W$ done by the system on its surroundings, following from the first law of thermodynamics, as equal to the net heat exchanged ($Q_{\text{in}}$ input heat and $Q_{\text{out}}$ output heat) by the system during one thermopneumatic cycle $W = Q_{\text{in}} - |Q_{\text{out}}|$. However, including heat losses during the separate thermodynamic processes is a non-trivial task while modeling our thermopneumatic approach, as they are related to the specific trajectory in the thermodynamic space, together with different timescales of phase transitions, thermal cycles, and material properties simultaneously. Therefore, we simplify our analysis by considering the ideal (lossless) behavior of such phenomena to simplify both the description and modeling, aware that our calculations will only be able to yield a theoretical upper limit for efficiency.

In our model, we choose to approximate the complex polytropic processes in the thermopneumatic processes with useful simplifying assumptions that we summarize here. Including a more detailed model, e.g., with a detailed description of phase transitions, would still require complex approximations and fitting of physical parameters that are not often accessible experimentally. Instead, we prefer to focus on outlining the main contributions to heat transfer and infer a first-order estimate for efficiency.

To evaluate the heat exchange over one thermopneumatic cycle, we study the compression, discharge, and recharge phases separately. For the remainder of this section, we will indicate them as processes 1, 2, and 3, respectively.

1. During the compression phase, we define $Q_{1,\,\text{air}}$ as the heat needed to bring the temperature of the mass of air inside the air reservoir from $T_{\text{lab}}$ to $T_{\max}$. As we know the volume of the reservoir, assuming the volume of the pouch is initially negligible with respect to the air reservoir volume, we can evaluate the heat $Q_{\text{air},\,1} = m_{\text{air},\,1} c_{\text{air}} (T_{\max} - T_{\text{lab}})$, being $m_{\text{air},\,1} \simeq 1.29\text{g}$, mass of $1L$ of air at ambient pressure and $T_{\text{lab}}$ and ambient pressure $p_{\text{amb}}$.

   Conversely, the increase in pressure is obtained as a consequence of heating up, and then evaporation of the LBF. We separate the $Q_{\text{LBF},\,1}$ contributions in $Q_{\text{LBF},\,1,\,T_{\text{lab}} \to T_{\text{PT}}}$, $Q_{\text{LBF},\,1,\,\text{PT}}$ and $Q_{\text{LBF},\,1,\,T_{\text{PT}} \to T_{\max}}$ as the heats required to heat from lab temperature to the boiling point, to evaporate and then to bring the LBF gas to maximum temperature. We observe experimentally that evaporation (condensation) starts to occur already at temperatures lower (higher) than the phase transition temperature for a given pressure of the fluid. We justify this observation by speculating that

the LBF molecules have to observe a Maxwell-Boltzmann distribution of velocities and that the phase transition, especially due to the contextually increasing/decreasing pressures of the LBF, is not sudden. Considering the small masses of LBF we use in our experiments, we assume the phase transitions happens in a fast time scale. At the same time, we approximate the phase transitions to occur at $T_{PT}(p_{\text{amb}}) = 34°\text{C}$, even when pressure is higher than ambient pressure. Nevertheless, for simplicity of the model, we model phase transitions to occur at once when the system reaches the transition temperature of $T_{\text{PT}}(p_{\text{amb}})$.

To raise the temperature of a mass $m_{\text{LBF}}$ of LBF up to its boiling point and starting from $T_{\text{lab}}$, we consider the LBF specific heat $c_{\text{LBF}}$, so that

$$Q_{\text{LBF, 1, } T_{\text{lab}} \to T_{\text{PT}}} = m_{\text{LBF}}\ c_{\text{LBF}} \cdot \left(T_{\text{PT}}(p_{\text{amb}}) - T_{\text{lab}}\right) \tag{S3.4}$$

To evaporate the mass of LBF at $T_{\text{PT}}(p_{\text{amb}})$, the environment must provide heat $Q_{1\ \text{LBF, PT}}$ so that, given the heat of vaporization of the LBF $L$

$$Q_{\text{LBF, 1, PT}} = m_{\text{LBF}} \cdot L \tag{S3.5}$$

We assume that once $Q_{\text{LBF, 1, PT}}$ is provided to the system at $T_{\text{PT}}(p_{\text{amb}})$, all LBF molecules evaporated, upon further increase of temperature up to $T_{\text{max}}$, can be achieved if $Q_{\text{LBF, 1, } T_{\text{PT}} \to T_{\text{max}}}$ is provided to the system, with

$$Q_{\text{LBF, 1, } T_{\text{PT}} \to T_{\text{max}}} = m_{\text{LBF}}\ c_{\text{LBF}} \cdot \left(T_{\text{max}} - T_{\text{PT}}\right) \tag{S3.6}$$

From the aforementioned equations, we infer that there is a minimum amount of heat required in order to bring the system from its initial condition up to the end of the compression phase $Q_1 = Q_{\text{LBF, 1}} + Q_{\text{air, 1}}$ where

$$\begin{aligned} Q_{\text{LBF, 1}} &= Q_{\text{LBF, 1, } T_{\text{lab}} \to T_{\text{PT}}} + Q_{\text{LBF 1, PT}} + Q_{\text{LBF, 1, } T_{\text{PT}} \to T_{\text{max}}} && \text{(S3.7)} \\ &= m_{\text{LBF}} \Big( c_{\text{LBF}} \left(T_{\text{PT}} - T_{\text{lab}}\right) + L\ + c_{\text{LBF}} \left(T_{\text{max}} - T_{\text{PT}}\right) \Big) && \text{(S3.8)} \\ &= m_{\text{LBF}} \Big( c_{\text{LBF}} \left(T_{\text{max}} - T_{\text{lab}}\right) + L \Big) && \text{(S3.9)} \end{aligned}$$

from which we infer that, given our approximations, the exact temperature at which the phase transition of the LBF occurs does affect the heat balance of the LBF during the compression phase.

2. We assume the discharge phase to occur fast enough compared to the timescales of compression and recharge phase. This observation is supported

by data in Figure S3.17**b** and Figure S3.3 where we observe that while the discharge and recharge phase have a duration in the order of hours, the discharge phase happens in about 100 s. We use this observation to model the discharge as an adiabatic, fast discharge of air molecules through the load. In addition to that, within our sensing resolution, the discharge process does not produce measurable effects on the air temperature inside the air reservoir. This approximation of adiabatic discharge can be considered valid up until the load connected to the output of the pressure-release valve is not large enough to slow down the discharge phase to time scales comparable with the heat exchange processes.

Therefore, when focusing on the heat exchange that we aim to model and use to evaluate the efficiency in Equation S3.3, we assume that no heat is exchanged during the discharge phase. The only thermodynamic consequence of the discharge we consider is that air molecules are expelled until the closing pressure is reached.

Starting from our experimental data and ideal gas law, we can compute the mass of air inside the air reservoir just at the end of the discharge process. When considering that at the end of the discharge phase (closing of the pressure-release valve), the air inside the air reservoir has pressure $\Delta p_{\text{close}} \simeq 11\text{kPa}$, volume .6L and temperature $T_{\text{discharge}} = 43°\text{C}$, we can derive from ideal gas law that the number of molecules in the system is $m_{\text{air, 2}} \approx 0.8\text{g}$. If we compare this mass with the initial air $m_{\text{air, 1}} \approx 1.3\text{g}$ obtained following the same procedure, we observe that almost one-third of the air mass is expelled as a consequence of the discharge phase.

3. For computing the heat exchanged during the recharge phase, we consider that the preserved amount of LBF has to undergo ideally the inverse of the processes we described in process 1. This means that the LBF undergoes cooling down up to the condensation temperature and condensation, before reaching the initial temperature $T_{\text{lab}}$. Thus, from a thermodynamic point of view, we assume that the amount of heat exchanged during this process, for what concerns the LBF, is $Q_{\text{LBF, 3}} = -Q_{\text{LBF, 1}}$.

   At the same time, for what concerns the air inside the air reservoir during the recharge phase, we observe that as the air cools down, it returns heat to the environment around the energy harvesting unit, before recharging air molecules through the one-way valve. This is mostly because the actual recharge can only take place when the pressure inside the air reservoir is lower than ambient pressure. We assume that such a condition can only manifest after the condensation of the LBF has occurred, as observed in Figure 3.1**d**. This means that during the recharge phase, the $m_{\text{air, 2}}$ mass of air is releasing energy to the environment while cooling down from

$T_{\text{discharge}} = 43°\text{C}$ to $T_{\text{lab}}$, returning to the environment

$$Q_{\text{air, 3}} = m_{\text{air, 2}} c_{\text{air}} \left(T_{\text{lab}} - T_{\text{discharge}}\right) \tag{S3.10}$$

Therefore, the actual air molecule recharge is instantiated by this slightly negative pressure generated by the condensation of the LBF. From a thermodynamic point of view, this process can be regarded as an isobaric expansion of the air at ambient pressure and temperature.

When considering the results of the individual processes, we can obtain an upper limit for the efficiency of the system from Equation S3.3

$$\eta = 1 - \frac{|Q_{\text{LBF, 3}} + Q_{\text{air, 3}}|}{Q_{\text{LBF, 1}} + Q_{\text{air, 1}}} \tag{S3.11}$$

$$= 1 - \frac{m_{\text{LBF}} \left( c_{\text{LBF}} \left(T_{\text{max}} - T_{\text{lab}}\right) + L \right) + m_{\text{air, 2}} c_{\text{air}} \left(T_{\text{lab}} - T_{\text{discharge}}\right)}{m_{\text{LBF}} \left( c_{\text{LBF}} \left(T_{\text{max}} - T_{\text{lab}}\right) + L \right) + m_{\text{air, 1}} c_{\text{air}} (T_{\text{max}} - T_{\text{lab}})} \tag{S3.12}$$

Given our experimental conditions with $m_{\text{air}} = 0.0013\text{kg}$, $m_{\text{LBF}} = 0.005\text{kg}$ and considering that $c_{\text{air}} = 700$ J/(kg·K), $c_{\text{LBF}} = 1300$ J/(kg·K), $L = 142000\text{J/kg}$, we obtain an upper theoretical value for efficiency in our experiment of $\eta = 0.87\%$, $\eta_{\text{Carnot}} = 5.06\%$, so that $\frac{\eta}{\eta_{\text{Carnot}}} = 0.172$. We report the scaling of $\eta$ as a function of $m_{\text{LBF}}$ in Figure S3.6.

For the aforementioned reasons, provided that the discharge phase is considered adiabatic, our approximations return an upper boundary for efficiency, irrespective of the load used to evaluate the efficiency of the thermopneumatic cycle. This also means that the work done on the environment by the pressurized air is independent of the loading conditions (trajectory in the pressure-volume plane), as is known in adiabatic processes.

Furthermore, we evaluate the theoretical lower bound for efficiency, based on the following arguments. First, we consider that when our system reaches the firing threshold, there is a minimal amount of work that it performs which is to expel a $\Delta V_{\text{firing}} \simeq 0.2\text{L}$ volume of air while decreasing its internal pressure by $\Delta p_{\text{firing}} = p_{\text{open}} - p_{\text{open}} = 26\text{kPa}$. Therefore, the minimal work that the system can perform is $W_{\text{min}} = \Delta V_{\text{firing}} \Delta p_{\text{firing}} \simeq 2.7J$, that we estimate from the area in the pressure-volume curve between the beginning and end of the discharge phase in Figure 3.1**c**. As for the minimal required input energy to bring the system to the discharge phase, we consider the ideal case in which the starting temperature is the boiling temperature of the LBF at ambient pressure ($T_{\text{boil}}(p_{\text{amb}}) = 34°\text{C}$). As maximum operating temperature, we consider the $T_{\text{max}}$ from our experiment in

Figure 3.1 $T_{\max} = 42°C$. When considering $Q_{\mathrm{LBF},1}$ heat related to the compression phase for the LBF, we have to take into account the energy to let its temperature increase within the operating ranges and the latent heat of vaporization, as we described in Equation S3.9. For the air in the reservoir, we only consider $Q_{\mathrm{air},1}$ heat required to heat it from $T_{\mathrm{boil}}(p_{\mathrm{amb}})$ to $T_{\max}$, given the air mass and heat capacity. Using these operating temperatures and repeating the calculations for the input energy $Q_1 = Q_{\mathrm{LBF},1} + Q_{\mathrm{air},1}$ heat. From our calculation, we derive a lower bound of 0.38% when using $m_{\mathrm{LBF}} = 0.005$g. Based on these calculations, in Figure S3.6**a** we report the scaling of the theoretical lower bound of efficiency with increasing mass of the LBF.

As we argue in Supplementary Material A6, incorporating more detailed hypotheses that, e.g, explicitly resolve phase transitions, would still entail substantial approximations. On top of that, it would also require the calibration of such additional physical parameters that are often not measurable in experiments. The same arguments apply when studying a lower bound for the efficiency, besides the trivial $\eta \geq 0$.

Determining a realistic efficiency value experimentally would require a substantially more advanced experimental setup. This setup would need to integrate our thermal regulation, pneumatic, and thermal measurements with calorimetry (e.g., a bomb calorimeter or heat flux meters). Moreover, adding more detailed hypotheses (e.g., explicitly resolving phase transitions) would still rely on significant approximations and introduce additional parameters that are difficult to access experimentally.

### A.7: Energy density, power density, and efficiency comparison

Only a few publications report data concerning the weight, energy, and power of the implementations in their studies. This means that only a few data points are available, compared to case studies where, e.g., the cost of transport is investigated. When data is available, we compare the claimed efficiency for the same publications, in order to have a metric to compare overall performances (Figure S3.7). This investigation is generally disregarded in the field. When comparing the efficiency of our system with the reported efficiency in different strategies, we use the theoretical upper limit of 1% for our case study.This decision is justified by the consideration that, unlike in case studies where the energy input can be determined with relative ease (for instance by knowing the enthalpy in a chemical reactor, by assuming adiabatic discharge conditions for pressurized canisters, or by integrating power consumption over time in an electrical battery) the direct experimental quantification of heat fluxes is substantially more challenging. In particular, heat exchange processes often involve complex boundary conditions, temperature gradients, and transient phenomena, all of which complicate accurate measurement and require more sophisticated instrumentation and analysis. As an example, calorimetric bombs and heat flux transducers would enable such

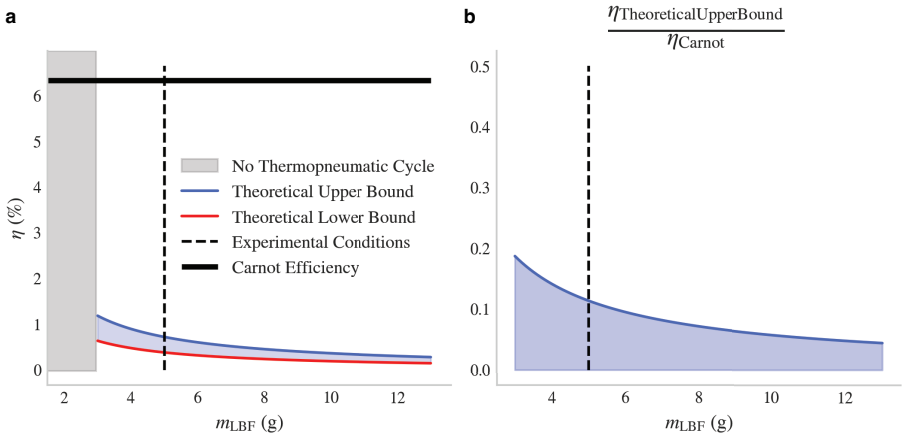


Figure S3.6: **Model for theoretical upper bound efficiency, lower bounds of efficiency and Carnot efficiency for different mass of LBF** ($m_{\text{LBF}}$). **(a)** Comparison of theoretical upper and lower bounds with corresponding Carnot efficiency. We highlight in blue the allowed values of efficiency for its corresponding $m_{\text{LBF}}$ value. With the dashed vertical black line we highlight $m_{\text{LBF}} = 5$g, since we used this amount in our experiments. The gray area indicates $m_{\text{LBF}}$ values for which, according to our experiments in Figure S3.1, the opening pressure of $\Delta p_{\text{open}} = 33$kPa is not reached, hence not of interest for our investigation on efficiency. **(b)** Comparison of theoretical upper bound for efficiency in our system over the correspondent Carnot efficiency.

measurements, thus allowing us to verify our theoretical approximation.
When an energy harvesting device is presented, we observe from the literature that devices capable of extracting energy from their environment, e.g., by incoming radiation [134], use it to directly perform work. Instead, in our case, we separate the energy accumulation and energy release phases through consecutive, non-simultaneous, compression and discharge phases. We include in Figure S3.7 the reported experimental performance in specific energy, specific power density, and efficiency of LiPo batteries [136] and $CO_2$ canisters [157] typically used to power untethered soft robots, in blue and green, respectively. We compare available data from literature of different energy storage strategies with our thermopneumatic energy harvesting and storage approach (represented as a red star) in Figure S3.7. We measure a specific energy density of $\approx 112.6 \frac{\text{J}}{\text{kg}}$ and a specific power density of $\approx 2.7 \frac{\text{W}}{\text{kg}}$, calculated using the 42s discharge time we have recorded in Figure 3.5 during the indoor locomotion experiments.

S3

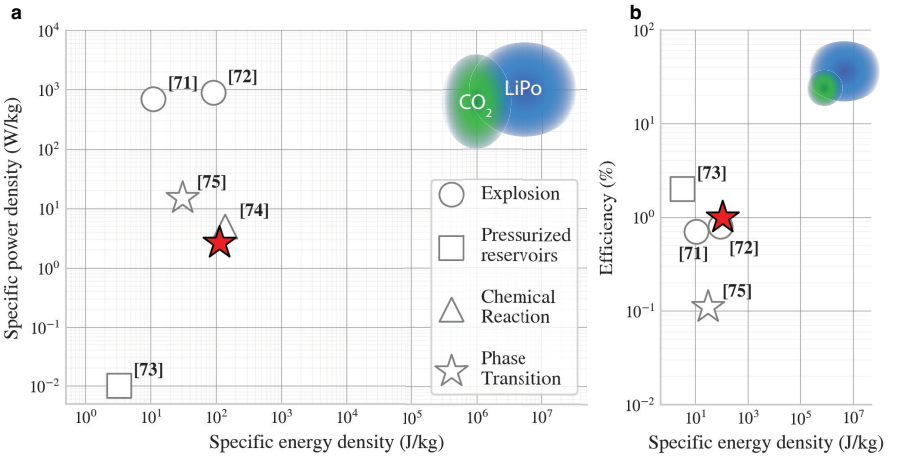


Figure S3.7: **Comparative study on literature examples for specific energy density, specific energy density, and efficiency to power energy autonomous soft robotic systems.** We compare available experimental data from different energy sources [152–156]. On top of that, we report metrics for LiPo batteries and $CO_2$ canister [157] in blue and green, respectively. With the red star, we report the extracted metrics from the upper theoretical limit in our case study. The efficiency we report is the upper threshold for the efficiency we study in Figure S3.6. In (**a**), we evaluate the power density using the discharge time of $\sim$ 40s we have observed in the indoor locomotion experiment. For the publication leveraging chemical reactions (triangle), no data was reported about efficiency.

From this comparative study, we observe that the different methods we report for energy autonomy can span several orders of magnitude for what concerns specific energy density, specific power density and efficiency. Some methods, such as explosion-based devices, can produce specific power density orders of magnitude higher than all the other methods we studied. This is mainly due to the high energy density of the fuels used and the impulsive nature of the work that those systems can manifest. This is in contrast to systems based, for example, on phase transitions or on the release of gas through pressure regulators.

At the same time, $CO_2$ canisters demonstrate performances comparable to LiPo batteries in specific energy density, specific power density, and efficiency. However, this is due to the high pressure in such pressurized stiff volumes ($\sim$ 60 bar). A few orders of magnitude separate LiPo batteries and $CO_2$ canisters from pneumatic,

chemical reaction, explosion, and phase-transition-based devices. Clearly, for all such systems, the most suitable energy source solution must be found by interpolating energy and power requirements with total weight and additional constraints, such as safety in, e.g., underwater environments, fire-hazard, and chemical toxicity.

For this reason, although we consider the analysis performed in Figure S3.7 to be representative for comparison, we acknowledge that there are fundamental differences, not only in energy autonomy strategies but also in initial purposes between the reported case studies.



### A.8: Comparison with other LBF candidates

Our choice of Novec 7000 was made to study the use of LBF compatible with temperatures obtainable from heat exchange from natural environments during circadian oscillations. A well-detailed overview of different media can be found, e.g., in Figure S3.4 of [156], where saturation pressure and enthalpy of vaporization are studied in detail for different (low-boiling-point) fluids. Based on the thermodynamic properties of different LBFs candidates, we can comment on their potential for being used in our thermopneumatic energy strategy.

**Efficiency:** We can leverage the model in Equation S3.12 to get insights into how efficiency would change if different powering media are used. In particular, for this study, we focus on acetone, ethanol, and water as they are potential alternatives for environmental applicability. Nevertheless, to reach the evaporation threshold at ambient temperature and instantiate the compression phase, higher temperatures are needed. The increase in operating temperature affects the overall Carnot efficiency of the system as well. Following the data reported when comparing such LBFs in Figure 3.3 of [156], and assuming we target to reach the same triggering pressure of 35kPa, we observe that our model in Equation S3.12 yields:

*Acetone*

- $T$ for reaching 35kPa $= 85°\text{C}$
- $\eta_{\text{acetone}} \approx 0.42\%$, $\eta_{\text{Carnont, acetone}} \approx 12.4\%$
- $\frac{\eta_{\text{acetone}}}{\eta_{\text{Carnot, acetone}}} \approx 3.4\%$

*Ethanol:*

- $T$ for reaching 35kPa $= 95°\text{C}$
- $\eta_{\text{acetone}} \approx 0.45\%$, $\eta_{\text{Carnont, acetone}} \approx 17.3\%$

- $\frac{\eta_{\text{acetone}}}{\eta_{\text{Carnot, acetone}}} \approx 2.5\%$

*Water:*

- $T$ for reaching 35kPa $= 110°\text{C}$
- $\eta_{\text{acetone}} \approx 0.60\%$, $\eta_{\text{Carnont, acetone}} \approx 22.7\%$
- $\frac{\eta_{\text{acetone}}}{\eta_{\text{Carnot, acetone}}} \approx 2.6\%$

S3

For these calculations, we assumed constant mass of 5g for the candidate LBFs, just like the one we have used throughout our experiments. For a better comparison, we recall that in our case study (using the the highest value of efficiency from our model) we got:

*Novec 7000 (our study):*

- $T$ for reaching 35kPa $= 43°\text{C}$
- $\eta_{\text{Novec 7000}} \approx 1.6\%$, $\eta_{\text{Carnont, Novec 7000}} \approx 6.32\%$
- $\frac{\eta_{\text{Novec 7000}}}{\eta_{\text{Carnot, Novec 7000}}} \approx 16\%$

Overall, our thermopneumatic strategy can operate at lower temperatures than the aforementioned LBF candidates. At the same time, using Novec 7000 a higher efficiency and ratio with corresponding Carnot efficiency can be reached.
**Actuation frequency:** A powering medium with lower thermal inertia (heat capacity, latent heat of vaporization) would yield a more reactive system. However, as we have seen in the case of the effects of moisture in Equation S3.15, given the masses of the powering and actuating media we use, we expect different LBF to affect only marginally the timescales for heating up and cooling down. As an example, for the LBF studied in [156], we can get a quantitative understanding of how much different thermodynamic properties of the system can affect the time scales of heating up and cooling down. For this analysis, we take into account specifically acetone, ethanol, and water as candidate powering fluids. When we take as reference values the latent heat of vaporization and heat capacity of Novec 7000 $L_{\text{Novec}} = 142\frac{\text{kJ}}{\text{kg}}$ and $c_{\text{Novec}} = 700\frac{\text{J}}{\text{kg·K}}$, we can infer that $\frac{L_{\text{acetone}}}{L_{\text{Novec}}} \sim 3.7$, $\frac{L_{\text{ethanol}}}{L_{\text{Novec}}} \sim 5.8$, $\frac{L_{\text{water}}}{L_{\text{Novec}}} \sim 15.7$ and $\frac{c_{\text{acetone}}}{c_{\text{Novec}}} \sim 3.0$, $\frac{c_{\text{ethanol}}}{c_{\text{Novec}}} \sim 3.4$, and $\frac{c_{\text{water}}}{c_{\text{Novec}}} \sim 5.9$.Our simulation framework can help validate that, for the same valve design and environmental circadian oscillations in temperature and light intensity, alternative LBF candidates such as acetone or ethanol would not be able to produce pressures high enough to trigger the discharge phase. This incompatibility of alternative LBFs to operate under environmental conditions is due to the combination of both higher heat capacity and boiling temperature. In our model, we consider

that, given good agreement between the vapor pressure curve of Novec 7000 and our experimental data (Figure 3.3), the $p(T)$ follows the vapor pressure curve of acetone. We compare our experimental data and fit of vapor pressure in Figure 3.2b with the vapor pressure of acetone in Figure S3.8**a**. At the same time, we perform the study on different geographical locations we introduced in Figure 3.3**d** in Figure S3.8**b**. When considering the relative boiling temperature and heat capacity of acetone, we observe that the system would need temperatures of $\sim 85°C$ in order to reach the firing threshold. On top of that, we observe that the system cannot reach the $T_{\text{boi}}(p_{\text{amb}}) = 56°C$, thus the evaporation threshold is never achieved, and fluctuations in pressure are due to the air volume inside the reservoir heating up, as we report in the simulations in in Figure S3.8**c**.

Such high temperatures are hardly ever compatibile with temperatures recorded in 2024 in the locations we highlight. At the same time, sunlight intensity is not sufficient to provide the additional required heat to bring the LBF the temperature necessary to trigger the discharge phase at 35kPa, as we show in Figure S3.8**c**.



**Environmental applicability:** It is worth mentioning that one major limitation of Novec 7000 is its global warming potential (100-year integrated time horizon, IPCC 2013) of $\text{GWP}_{\text{Novec}} = 530$. For a comparison, $\frac{\text{GWP}_{\text{acetone}}}{\text{GWP}_{\text{Novec}}} \sim 5 \cdot 10^{-4}$, while GWP tables focus on well-mixed, long-lived greenhouse gases, so we could not identify from literary sources $\text{GWP}_{\text{ethanol}}$, nor $\text{GWP}_{\text{water}}$, which we expect to be too low to be determined in the first place.This means that Novec 7000 can be considered extremely more pollutant as LBF then the aforementioned LBF candidates. This feature in particular prompted us to use utmost care and precautions during fabrication Novec 7000 (storing Novec 7000 in a refrigerated environment to prevent it from escaping the 3M container in its gaseous form, manipulating it always and only under a fume hood) while preventing leakages and spills.

In conclusion, design changes are required to explore the use of different LBFs that could be more environmentally friendly while guaranteeing the same performances and applicability in open-world scenarios. We have updated the discussion of our article to include this additional information.

### A.9: Strategies to reduce potential leakages of LBF

As for the leakages of LBF through the pouch, we consider the following arguments. To our knowledge, the long-term degradation of TPU in contact with Novec 7000 has not been quantified in the literature, and our early samples showed roughly unchanged pouch weight over about one year, although detecting small losses is difficult given the small LBF mass (5 g) relative to the pouch/connectors ($\approx 30$ g). To further reduce leakage, a practical alternative would be replacing the nylon-coated TPU pouch with a mylar (foil) balloon. Aluminised films (e.g., PET with a

S3

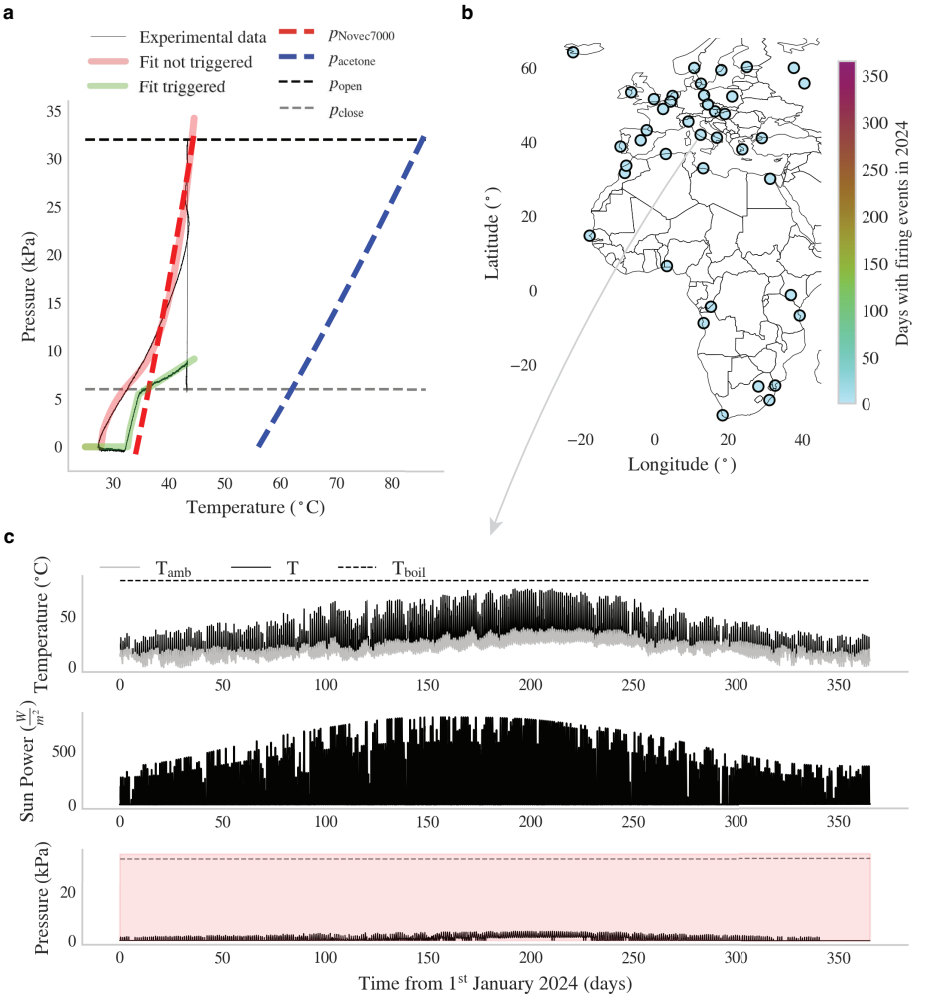


Figure S3.8: **Simulated experiment with acetone as LBF fluid. (a)** We compare the data in Figure 3.3**b** with the vapor pressure curve for acetone in (dashed blue). The ambient temperature necessary to reach the firing threshold at 35kPa while using acetone is now 85°. **(b)** By running the simulation on different locations during 2024 as in Figure 3.3**d** and using acetone thermodynamic properties, only a few firing events are achieved. **(c)** Example output data for the case of acetone as LBF in Rome throughout the whole 2024.

thin aluminium layer) provide a strong diffusion barrier that substantially lowers permeability, and they can be manufactured with heat-sealed seams similarly to our current pouches. Recent studies [158] have quantified that, by including aluminum foil, oxygen permeability can reach $0.7\boldsymbol{\nabla} \cdot 0.049\text{cm}^3 \cdot \text{m}^{-2} \cdot \text{day} \cdot$ atm, equivalent to $14\boldsymbol{\nabla} \cdot .8 \cdot 10^{-5}\text{L/day}$ in our case study. As LBF molecules are larger than $O_2$ molecules, we expect these leakages to be even less pronounced when an aluminum coating is introduced in the design of the pouch.

S3

S3

## B: Heat transfer model

Our approach to model the heat transfer in our thermopneumatic cell is to consider the different subsystems of rigid air reservoir, LBF and air as a whole. To our knowledge, this approach has been only partially explored in literature [123] where, once the heat transfer equation has been defined, a fit on experimental data is performed to predict the response of pouch filled with LBF undergoing phase transition. Similarly, our approach first aims to identify the most significant contributions to heat transfer equations and fit the model to the observed results. Still, while performing this approximation, we inform our model with fundamental heat-transfer knowledge, based on convection, radiative losses, and light-intensity absorption.

We demonstrate that this simplification allows us to capture all the relevant features of the evolution in time $t$ of the temperature $T(t)$ for given ambient temperature $T_{\text{amb}}(t)$ and incoming sun radiation $I(t)$. In our model for heat transfer, we include the different contributions to heat flux $\dot{Q}$ from convection, radiative losses, and absorption of sun radiation considering respectively the three following equations:

$$\dot{Q}_{\text{convection}} = A\,h\,(T(t) - T_{\text{amb}}(t)) \tag{S3.13a}$$

$$\dot{Q}_{\text{radiative losses}}(t) = A\,\epsilon\,\sigma\,(T^4(t) - T^4_{\text{amb}}(t)) \tag{S3.13b}$$

$$\dot{Q}_{\text{absorption}}(t) = \alpha\,A\,I(t) \tag{S3.13c}$$

in which $A$ represents the surface area of the system, $h$ the heat transfer coefficient, $\epsilon$ the emissivity of the system, $\sigma$ the Stefan-Boltzmann constant and $\alpha$ a geometrical coefficient that accounts for projection effects due to the position of the sun during the day with respect to our system. In our model, we tune the coefficient for the heat transfer model using available data from the literature for transparent PET, so that we consider $h = 5.5\frac{\text{W}}{\text{m}^2\cdot\text{K}}$ [159], $\epsilon = .9$ [160, 161] and consider an area $A = 0.042\text{m}^2$ and $\sigma = 5.670 \cdot 10^{-8}\frac{\text{W}}{\text{m}^2\cdot\text{K}^4}$. By setting $\alpha < 0.5$, we impose that only half of the bottle is exposed to incident sun radiation while, for the sake of performing a first-order approximation, we do not directly account for latitude and how $\alpha$ could change during the daylight hours due to the different relative position of the sun with respect with our system. Moreover, in our model we disregard contributions from advection as wind speed is negligible when considering elevation so close to ground level ($\mathcal{O}(10\text{cm})$), as in the case we show in our demonstrator in Video 1 [162]. Therefore, we model temperature changes in the system as

$$(m_{\text{air}}c_{\text{air}} + m_{\text{LBF}}c_{\text{LBF}})\frac{\text{d}T(t)}{\text{d}t} = -\dot{Q}_{\text{total}} = -(\dot{Q}_{\text{convection}} + \dot{Q}_{\text{radiative losses}} + \dot{Q}_{\text{absorption}}) \tag{S3.14}$$

where we used $m_{\text{air}} = 1.293\text{g}$ (mass of 1L of air), $m_{\text{LBF}} = 5\text{g}$ as from our experiments and heat capacities $c_{\text{air}} = 700\frac{\text{J}}{\text{kg}\cdot\text{K}}$ and $c_{\text{LBF}} = 1300\frac{\text{J}}{\text{kg}\cdot\text{K}}$ for air and LBF respectively.

To calibrate the value of $\alpha$ that could fit the values we observe in the experimental realization of our system, we consider the outdoor experiment in Figure 3.4. During the outdoor experiment, we visually access information from pressure, we gather data from local weather stations, reproduce the experimental conditions in simulation, and fit $\alpha$ to the experimental observations. In particular, we consider that, starting from $T_{\text{lab}}$, the system took $\simeq 2$ hours to reach the opening pressure. Therefore, we choose $\alpha = 0.275$ value that returns a similar time scale for reaching the firing pressure, giving the experimental condition. We report the effect of different $\alpha$ in Figure S3.9 on the simulated data from the same day and location as the one experimentally probed in Figure 3.4 for the outdoor experiment. From these simulations, we observe that the different $\alpha$ yield different contributions to the heat transfer, following from Equation S3.13c as we report in Figure S3.9**a-b**. This has direct consequences on $p(t)$ that, in our model, solely depends on air temperature $T(t)$ and $F(t)$ firing state.

Following the description we provided while presenting the model in Figure 3.3**b**, we report the different values of $p(t)$ associated with the corresponding $\alpha$ values in Figure S3.9**c**.

Moreover, from experimental observations in Figure S3.17**b**, we observe that an opening event does not significantly affect the temperature inside the air reservoir. Therefore, in our model, the air pressure $p(t)$ is a function of temperature $T(t)$ and firing state $F(t)$ whereas we consider $T(t)$ not to be affected by $p(t)$ nor $\dot{p}(t)$.

To evaluate air pressure, we perform a fit on the data in Figure 3.3**b** using a cubic function for $F = false$ and a piecewise linear function for $F = true$. We gather weather data through `meteodata` Python package to access *National Oceanic and Atmospheric Administration* (NOAA) and *Deutscher Wetterdienst* (DWD) historical database of temperatures $T_{\text{env}}(t)$, `solarpy` and `meteostat` Python libraries to access data on sun intensity, comprehensive of how cloud coverage affects oscillations in solar power on ground, at any given location in time. Since the air heat capacity increases with absolute humidity $H$ [163],

$$c_{\text{air}} = c_{\text{V,air}} + 1820H \ \frac{\text{J}}{\text{kg}\cdot\text{K}}, \tag{S3.15}$$

we extended the model accordingly. However, because the air mass in the 1 L cell ($m_{\text{air}} = 1.293\,\text{g}$) is small compared to the LBF mass ($m_{\text{LBF}} = 5\,\text{g}$, $c_{\text{LBF}} = 1300\frac{\text{J}}{\text{kg}\cdot\text{K}}$), the system's thermal inertia is dominated by the LBF, and incorporating Equation S3.15 yields only marginal changes in the simulation results.

To better highlight how seasonal changes in temperature and sunlight exposure

can affect the amount of environmental energy that can be harvested by our proposed design, in Figure S3.10 we report an example of output throughout the whole 2024 in Toulouse and Rome. Also, in this case, we observe that, although ambient temperature is often not high enough to trigger our energy harvesting device, sunlight intensity can play a major role in the energy balance to activate our system. This is particularly true when considering locations at different latitudes, e.g., by comparing Casablanca to Reykjavik.

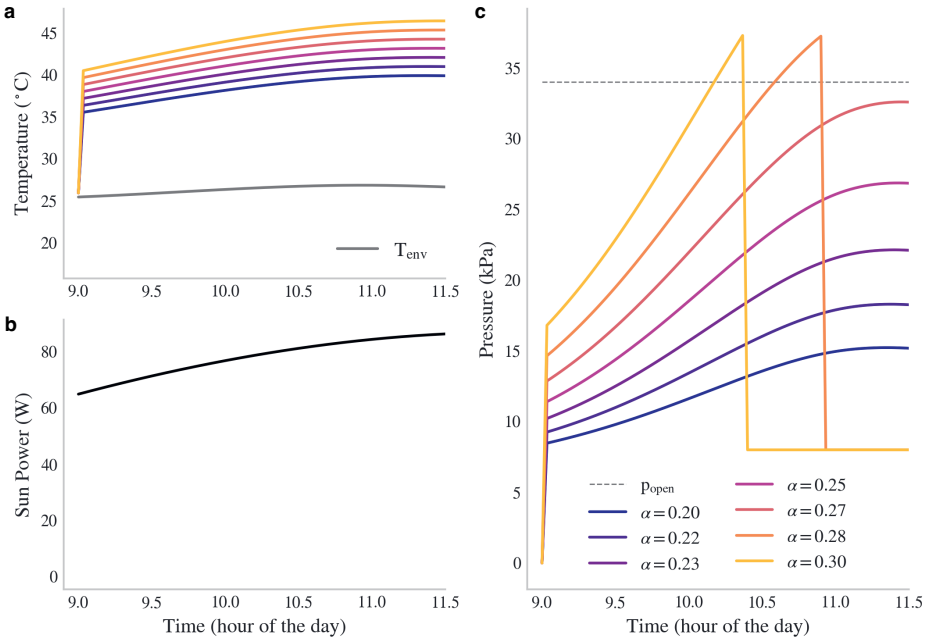


Figure S3.9: **Calibration simulation for the greybox model of heat exchange.** We gather weather data from the experiment performed on June 27$^{\text{th}}$ 2024 in Amsterdam and compare it with the numerical results from Equation S3.14. **(a)** Ambient temperature in gray and simulated air temperature inside the reservoir. **(b)** Power from sunlight intensity impinging on part of the surface of the air bottle. **(c)** Simulated pressures. In **a** and **c** we represent with different colors the simulations performed for increasing values of $\alpha$ in Equation S3.13c, to visualize their effect on $p(T)$.

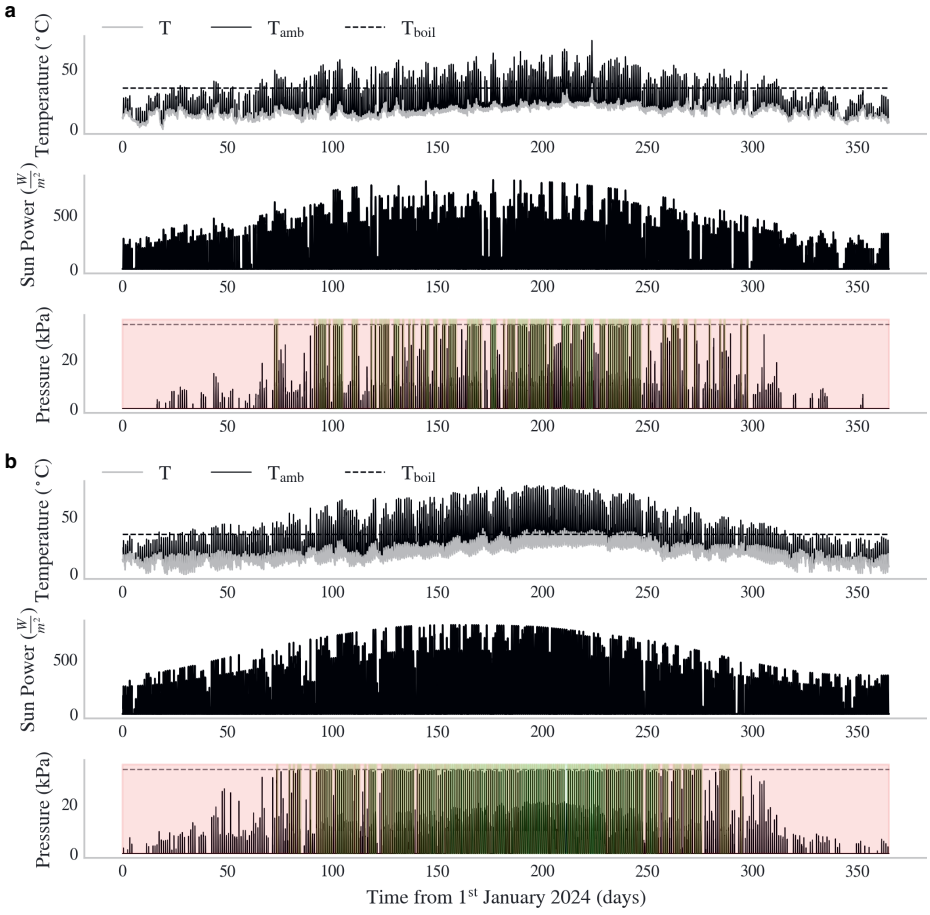


Figure S3.10: **Simulation output examples based on historic weather data at different location.** Example output from the model for the thermopneumatic response of our energy harvesting system throughout 2024. We report temperatures, solar power and pressure for two example cases in **(a)** Toulouse and **(b)** Rome. The dashed line in the pressure plots represents the opening pressure of the pressure relief valve, while the green color represents the occurrence of a firing event, just like in Figure 3.3**c**.

## C: Figures for Methods

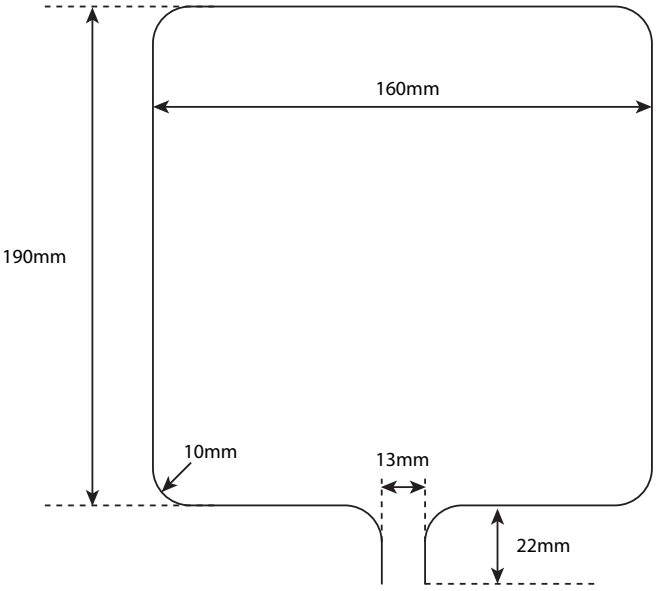


Figure S3.11: **Sketch of the heat-sealed pattern used to obtain the compliant TPU pouch to contain and isolate the LBF.** We use two sheets of Nylon, 70den, TPU-coated one side, 170g/sqm, sealing them at 270°C back to back so that the TPU sides face each other.

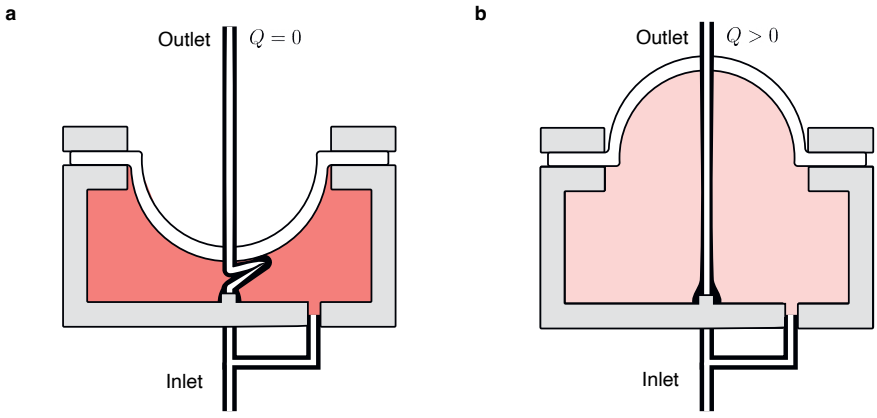


Figure S3.12: **Schematic representation of the working principles of the non-leaky pressure-release valve inspired by [62]. (a)** In the closed state, the silicone tube is kinked by the silicone dome as the air pressure at the inlet is not sufficient to snap the dome out of its stable configuration. **(b)** In the open state, the forces generated by the pressure on the inlet side cause the dome to snap, therefore unkinking the silicone tube and allowing positive air flow.

S3

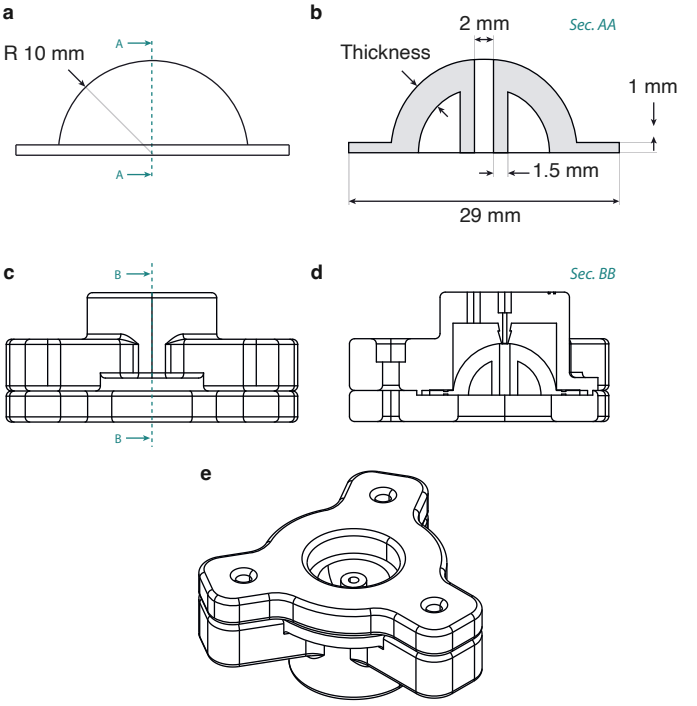


Figure S3.13: **Dimension of silicone dome and holder used to obtain the leakage-free pressure-release valve.** **(a)** Silicone dome size. **(b)** Cross section of silicone dome, highlighting its thickness and sizes of the channel passing through the pole of the dome. **(c)** Side view of the holder. **(d)** Cross-section view of the holder. **(e)** Isometric view of the assembled valve.

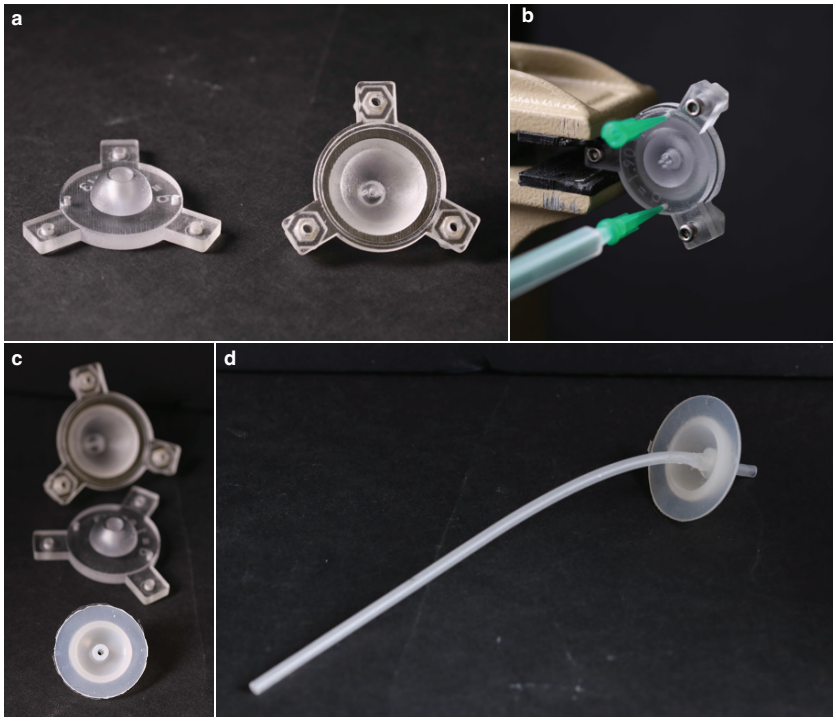


Figure S3.14: **Fabrication of the silicone dome structure used in the custom pressure-release valve.** Through injection molding of silicon, we obtain the dome structure with the parameters as in Figure S3.13. **(a)** Highlight of the top (left) and bottom (right) Veroclear molds used for the injection molding of Dragon Skin® 30 silicone. **(b)** Detail of injection molding process. Injecting silicone while holding the molds in the vertical position facilitates the escape of air bubbles that could compromise the functionality of the valve. **(c)** Veroclear molds and silicone dome after the 16 hours curing time. **(d)** Resulting structure after we slide the silicone tube inside the pole of the silicone dome and use SilPoxy® to seal the connection between the two on the concave side of the silicone dome.

S3

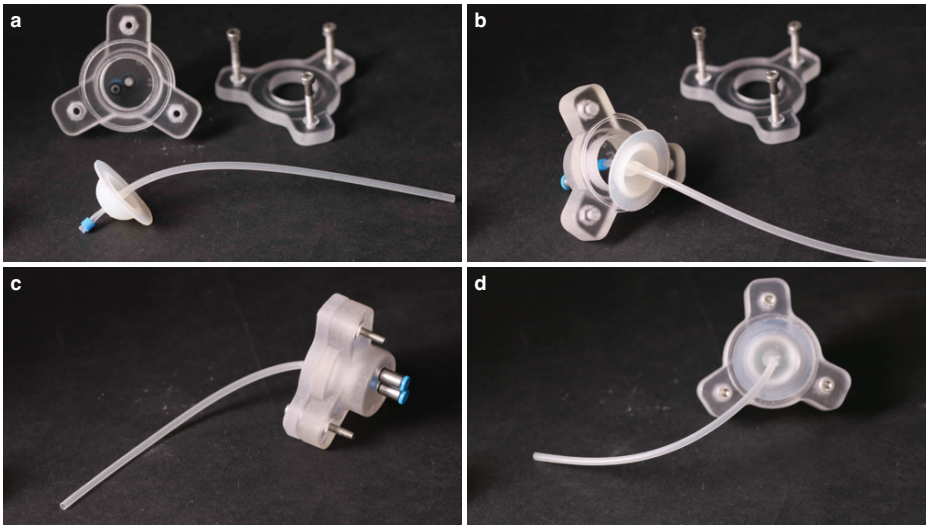


Figure S3.15: **Assembly of the pressure-release valve.** Starting from the component in Figure S3.14**d**, we assemble it using 3D printed holders with parameters as specified in Figure S3.13. **(a)** We place 2mm of FESTO® 4 tube on the end of the silicone tube connected to the bottom holder to guarantee a firm connection between the two. **(b)** We then slide the silicone tube on the bottom holder. **(c-d)** Inlet and outlet view of the assembled pressure-release valve.

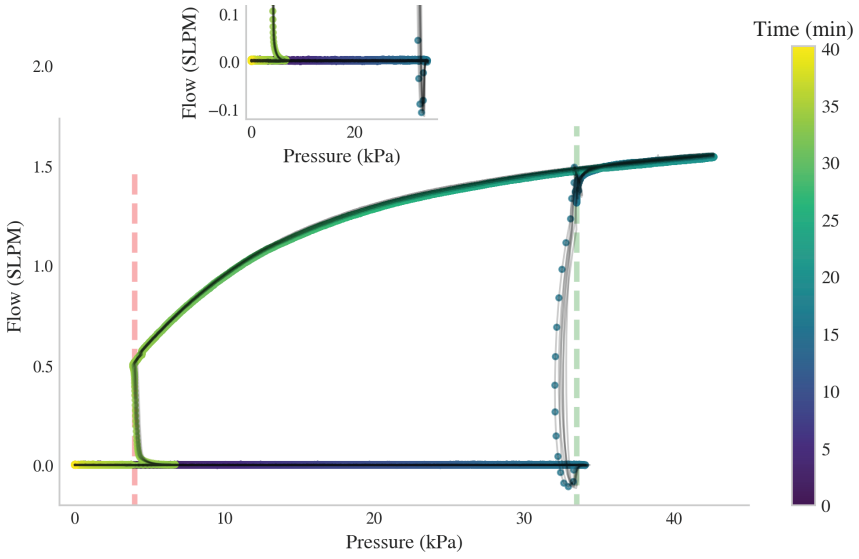


Figure S3.16: **Example data used to validate the presence of leakages in the pressure-release valve.** The black thin lines represent the measured data of the five continuous loops of pressurization and depressurization. The colored scatter plot represents the average of the values reached in the pressure-flow space over the time indicated. The dashed green and red lines represent the opening and closing pressures respectively. This data refers to the pressure-release valve with thickness $t = 1.9$mm used in the experiments in Figures 3.1-3.2-3.4-3.5.

S3

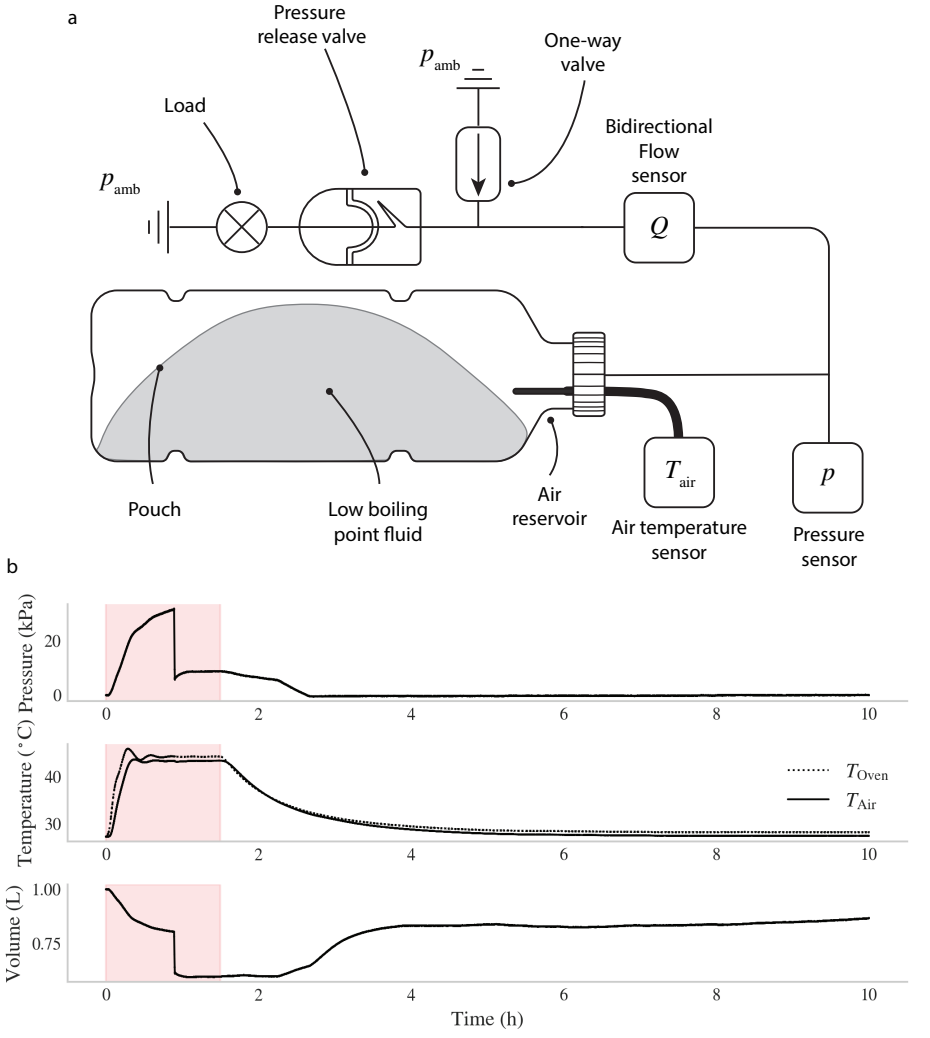


Figure S3.17: **Schematics of assembly for thermopneumatic measurements and example of data output in time**. (**a**) Thermopneumatic circuit with highlighted components and sensors. **(b)** Example of measured pressure and temperature data with inferred volume using Equations 3.4-3.7. We highlight in red the time span during which we regulate the oven temperature to 43°C.

S3

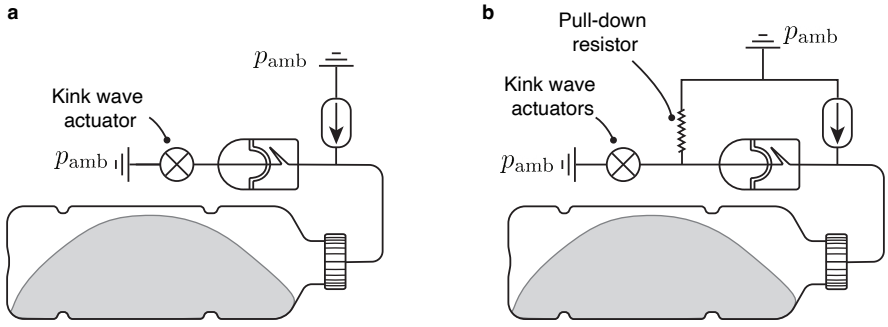


Figure S3.18: **Pneumatic circuits used in the demonstrators. (a)** Pneumatic circuit for the experiment performed outdoor in Figure 3.4. **(b)** Pneumatic circuit for the thermopneumatic walker demonstrator in Figure 3.5.

## D: Description of videos

- **Video 1: Outdoor demonstrator** Video of experimental execution of experiments presented for outdoor motion in Figure 3.4. At 9.15AM June 27$^{th}$ 2024, we brought the system outside the AMOLF building in Amsterdam and then connected it following the schematics in Figure S3.18**a**.

- **Video 2: Indoor locomotion demonstrators in laboratory environment** We assemble two self-oscillating actuators on the thermopneumatic cell as in Figure 3.5**a** and follow the pneumatic connections as in Figure S3.18**b**. To drive the temperature oscillations in our indoor locomotion demonstrators, we use a heat gun regulated at 220°C and progressively bring it closer to the setup to simulate an increase in temperature. In the first part of the video, we report the experimental realization from which the data in Figure 3.5 has been extracted. In the second part of the video, we repeat the indoor locomotion test controlling two consecutive thermopneumatic cycles and showing the potential for repeatability of the thermopneumatic loop for locomotion. After heating the system using the same protocol as in the first locomotion experiment in Figure 3.5, we wait 6 hours to let the system undergo its recharge phase before repeating the same heating procedure.

## E: Table of fluidic setup details

| Reference (Sampling Frequency) | Variable | Details |
|---|---|---|
| Figure 1**c-d** (1kHz) | $p$ | Honeywell® SSCDRRN015PDAA5 |
| | $T_{\text{oven}}$ | LKMelectronic® 224 , PT100 |
| | $T_{\text{air}}$ | LKMelectronic® 224 , PT100 |
| | Flow In | Honeywell® AWM5000-5SLPM |
| | Flow Out | Honeywell® AWM5000-15SLPM |
| | Load | VWR® Luer 22 Gauge Needle |
| Figure S3.4 (100Hz) | $p$ | Honeywell® SSCDRRN015PDAA5 |
| | $T_{\text{oven}}$ | LKMelectronic® 224 , PT100 |
| | $T_{\text{air}}$ | LKMelectronic® 224 , PT100 |
| | Flow In | Honeywell® AWM5000-5SLPM |
| | Flow Out | Honeywell® AWM5000-15SLPM |
| | Load | VWR® Luer 22 Gauge Needle |
| Figure 3.4 | $p$ | FESTO® Analog Pressure gauge |
| Figure 3.5 (50Hz) | $T$ | Flir® I60 |
| | Distance | ArucoTracking |
| | Pull-down Resistor | VWR® Luer 21 Gauge Needle |
| Figure S3.1(1kHz) | $p$ | Honeywell® SSCDRRN015PDAA5 |
| | $T_{\text{oven}}$ | LKMelectronic® 224 , PT100 |
| | $T_{\text{air}}$ | LKMelectronic® 224 , PT100 |
| Figure S3.2 (1kHz) | $p$ | Honeywell® SSCDRRN015PDAA5 |
| | $T_{\text{oven}}$ | LKMelectronic® 224 , PT100 |
| | $T_{\text{air}}$ | LKMelectronic® 224 , PT100 |
| | Flow In | Honeywell® AWM5000-5SLPM |
| | Flow Out | Honeywell® AWM5000-15SLPM |
| | Load | VWR® Luer 22 Gauge Needle |
| Figure S3.5 (1kHz) | $p$ | Honeywell® SSCDRRN015PDAA5 |
| Figure S3.16 (1kHz) | $p$ | NXP® MPX5100DP |
| | Flow | Honeywell® AWM5000-5SLPM |
| Figure S3.17 (1kHz) | $p$ | Honeywell® SSCDRRN015PDAA5 |
| | $T_{\text{oven}}$ | LKMelectronic® 224 , PT100 |
| | $T_{\text{air}}$ | LKMelectronic® 224 , PT100 |
| | Flow In | Honeywell® AWM5000-5SLPM |
| | Flow Out | Honeywell® AWM5000-15SLPM |
| | Load | VWR® Luer 22 Gauge Needle |

Table S3.1: **Details of experimental setup components**

S3

# Chapter 4

# Symmetry Breaking in $N = 2$ Kuramoto-Inspired Oscillators: Excitability and Frustration for Soft Robotic Applications

4


Abstract

The formalism of networked dynamical systems offers an interpretable and adaptable mathematical foundation to study the occurrence of periodic events and obtain predictive power on pattern emergence. This approach has enabled explainable models with the potential to describe phenomena ranging from oscillations in populations of species to animal locomotion, stochastic and secular resonance in planetary orbits. In this work, we explore the interplay of excitability and frustration for emergent spiking patterns in the minimal case study of $N = 2$ oscillators and motivate their relevance in soft robotics and medical applications. By jointly analyzing properties of the oscillators and their coupling, we provide analytical tools to understand and navigate the rich phase portraits that can emerge from this low-dimensionality case. We provide an application example by modeling the behavior of coupled mechanofluidic oscillators. We demonstrate that by informing our model with physics knowledge of the coupling, our framework can be used to model and predict experimentally observed synchronization thresholds in soft robotic systems.


Based on: *Symmetry Breaking in $N = 2$ Kuramoto-Inspired Oscillators: Excitability and Frustration for Soft Robotic Applications*, Sergio Picella, Erik Steur, and Johannes T. B. Overvelde, *in preparation*

## 4.1 Introduction

The mathematical description offered by the seminal work of Hodgkin-Huxley (HH)[164], FitzHugh-Nagumo (FHN) [165], and Hindmarsh-Rose (HR)[166], among the many [167, 168], has proven to be fitting to describe the behavior of biological neurons using the framework of networked dynamical systems. Neurons modeled within this framework can exhibit naturally observed responses, such as *excitable* and *spiking* behavior, depending on the chosen parameters. The excitable of neurons remains at rest until a sufficiently high stimulus is provided, while the spiking includes self-oscillating neurons that autonomously express periodic firing. To achieve this variety of responses while maintaining the same mathematical structure, models such as HH are built on a physical interpretation of biological features in neurons (i.e. electrical resistances, capacitances) in terms of an electrical circuit analogy. This approach then allows a coupled ODE representation of these systems using multidimensional state variables. In some cases, such as in the case of reaction-diffusion phenomena interpreted through the FHN model, it is possible to use the same mathematical description to model different (biological) systems that share similar oscillating behaviors and dynamics. Nevertheless, establishing a direct correlation with measurable and physically observable quantities, which are essential for characterizing the phenomena under investigation, is often not feasible. This limitation is particularly evident in complex systems where the variables of interest are either abstract or not directly quantifiable, thereby posing significant challenges to deriving meaningful conclusions from high-level representations. Moreover, the high number of parameters of these models can make grounding the interpretation of physical parameters in the mathematical formulation a challenging task.

To discuss our contributions, we present the results section in two parts. In the first part, we introduce the model we use for the excitable oscillator and discuss fundamental observations concerning the possible emerging oscillating behavior for this class of oscillators. For our work, we specifically focus on phase oscillators and consider no coupling between the amplitude and the phase of the oscillators. In the second part, we motivate the choice of the frustrated coupling function we use to model the interaction between the oscillators before presenting the numerical and analytical results for the case of $N = 2$ oscillators. We discuss the fundamental ingredients to achieve a given phase difference between the oscillators and provide tools for designing spiking patterns, based on intuitions on the excitability of the oscillators and frustration in their coupling function. In this work, frustration refers to the inability of a system to simultaneously satisfy all local constraints or minimize all competing interactions. The term *frustration* is borrowed from well-established case studies in mathematics and physics and, in the present context, results from the nature of the coupling imposed on the

system.

Ultimately, we report the case study application of our model to the coupling of mechanofluidic oscillators for soft robotics, and discuss the potential of our approach in the context of designing patterns in prosthetic organs.

## 4.2 Model

The motivation for our investigation stems from the possibility of obtaining a higher-level perspective on oscillating networks and pattern emergence in networks of coupled one-dimensional oscillator models. We specifically focus on spiking systems and study a model for phase oscillators based on two key ingredients. First, we use a formulation for *excitable* oscillators proposed by Strogatz and O'Keefee [169]. At the same time, we consider a frustrated coupling function introduced in the Kuramoto-Sakaguchi (KS) while modeling the interaction between oscillators [170]. While this high-level modeling approach does not allow a direct correspondence between parameters and physical quantities, which is typically observed in neuron models, we illustrate its capabilities by examining the phenomenon of pattern formation within a particular instance from the realm of soft robotics. In particular, we demonstrate that our approach can be used to study synchronization in fluidically coupled self-oscillating systems, enabling the quantitative prediction of synchronization patterns and thresholds for phase locking. By delving into this example, we aim to underscore the utility and applicability of this modeling approach, despite its abstract nature. The exploration of such emergent patterns in soft robotics serves as a demonstrator of the method's effectiveness in capturing complex behaviors. Finally, we discuss the broader applicability of our modeling strategy to biological systems of coupled oscillators.

We focus specifically on systems with $N = 2$ oscillators. The motivation for this choice is twofold. On the one hand, the $N = 2$ case is an analytically tractable case study to understand the critical parameters in pattern emergence of coupled excitable oscillators. The low dimensionality allows us to fully grasp the influence of each of the system's parameters on the dynamical system's response. At the same time, as we argue when discussing the role of symmetry breaking for this scenario, several biological systems, such as heart ventricles, do operate as a pair of fluidically coupled, asymmetrical oscillators. A thorough investigation of these minimal networks of oscillators can help elucidate strategies to mimic heartbeat asymmetries and guide the design of robust beating patterns compatible with biological functions. On the other hand, the interest in systems of a large number of oscillators has predominantly a mathematical motivation in the possibility of predicting the long-term dynamics of these systems using a mean-field approach. Although this strategy enables analytical solutions for stable emerging patterns in

the $N \to \infty$ limit [171], this study has limited relevance for physically grounded experiments. When mean-field solutions are studied, it is possible to recover dynamics for finite $N$ with due approximations [172], but the lower the number of oscillators involved, the worse the mean-field approximation holds. Instead, for the $N = 2$ case, it is possible to compute and numerically verify solutions without such approximations.

Furthermore, we demonstrate that the $N = 2$ system exhibits saddle-node bifurcations that can be used to design spiking behavior and indicate the presence of asymmetric spiking patterns when combining frustration and excitability. To the best of our understanding, this particular case study concerning synchronization has not yet been thoroughly examined in existing academic literature.



### Excitable Phase Oscillator

The building block we consider for our analysis is a variation of the phase oscillator studied for the case of large populations of oscillators, among the many, by O'Keeffe and Strogatz [169]. We introduce the parameter $\beta$ to modulate the time evolution of a phase $\theta \in [0, 2\pi)$ of an oscillator with natural frequency $\omega$ following Equation (4.1). We study the case of $\beta \in \mathbb{R}^+$ and $\omega \in \mathbb{R}^+$

$$\dot{\theta} = \omega + \beta \cos(\theta) \tag{4.1}$$

We arbitrarily define the phase $\theta = 0$ as a *firing state* and, depending on the values of $\beta$, obtain excitable and spiking behavior from this one-dimensional system.

For our investigation, we introduce the response of the system in Equation (4.1) to input signal

$$s_{t_1,t_2}(t) = s_0[H(t - t_1) - H(t - t_2)] \tag{4.2}$$

with $H(t)$ Heaviside step function. Through this choice, we tune different magnitudes of input stimuli by adding a $s_{t_1,t_2}$ to Equation (4.1). As a result, we obtain

$$\dot{\theta} = \omega + \beta \cos(\theta) + s_{t_1,t_2} \tag{4.3}$$

In Figure 4.1**a**, we schematically represent the behavior of this excitable phase oscillator, and report numerical simulations for different values of $\beta$ in Figure 4.1**b-e**, as we sweep $\beta \in \{0\omega, 0.7\omega, 0.9\omega, 1.1\omega\}$. We show the results for increasing intensities $s_0 \in \{0.1\omega, 0.5\omega, \omega\}$ in Figure 4.1**b-e**, for different time windows as in as in Figure 4.1**f**.

The $\beta$ excitability parameter breaks the rotational symmetry of the system as $\dot{\theta}(\theta \to 0) > \dot{\theta}(\theta \to \pi)$ and so that it affects the value of equilibrium configurations. By imposing $\dot{\theta} = 0$, in the $s_0 = 0$ case (Equation (4.1)), we observe that a steady state $\theta^{\text{eq}}$ can be achieved only if $\frac{\omega}{\beta} < 1$. Under this condition, equilibria of

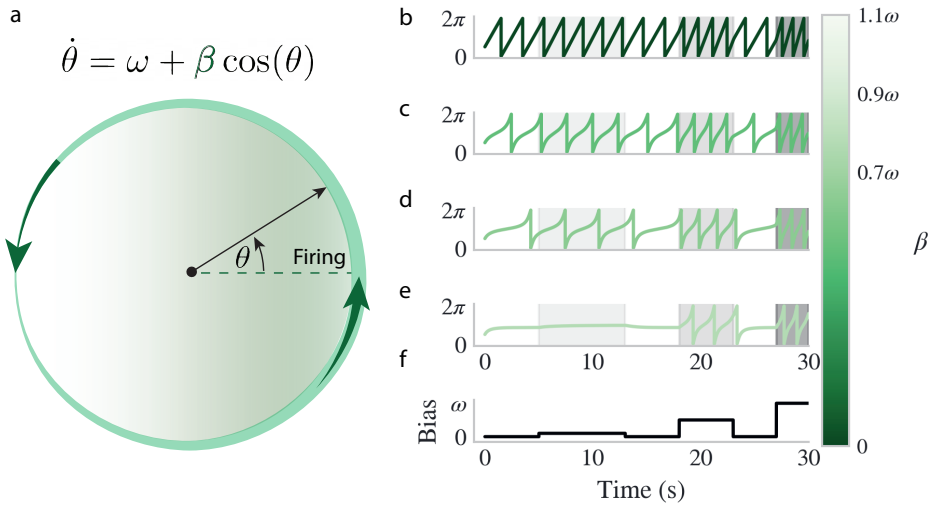


Figure 4.1: **Behavior of an excitable phase oscillator. (a)** We define a firing threshold at $\theta = 0$. The value of $\beta$ affects the oscillator dynamics so that it manifests increases of $\dot{\theta}$ close to the firing threshold and slows down when the phase is opposite to it, as we represent with the green arrows. **(b)-(e)** Behavior in time for excitable phase oscillators sharing the same $\omega$ and with increasing values of $\beta \in [0, 0.7\omega, 0.9\omega, 1.1\omega]$, respectively. **b-c** can represent self-oscillating systems. **e** is an excitable oscillator. **(f)** Intensity of bias input $s(t)$ (Equation (4.2)) used to study the response of the phase oscillators in time for different time windows.

Equation (4.1) exists at $\theta^{\text{eq}}_{\pm} = \pm\arccos\left(-\frac{\omega}{\beta}\right)$, and their stability can be assessed by studying the sign of $d\dot{\theta}/d\theta = -\beta\sin(\theta)$. For $0 < \omega/\beta \leq 1$, one asymptotically stable $\theta^{\text{eq}}_{+} \in (\frac{\pi}{2}, \pi)$ and one unstable equilibria $\theta^{\text{eq}}_{-} \in (\pi, \frac{3}{2}\pi)$ emerge. When the system is attracted to the $\theta^{\text{eq}}_{+}$ coordinate, the oscillator has quiescent behavior if not subjected to an external signal, otherwise, it can manifest asymmetric self-oscillating behavior. If $s_0 \neq 0$ (Equation (4.3)), following a similar procedure, we recover the trivial case of no $\theta^{\text{eq}}$ when $\beta = 0$, as well as a threshold for the magnitude of the stimulus to obtain spiking behavior from an excitable oscillator when there is no $\theta^{\text{eq}}$, namely when $|\frac{\omega+s_0}{\beta}| > 1$. This critical value then sets the threshold for the saddle-node bifurcation on invariant circle (SNIC) [173] to occur in our case study.

For higher values of $\frac{\omega}{\beta}$ (Figure 4.1**a-d**), the system is self-oscillating and we observe only an increase of firing frequency upon the presence of the bias current.

However, when looking at the excitable case in Figure 4.1**e**, we observe that the system has a response in time similar to that of an *integrate-and-fire* neuron. If $s_0$ is not sufficiently large, when the system is perturbed outside of its equilibrium configuration $\theta^{\text{eq}}$, it settles to a new equilibrium value. It recovers its $\theta^{\text{eq}}$ when the bias is removed. Conversely, for increasingly stronger $s_0$, the spiking behavior is recovered, and the magnitude of the bias term mostly dominates the spiking frequency. On top of that, there is an interplay between the amplitude of the input signal $s_0$ and the duration of the stimulus to bring the system to the self-oscillating behavior, which also depends on the phase $\theta$. Nevertheless, as we focus on emerging patterns after equilibration has been achieved, we do not investigate this aspect further.



**Relevance of Excitable Oscillators for (Soft) Robotics** Besides their widespread use for modeling neurons in mathematical neuroscience, excitable oscillators have been recently investigated in very different contexts to simulate the behavior of relaxation oscillators. For example, components based on mechanical non-linearities, such as pressure release valves, exhibit periodic oscillatory behavior under constant input flow. Such devices can release air to reduce internal pressure whenever a critical opening pressure value is reached, therefore operating as a hysteretic, variable fluidic resistance. Based on these and similar principles, soft hysteretic valves in soft robotics [69] undergo snap-through instabilities to convert constant inputs to pulsatile outputs of air flows, pneumatic ring oscillators network [174], and relaxation oscillators [175]. The common ingredients for the emergence of oscillatory patterns across diverse systems have been discussed extensively [176] and can be justified by studying the phase portrait representation of the system under investigation. These integrate-and-fire systems have also been studied in the context of coupled oscillators starting from the work of Kuramoto [177]. The oscillation in time of their characteristic state variable often has a slow time scale for building up, e.g., pressure, with a faster time scale during the *firing* state that, in these systems, corresponds to the fast release of air pressure.

At the same time, the discussion about the effect of timed inputs is of utmost importance when studying emerging patterns, not only when these inputs are externally provided from the environment, but also when designing the coupling between excitable oscillators. As an example for the first case, we mention the possibility to trigger excitable oscillators when developing, e.g., a pneumatic circuit for sequenced actuation [178] or a network of electronics-free circuits that respond to external stimuli [150]. External stimuli can be used, e.g., to trigger sequences or patterns of actuation upon proprioception of interaction of the system with its environment, even without using electronics to sense or control such actuation patterns. Interestingly enough, van der Pol performed studies using his set of equations for modeling relaxation oscillators and pattern formation

in the heartbeat [179]. We will refer to this case study while discussing how to implement spiking asymmetry in coupled excitable oscillators.

The nature of the coupling function to model the interaction between excitable oscillators (e.g., odd or even, periodic, non-linear, ...) is a crucial ingredient to prevent or guarantee the emergence of certain oscillating patterns [180].

### Frustration

Coupling between oscillators is a key ingredient for understanding pattern formations across spatial and temporal scales greater than those of the individual oscillator. Examples in this context range from biological periodic events like the swallowing reflex [181] to the Josephson effect in superconductors [182]. Without coupling, the spiking pattern of an oscillator is fully determined by its initialization, so it cannot be considered robust from a dynamical system point of view.



We introduce a sinusoidal coupling with a frustration term, presented in the 1986 paper of Kuramoto-Sakaguchi [183] for the coupling of our excitable oscillators. From a higher-level perspective, frustration occurs whenever competing coupling constraints, such as antiferromagnetic bonds on a ring network with an odd number of nodes, cannot all be simultaneously satisfied. This combined effect of topology and antiferromagnetic coupling yields degenerate static ground states or dynamical behaviors. We consider a system of $N$ oscillators on an undirected and unweighted graph with an $N \times N$ adjacency matrix $A$. The state of the coupled system is expressed in terms of a phase vector in terms of $\boldsymbol{\theta} = (\theta_1, \theta_2, \ldots, \theta_N)^T \in [0, 2\pi)^N$. We assume that each oscillator has a natural frequency $\boldsymbol{\omega} = (\omega_1, \omega_2, \ldots, \omega_N)^T \in \mathbb{R}^N$, so that the networked dynamical systems we study are described by Equation (4.4)

$$\dot{\theta}_i = \omega_i + \beta \cos(\theta_i) + \frac{K}{\mathcal{N}_i} \sum_{j=1,\, i \neq j}^{N} a_{ij} \sin(\theta_j - \theta_i - \alpha), \quad i \in [1, \ldots, N] \tag{4.4}$$

where we define $K$ coupling strength, and we use the notation $\mathcal{N}_i$ to denote the degree of the $i$-th oscillator in the network. As we investigate undirected graphs, we focus on symmetric interactions only, so that the adjacency matrix describing the topology of the network $A = (a_{ij})$ is symmetric. We consider exclusively cases where $a_{ij} = 0$ and $a_{ij} = 1$ when the i-th and j-th oscillators are not coupled and coupled, respectively. As for the coupling between the oscillators, we use the same expression suggested in the KS formulation by introducing a constant in time frustration parameter $\alpha \in [0, 2\pi)$, and excitability $\beta$.

### Central Pattern Generators (CPG) and KS model

The framework of networked dynamical systems has proven to be a valuable asset for modeling the pattern emergence in, e.g., animal locomotion [184, 185] and lies at the foundation of controllers for adaptive locomotion gaits [186]. The complexity of this approach can range from modeling each oscillator as a leaky integrate-and-fire neuron [187] to using a network of KS oscillators [188]. This last case has been thoroughly investigated in recent years [189] and shares the same mathematical formulation as the one presented in Equation (4.4) with $\beta = 0$. For application purposes, in the CPG formulation, an additional variable is used to represent the amplitude of the oscillator, using a leaky integrate-and-fire-like equation [187].

For CPGs, it is usually the case that $\alpha = 0$ or $\alpha = \pi$ is used by default [190] as it only accounts for positive and negative coupling and is globally simpler to treat and interpret. Instead, we focus on exploring different values of $\alpha$ and their interpretation in the context of physical systems, and discuss their relevance, as we illustrate through the soft robotic example in the next section. Furthermore, we demonstrate that introducing the excitability can allow the emergence of multiple critical points of the dynamical system in Equation (4.4) even for $N = 2$, so that low-dimensional systems can still manifest complex behavior. The analysis we perform helps navigate the parameter space to obtain robust spiking patterns in reduced-dimensionality systems.

Moreover, for the CPG formulation, in the presence of proprioception in the mechanical domain of, e.g., an actuator making contact with the ground, information about the interaction with the environment feeds back into the equations governing the dynamical system. This proprioceptive feedback affects the phase evolution of the system of oscillator, similarly to the way we introduced the $s$ input stimulus while studying the case in Figure 4.1. Recent works focusing on the role of feedback to instantiate locomotion gaits would suggest that, in the case of biped locomotion, locomotion gaits might be driven by sensory feedback and reflexes, rather than controlled by CPG-like networks [191, 192].

Steering pattern formation towards a certain spiking sequence becomes a complex task when networks of $N \geq 3$ oscillators are considered, so that numerical (gradient descent [193], harmonic balance methods [194]) and heuristic (reinforcement learning [195], genetic algorithms [196]) methods often required to tackle the design complexity. From a theoretical point of view, finding the most fitting topology and network parameters for a given reward function turns out to be an NP hard problem [197]. Therefore, it is often the case that these systems are solved in the $N \to \infty$ limit [198], as this method allows, up to some extent, analytically tractable solutions. Alternatively, pattern emergence and stability can be computed in some particular cases, i.e. $(\alpha, \beta) = (0, 0)$ using a Hamiltonian approach [199].

### 4.2.1 Results

### 4.2.2 $N = 2$ coupled oscillators

We now consider the system in Equation (4.5)

$$\begin{cases} \dot{\theta}_1 = \omega_1 + \beta\cos(\theta_1) + K\sin(\theta_2 - \theta_1 - \alpha) \\ \dot{\theta}_2 = \omega_2 + \beta\cos(\theta_2) + K\sin(\theta_1 - \theta_2 - \alpha) \end{cases} \tag{4.5}$$

To study under which conditions the system can reach steady state equilibrium, we introduce the difference in phases and natural frequencies with $\Delta\theta = \theta_1 - \theta_2$ and $\Delta\omega = \omega_1 - \omega_2$ and study the case in Equation (4.6).

$$\dot{\Delta\theta} = \Delta\omega + \beta\big(\cos(\theta_1) - \cos(\theta_2)\big) + 2K\,\sin(\Delta\theta)\,\cos(\alpha) \tag{4.6}$$

Following arguments from Strogatz and O'Keefee [169], in the case for $\alpha = 0$, $\beta \neq 0$, the system is expected to manifest multiple behaviors, spiking and excitable ones, for the same setting of parameters, depending on the initial condition. To understand what are the minimal requirements for spiking behavior in this system, we solve for $\dot{\Delta\theta} = 0$ (phase locking) in Equation (4.6). In Equation (S4.4) and Equation (S4.6), we find the analytical solutions for equilibria of $\dot{\Delta\theta} = 0$ for the cases of $\Delta\omega = 0$ and $\Delta\omega \neq 0$, respectively. However, through this approach, for the case of $\beta \neq 0$, only non-oscillating states can be found in dependence of $\alpha$, $\beta$, and $\Delta\omega$, while it is less straightforward to determine emerging spiking patterns from firing events in the two oscillators.

We perform a numerical investigation and report our results in Figure 4.2, where we show typical trajectories of $\boldsymbol{\theta} = \begin{pmatrix} \theta_1 \\ \theta_2 \end{pmatrix}$ and $\Delta\theta = \theta_1 - \theta_2$ in time for different $(\alpha, \beta)$. In Figure 4.4, we approach pattern emergence from an analytical point of view by studying the possible $\boldsymbol{\theta}$ trajectories in the phase space.

In cases where the parameter $\beta$ equals zero and the parameter $\alpha$ does not is far from the value $\frac{k\pi}{2}$, with $k \in \{1, 3\}$, the system exhibits harmonic oscillations. Conversely, in all other circumstances, the oscillations are non-harmonic, occurring when the oscillators achieve the firing threshold. When $\alpha = \frac{k\pi}{2}$ instead, the coupling terms in the single oscillator dynamics can be expressed in terms of cosine. The presence of this even coupling function for $\alpha = \frac{k\pi}{2}$ makes the coupling terms equal, so that the effect of coupling in Equation (4.6) is null. Nevertheless, when studying the dynamics of the individual oscillators (Equation (4.2)), the coupling terms contribute with a common bias input in $\dot{\boldsymbol{\theta}}$ equations. We have numerically observed that this behavior persists when studying the response of the system for $\alpha \approx \frac{k\pi}{2}$.

We qualitatively show the $\boldsymbol{\theta}$ in time in Figure 4.2 through a few examples of

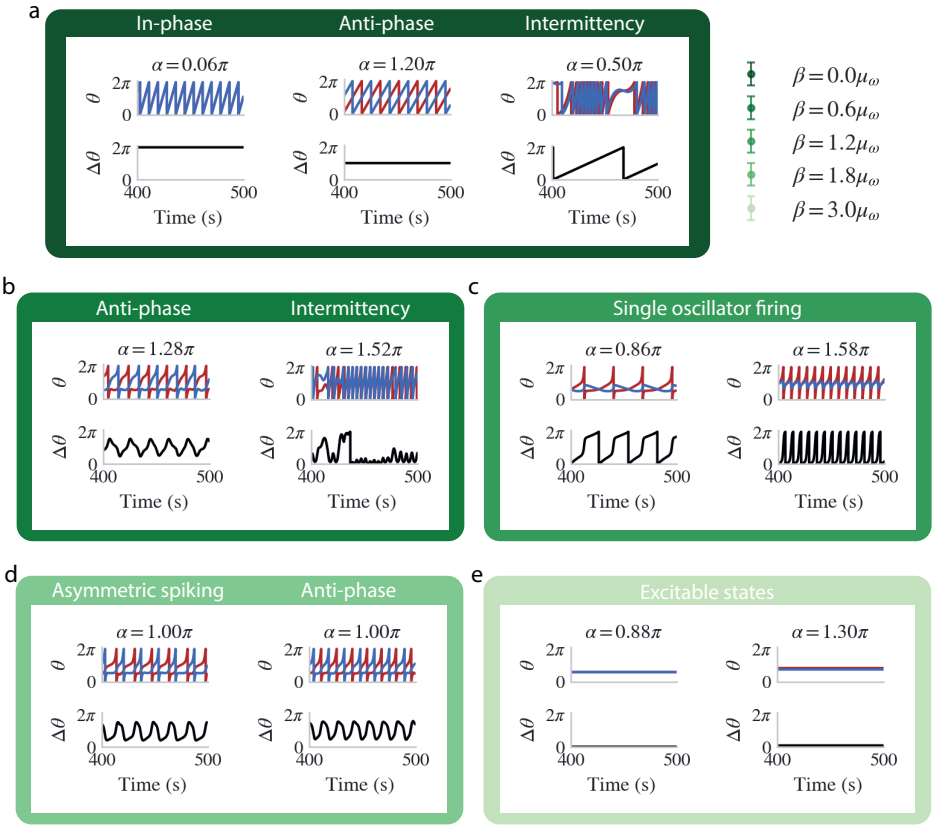


Figure 4.2: **Simulations for $N = 2$ oscillators as in Equation** (4.5) for different values of $(\alpha, \beta)$. **(a)** Coupled phase oscillator with constant natural frequency ($\beta = 0$) in-phase (left), anti-phase (center), and non-harmonic (right) spiking behavior. **(b)** Example of different non-harmonic spiking patterns for $\beta = 0.6\mu_{\omega}$. **(c)** Single oscillator firing behavior for $\beta = 1.2\mu_{\omega}$. **(d)** Phase locking of asymmetric and anti-phase synchronized states, for the same $\alpha$ value but different initial conditions and natural frequencies for $\beta = 1.8\mu_{\omega}$. **(e)** When $\beta = 3\mu_{\omega}$, oscillations are mostly suppressed and the two oscillator equilibrate at a quiescent, stable state.

trajectories for different values of $(\alpha, \beta)$, and quickly discuss the main observations in the emergent trajectories before introducing a metric to study spiking asymmetries in our system. For the remainder of our work, we use $\mathcal{U}[a, b)$ to

represent a uniform distribution supported on $[a, b)$, and $\mathcal{N}(a, b)$ to refer to a normal distribution with mean $a$ and variance $b$. For our simulations, we used random initial conditions $\boldsymbol{\theta} \in \mathcal{U}[0, 2\pi) \times \mathcal{U}[0, 2\pi)$, $\boldsymbol{\omega} \in \mathcal{N}(\mu_\omega, \sigma_\omega) \times \mathcal{N}(\mu_\omega, \sigma_\omega)$, with $(\mu_\omega, \sigma_{\boldsymbol{\omega}}) = (1, 0.05)\frac{2\pi}{s}$, where we use the notation $\mathcal{U}$ and $\mathcal{N}$ to refer to uniform and normal distributions. We provide further examples of trajectories of $\boldsymbol{\theta}$ and $\Delta\theta$ in Figure S4.2. Following our definition, e.g., the patterns in Figure 4.2**a** for $\alpha = 0.06\pi$ and $\alpha = 1.20\pi$ are phase-locked, symmetric spiking states, in phase and anti-phase, respectively. When observing the pattern in Figure 4.2**b** for $\alpha = 1.28\pi$, we observe a symmetric, anti-phase, non-phase-locked state with no frequency locking, as we can observe from the $\Delta\theta$ plot.

Similarly to what we observed in Figure 4.1, as values of $\frac{\mu_{\boldsymbol{\omega}}}{\beta}$ increase, the asymmetries in the evolution of the phase in time become more and more pronounced (Figure 4.2**d**), up to the point where for $\frac{\mu_{\boldsymbol{\omega}}}{\beta} > 0.5$, we observe that the system is non-oscillating mainly (Figure 4.2**e**). By studying stationary states $\dot{\Delta\theta} = 0$, we observe that, in the case of $\beta = 0$, $\Delta\theta^{\text{eq}} = \pm \arcsin\left(\frac{\Delta\omega}{2K\cos(\alpha)}\right)$. As a result, in this particular case, $\Delta\theta^{\text{eq}}$ is not defined if $\alpha = \frac{\pi}{2}$ and $\alpha = \frac{3}{2}\pi$, leading to non-harmonic oscillations such as the ones we report in Figure 4.2**a**. When $\alpha = \frac{\pi}{2}$ and $\alpha = \frac{3}{2}\pi$, the coupling term nullifies in Equation (4.6), so that

$$\dot{\Delta\theta} = \Delta\omega + \beta\big(\cos(\theta_1) - \cos(\theta_2)\big) \tag{4.7}$$

As a consequence, $\Delta\theta$ has a non-zero drift that accumulates, similarly to scenarios observed in Type I intermittency by Pomeau–Manneville [200], when the system approaches a saddle-node bifurcation. Through additional numerical integration of the system in Equation (4.5) that we report in Figure S4.2, we confirm that non-harmonic trajectories of $\Delta\theta$ emerge when $\alpha \simeq \pi/2$ and $\alpha \simeq 3\pi/2$ also for $\beta \neq 0$, such as in the case we report in Figure 4.2**b**. These trajectories exhibit behavior with spiking patterns that oscillate with sweeping, varying frequencies over time. Interestingly enough, we observe that asymmetric spiking patterns can emerge, for particular initial conditions and $(\alpha, \beta)$ parameters, as we show in Figure 4.2**d**. We further address this case in the following section.

Conversely, as $\frac{\beta}{\omega}$ increases to values greater than one, we observe mostly suppressed oscillations and stationary behavior, as in Figure 4.2**e**.

It is interesting to point out that spiking of the oscillators can emerge even in the case of $\frac{\mu_{\boldsymbol{\omega}}}{\beta} < 1$, differently from what we observed when studying the individual oscillator (Figure 4.2**c-d**). This is since, similarly to what we have discussed in the case of the $s$ input signal in Figure 4.1, the coupling between the oscillators now operates as an amplitude-modulated input signal in Equation (4.6). For the remainder of our work, we particularly focus on differences in time between firing events to define an asymmetry in spiking patterns. In particular, we use the term *symmetric* spiking to refer to spiking configurations where both

oscillators reach the firing threshold either at the same time (in-phase) or at half-period of the opposite oscillator (anti-phase). With the term *asymmetric* spiking instead, we refer to all other configurations in which the firing threshold is achieved by both oscillators that are non-spiking symmetric. Therefore, our metrics are based on the asymmetry in firing times, rather than phase or frequency locking. Note that the definitions we introduced are independent of definitions of phase locking or phase-resetting (introduced by Izhikevich-Kuramoto [201], as the presence of $\beta \neq 0$ breaks rotational symmetry. Nevertheless, forward integration cannot inform us with any analytically grounded motivation for the emergence of spiking patterns, nor tools to measure and design spiking asymmetry. Therefore, we introduce a different metric to study the distribution of firing events in this $N = 2$ case study and their asymmetry.



### 4.2.3 Towards spiking asymmetries

As we show in Figure 4.2**d**, we observe that asymmetric spiking patterns can seldom emerge when combining non-zero values of $\alpha$ and $\beta$. However, the methodology employed to establish asymmetrical spiking behavior is contingent upon both the disparities in the intrinsic frequencies of the oscillators and the distinct initial conditions of the system. Consequently, this method is demonstrated to be an unreliable means of generating such asymmetric spiking patterns due to its dependence on these specific factors. We now introduce the metric we use to quantify the spiking asymmetries, and then provide an overview of the relevance of such asymmetric patterns both in the context of biological oscillators and soft robotics.

#### Quantifying spiking asymmetries

We introduce the *percentual circular mean asymmetry* $A$ and its standard deviation $\sigma$ [202] to statistically quantify these asymmetries in spiking patterns. We use these quantities to measure the differences in time between the firing events of the two oscillators relative to each other. To do so, we use one of the oscillators' phases and period to define a *spiking phase asymmetry*, based on the spiking time of the second oscillator compared to the period of oscillation of the first one.

We simulate the system in Equation (4.5) and, for each of the runs, we consider the last half of the simulation time and define the vectors $\boldsymbol{t}_{f1,2}$, timestamps at which a firing event occurs in two oscillators. We consider contiguous time stamps of firing events, compute their mean average, and divide by the $T_1$ period of oscillator 1 to obtain the vector $\boldsymbol{\rho}$ defined as:

$$\boldsymbol{\rho} = 2\pi \cdot \frac{\boldsymbol{t}_{f1} - \boldsymbol{t}_{f2}}{T_1} \tag{4.8}$$

We use $\boldsymbol{\rho}$ to determine a circular mean asymmetry and standard deviation in our case study. This is necessary to avoid the circular data wrapping problem when considering the angular distance of points lying, e.g., at $0^+$ rad and $0^-$ rad positions on the unit circle.

To define the circular mean asymmetry $A$ and its standard deviation $\sigma$, we introduce

$$\begin{cases} \bar{c} =< \cos(\boldsymbol{\rho}) > \\ \bar{s} =< \sin(\boldsymbol{\rho}) > \end{cases} \implies \begin{aligned} A &= \frac{100\%}{2\pi} \cdot \arctan\left(\frac{\bar{s}}{\bar{c}}\right) \\ \sigma &= \sqrt{-2\ln\left(\sqrt{\bar{c}^2 + \bar{s}^2}\right)} \end{aligned} \tag{4.9}$$

By construction, $A$ values close to 0% and 100% indicate almost perfect, in-phase synchrony, while a value of 50% indicates $\Delta\phi = \pi$, namely anti-phase. These states can also be phase-locked when $\beta = 0$. At the same time, we ensure that this quantity is defined exclusively for configurations that return spiking behavior in both oscillators.

We study the influence on dispersion of natural frequencies $\boldsymbol{\omega}$ by scanning different ratios between dispersion over the mean value of natural frequencies $\sigma_{\boldsymbol{\omega}}/\mu_{\boldsymbol{\omega}}$. For our analysis, we explore values of $\sigma_{\boldsymbol{\omega}}/\mu_{\boldsymbol{\omega}} \in [0, 0.05, 0.10, 0.20]$. For this numerical experiment, we run the system in Equation (4.5) with $\boldsymbol{\omega}$ drawn randomly from a normal distribution $\mathcal{N}(\mu_{\boldsymbol{\omega}}, \sigma_{\boldsymbol{\omega}}) \times \mathcal{N}(\mu_{\boldsymbol{\omega}}, \sigma_{\boldsymbol{\omega}})$, using $(\mu_{\boldsymbol{\omega}}, \sigma_{\boldsymbol{\mu}}) = (1, 0.05)\frac{2\pi}{s}$, $\boldsymbol{\theta}$ drawn randomly from a uniform distribution $\mathcal{U}[0, 2\pi) \times \mathcal{U}[0, 2\pi)$, and with $K = \mu_{\boldsymbol{\omega}}$. We perform 500 runs per set of $(\alpha, \beta)$ and let the system run for 500s. For each run, we consider only the results from the last half of the simulation to allow the system to equilibrate to its steady state.

In Figure 4.3, we report the spiking asymmetries for the system in Equation (4.5). For $N = 2$, non-symmetrical patterns emerge mainly as a consequence of inhomogeneities in natural frequencies of the oscillators that we quantify in terms of the ratio between standard deviation and mean value in the distribution of the $\boldsymbol{\omega}$, rather than from specific combination of $(\alpha, \beta)$. This case is highlighted in the second column of Figure 4.3, where we report with a red square the configuration that we observed in Figure 4.2**d** for which we obtained, only sporadically, asymmetric spiking behavior.

Such a result is to be expected as the system in Equation (4.5) is symmetric for swaps of $\theta_1$ and $\theta_2$. This also means that Equation (4.5) can sustain only symmetric spiking behavior, when the mean asymmetry $A$ is either 0% (w.l.o.g. 100%, given the definition in Equation (4.9)) or 50%. Deviations from this intuition are more evident for increasing values of $\sigma_{\boldsymbol{\omega}}/\mu_{\boldsymbol{\omega}}$. This is mainly because increasing $\sigma_{\boldsymbol{\omega}}/\mu_{\boldsymbol{\omega}}$ values can, on a single realization of the experiment, partially break the symmetry in Equation (4.5). Nevertheless, on average, we observe that

only the phase-locked in-phase and anti-phase behavior is supported.

However, these spiking asymmetries are intrinsically bound to the specific initial conditions and dispersions in natural frequencies, rather robustly occurring as a result of the networked system's properties. To obtain spiking asymmetry, the system of equations in Equation (4.5) must also break the symmetry between $\theta_1$ and $\theta_2$.

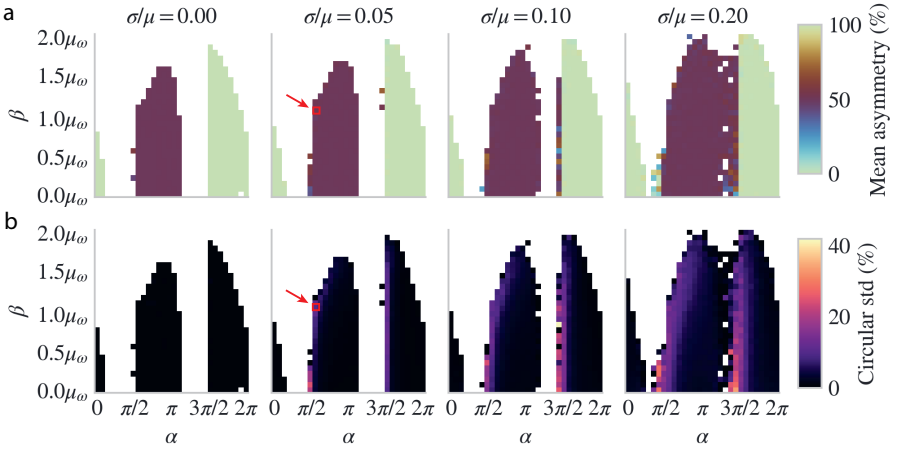


Figure 4.3: **Statistical study of spiking phase asymmetry for system of two oscillators as in Equation (4.5) for different combinations of $(\alpha, \beta)$ and $\frac{\sigma_\omega}{\mu_\omega}$.** We perform 500 runs per configuration of $(\alpha, \beta)$ and $\sigma_\omega/\mu_\omega$ and perform our investigation on the last half of the simulation time $T = 500$s, using $\mu_\omega = \frac{2\pi}{s}$. **(a)** Percentual circular mean asymmetry $A$ (Equation (4.9)). Values of 50% indicate anti-phase spiking behavior of the two oscillators. Values close to 0% and 100% refer to configurations in which the spiking pattern is closer to a fully in-phase behavior. **(b)** $\sigma$, standard deviation of $A$, for the corresponding configurations on the top row. We highlight the configuration in Figure 4.2**d** with the red square in the second column, where we measured $\sigma = 10\%$. Given the definition of $A$ and $\sigma$, we only show data for the case in which both oscillators reach the firing threshold.

### Relevance of asymmetric spiking patterns

In the context of locomotion gaits (e.g., walk and gallop [203]) or prosthetic organs (e.g., left and right ventricular asymmetry in the heart [204]) that aim to mimic the asymmetric, pulsating behavior of muscles, spiking asymmetries in oscillators are often observed. In the case of the human heart, the two ventricles themselves

are mechanically coupled, non-identical pumps that operate under different loads, as they serve different biological purposes. Cardiac asymmetry in systolic and diastolic function reflects the distinct roles of the ventricles. The left ventricle generates higher pressures for systemic circulation. In contrast, the thinner-walled right ventricle supports the lower-pressure pulmonary circuit, resulting in variations in contraction timing and force [205]. In a healthy adult heart, the delay between the firing of $\sim 40$ms in a period of $\sim 800$ms at rest typically corresponds to a spiking asymmetry of $\sim 5\%$, which, in principle, can be achieved by considering non-identical oscillators (with different natural frequencies) [206]. Deviations from this low spiking asymmetry are indicators of cardiac disease and failure. These intuitions can become a valuable asset to guide and inform the design of artificial heart prosthetic systems and artificial organs in general that are capable to reproduce robust, asymmetric oscillatory patterns.

To study these spiking asymmetries, we perform a statistical analysis on the system in Equation (4.5) and focus specifically on $(\alpha, \beta)$ combinations that yield spiking behavior in both oscillators.



### 4.2.4 Frustration mismatch for asymmetric spiking behavior

In Equation (4.10), we introduce a variation on Equation (4.5) to obtain asymmetric spiking behavior in excitable KS systems by considering non-identical frustration for the two oscillators. Spiking asymmetries can equivalently be introduced by using inhomogeneity on the $\beta$, but we rather focus on the role of frustration asymmetries alone to induce asymmetric spiking patterns. This choice is motivated by the fact that differences in loads after the individual spiking oscillators can cause asymmetries in the relative phase offsets supported by the coupling function, which we interpret through frustration. To materialize this idea into the dynamical system, we consider non-uniform $\alpha$, rather than in the $\beta$. Through this choice, the behavior of the two oscillators in isolation remains unaltered, and we can study the effect of the coupling and the influence of the frustrations alone. Through analytical observations and numerical experiments, we demonstrate that the breaking of frustration symmetry, together with the presence of the excitability parameter, can shape the resulting spiking pattern and determine spiking asymmetries in the system. Note that, unlike Equation (4.5), we now allow for non-identical frustration terms.

$$\begin{cases} \dot{\theta}_1 = \omega_1 + \beta\cos(\theta_1) + K\sin(\theta_2 - \theta_1 - \alpha_1) \\ \dot{\theta}_2 = \omega_2 + \beta\cos(\theta_2) + K\sin(\theta_1 - \theta_2 - \alpha_2) \end{cases} \tag{4.10}$$

### Phase portrait representation

To gain analytical insights on the minimal conditions required for obtaining spiking behavior, we study the phase portrait representation of the system in Equation (4.10). We demonstrate that this analysis provides geometrical intuitions on how the different parameters in the dynamical system can guarantee or prevent oscillatory patterns. For this analysis, we start by studying the nullclines for Equation (4.10). As we know that the system always manifests spiking behavior when $\beta = 0$, we particularly focus on cases with $\beta > 0$.

We observe that the nullcline profiles live on a $\mathbb{T}^2$ space and enclose ellipsoid-like areas as we show in Figure 4.4, where we trace with dashed red and blue lines the nullclines for $\dot{\theta}_1$ and $\dot{\theta}_2$, respectively. This representation suggests that, if there is no intersection between the nullclines, the system does not have equilibria, thus it never reaches an asymptotically stable state and it manifests spiking behavior, as in Figure 4.4**a**. When the nullclines intersect, up to four critical points can emerge, and their nature can be determined by studying the eigenvalues of the Jacobian matrix of the system. For this analysis, we only report results when the stability analysis test is not inconclusive. As a result of this analysis, we observe that the critical point in the dynamical system in Equation (4.10) can be asymptotically stable nodes (filled squares), unstable nodes (empty squares), asymptotically stable spirals (filled circles), unstable spirals (empty squares), or saddle points (crosses), depending on the specific choice of $(\beta, \alpha_1, \alpha_2)$.

In general, when the nullclines are secant, we always observe the emergence of a saddle node and of another critical point, of which the nature can vary in dependence on the specific parameters of the dynamical system. Therefore, the system in Equation (4.10) manifests saddle node bifurcation on an invariant torus. In the presence of unstable critical points, the system in Equation (4.10) manifests spiking patterns in cases such as the ones in Figure 4.4**b-d** where there are two and four intersections of nullclines, respectively. Conversely, when the dynamical system has an asymptotically stable critical point, there are initial conditions that allow the system to access non-spiking behavior (Figure 4.4**c**). To give a visual representation of potential trajectories in the $\mathbb{T}^2$ space of the dynamical system, for each of the plots in Figure 4.4, we initialize randomly $\boldsymbol{\theta}$ and trace the trajectory of the dynamical system over time, as indicated by the colorbar. In this representation, when the endpoint of a trajectory is not visible, it means that the dynamical system has been attracted to the corresponding asymptotically stable point, as in Figure 4.4**b-c**. The existence or non-existance of these critical points then becomes an indicator for the existence of robust trajectories in the phase space.

As a general trend, we observe that the area enclosed by a nullcline increases with increasing values of $\frac{\beta}{\omega}$, thus increasing the potential occurrences for the intersection between the nullclines. This trend confirms the intuitions about the

effect of excitability introduced in Equation (4.1), as for increasing values of $\beta$, the system is more likely to exhibit non-spiking behavior. At the same time, the frustration $\alpha_1$ and $\alpha_2$ controls the relative position in the periodic boundary conditions imposed by the $\mathbb{T}^2$ space along the x-axis and y-axis, respectively.

In conclusion, spiking patterns are guaranteed to exist under the condition of no intersection of nullclines, or in the presence of saddle points and unstable critical points. Instead, when asymptotically stable points are present, the system can manifest spiking behavior, in dependence on the initial conditions. We provide further examples of emerging phase portraits in Figure S4.3-Figure S4.4.

### Numerical Study

For this study, we average the results from the individual realization of the system in Equation (4.10) for the different sets of $(\alpha_1, \alpha_2)$ for different $\beta$, while keeping $\sigma_{\boldsymbol{\omega}}/\mu_{\boldsymbol{\omega}} = 0.05$, and report our results in Figure 4.5. We numerically scan the $(\beta, \alpha_1, \alpha_2)$ space using the same simulation hyperparameter settings we used for the numerical experiment in Figure 4.3.



These results show that there is a range of parameters in which it is possible to obtain asymmetric spiking patterns even in the case of two oscillators alone, given that their behavior can be described as in Equation (4.10). This property of the system can also be observed when looking at the ratio between $\theta_1, 2$ and $\theta_2, 1$ when $\theta_1, 2$ reaches the firing threshold. Conversely, in the case of $\alpha_{12} = \alpha_{21}$, such asymmetric patterns can emerge only when considering networks with $N > 2$ oscillators or discrepancies in natural frequencies, such as in Figure 4.3. As a result of the numerical experiment, we observe in Figure 4.5 regions with low standard deviation of circular mean asymmetry that span the whole $0 - 100\%$ range of spiking asymmetry. Furthermore, similarly to what we have observed while studying the system in Equation (4.5), we observe that valid spiking patterns for the metric we introduced in Equation (4.9) are obtained for values of $\alpha_{21,21}$ far from $\frac{k}{2}\pi$, $k \in \{1, 3\}$.

In Figure 4.5**f**, we observe that, even if a spiking pattern in both oscillators has not been achieved, oscillations can be achieved in the non-firing system. Patterns where only one oscillator out of the two reaches the firing thresholds, such as the one we show in this example, can be of interest in the field of hidden oscillators. This case study can be of interest, e.g., in the context of locomotion and CPG, but further investigations in this direction are outside the scope of our work.

The modeling assumption we have explored through Equation (4.10) allows to study emerging patterns in phase oscillators only by using a limited number of parameters. On the one hand, this simplification allows guiding the exploration of parameters to specific applications in mind. On the other hand, working with such a reduced model only partially helps clarify accessible states, and finding a general analytical solution for finite $N$ is still an open challenge in

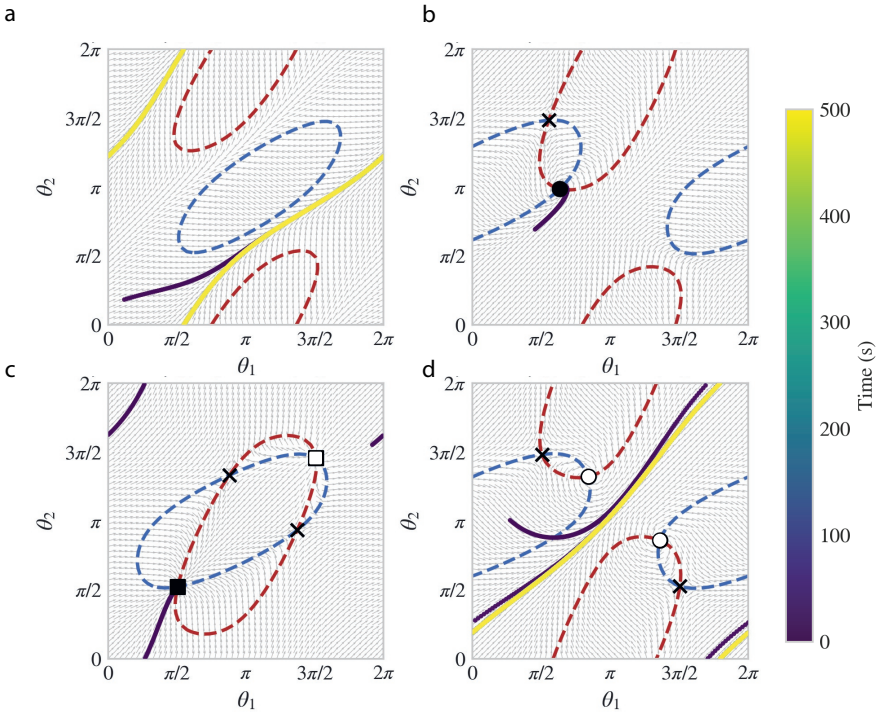


Figure 4.4: **Phase portrait of system in Equation** (4.10)**.** We represent the nullcline for $\dot{\theta}_1 = 0$ and $\dot{\theta}_2 = 0$ with the dashed red and blue lines, respectively. The gray arrows represent the vector field for the system in Equation (4.10). Through the colored points, we represent a randomly initialized trajectory in the phase space in time. As for the representation of the critical points when the two nullclines intersect, we use the crosses to represent saddle points, filled (empty) squares to represent asymptotically stable (unstable) nodes, and (empty) circles to represent (un)stable spirals. For each configuration, we overlay the trajectory in time of a randomly initialized $\boldsymbol{\theta}$ and trace its path in the $\mathbb{T}^2$ space according to the colormap. For this analysis, we fix $\boldsymbol{\omega} = (.95, 1.05)\frac{2\pi}{s}$. **(a)** $(\beta, \alpha_1, \alpha_2) = (0.7\frac{2\pi}{s}, 1.4\pi, 0.6\pi)$. **(b)** $(\beta, \alpha_1, \alpha_2) = (1.2\frac{2\pi}{s}, 1.2\pi, 1.6\pi)$. **(c)** $(\beta, \alpha_1, \alpha_2) = (1.2\frac{2\pi}{s}, 0.4\pi, 0.4\pi)$. **(d)**$(\beta, \alpha_1, \alpha_2) = (1.5\frac{2\pi}{s}, 1.6\pi, 1.6\pi)$.

the field [207]. In addition to that, this simplification comes at the cost of an additional step to relate idealized quantities, such as frustration and excitability, to physical magnitudes when trying to apply this model to real-case applications. Nevertheless, it is possible to use the model in Equation (4.10) to study the

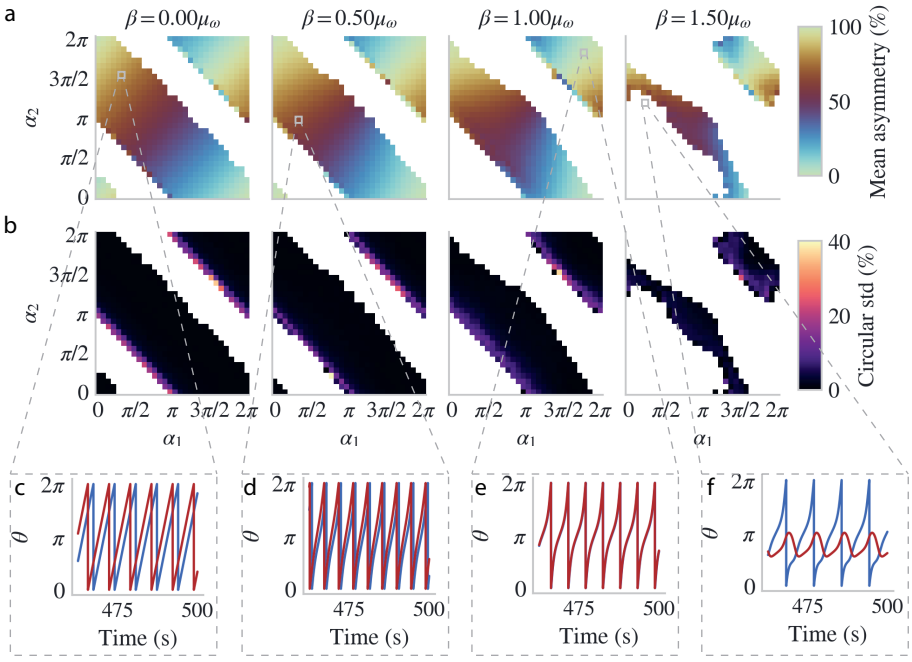


Figure 4.5: **Statistical study of spiking phase asymmetry for system of two oscillators as in Equation** (4.10) **with** $\sigma_\omega/\mu_\omega = 0.05$**. for different values of** $\beta$ **(a)** Circular mean asymmetry. **(b)** Standard deviation of the circular mean asymmetry. **(c-e)** Highlights of oscillating patterns obtained for the corresponding configurations of $(\alpha_{21}, \alpha_{12})$ and $\beta$. **(f)** Example of parameters when $A$ and $\sigma$ could not be computed as only one oscillator hits the spiking threshold. Values of spiking phase asymmetry of 50% (0% or 100%) indicate symmetrical antiphase (in-phase) spiking behavior from the two oscillators. By definition (Equation (4.9)), we report datapoints only when both oscillators reach the firing threshold.

dynamics of coupled oscillators by incorporating fundamental physics knowledge into the aforementioned model, thereby obtaining predictive, quantitative insights.

Our results show that, as a general design choice to obtain stable, asymmetric spiking behavior, regions close to $\alpha_2 = k\pi - \alpha_1$, $k \in \{1, 3\}$ are to be avoided. Moreover, the definition for asymmetry we introduced through $A$ and $\sigma$ cannot inform us about potential bistability of spiking and excitable systems that can occur for the same $(\beta, \alpha_1, \alpha_2)$ configurations, as we show in Figure S4.3**c-d**. We speculate that a different metric should be introduced specifically to quantify and

study the presence of bistability in these scenarios.

## 4.3 A soft robotic application of excitable, frustrated KS model

We now introduce an example of applications of the Equation (4.10) that finds application in the context of fluidic relaxation oscillators in soft robotics. The hardware implementation we refer to is based on an elastomeric tube constrained at its ends to form a kink. When one end of the tube is connected to a continuous airflow input, air pressure on the inlet increases, displacing the kink position along the longitudinal direction of the tube. The accumulated pressure then releases when the kink reaches the opposite end of the tube, causing an airflow discharge through it. The fast motion of the kink through the linear length of the tube, together with its mechanical properties, instantiates a periodic, self-regulated motion. The dynamic of this motion is dominated by the interplay between the mechanical and fluidic properties of the tube, resulting in mechanofluidic oscillations. The Kink Wave Oscillator (KWO) can reach frequencies ranging from $\in [20, 300]$Hz, depending on the airflow input and configuration [208]. We report the typical self-oscillatory behavior observed when KWO is subjected to an input flow (from the right end of its boundary conditions) in Figure 4.6**a**. The results in our previous work [208] show how the geometrical constraint on the length of the tube, together with the fast increase in pressure due to the input airflow, contributes to the formation of a dominant and non-dominant kink in the elastomeric tube, in black and gray, respectively, in panel Figure 4.6**b**. The traveling of the kinks throughout the length of the elastomeric tube under constant airflow of 15 SLPM produces oscillations in pressure, has been reported in Figure 4.6**c**. From this plot, we observe that these pressure oscillations are periodic and non-harmonic, with a frequency in the order of $f_{\text{KWO}} = 20$Hz.

An in-depth fluid-dynamic investigation, combined with studies on dynamic fluid-structure interaction, could potentially justify the observed pressure oscillations in the KWO. Instead, we probe the potential of high-level representations of such oscillatory patterns in the presence of coupling between KWO oscillators. To achieve this goal, we inform the Equation (4.10) with fundamental knowledge about pressure waves and acoustics. Eventually, we demonstrate that our approach has explanatory power over the oscillatory patterns emerging in this soft robotic case study. Through our model, we match experimentally observed thresholds for transitions between oscillatory behaviors and justify the presence of in-phase and anti-phase synchronization.

### 4.3.1 Modeling a single oscillator

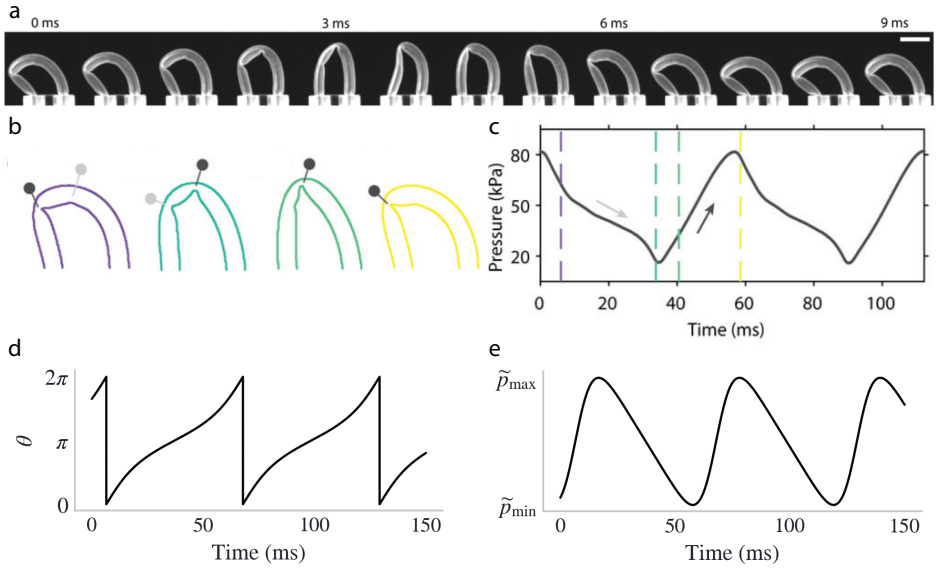


Figure 4.6: **Typical behavior of a single KWO oscillator and model obtained using Equation** (4.1)**. Adapted from** [208]. **(a)** High speed behavior in time of the self-oscillation induced under an constant input flow of 15SPLM. Scale bar is 1cm. **(b)** Extracted data for the position of the dominant (black) and secondary (gray) kink emerging at different timestamps during one oscillation cycle. **(c)** Pressure in time, with highlighted timestamps from **b**. **(d)** Excitable oscillator model obtained with $f_{\text{KWO}} = 16\text{Hz}$ and $\beta = .8 \cdot 2\pi f_{\text{KWO}}$. **(e)** Mapping from $\theta$ to normalized pressure $\widetilde{p}$ as in Equation (4.11).

To represent this oscillatory behavior, we use the excitable phase oscillator model we introduced in Equation (4.1). We demonstrate that the remapping we perform can approximate the spiking asymmetry in the single oscillator observed experimentally when we choose a $\beta_{\text{KWO}} = 0.8\omega$ with $\omega = 2\pi f_{\text{KWO}}$. For our modeling purposes, we define the $\theta = 0$ value as the onset of the depressurization (firing state) of the oscillator. As a result, we obtain the non-harmonic oscillations in Figure 4.6**d**. To map these phase to the oscillations in pressure we aim to approximate, we consider the following expression:

$$\widetilde{p}(t) = \widetilde{p}_{\text{min}} + \left(\widetilde{p}_{\text{max}} - \widetilde{p}_{\text{min}}\right) \sin\left(\theta(t)\right) \tag{4.11}$$

Following this procedure, we map $\theta(t)$ (Figure 4.6**d**) to a normalized pressure $\widetilde{p}$, as in Equation (4.11) and in Figure 4.6**e**, to observe a behavior similar to the one in Figure 4.6**c**. The values of $\widetilde{p}_{\max}$ and $\widetilde{p}_{\min}$ can be chosen to match the actual pressure values observed in the experimental realization of the setup. Nevertheless, as we focus only on phase oscillators, these two parameters remain arbitrary. As we use $\theta$ as a state variable, this procedure does not affect the behavior of the oscillations that we introduced above, nor affects the coupling dynamics in the case we are about to introduce with multiple KWOs. At the same time, this approach helps to better exemplify how the phases of the oscillators can be remapped to physically observed variables. However, this remapping remains arbitrary. Our focus and efforts aim towards understanding and modeling the spiking patterns observed experimentally through the lens of coupled, excitable oscillators, rather than numerically fitting their oscillatory behavior. Moreover, as we represent the state variable of the system using phases, we disregard further investigations about the ways to perform more fitting mappings to obtain better approximations of $\widetilde{p}$ to actual pressure values.



Focusing exclusively on the phase oscillator and overlooking amplitude aspects of the oscillations allows us to obtain a remapping for this non-harmonic oscillator using only $\beta$ as a free parameter, once the experimental natural frequency of the oscillator is taken into account.

### 4.3.2 Modeling coupling of oscillators

We study the case of two KWO connected in parallel to the same input, as shown schematically in Figure 4.7**a**. Experimental results indicate that, once two KWOs are connected in parallel, their pressure phase locks either in-phase (Figure 4.7**b**) or anti-phase states (Figure 4.7**d**), depending on the length of the coupling tube (Figure 4.7**c**). At the same time, there is a sharp threshold separating these two regimes that occurs at about $\sim 5$cm of length of the coupling tube.

To model this phenomenon using the intuitions from Equation (4.10), we consider the following hypothesis:

1. The tube connecting the two KWOs operates as a fluidic resistance, so the pressure difference scales linearly with the length of the coupling tube. This assumption holds both in laminar and in the turbulent regimes ($Re > 4000$) we investigate [209]. We consider this first-order approximation for the regimes investigated experimentally in [208]. Nevertheless, it is reported that for coupling tubes longer than 15cm, the two KWOs become weakly coupled again, before becoming practically uncoupled when the coupling tube is longer than 45cm.

2. It takes a finite time for the depressurization wave generated by one KWO

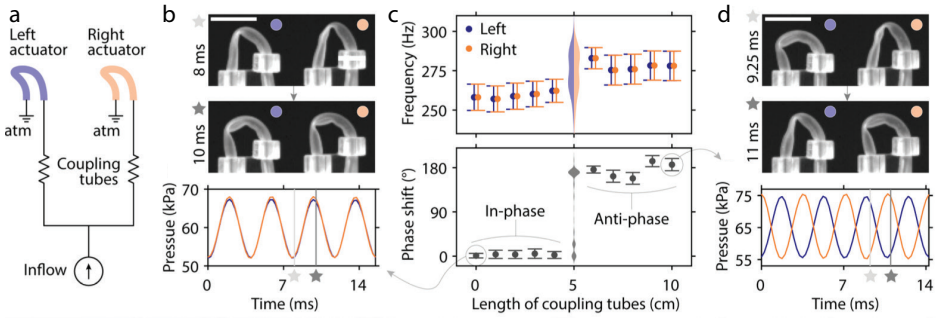


Figure 4.7: **Experimental setup and realization for the coupling of two KWO oscillators with $\approx 28$SLPM input airflow and different lengths of the coupling tube. Adapted from** [208] . **(a)** Schematics of the pneumatic circuit. **(b)** Snapshots and pressure in time for the in-phase oscillations. **(c)** Dependency of frequency of the two oscillators (top) and phase shift as a function of the length of the coupling tube. **(d)** Snapshots and pressure in time for the anti-phase oscillations. Scale bar in **b** and **d** is 1cm.



to travel the length of the coupling tube and reach the opposite KWO. This time is related to the speed of sound and the length of the coupling tube.

3. Experimentally, we observe a sharp critical threshold between phase locking of in-phase and anti-phase when two KWOs are coupled. From a comparison with experimental data, we only study the case of constant airflow of 15 SLPM. Given the reported experimental discrepancies between the oscillator, for this value of input airflow, we investigate natural frequencies for the oscillators of drawn by a normal distribution $\omega_{1,2}, \in \mathcal{N}(\mu_{\boldsymbol{\omega}}, \sigma_{\boldsymbol{\omega}}) = \mathcal{N}(2\pi\overline{f}, 2\pi\sigma_f)$, with $\overline{f}, \sigma_f = (285, 5)$Hz. At the same time, we treat the individual KWO as an excitable oscillator with the same $\beta_{\text{KWO}} = 0.8\mu_{\boldsymbol{\omega}}$ as we discussed when presenting the results in Figure 4.6**d-e**.

To include the first hypothesis in our modeling framework, we consider that the coupling between the two KWOs results from pressure waves caused by the sharp transitions between the open and the closed state of one KWO to the other. Therefore, we consider undirected coupling where the coupling strength relates to the amplitude of the traveling pressure wave from one KWO to the other inside the coupling tube. We approximate the coupling strength with a linear-piecewise function

$$K(L) = \mu_{\boldsymbol{\omega}} \cdot \min(1 - \frac{L}{L^*}, 0) \tag{4.12}$$

where $L$ is the length of the coupling tube. As negligible coupling has been

observed for length of the coupling tube longer than $L^* = 45$cm, we consider a linear drop of coupling strength from $\mu_{\boldsymbol{\omega}}$ to 0 between $L \in [0, L^*]$. However, as the interest in synchronization in experimental investigations is primarily targeted towards locomotion and soft robotic applications, the experimental data in [208] only focuses on coupling lengths up to 10 cm, length scale of interest for the manufacturing of demonstrators for locomotion. Moreover, when performing our numerical analysis, we take into account that in the experimental realization, the reported $L = 0$ cm actually corresponds to $L_{\text{offset}} = 3.5$ cm, the minimum length of the connectors needed to physically connect the two KWOs. Therefore, when presenting our results, we subtract $L_{\text{offset}}$ to more easily relate our numerical results to the experimental realization of the setup.

Through the multiplicative factor $\mu_{\boldsymbol{\omega}}$ in Equation (4.12), we obtain that, especially for small $L$, the system is in strong coupling regime. This choice mirrors the cases studied in Equations (4.5)-(4.10). Additionally, for the paired KWOs case, this is motivated by the fact that the pressure oscillations observed experimentally transition from non-harmonic to harmonic oscillations as the coupling is introduced. At the same time, the amplitude of the oscillations decreases by a factor of two, compared to the case when an single KWO is considered, as we can see when comparing experimental data in Figure 4.6**c** with Figures 4.7**b-d**. This suggests that the coupling between KWO oscillators falls into the strongly coupled regime, namely, where the coupling strength has a magnitude comparable to the natural frequency of the individual oscillator. To match also results concerning pressure amplitudes and their changes upon coupling in our framework, we would need to include terms in Equation (4.10) that also account for the amplitude of the oscillators. Nevertheless, this investigation falls outside the scope of the present work.

We interpret the coupling strength $K$ as a coefficient that influences the depressurization wave taking place upon the firing from one oscillator onto the other, as (de)pressurization waves materially provide local and instantaneous variations in input flows. For practical purposes, we speculate that increasing (decreasing) the diameter of the coupling tube can help increase (decrease) the magnitude of the coupling strength and affect $L^*$. Nevertheless, this analysis falls outside the scope of the present investigation.

By only including this first hypothesis in the model, it would be possible to achieve phase-locking only for synchronized states, when $K(L) \neq 0$. However, starting from the second hypothesis, we speculate that when one of the KWO undergoes a firing event, air pressure is released through the tube, so that a depressurization wave travels to the opposite KWO in a finite time $t_{\text{tube}} = \frac{L}{v_{\text{sound}}}$. On top of that, these depressurization waves are generated at the frequency $\omega$, the natural frequency of the opposite KWO. This means that, when the system reaches steady state oscillations, these depressurization pulses have a wavelength

of $\lambda = \frac{2\pi}{\omega} v_{\text{sound}}$.

Although a delay differential equations representation would facilitate the modeling of transient states, we speculate that it is possible to relate the effect of time delay to the frustration in the coupling function. We consider this approach to be valid in the steady state spiking regimes we mean to investigate. We draw a parallelism between frustration and time-delay effects by considering a first-order expansion in Equation (S4.18). Moreover, our first-order in time approximation does not have the potential to describe transient phases, e.g., when there is a change in the length of the coupling tube or greater input airflow. Overall, the approximation in Equation (S4.18) is considered to be valid only for very small delays [210]. However, reproducing the behavior of transient regimes, as well as the conditions and limits of the time-delay approximation, falls outside the scope of our investigation.

The argument in the coupling function results from constructive and destructive interference occurring between the state of one of the KWOs and the phase of the pressure wave generated by the opposite one. We treat this mismatch as a frustration term. This means that the two KWO oscillators will perceive each other in phase when an $n \in \mathbb{N}$ integer number of $\lambda$ can fit the length of $L$, so that a constructive interference builds up between the pressure waves generated by one KWO on the other. Conversely, when $\frac{L}{\lambda} = n + \frac{1}{2}$, the depressurization wave from one KWO will reach the opposite one half a period after it has reached its own depressurization, causing a destructive interference. By doing so, when $L = n\lambda$, the two oscillators can synchronize to each other's in-phase, leading to effective positive coupling, whereas when $L = (n + \frac{1}{2})\lambda$, the wave reaches the other oscillator half a period out of sync, enforcing anti-phase coupling as $\sin(\theta_1 - \theta_2 - \pi) = \sin(\theta_2 - \theta_1)$.

Therefore, the length of the coupling tube, together with the speed of sound and natural frequency of the oscillators, determines a frustration term we model as

$$\alpha_i(\omega_j, L) = 2\pi \sin\left(2\pi \frac{L}{\lambda_j}\right) = 2\pi \sin\left(\frac{\omega_j L}{v_{\text{sound}}}\right) \tag{4.13}$$

where we use the indices $i$, $j$ to refer to the two oscillators and include the multiplicative factor $2\pi$ before the sine to normalize the frustration values to the $[0, 2\pi)$ interval.

In Figure 4.8**a-b**, we show the trends of $K(L)$ and $\alpha_i(\omega_j, L)$ based on Equations (4.12)-(4.13), respectively. According to our modeling framework, the higher the $\mu_{\boldsymbol{\omega}}$, the more transitions between in-phase and anti-phase behavior can occur before the coupling strength becomes negligible. For the experimental case study we seek to model, we use $\overline{f} = 285$Hz, which we highlight in red in Figure 4.8**b**, and $\sigma_f = 5$Hz that matches the experimental realization of the KWO oscillators. By using oscillators with greater differences in natural frequencies (i.e. $\alpha_1 \neq \alpha_2$),

our framework and study in Equation (4.10) and Figure 4.5 would then allow us to design lengths of the coupling tube necessary to access a broader range of spiking asymmetries.

When moving towards the numerical results, we are using Equations (4.12)-(4.13) in the dynamical system in Equation (4.10) to obtain a first-order in time description of the system of coupled KWO oscillators as in Equation (4.14).

$$\begin{cases} \dot{\theta}_1 = \omega_1 + \beta\cos(\theta_1) + K(L)\cdot\sin\left(\theta_2 - \theta_1 - \alpha_1(\omega_2, L)\right) \\ \dot{\theta}_2 = \omega_2 + \beta\cos(\theta_2) + K(L)\cdot\sin\left(\theta_1 - \theta_2 - \alpha_2(\omega_1, L)\right) \end{cases} \tag{4.14}$$

We demonstrate that this approximation can match experimental observation in Figure 4.8.



### 4.3.3 Numerical Results

When running numerical experiments on the system in Equation (4.14), we simulate 500 simulations with different $\boldsymbol{\theta} \in \mathcal{U}[0, 2\pi) \times \mathcal{U}[0, 2\pi)$, $\omega_{1,2} \in \mathcal{N}(\mu_{\boldsymbol{\omega}}, \sigma_{\boldsymbol{\omega}})$, 5s for each value of $L$ we scan, and study the results from the last half of the simulation. In each simulation, we perform data analysis of spiking asymmetry following the same method we introduced when presenting the circular mean asymmetry in Equation (4.9). We then gather information about the distribution of the circular mean asymmetry that relates to a specific $L$ value and visualize it through violin plots. To show that $\beta$ now only marginally affects the dynamics of the oscillators as a consequence of the strong coupling, we report results in the violin plot for $\beta = \{0, 0.8\mu_{\boldsymbol{\omega}}\}$. This suggests that the coupling strength dominates over the excitability parameter in Equation (4.14). To support this statement, we consider that the non-harmonic oscillations in pressure for the free oscillation of a single KWO in Figure 4.6**c** turn into harmonic ones in the coupled cases in Figure 4.7**b-d**. Such observation implies that, for this model specifically, the excitability does not play a dominant role in determining the emerging patterns. Numerical results in Figure 4.8**c** show that our modeling can reproduce the observed transition between in-phase and anti-phase, with the transition between the two occurring at $\mathcal{L} \approx 5$ cm, consistent with the experimental realization. Nevertheless, increasing the numerical resolution to pinpoint the exact value of the synchronization threshold would have only speculative power, as this datum is not reported experimentally. Furthermore, similarly to the experimental results, we observe only minimal intermediate phase-locked behavior between the in-phase and anti-phase regimes at $\mathcal{L}$. To relate the numerical results with those in Figure 4.7, we apply the mapping in Equation (4.11) to the results of the simulations and report the resulting oscillatory pattern in the insets in Figure 4.8.

To allow a better comparison with the experimental results, we only investigate here the range $L \in [0, 10]$cm. It is relevant to point out that the results in Figure

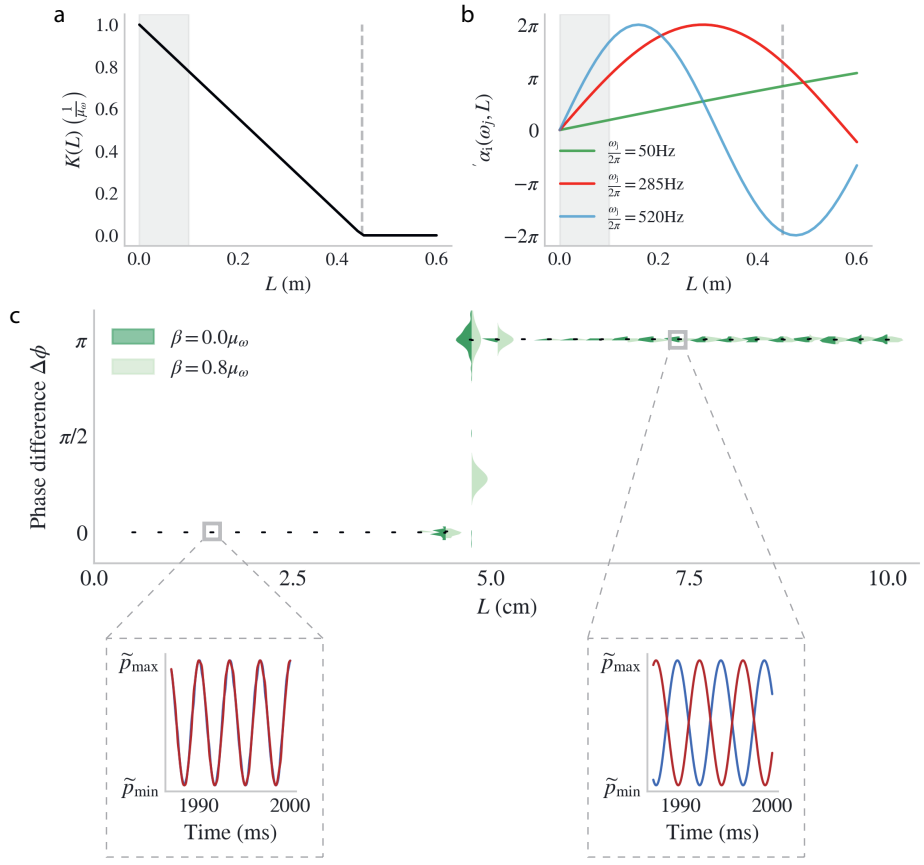


Figure 4.8: **Numerical results for the simulation of the coupled KWO system (a)** Coupling strength dependence on length of the coupling tube (Equation (4.12)). **(b)** Frustration dependence on length of the coupling tube (Equation (4.13)) for different natural frequencies. In red, the frustration for the frequency that matches the experimental results, and we used for the numerical experiment. The gray areas in **a** and **b** represent the length range in which the phase shift analysis was experimentally performed in [208], with the gray vertical dashed lines representing the position of the cutoff distance $\mathcal{L}$. **(c)** Phase difference distributions evaluated after 500 runs per configuration, initialized with $\boldsymbol{\theta} \in \mathcal{U}[0, 2\pi) \times \mathcal{U}[0, 2\pi)$ and $\boldsymbol{\omega} \in \mathcal{N}(\mu_{\boldsymbol{\omega}}, \sigma_{\boldsymbol{\omega}}) \times \mathcal{N}(\mu_{\boldsymbol{\omega}}, \sigma_{\boldsymbol{\omega}})$ for $\beta \in \{0, 0.8\}\mu_{\boldsymbol{\omega}}$, $\mu_{\boldsymbol{\omega}} = 2\pi\overline{f}$ and $\sigma_{\boldsymbol{\omega}} = 2\pi\sigma_f$. We further report typical stable state behavior after the mapping to normalized pressures $\widetilde{p}$ we reported in Equation (4.11) for different $L$ lengths of the coupling tube in the insets.

4.8**c** are obtained after different realizations of Equation (4.14) with different $\boldsymbol{\theta}$ and $\omega$ drawn from the corresponding random distributions. Instead, in the experimental realization of the KWO coupling in [208], the same KWO oscillators have been used. This means that the violin plots in Figure 4.7**c** and Figure 4.8**c** have different meanings. In the statistical results from the simulation, the violin plots are the result of different realizations with different initial conditions $\boldsymbol{\theta}$ and $\boldsymbol{\omega}$. In the experimental case, the reported error bar and violin plot distributions are from the same set of oscillators (thus, we can assume constant $\boldsymbol{\omega}$), but averaged over time. In the experimental realization, at $L \approx \mathcal{L}$, a sweep between in-phase and anti-phase actuation was observed, resulting in the reported two-peaked distribution. Numerically, this behavior was not observed, as the simulations resulted in either in-phase or in anti-phase per initial conditions. We speculate that by including the amplitude of oscillations and inertia in our model, it might be possible to reproduce this switch between oscillatory patterns for $L \approx \mathcal{L}$. In our simulations, we observed that the coupling length at which the switch from in-phase to anti-phase synchronization occurs takes place when, as we increase $L$, the frustration parameters grow past $\pi/2$, suggesting again a similar behavior to the one we have discussed in Figure 4.3.



As a result of our numerical analysis, we observe that mostly in-phase or anti-phase behavior is supported by the coupled KWO system, just like what was observed experimentally when $L$ is other than $\mathcal{L}$. We justify this behavior, also in the context of non-identical oscillators, by considering the discrepancy between the natural frequencies ($\sigma_{\boldsymbol{\omega}}/\mu_{\boldsymbol{\omega}} \simeq 1.7\%$). This ratio yields a discrepancy of frustration terms of $\approx 3\%$. Similarly to what we have discussed while studying the system in Equation (4.5), the coupled KWO system is mostly symmetric, while deviations from fully symmetric spiking patterns can be obtained when larger frustration discrepancies are considered. As a consequence, this system predominantly behaves symmetrically as the system in Equation (4.5), where only phase locking of in-phase and anti-phase synchronization is supported. Should the natural frequencies be farther apart from each other, it should be possible to observe behavior of non-trivial phase locking of spiking configurations such as the one we presented in Figure 4.5.

## 4.4 Discussion

Modeling pattern formation in networked dynamical systems requires simultaneously capturing the intrinsic dynamics of individual oscillators and the structural constraints imposed by network topology. At the same time, the emergent effects of their interaction, as intermediate nodes, can attenuate or delay signal propagation, can alter collective behavior, increasing the complexity of emerging patterns in networked dynamical systems. Examples in this context range from

creating soliton waves in mechanical metamaterials [211] to stabilizing oscillating turbulent flows [212].

We analyzed a minimal networked dynamical system ($N = 2$) capable of supporting both symmetric and asymmetric spiking patterns. Drawing inspiration from Kuramoto-like oscillators, we focused on excitability and frustration to derive a low-dimensional model for synchronization. While the model facilitates parameter exploration for specific applications, its reduced form only partially clarifies accessible states, and a general analytical solution for finite $N$ remains an open challenge in the field [207]. Moreover, relating abstract quantities such as frustration and excitability to physical observables requires an additional step for real-world applications. Even so, we show that the model in Equation (4.5), supplemented with basic physical insight, can yield predictive and quantitative power into the dynamics of coupled oscillators in the soft robotic domain. For our results, we take advantage of both analytical and numerical results. On the one hand, analytical results allow us to define minimal existing conditions for spiking patterns to occur. On the other hand, numerical results highlight clear patterns that emerge for given sets of oscillator parameters and can assist in guiding the design of spiking asymmetries. Nevertheless, methods such as sensitivity analysis and numerical continuation methods will be needed in future studies to assess the ranges of validity and robustness of our model.

Despite the experimental relevance of inhomogeneous integrate-and-fire oscillators, the study of spiking asymmetries in the case $N = 2$ with combined frustration and excitability has not, to our knowledge, been studied before. Our framework addresses this gap and is relevant for designing spiking patterns for applications such as locomotion in soft robots or networked systems emulating human biorhythms (e.g., artificial heart rhythms [213]).

Although spiking asymmetry is usually associated with $N > 2$ homogeneous oscillators or directed graphs, we show that it can also arise in networks of only two non-identical oscillators. Furthermore, through the KWO case study, we further demonstrate that differences in natural frequencies and frustration terms can be related to physical properties of the system.

Our model treats the two oscillators as coupled but standalone elements that respond only to exogenous inputs (e.g., airflow in the KWO case). To move toward applications, Equation (4.10) can be further modified with feedback terms that capture interactions with the environment, as explored, among the many other case studies, in [177, 185, 214]. Moreover, in the cardiac example discussed above, two hidden oscillators can be added to the $N = 2$ network to represent better the way they discharge energy from a pulsation. As an example, one node can be coupled to the left-ventricle node to represent pulmonary circulation, and another coupled to the right-ventricle node to represent systemic circulation, to account for the different dissipation in the human body, thus obtaining a line

network to represent blood circulation in the body. Although such reductions cannot reproduce the full complexity of biological rhythms, the framework in Equations (4.10)–(4.14) provides a high-level tool to navigate the parameter space and design of spiking patterns. Studying how feedback can affect $\dot{\boldsymbol{\theta}}$ is of utmost importance when designing networks to be used as a control policy, for example, for mimicking biological periodic signals or studying locomotion, as in the case of CPG. This future work direction would help clarify the role of (timed) inputs from the environment around the system of oscillators and provide insights into the context of the hidden oscillator's dynamics.

Our model could be expanded to include the oscillator's inertia and amplitudes, so that it could grasp transient behaviors, e.g., when sweeping the parameters in the coupled KWO case study within the simulation time. Additional fitting to experimental results and hypothesis on remapping of physical quantities to the oscillators framework would be needed to meet this and similar modeling purposes. Nevertheless, this investigation falls outside the scope of our work, as we focus on the first-order approximation of the phenomenon.



In summary, we show that even the minimal case of two coupled oscillators can give rise to useful asymmetric spiking patterns when excitability and non-trivial frustration (i.e., values other than 0 or $\pi$) are combined simultaneously. By bridging analytical modeling, numerical exploration, and experimental validation in a soft robotic case study, we demonstrated that reduced oscillator models can retain predictive power when informed by physical intuitions, despite their abstraction. Such insights are directly relevant for the development of soft robotic controllers, fluidic circuits, and even biomedical devices that seek to replicate natural rhythmic behavior, such as prosthetic organs or artificial heart drivers. While further work is needed to incorporate amplitude dynamics, environmental feedback, and broader experimental validation, the present results highlight how minimal models can serve as powerful design tools for dynamical systems meant to operate in (bio)engineering scenarios.

### 4.4.1 Link to the following chapter

The focus of the chapters presented so far has been on the development, characterization, and integration of electronics-free mechanisms for control, energy management, and pattern formation in electronics-free soft robotic systems. While these technical investigations provide a necessary foundation for understanding how mechanical adaptability can be achieved, they also motivate a broader reflection on what is meant by adaptability, intelligence, and autonomy in artificial systems. Engaging with these questions requires taking a step back from specific implementations toward a more abstract perspective.

In the following chapter, we adopt this broader viewpoint to articulate and

critically examine definitions of adaptability, intelligence, and autonomy and reconsider their common use in robotics and related fields. From the perspective of a researcher working in the emerging field of soft robotics, such reflection is essential not only to frame technical work within a coherent and broader conceptual framework, but also to assess its implications and responsibilities in both academic and societal contexts.

## 4.5 Supplementary Materials

### Stable state solutions for $\Delta\theta$, $\beta \neq 0$

The goal of these calculations is to provide minimal conditions of existence of solutions for $\dot{\Delta\theta} = 0$. Starting from Equation (4.6)

$$\dot{\Delta\theta} = \Delta\omega + \beta\big(\cos(\theta_1) - \cos(\theta_2)\big) + 2K\sin(\Delta\theta)\,\cos(\alpha) = 0 \tag{S4.1}$$

we define $A = -2K\cos(\alpha)$ and impose $\dot{\Delta\theta} = 0$. By taking advantage of the relation $\cos(\theta_2) = \cos(\theta_1 - \Delta\theta) = \cos(\theta_1)\cos(\Delta\theta) + \sin(\theta_1)\sin(\Delta\theta)$ and by introducing $p = \tan\big(\frac{\Delta\theta}{2}\big)$, so that $\cos(\Delta\theta) = \frac{1-p^2}{1+p^2}$ and $\sin(\Delta\theta) = \frac{2p}{1+p^2}$, we derive:

$$\Delta\omega + \beta\left(\cos(\theta_1)\left(1 - \frac{1-p^2}{1+p^2}\right) - \sin(\theta_1)\frac{2p}{1+p^2}\right) - \frac{2Ap}{1+p^2} = 0 \tag{S4.2}$$

$$\Delta\omega + \frac{2p\beta}{1+p^2}\Big(p\cos(\theta_1) - \sin(\theta_1)\Big) - \frac{2Ap}{1+p^2} = 0 \tag{S4.3}$$

From which the solutions are

$$\overset{\Delta\omega=0}{\Longrightarrow} \begin{cases} p = 0 \rightarrow \Delta\theta^{\text{eq}} = 2k\pi \\ p \neq 0 \rightarrow p = \dfrac{A + \beta\sin(\theta_1)}{\beta\cos(\theta_1)} \rightarrow \Delta\theta^{\text{eq}} = 2\arctan\left(\dfrac{\beta\sin(\theta_1) + A}{\beta\cos(\theta_1)}\right) + 2k\pi \end{cases} \tag{S4.4}$$

with $k \in [0, 1]$. Conversely, for the case of non-identical oscillators and $\Delta\omega \neq 0$, the solution reads

$$\begin{aligned} p &= f(A, \beta, \theta_1, \Delta\omega) \\ &= \frac{2A + 2\beta\sin(\theta_1) \pm \sqrt{\big(2A + 2\beta\sin(\theta_1)\big)^2 - 4\Delta\omega(2\beta\cos(\theta_1) + \Delta\omega)}}{2(2\beta\cos(\theta_1) + \Delta\omega)} \end{aligned} \tag{S4.5}$$

$$\Delta\theta^{\text{eq}} = 2\arctan\Big(f(A, \beta, \theta_1, \Delta\omega)\Big) + 2k\pi \tag{S4.6}$$

that reduces to the case in Equation (S4.4) for $\Delta\omega = 0$. We report numerical solutions for Equation (S4.4) for different specified values of $\alpha$ and $\beta$ as a function of $\theta_1$ in Figure S4.1. By studying when the denominators in Equation (S4.4) and Equation (S4.6) are non-zero, we can determine the existence condition for $\dot{\Delta\theta} = 0$.

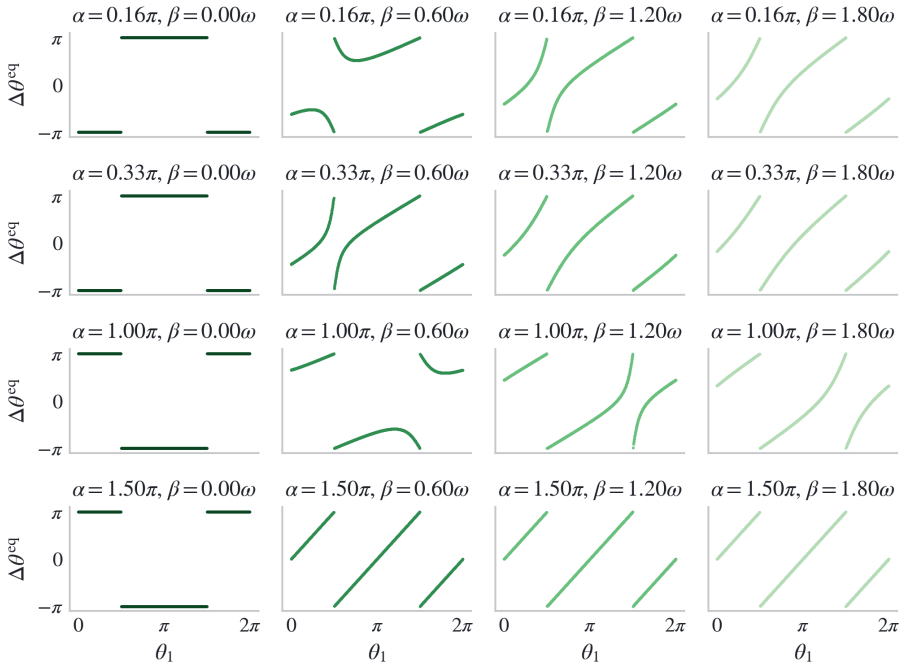


Figure S4.1: **Numerical solutions for $\dot{\Delta\theta} = 0$ indicated by Equation** (S4.4)**.** We report the numerical solutions of the equation for $N = 2$, $\Delta\omega = 0$ for different values of $\alpha$ and $\beta$.

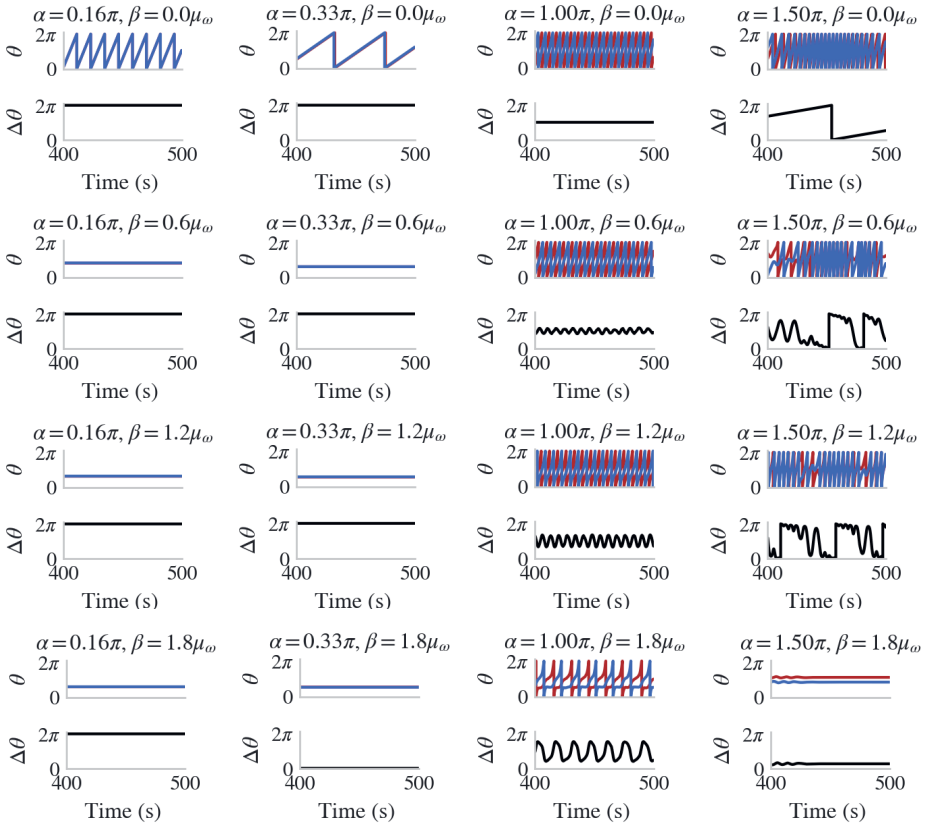


Figure S4.2: **Example of trajectories of the dynamical system in Equation (4.5).** Trajectories for $N = 2$ for increasing values of $\alpha$ (left to right) and $\beta$ (top to bottom). The $(\alpha, \beta)$ parameters we investigate are the same as in Figure S4.1.

## Stability analysis through phase portrait characterization of Equation (4.10)

To get conceptual insights on the conditions of existance for stable, non-oscillating states, we represent the vector field of the ODE system in Equation (4.10) and its nullclines (Equation (S4.7)) in Figures S4.3.

$$\begin{cases} \dot{\theta}_1 = \omega_1 + \beta\cos(\theta_1) + K\sin(\theta_2 - \theta_1 - \alpha_1) = 0 \\ \dot{\theta}_2 = \omega_2 + \beta\cos(\theta_2) + K\sin(\theta_1 - \theta_2 - \alpha_2) = 0 \end{cases} \tag{S4.7}$$

Through this representation, we observe that stable state solutions are accessible only when the two nullclines overlap in the periodic phase space $(\theta_1, \theta_2)$. This means that all configurations for which the two nullclines have no intersection, like in the example in Figure S4.3**a**, can support oscillatory behavior of the system. Conversely, when the two nullclines overlap, critical points emerge and the system, and by studying the eigenvalues of the Jacobian matrix in these critical points, we characterize their stability. Globally, we observe that for increasing values of $\beta/\mu_{\boldsymbol{\omega}}$, the area enclosed by the nullclines increases, making it more likely for intersections between the nullclines to emerge. This result is in agreement with the observation from above, where for increasing $\beta/\mu_{\boldsymbol{\omega}} > 2$, the system is more easily attracted to excitable states, rather than self-oscillating.

For stability analysis purposes, it is worth mentioning that as we are working in a $\mathbb{T}^2$ space, periodic boundary conditions and that each nullcline encloses an ellipsoid-like convex areas. This feature means that their intersection can result in a set of cardinality from zero to four. As an example, when the two nullclines intersect, a saddle point always emerges together together with an asymptotically stable node, either a spiral (Figure S4.3**b**) or an asymptotically stable spiral (Figure S4.3**c**).

Nevertheless, it is relevant to highlight that the presence of an asymptotically stable point does not guarantee the presence of non-spiking behavior, as we can observe when comparing Figure S4.3**c-d** where we initialized the system with same $(\beta, \alpha_1, \alpha_2)$ in two different initial conditions. This feature suggest that the initial conditions can affect whether the system can access spiking behavior, thus the presence of an asymptotically stable point does not automatically guarantee non-spiking behaviors.

Conversely, if a unstable node (Figure S4.4**a**) or spiral (Figure S4.4**b**) appear together with the saddle node, the system does not support asymptotically stable points. Therefore, we infer that it manifests spiking behavior, irrespective of the initial conditions.

When the parameters allow four intersections of the nullclines, two of these

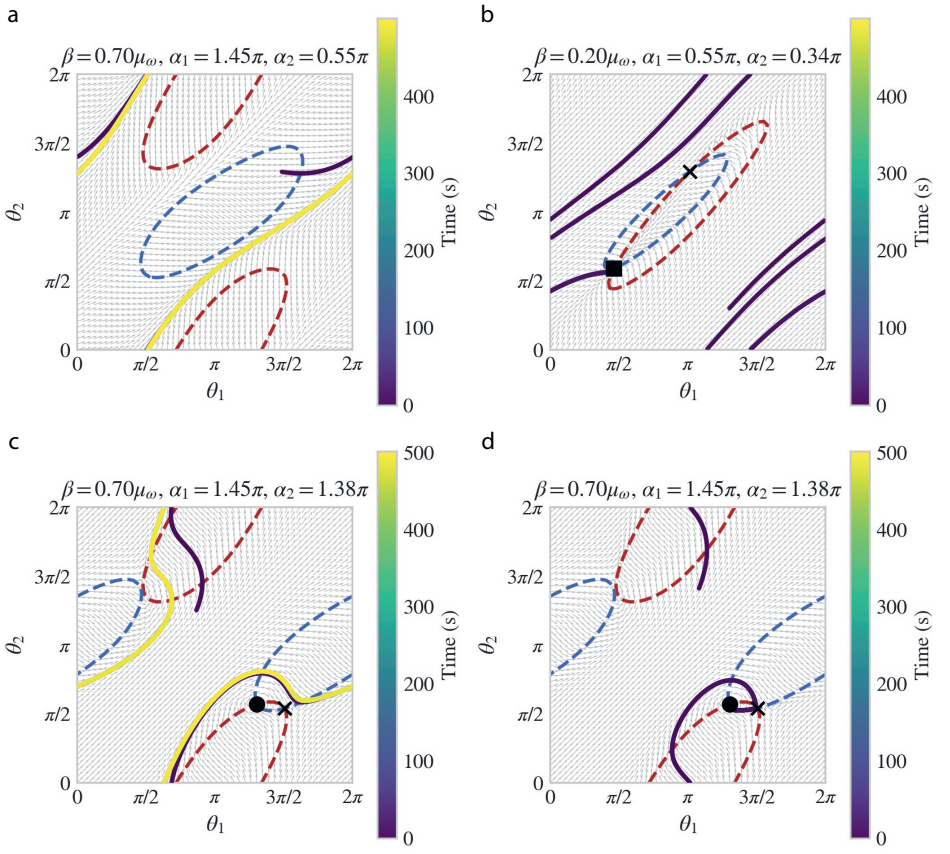


Figure S4.3: **Phase portrait, nullcline analysis and example trajectories for the dynamical system in Equation** (4.10). For this analysis, we consider $\boldsymbol{\omega} = (0.95, 1.05)\frac{2\pi}{s}$, $K = \frac{2\pi}{s}$. We report the $\dot{\theta_1}$ and $\dot{\theta_2}$ using a red and blue dashed line, respectively. As for the classification of critical points, we indicate (un)stable nodes with full (empty) squares, (un)stable spirals with full (empty) circles, and saddle points with crosses. Through the colored points, we represent a randomly initialized trajectory in the phase space in time. Note that c and **d** phase portraits share the same set of $(\beta, \alpha_1, \alpha_2)$.

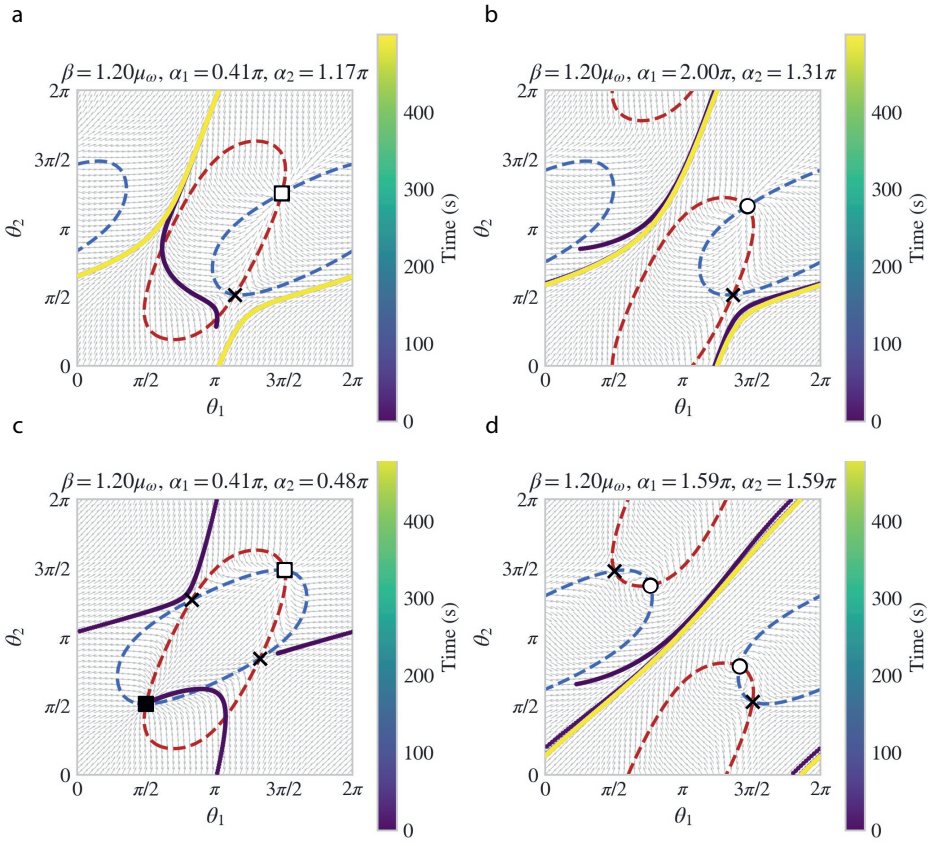


Figure S4.4: **Phase portrait, nullcline analysis and example trajectories for the dynamical system in Equation** (4.10). For this analysis, we consider $\boldsymbol{\omega} = (0.95, 1.05)\frac{2\pi}{s}$, $K = \frac{2\pi}{s}$. We report the $\dot{\theta}_1$ and $\dot{\theta}_2$ using a red and blue dashed line, respectively. As for the classification of critical points, we indicate (un)stable nodes with full (empty) squares, (un)stable spirals with full (empty) circles, and saddle points with crosses.

critical points are saddle points, while the other two can be asymptotically stable or unstable spirals or nodes, or a combination of those, as we show in Figure S4.4**c-d**.

Studying how the phase portrait changes as a function of the system parameters can help elucidate how the spiking asymmetry we presented in Figure 4.5 can be shaped in dependence on frustration asymmetries and excitability. When comparing these results to the plots in Figure 4.3 and Figure 4.5, we observe that there is a correspondence to the set of parameters for which there is an overlap of nullclines and the regions where no spiking data was reported.

## Analytical threshold for spiking conditions for Equation (4.5)



Our focus is to determine for which conditions Equation (4.5) does not show stationary solutions. This condition helps define existence conditions to guarantee the presence of spiking behavior. However, this approach cannot inform about the presence of emerging spiking asymmetries.

We define $\varphi_{i,j} = \theta_{j,i} - \alpha$ and rewrite Equation (4.5) as :

$$\begin{aligned}\dot{\theta}_i &= \omega_i + \beta\cos(\theta_i) + K\sin(\theta_j - \theta_i - \alpha) \\ &= \omega_i + \beta\cos(\theta_i) + K\sin(\varphi_i - \theta_i) \\ &= \omega_i + \beta\cos(\theta_i) + K\big(\sin(\varphi_i)\cos(\theta_i) - \cos(\varphi_i)\sin(\theta_i)\big) \\ &= \omega_i + \cos(\theta_i)\underbrace{\big(\beta + K\sin(\varphi_i)\big)}_{A_i} - \underbrace{K\cos(\varphi_i)}_{B_i}\sin(\theta_i) \\ &= 0\end{aligned} \tag{S4.8}$$

(S4.9)

where we use the index $i$ and $j$ for the oscillator 1 and 2 equivalently. We define

$$\begin{aligned}R_i(\theta_j, \alpha, \beta, K) &= \sqrt{A_i^2 + B_i^2} = \sqrt{\beta^2 + 2\beta K\sin(\varphi_i) + K^2\sin^2(\varphi_i) + K^2\cos^2(\varphi_i)} \\ &= \sqrt{K^2 + \beta^2 + 2\beta K\sin(\varphi_i)} \geq 0\end{aligned} \tag{S4.10}$$

$$\cos(\delta_i) = \frac{A_i}{R_i}, \quad \sin(\delta_i) = \frac{B_i}{R_i} \tag{S4.11}$$

$$\delta_i = \arctan\left(\frac{B_i}{A_i}\right) \tag{S4.12}$$

Through these variables, we can rewrite

$$\begin{aligned}\omega_i + A_i\cos(\theta_i) - B_i\sin(\theta_i) &= \omega_i + R_i\left(\cos(\theta_i)\frac{A_i}{R_i} - \sin(\theta_i)\frac{B_i}{R_i}\right)\\ &= \omega_i + R_i\Big(\cos(\theta_i)\cos(\delta_i) - \sin(\theta_i)\sin(\delta_i)\Big)\\ &= \omega_i + R_i\underbrace{\big(\cos(\theta_i+\delta_i)\big)}_{\in[-1,1]} = 0\end{aligned} \tag{S4.13}$$

In conclusion, we derive that an equilibrium phase $\theta_i^{\text{eq}}$ can exist for the $i$-th oscillator only if the following condition is verified

$$\theta_i^{\text{eq}} = \pm\arccos\left(-\frac{\omega_i}{R_i}\right) - \delta_i + 2k\pi \Rightarrow \frac{\omega_i}{\sqrt{K^2+\beta^2+2\beta K\sin(\theta_j-\alpha)}} \leq 1 \tag{S4.14}$$

where we do not consider the absolute value as in our case study we focused on natural frequencies strictly positive, $K \simeq \mu_{\boldsymbol{\omega}} > 0$, $\beta \simeq \mu_{\boldsymbol{\omega}} > 0$. Equation (S4.14) sets an analytical threshold that, in dependence of $\alpha$, $\beta$, $K$, and $\omega$, dictates minimal conditions for accessing stable state behavior in the system. As $\beta$ breaks rotational symmetry and we consider $\boldsymbol{\omega} \in \mathbb{R}^+ \times \mathbb{R}^+$, this means that equilibrium configurations correspond to states in which oscillators are in the excitable regime, rather than maintaining a constant phase difference. These configurations, for which frequencies and phases are periodic, are generally referred to in literature as *phase-trapped* states.

By considering that the equilibrium conditions must be simultaneously satisfied in both oscillators, we obtain:

$$\begin{cases}\theta_1^{\text{eq}} = \pm\arccos\left(-\dfrac{\omega_1}{\sqrt{K^2+\beta^2+2\beta K\sin(\theta_2-\alpha)}}\right) - \arctan\left(\dfrac{K\cos(\theta_2-\alpha)}{\beta+K\sin(\theta_2-\alpha)}\right)\\ \theta_2^{\text{eq}} = \pm\arccos\left(-\dfrac{\omega_2}{\sqrt{K^2+\beta^2+2\beta K\sin(\theta_1-\alpha)}}\right) - \arctan\left(\dfrac{K\cos(\theta_1-\alpha)}{\beta+K\sin(\theta_1-\alpha)}\right)\end{cases} \tag{S4.15}$$

When considering that in Equation (S4.15) the term $|2\beta K\sin(\theta_j-\alpha)| \in [0, 2\beta K]$, we obtain a lower boundary that, irrespective of $\theta_j$, suggests that

oscillatory behavior is achieved when

$$\frac{\omega_i}{\sqrt{K^2 + \beta^2 + 2\beta K \sin(\theta_j - \alpha)}} \geq 1 \Rightarrow \omega_i \geq \sqrt{K^2 + \beta^2 + 2\beta K} \tag{S4.16}$$

$$\geq K + \beta \tag{S4.17}$$

where we do not consider the absolute value as we chose $\boldsymbol{\omega} \in \mathbb{R}^+ \times \mathbb{R}^+$, $\beta \in \mathbb{R}^{*+}$, $K > 0$. The condition we obtained confirms that, when the natural frequency of one oscillator is greater than the coupling strength and excitability, the system is guaranteed to oscillate. This result confirms and expands the result we presented for minimal conditions for firing events while introducing the excitability parameter $\beta$ in the presence of an external stimulus in Equation (4.3), to the case where the coupling operates as an external signed stimulus.

When the condition in Equation (S4.17) is met for both oscillators, the system is guaranteed to have spiking behavior, although further analyses would be needed to assess pattern emergence in this case. Due to the small dimensionality of the system, for our purposes, it is more convenient to grasp intuitions about potential spiking patterns using a numerical analysis such as the one we introduce in Figures 4.3-4.5.

The result in Equation (S4.17) can be expanded to the case in which the frustration parameters for the two oscillators are non-identical.

## On the parallelism between delay differential term and Frustration in KWO model

When modeling the depressurization wave dynamics, it is relevant to recall that depressurization waves are generated only when a firing event occurs. Therefore, it would be more physically correct to include a term of the coupling strength to account for that coupling when one KWO hits the firing threshold $\theta = 0$, and that the signal takes a finite time $t_{\text{tube}}$ to reach the opposite KWO. An extension of our model to grasp this effect would require using delay differential equations (DDEs). However, this alone would not be sufficient to grasp the physics of the phenomenon, as in a DDE formulation, the delayed coupling would occur continuously, rather than as a result of a periodic spiking signal in time. Moreover, through preliminary numerical tests, we verified that DDE formulation with no frustration could not reproduce the phenomena observed experimentally, as the system exclusively set to fully in-phase synchronized states. This would indicate that interference between sound waves, rather than time delay, predominantly determines the emergence of different phase locking regimes in our system. We speculate that a different model for the coupling term in the form $K(L)\delta(t - t_{f_j}) \sin(\theta_j(t - t_{tube}) - \theta_i)$, $t_{f_j}$

time of firing of the $j$th oscillator, could be used instead. With such a coupling, it would be possible to grasp the pulsatile nature of the coupling while injecting knowledge about acoustic coupling.

To motivate how the frustration parameter can interpret at steady state the the delay due to the presence of the finite velocity for the signal to travel from one KWO to the other and its high-level representation through the frustration is the following, we consider the following argument. We define a time delay $t_{\text{tube}}$ and indices $i$ and $j$ for the two oscillators, and use a first-order approximation to obtain that, for small $t_{\text{tube}}$, $\theta_j(t - t_{\text{tube}}) \approx \theta_j(t) - \omega_j\, t_{\text{tube}}$. By doing so, we obtain:

$$\begin{aligned} \dot{\theta}_i(t) \;&\approx \omega_i + \beta\cos(\theta_i) + K(L)\,\sin\big(\theta_j(t) - \omega_j\, t_{\text{tube}} - \theta_i(t)\big) \\ \omega_j\, t_{\text{tube}} &= \omega_j\,\frac{L}{v_{\text{sound}}} = 2\pi\frac{L}{\lambda_j} \end{aligned}$$

Thus, the term $\omega_j t_{\text{tube}}$ is also an expression for the amount of wavelength $\lambda_j$ of the signal generated by the $j$th oscillator within the length of the coupling tube $L$. Through this approximation, it is then possible to relate time-delay with emergence of constructive and destructive interference, as we argued while presenting Equation (4.13). On top of that, this first-order approximation allows us to model the behavior of the coupled KWOs using an ODE, instead of a DDE formulation.

S4

S4

# Chapter 5
# On the Design of Adaptability and Autonomous Systems

Abstract

As robots increasingly move from controlled lab environments into open-ended landscapes, the stakes for autonomy, as well as safety, are higher than ever. The design of an autonomous vehicle's control system or an artificial heart's regulation mechanism hinges on the level of decision-making of the machine itself. For this reason, control loops are often favoured over self-optimizing, autonomous algorithms that might "learn" themselves into creative, yet unwanted, operational patterns, potentially leading to catastrophic consequences. For the very same reason, as engineers and scientists designing devices around ourselves that are supposed to become less dependent on human interventions, working under the banner of "smart" robots poses a serious conceptual threat as it foments discord about common goals and expectations. We introduce definitions for automatic and autonomous systems and explore practical implications and challenges in design (selecting appropriate hardware and software architecture), control theory (maintaining stability and responsiveness), and safety assurance (forecasting the robot's behavior in edge scenarios and determining its accountability during failures).



Based on: *Proficient Without Training: On the Design of Automatic Machines*, Sergio Picella, Erik Steur, and Johannes T. B. Overvelde, *in preparation*

# 5.1 Introduction

## 5.1.1 Machines and robots

The desire to use tools to simplify human tasks, until humans are able to get out of the chain of resource transformation, has been one of the driving forces behind technological breakthroughs. The goal of automation and robotization has been and still is to develop machines that could operate as proficient human substitutes. However, mimicking human behavior and the capability needed to adapt to unexpected changes that would otherwise jeopardize the machine's functioning has been proven notoriously difficult, limiting the autonomous operation of devices we see around us. Overcoming this obstacle remains one of the main challenges in, e.g., the field of robotics to date.

To work around this limitation, engineers depended mostly on two compromises that allow to benefit to some extend from technical advantages. The first approach to handle environmental uncertainty is to delegate the actuation to the machine while keeping a *human-in-the-loop* for what concerns the control. This approach results in what we refer to as *marionette* systems: (tele-)operated actuators, often able to sense their environments and help a human operator in resource manipulation, exploration, and decision-making. Such designs facilitate our tasks by enhancing precision, power conversion, accuracy, and speed of interactions with the environment. Examples of this approach range from hammers to the most advanced teleoperated surgical tools, from bicycles to telescopes. However, this first solution only partially addresses the initial drive to release humans from the burden of repetitive tasks and increasing efficiency and cost-effectiveness in industry.

The second approach is to design adapting tools that are programmed to respond to the expected variability of the environment automatically. Watt's governor, robotic vacuum cleaners up to synthetic feedback loops made with RNA molecules [215] represent some of the devices in this category. Although these machines can appear to manifest *seemingly* intelligent behavior as they adapt to their environment, they are still input-output devices with automatic reactions that have been specifically designed. In fact, these devices often depend on highly controlled environments and can exhibit only limited degrees of freedom. Such programmed machines can be used without human supervision, yet they lack the capability to *dictate* their own set of operating principles, therefore lacking the autonomy that we often associate with (human) intelligence [216].

If we were to adhere to the original 1920s intended definition of a *robot* [217], the first marionette approach that requires human supervision would not be classified as a robot, while the second approach that consists of preprogrammed behavior in pre-shaped environments could be classified as a robot. Yet, in the

present time, the definition of robots is associated with the complexity of the task and the degrees of freedom that the device has, but also with other characteristics such as material (typically metal), actuators (typically electrical), and control (embedded software).

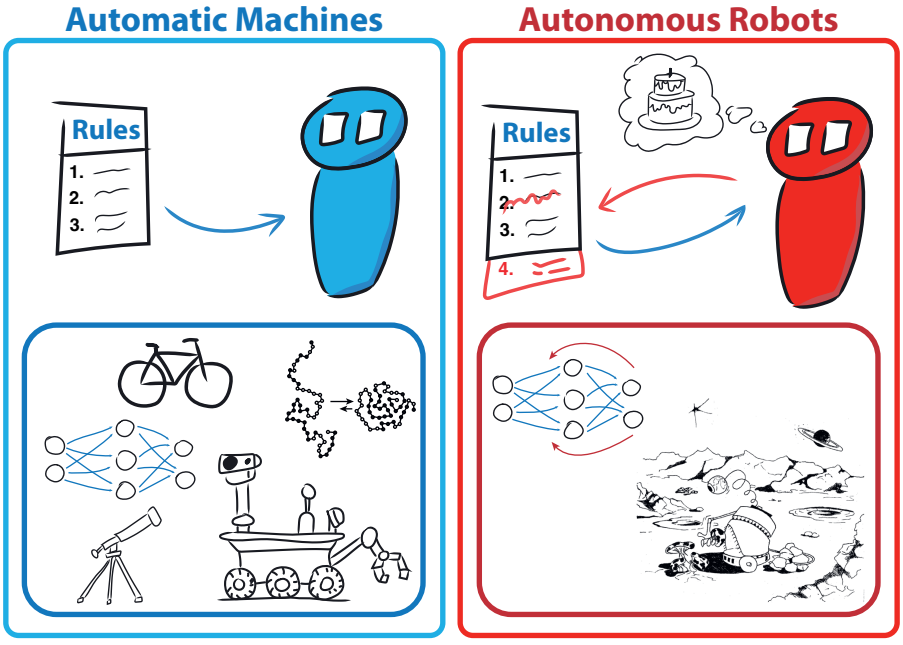


Figure 5.1: **An overview of the differences we use to distinguish automatic from autonomous systems.** Schematic representation of some examples we use to highlight differences between automatic and autonomous systems. We report the "Fungus Eater" example for autonomous machines from Rolf Pfeifer (cartoon by Isabelle Follath, Zurich).

### 5.1.2 Steering the debate to *automatic* and *autonomous* behavior

In scientific literature, it is often the case that terms like *intelligent*, *autonomous*, *adaptive* and *learning* are used interchangeably to highlight similar features such as the capability to reshape hardware according to external stimuli or navigate complex environments [104, 218, 219]. We believe that this uncertainty

enhances confusion and limitations for science communication, policy making, and application of legal boundaries. In particular, we believe this to be true, especially when communicating between different academic environments and, more importantly, when presenting a research topic to the general public, seeding unclear expectations about usage, performances, and safety. Examples of this practice in scientific literature can be, e.g., hinting that intelligence can be easily obtained as the result of programmed input-output strategies. The current explosion of chatbots within the field of Artificial Intelligence (AI) is a prime example of a field where this discussion is being fueled.

As we know that there is no universal consensus on the definition of intelligence itself [216, 220, 221], we deem that a discussion of two definitions that operate at a more fundamental and underlying level than *intelligence* should be treated first. For these reasons, we believe that the scientific community could benefit from an open dialogue on the key differences between the definitions of *automatic* and *autonomous* systems. Our goal is to spark discussions in this direction, building on arguments from literature, while arguing about the relevance of this topic for both technical, legal, policy, and ethical reasons. This, in turn, would improve both the clarity of goals and expectations on a technical level, while improving the communication of scientific findings to the general public and across multiple academic disciplines.



### 5.1.3 The relevance of responsibility and explainability

The quest for the definition of autonomy was historically delegated to the philosophical debate, but artificial agent design is increasingly offering a physical platform to test, validate, and probe such (theor)ethical questions in practise. At present, this appears to be even more of interest, when the debate on the (excess of) autonomy for synthetic systems permeates society, from pop culture to political debate. The more artificial systems become embedded in our everyday lives, the greater the necessity to move beyond opaque, black-box methods that manifest *seemingly* intelligent results. This argument gains support from the growing significance of explainability and interpretability in the context of AI [222], as exemplified by the AI act.

Moving beyond the digital world, the same considerations are essential for applications that deal with the autonomous operation of, e.g., artificial organs [213] or vehicles [223]. In these areas, clearly understanding the rationale behind decisions made by autonomous systems is essential for accountability, should a system failure occur. Emphasizing explainability and interpretability in system behaviors becomes then a crucial requirement that could limit and put constraints on the autonomy of a system. Not only for design purposes, but also for building

trust, ensuring accountability, and maintaining operational safety.

## 5.2 Setting goals as a requisite for autonomy

The interest in agreeing on a common definition of autonomy in the field diverged quite rapidly from the technical and technological aspects, widening the gap between the definition of autonomous robots and their potential implementation. Starting approximately from the late 1960s, software and theoretical limitations of the computability of programs started to stimulate debate and research in the theoretical and ethical aspects. It would be an understatement to say that there is no universal consensus on the *autonomous* definition in the literature.

On the one hand, more precise definitions in the robotics field, where autonomy is described as *independence of control* where *self-sufficiency, situatedness, learning or development, and evolution increase an agent's degree of autonomy* [224], raise debates and criticism [225, 226]. This is particularly true for recent developments in artificial agents with a sharp separation between hardware and software. On the other hand, inflating available definitions to include all singular cases is also a tedious operation that rarely helps in outlining what autonomous systems are in the first place.

Without diving into a full and detailed definition of autonomy, we suggest high-level and fundamental features that could help distinguish autonomous robots from automatic machines in general. We believe that autonomous systems must operate following teleonomic behavior, meaning that they must be able to tend to specified (pre)determined goals. Thus, when discussing whether a system is autonomous, the first question to ask is what the goal is that the system is trying to achieve [227]. We believe this question is a fundamental and necessary one, although not sufficient to distinguish between autonomous from automatic systems. On the contrary, automatic systems can only follow rules and their updates in an algorithmic way, without modifying their underlying working principles and executing programs for the sake of completing them, rather than because of internal goals. This means that, even if a (synthetic) agent can switch between different behaviors, then this agent still falls within our definition of automatic systems if this switch in output is predetermined for a certain set of inputs. We provide a visual summary of our definitions in Figure 5.1.

Still, it is no surprise that automatic systems with an increasing number of inputs and outputs are often deemed autonomous or intelligent.

### 5.2.1 Vacuum cleaners and self-driving cars

Following from the aforementioned arguments, although often sufficient to operate in diverse and ever-changing scenarios and capable of unsupervised operation,

most devices we develop fall within the category of *automatic* systems. In practical terms, an automatic robotic vacuum cleaner demonstrates independence by performing tasks without human intervention. It can navigate rooms and clean without relying on external commands during operation. However, this device typically does not reflect on the cleanliness of the floor to adapt its behaviour accordingly. Instead, it follows predetermined patterns to move through the room, thus, it is not autonomous, as it follows fully prescribed programs. The cleaning from an automated vacuum cleaner then emerges from external design, and its capability to algorithmically execute programs, rather than from learning or autonomous processes. The designs we introduced in Chapters 2, 3, and 4 also fall under the category of *automatic* machines.

Conversely, an autonomous system, such as a self-driving car, should not only operate independently from direct human control but also actively make decisions, evaluate risks, and adapt to unforeseen scenarios by leveraging its internal reasoning processes, all while trying to reach a certain location. Such self-driving systems should be able to cope with unpredictable events that might occur while in charge of driving tasks. Clarifying expectations and accountability in this context (compared to the circumstance of an automatic vacuum cleaner) becomes of utmost importance for both technical and ethical challenges to be overcome, and to incorporate such self-driving systems in our daily lives.



### 5.2.2 The role of learning

Autonomy, therefore, incorporates elements of judgment and intentionality beyond mere operational independence. If we look at neural networks, we observe that during the training phase, such synthetic agents can explore and rewrite their internal weights to optimize their response to inputs towards an external goal. This capability not only to change weights, but to reshape their internal structure as a dynamical system, sets neural networks apart from other adaptive control strategies. Nevertheless, neural networks are deployed and put to use after their training phase (at least, following the implementation of the AI act), so that their response to stimuli can be assessed to be efficient with the given target goals under conditions relatable to the training ones. At the same time, this strategy prevents them from improvising or exploring original solutions during operation in unsupervised scenarios that might be detrimental to their tasks and, therefore, restricts their autonomy.

We suggest one crucial difference that sets apart automatic systems from autonomous systems that can cope with unknown scenarios is learning. We deem the ability to change responses over time, based on intuition from rewards and punishments, a fundamental building block for intelligent and autonomous systems. In this context, we consider systems for which the change in internal states drives

the learning process and guides the self (re)determination of operating rules as autonomous. Our definition complies with similar attempts to outline a potential definition that could help in understanding, analyzing, and designing autonomous systems [228]. We care to clarify that similar and complementary classification attempts have been made to discriminate autonomy in diverse biological and artificial systems [227, 229, 230].

Our argument can be generalized to (natural) systems that are (described) designed using differential equations formalisms. It is often the case that, e.g., in neuron models in mathematical neuroscience [231] as well as in mechanical [232] and multiagent systems [233], environmental conditions and input variables can change the magnitude of the parameters in the dynamical system formulation, thus switching or disrupting the overall expected output. This is a peculiarity of non-linear systems that we studied in this thesis. Based on our definition, autonomy cannot emerge from holistic automatic behavior shifting over time as a consequence of plasticity in the control policy. We support this statement by considering that, in this scenario, systems still output programmed responses, but there is no well-defined goal that the system strives for. This strategy, often related to Hebbian learning or Pavlovian conditioning [25], is linked to induced hysteresis in fixed control policies, which does not directly translate into goal-directness we associate with autonomous systems. Similarly, self-regulation (programmed automatic reaction) does not translate to self-law-making capabilities (autonomous response) [234].



Therefore, although often considered *seemingly autonomous*, we still can think of these systems more as automatic, as they have no self-determination of operating rules nor goal-directness. Similarly, (robotic) systems that work purely based on algorithms fixed in time still fall under the definition of automatic systems. In Rodney A. Brooks' perspective, *"intelligence is determined by the interaction with the world"*. At the same time, *"it is hard to identify the seat of intelligence within any system, as intelligence is produced by the interactions of many components. Intelligence can only be determined by the total behavior of the system and how that behavior appears in relation to the environment"* [29, 30]. It is often the case that these reactive systems designed in the context of, e.g. *wired* or *embodied* intelligence, are deemed to manifest *seemingly* autonomous or intelligent behavior, while they are fundamentally designed automatic behavior injected by design, and do not change their behavior in time.

We summarize our observations in Figure 5.2, where we place on one side automatic behaviour, which is characterized by executing rules. When similar systems start to operate with goal-directedness, and can define their own operating rules accordingly, we move towards autonomous behaviour. When learning comes into play, such autonomous systems start to behave more intelligently.

## 5.3 Towards design rules for synthetic agents

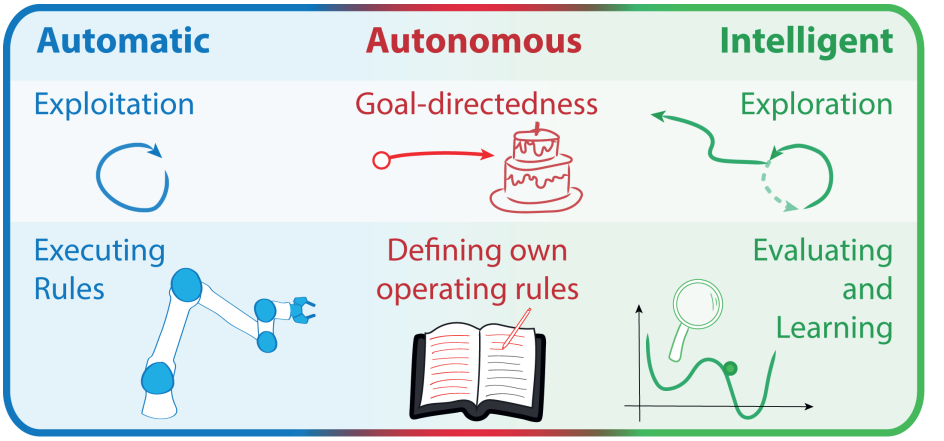


Figure 5.2: **Our proposed classification of system behaviors. (Tentative Figure)** We schematically represent some of the main differences that we use to identify automatic, autonomous, and intelligent systems. We propose that autonomy lies at the intersection between automatic and intelligent behaviors, although boundaries are not often sharp and remain dependent on the observer's perspective.

Building on these insights, we conclude that certain scenarios are better suited for automatic systems (machines) rather than more autonomous or intelligent ones (robots), particularly when solution exploration is unnecessary or undesirable. The choice between these systems depends on whether the task requires greater exploration or exploitation of solutions by artificial agents (Figure 5.2). Both kinds of systems are valuable assets for different problem domains.

However, it is essential to recognize that some applications inherently benefit from one approach over the other. Therefore, the (scientific) community should carefully consider this distinction when designing and presenting their systems, as the terms *machine* and *robot* refer to fundamentally different concepts. Consequently, we suggest that there is no necessity to classify all systems as autonomous if they do not exhibit at least the capability to balance exploration and exploitation behaviors. Similarly, there should be no reluctance in identifying a system as an automatic machine when appropriate, as reducing complexity is highly valuable from an application and design perspective, but also from a legal or ethical perspective.

On top of that, versatile solutions often emerge at the intersection of these

two domains. In particular, when dealing with the design of artificial agents, we believe that a combination of automatic and autonomous behaviors can facilitate balanced exploration and exploration strategies while navigating complex problem space more effectively. Moreover, we recall that the tradeoff between exploration and exploitation can be balanced by the necessity to maximize reward or information during operation [235]. At the same time, while the classic hardware-software perspective has driven technological advancements, it has often boxed the possibility for more problem-effective, hybrid solutions. We argue that a more integrated approach to synthetic system design could unlock new possibilities by leveraging the strengths of both hardware and software solutions in a more integrated manner.

5

# Chapter 6
# Conclusions

## 6.1 Outlook

This thesis introduces the concept of mechanical adaptability in the context of fluidic soft robotics, where fluid–structure interactions and non-linearities serve as building blocks for designing behaviors in robotic systems. What follows is a reflection on how each chapter contributes to shaping and refining these principles, gradually building from the foundations of our work to the outlook of this thesis.

In Chapter 2, we develop compliant hardware as an alternative to software in the context of soft robotics, using pneumatic coding blocks that operate as an electronics-free programming language. Our vocabulary of pneumatic circuits can be used to program both behavior and switch between behaviors in electronics-free soft robotic systems, enabling the design of reaction-based machines modeled after intuitions in *wired-intelligence*. This approach leverages non-linearities in the interactions between fluids and compliant geometries to go past the formalism of binary logic and program high-level behavior. Moreover, instead of relying on a central processing unit to dictate actuation and sensing, we decentralize these functions into the distributed hardware components themselves, as we show by combining the *If... break* and *For* pneumatic circuits to the program for the retriever demonstrator.

To enable long-term operation and unsupervised energy harvesting capabilities, we expand and blur the definition of robotic system, from the individual agent up to and including its surroundings. This change in perspective enables the design of thermal engines driven by environmental oscillations that we use to develop a thermopneumatic energy harvesting cycle in Chapter 3. To enable mechanically adaptive power management in the energy harvesting strategy, we leverage the pneumatic circuit design strategies we introduced in Chapter 2. In particular, we use the intuitions behind the *If* coding statement, on a different hardware from the one we implemented in Chapter 2, to trigger the discharge phase in the pneumatic circuit of Chapter 3. Through thermodynamic investigations, coupled with knowledge of responses of non-linear fluidic components, we design a unit cell that simultaneously has energy harvesting and energy storage capabilities. To prove that our design is compatible with the operation of soft robotic systems, we perform both outdoor and indoor experiments and use our design to achieve motion and locomotion. For this case study, the idea of bodyware is a driving force

and motivation to design electronics-free soft robotic systems meant directly for out-of-the-lab environments, and let them operate as human-independent agents.

For achieving mechanical adaptability, the capability to shape energy landscapes in dynamical systems becomes a crucial ingredient for accessing different behaviors. On top of that, studying the existence of attraction basins helps assess the behavior of these systems. In the cases we introduce in Chapter 2 and Chapter 3, mechanical adaptability, and thus such behaviors, are hardwired in the physical connection between components in fluidic circuits. In Chapter 4, instead, we take advantage of emergent phenomena in networked dynamical systems to design behaviors through phase portraits of coupled oscillators. The mathematical formalism of coupled oscillators is key to understanding and predicting how oscillatory patterns can be encoded in the phase portrait of idealized oscillatory systems. Starting from a high-level mathematical formulation of frustrated, excitable oscillators, we model and predict the behavior of experimentally observed synchronization phenomena in soft robotic oscillators. The foundations we provide in this work can simplify the interpretation of complex phenomena in synchronization and be leveraged for the design of sequenced actuation in, e.g., robotic limbs and artificial organs.

While emergent behavior we investigate in Chapter 4 differs from the hardwired responses to stimuli and inputs examined in Chapters 2 and 3, its presence shows that predictable, programmable behavior can be obtained through emergence. Therefore, following our definitions in Chapter 5, we suggest that systems such as the oscillator networks we investigate in Chapter 4 still fall within the definition of automatic systems. As a matter of fact, while essential for generating rich and adaptive responses, emergent phenomena such as the ones we investigate lack the element of goal-directedness that we deem necessary to characterize autonomous systems as discussed in Chapter 5.



Through this self-analysis, we suggest that the design solutions we describe in Chapter 2, Chapter 3, and Chapter 4 are intended to pave the way towards autonomous systems, although they are not yet an implementation of autonomous agents. Our design solutions for controlling and powering electronics-free soft robots belong instead to the *mechanically adaptive systems* discussed in Chapter 1, where goals and behaviors are injected and crystallized during the design phase. To retrospectively evaluate the relevance of the goals and results presented in this thesis, we evaluate the role of mechanical adaptability within automatic, autonomous, and intelligent systems, introducing the idea of *perceived behavioral spectrum*.

In this analysis, we find it helpful to subdivide the concept of autonomy into adaptive and proactive categories, aiming to address safety, legal, and ethical concerns while inspiring the dialogue about the future of autonomous systems.

## 6.2 Adaptability and the perceived behavioral spectrum

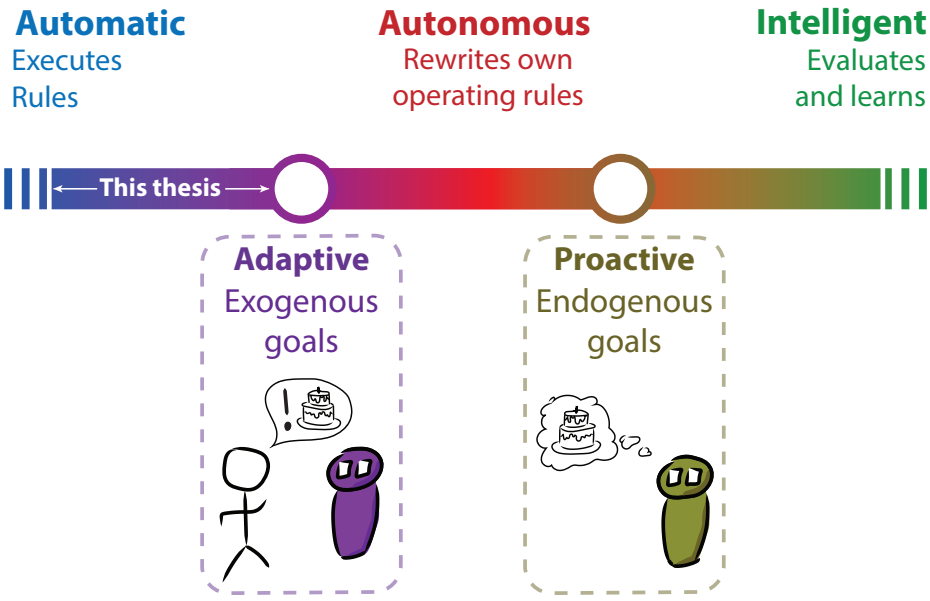


Figure 6.1: **Perceived behavioral spectrum.** Schematic representation of the main feature of automatic, adaptive, autonomous, proactive, and intelligent systems areas on an ideal axis of perceived behavioral spectrum. We highlight the contributions of this thesis in the range spanning from automatic systems to adaptive ones.

We outline our intuitions in the taxonomy of behaviors manifested by robotic agents, specifically, we use the representation in Figure 6.1, which we refer to as the perceived behavioral spectrum. With the *perceived* adjective, we indicate the necessity for an observer, thus a biased opinion, to evaluate and categorize these behaviors. It has been demonstrated that perceptual biases and human-like features can alter our judgment in defining a system, e.g., intelligent or animated [236], as shown also in early and contemporary automata in Figure 1.6.

In the same way as we can only perceive a limited portion of the electromagnetic spectrum through vision, for the perceived behavioral spectrum we focus on the behaviors that relate to our observation capabilities in terms of spatial and temporal scales. Following the analogy with the perception of the visible

light spectrum, the range of each definition and shades between regions remains arbitrary and observer-dependent. Differently from the light spectrum, the quantification of coordinates along this spectrum is not based on physical quantities. Therefore, positions and distances between coordinates in the perceived behaviors also remain arbitrary. Nevertheless, we take advantage of this representation and the regions of in-between regimes to pinpoint both the scope of our present work and directions for future research.

This framework allows us to revisit the concept of *adaptive* as an intermediate between automatic and autonomous behavior. At the same time, we suggest that systems that manifest perceived behavior in between autonomous and intelligent ones belong to the category of what we define as *proactive* systems, where the goal is endogenous. Through this representation, we suggest that it could be beneficial to specify the capability of a system to manifest preprogrammed behavior (*adaptive systems*) or take initiative based on internal goals (*proactive systems*), when describing potentially autonomous systems. We elucidate the ideas behind these definitions in the context of robotic behaviors and how reflections on the perceived behavioral spectrum can suggest a future outlook for soft robotic systems specifically.

### 6.2.1 Adaptive and *mechanically* adaptive systems



Adaptive systems modify their manifested behavior to comply with variations in their surroundings. Although they manifest the capability to display variation of a given behavior based on external cues, e.g., through closed-loop controllers, these systems only follow given algorithmic or preprogrammed pathways. Examples in this context range from emergent phototaxis in modular systems running stochastic learning [47], up to rich, yet only mechanically preprogrammed, responses in compliant structures [237] and emergent dynamics [238]. These systems exhibit the capability to adapt to ever-changing environmental conditions [239, 240], although they manifest none [101, 117] or externally determined (exogenous) goals and triggers [241], injected during the design phases.

Following this argument, a robot that escapes a maze as a result of a prescribed policy is only operating following a set of instructions dictated by its design. It is not solving a maze while striving to get out of a maze as a mouse might want to. For this reason, we believe that, to meet expectations from both academic and non-academic endeavors, we should not define such systems as autonomous. Such systems instead follow operating policies injected during the design phase, at most in an adaptive way.

For these reasons, we position adaptive systems between automatic and autonomous ones on the perceived behavioral spectrum. Although in this thesis we aimed towards autonomous systems, all the designs we introduce point mostly in

the direction of adaptive systems, as we highlight in Figure 6.1. In our studies, the energy landscapes and accessible behaviors are crystallized during the system design phase, as illustrated by the pneumatic coding blocks in Chapter 2, the thermopneumatic energy harvesting example in Chapter 3, and phase portraits for coupled oscillators in Chapter 4. Consequently, the pathways that we interpret as behaviors remain fixed, and our systems lack the goal-directedness and policy redetermination capabilities that we consider essential for autonomy.

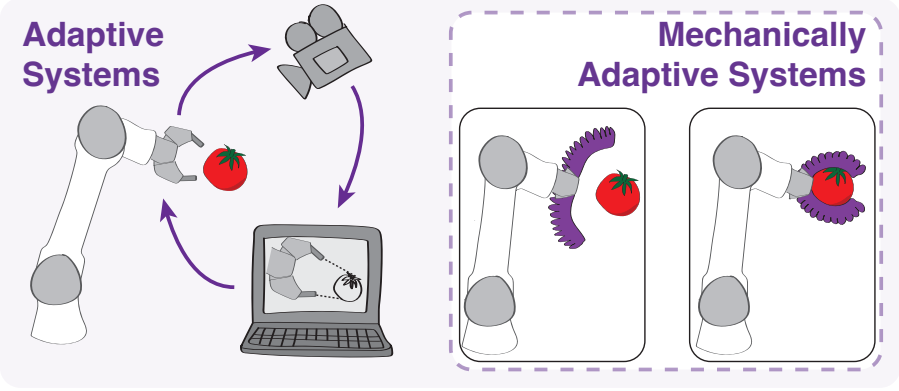


Figure 6.2: **Example of adaptive and mechanically adaptive systems for a gripping task.** In the case of adaptive systems, precise knowledge of the task environment, on top of signal transduction, is needed to assess and control a stiff gripper for achieving the gripping task of fragile objects. Conversely, for underactuated soft grippers, i.e., mechanically adaptive systems, only one scalar actuator signal, e.g., pressure, is needed to comply with the target object and assess the success of gripping tasks, as we demonstrated in [23]. We represent in purple the interfaces of the system where adaptability lies in the two different examples.

The mechanically adaptive systems we investigate in this thesis are a subclass of adaptive systems, where adaptive behavior is encoded in physical energy landscapes and mechanical properties, rather than dictated by a dedicated supervising system. We depict such a difference in Figure 6.2, in which we present an example in the gripping tasks (externally defined) where, for the adaptive system on the left, there is a supervising feedback to control and fine-tune the position of the gripper. Conversely, for the mechanically adaptive system on the right, the gripper is controlled, e.g., only by one (pneumatic) input, and, owing to its compliance, it was intrinsically designed to adapt to the target object even in an open-loop control strategy. Therefore, both systems are to be considered adaptive, yet there

are fewer control degrees of freedom in the soft robotic gripper. On the one hand, this feature makes its controller policy work in a lower-dimensional space. On the other hand, the system can now have infinite degrees of freedom with a finite amount of control degrees of freedom [242]. Therefore, as the system is underactuated, having precise control, e.g., over forces exerted and the position of the gripper, is a challenging task.

Although adaptability, and mechanical adaptability in particular, can come with the cost of sacrificing precision, we believe that mechanical adaptability can improve performance in several tasks. As an example, adaptability can still simplify control strategies over non-soft gripper counterparts, especially where high precision is not a strict requirement [50]. For this reason, we believe that soft robots and underactuated compliant systems in general are a fundamental hardware to embody the principles in mechanically adaptive systems we focus on. Rather than implying a due teleological progression from automatic to autonomous and intelligent systems, we consider mechanical adaptability as a conceptual and practical scaffold and stepping stone to move towards autonomous systems.

### 6.2.2 Proactive behavior

Proactive systems, as we define them, can reorganize controller-body-environment dynamics based on evaluations of their endogenous (internal) goals. This allows behavior to emerge as a result of learning from interaction with their environment and be defined relative to a certain environment and an internal set of goals. Unlike adaptive systems, whose control scheme can only change parametrically while keeping a fixed control scheme [243, 244] as in algorithmic programs, proactive systems have the capacity to rewire their operational scheme. These adjustments are based simultaneously on external stimuli and endogenous objectives rather than being exclusively the result of a compliant response to environmental changes. Manifesting a component of intelligence is fundamental for proactive systems for developing knowledge of their operating environments, evaluating their current policies, and exploring new strategies that are aligned with their internal goals.

The revision of these policies represents a critical element of autonomous systems and enables the adaptation of operational strategies grounded in real-world experiences and internal objectives. Consequently, both autonomous and intelligent components are essential for demonstrating proactive behavior. Proactive systems can also express a degree of adaptivity. However, their defining characteristic lies in the combination of autonomy and intelligent behavior, aimed at achieving internal goals. The task of developing and deploying proactive systems, alongside the critical examination of the consequences that arise from coexisting with proactive machines within the same environment, remains an open challenge for future research.

### 6.2.3 *Umwelt* and mechanical adaptive systems

When designing systems with exogenous goals, it is crucial to define a common ground and representation of the task environment and challenges to impose such goals on adaptive and automatic systems. Although some high-level overlap is necessary, it is not required for the representations between the artificial agent and the designer to be identical. These external representations are often referred to in literature as *umwelt* [245], in the broader sense of the sensory world of an organism, shaped by its perceptual capabilities. The umwelt representation is therefore fully determined by hardware (biological) constraints in design (evolution). To impose to an artificial system to perform a task in our shared environment, it must have sensory inputs that can align, to some extent, with our representation of the same surroundings. At the same time, the design of artificial agents must provide a representation of the task comprehensible in terms of the machine's umwelt.

To pinpoint the context of the umwelt definition and better relate it to the idea of (mechanically) adaptive systems, we use the following example. Automatic devices meant to operate in our personal space, such as an automatic mowing machine or a robotic vacuum cleaner, need to have an encoded representation of our living spaces to navigate our shared environment and perform their respective tasks. From an abstract point of view, our everyday environment becomes encoded as a percentage of area coverage in a certain preprogrammed routine of these machines. Devices such as robotic lawn mowers can, up to an extent given by their hardware and software constraints, adapt to variability in their respective environment to accomplish their tasks. However, these automatic, adaptive systems do not need to have an internal representation of the idea of short grass while striving for their exogenous goal. Therefore, their goals are not represented in human terms, but rather translated into the corresponding machine umwelt.

This translation operation is often a complicated task when many degrees of freedom are considered in complex, unstructured environments. Mechanically adaptive systems intrinsically solve some of these complications by relying on underactuated, low-dimensional systems. Consequently, these systems have an umwelt that is easier to interpret and navigate, both during the design and operation phases.

For this reason, we argue that mechanically adaptive systems can improve on automatic ones in robustness, particularly in unstructured environments. We believe that working principles such as the ones we introduced through the pneumatic coding blocks in Chapter 2 and thermopneumatic energy harvesting in Chapter 3 can facilitate these translation efforts to move towards mechanical adaptability.

At the same time, mechanical adaptability can also facilitate part of the control strategies of hybrid systems, as some operating responses can be delegated to material and geometric structure rather than mediated by controllers [246]. While

traditionally control theory focuses on causal input-output relations, in mechanical adaptive systems we allow bidirectional interactions between the controller and the to-be-controlled system and its umwelt.

## 6.3 Perspective

### 6.3.1 Reflections and open challenges

Taken together, the results presented in Chapters 2-4 reveal consistent trade-offs between control and emergent behavior in electronics-free soft robotic systems. Although emergent dynamics are often associated with adaptability, the work presented here shows that the observed behaviors are largely shaped by design choices at the level of hardware architecture and parameter selection. In this sense, emergence is not unconstrained but guided, favoring predictability and reliability. While this is advantageous from an engineering perspective, it also limits the degree to which genuinely open-ended behavior is explored.

A related limitation concerns the distinction between adaptability and versatility. The systems developed in Chapters 2 and 3 exhibit robust performance and can tolerate environmental variability, yet they remain strongly task-specific. Modularity and hardware programmability enable reuse across contexts, but higher-level reconfigurability is not explicitly encoded. Addressing this limitation will likely require the integration of reprogrammable structures and hierarchical control mechanisms, moving beyond fixed embodied control strategies.



Despite these limitations, the work presented here highlights the potential of soft robotics as a platform for bioinspired approaches to control, energy management, and coordination. Realizing this potential requires an interdisciplinary effort that integrates materials science, mechanics, control theory, and the life sciences within a shared framework. In this context, the themes of adaptability and autonomy emerge as central design objectives, particularly for developing systems capable of operating with progressively reduced human intervention.

### 6.3.2 Moving towards autonomy

The perceived behavioral spectrum we introduce in Figure 6.1 suggests that there is untapped potential in the direction of autonomous and proactive systems.

However, to move towards proactive and then autonomous systems, we deem it of utmost importance the progress of interdisciplinary approaches that integrate robotics, control theory, biology, and physics, while treating ethics and behavioral guardrails as essential design constraints. In parallel, the community should establish shared benchmarks and evaluation protocols for autonomous and proactive systems to benefit from shared definitions and visions towards autonomous

systems design. Together, these steps might produce synthetic agents that are not only proficient, performant, and resilient, but also self-improving, capable of operating safely with minimal to no supervision in real-world, out-of-the-lab conditions.

### 6.3.3 Going past dichotomies

The question of when and how *"...just physics become cognition, decision-making, memory, agency..."* [247] (and autonomy) clearly requires more in-depth study about the requirements and implications of autonomy. This investigation requires a broader philosophical and ethical inquiry that has not been touched upon in this thesis. Nevertheless, following the inspiration from examples we mention in Chapter 1, we envision that only by allowing artificial agents to operate, make *creative mistakes*[1], and learn from them, there is hope for the *Pinocchio-like* systems we design to become autonomous, artificial systems. To meet this purpose, we believe that some characterizing features, typical of soft robotics systems, are cornerstones for materializing autonomy in synthetic agents. In the following section, we discuss some of these aspects and retrospectively analyze the content of this thesis.

Aware that no singular definition nor solution could fit the plethora of scenarios systems are required to face [31], one of our goals is to introduce a different perspective by relaxing several dichotomies concerning the design of (soft) robotic systems. Through this process, we suggest that the *gray areas* in between available options are, as a matter of fact, fertile ground for innovation and future direction for the design of increasingly autonomous soft robots.

Still, we envision that going past the following dichotomies can guide and simplify choices during the design phase of adaptive and potentially autonomous systems.

**Hardware and software** The first dichotomy we suggest revising as a design strategy to advance towards autonomous systems is the role separation between hardware and software. Just like in the first Braitenberg vehicles [28] and other soft robotic implementations of such principles [248], wired intelligence [249] and embodied intelligence principles [250] prompt us to reconsider this role separation between brain and body in soft robotic systems. This simultaneous role as hardware and software building blocks can be itself distributed throughout soft robotic matter systems [100] to achieve robust and adaptive behaviors. The design approaches introduced in Chapters 2, 3, and 4 point toward a progressive reduction of the distinction between hardware and software, emphasising the

[1] Quote from Daan Frenkel, April 21st, 2023 at AMOLF (Amsterdam, NL), during the *Autonomous Matter Symposium*

embodiment of software within soft hardware. Similar to natural systems, in our work, a combination of hardware and software capabilities in decentralized, distributed, and centralized architectures can result in outputs that are more robust and compatible with a progression toward autonomous systems [251].

We propose that delegating certain software capabilities to compliant hardware represents an effective approach to move towards adaptive systems and pave the way for autonomous ones. This approach should be more integrated across the disciplines of both soft and non-soft robotics communities.

**Stiff and soft hardware** While aiming for mechanical adaptability, integrating stiff and soft hardware components in hybrid systems can enhance their operational capabilities, as often demonstrated in gripping tasks [252], or stabilizing dynamic locomotion [253]. This approach to include compliance into robotic systems by design is often considered counterintuitive, as it involves systems with infinitely many degrees of freedom that demand innovative control strategies to achieve accurate outputs in, for example, force or position [254, 255]. In these systems, additional efforts are required to ensure that the performance of soft robotic systems remains compatible and competitive with that of their non-soft counterparts. Conversely, soft hardware is already widespread, e.g., in the food industry nowadays, takes advantage of material properties only passively to compensate errors and inaccuracies in exerted forces and positions. For these reasons, we believe that embedded reflexes and responses, such as the ones we introduced in Chapter 2, together with, e.g., proprioception sensing capabilities [256] can improve the operational capabilities in out-of-the-lab scenarios. This approach will help move beyond passive adaptability in soft robots while advancing towards autonomy in artificial agents.



**Technical, ethical and legal focus** We reckon that a claim for autonomy is valid only when it is backed by an internally coherent definition that informs specific research choices and the interpretation of results. This requirement is crucial for evaluating the operational boundaries and expectations linked to research objectives.

The reflections present in Chapter 5 raise concerns that extend beyond technical considerations to encompass ethical implications related to autonomous systems in general. Embracing the idea of autonomous machines necessitates complete trust in their design limitations, capabilities, and accountability for any errors or malfunctions. Especially in the current era of the AI revolution, the world is becoming increasingly populated with devices and synthetic agents that are often referred to as "autonomous". These agents are designed to be employed in different scenarios [257], ranging from civil applications, such as domotics, artificial organs, and self-driving cars, to military uses. In this context, assessing

trust and establishing appropriate precautions are of utmost importance to avoid unwanted consequences arising from autonomous behavior.

The goal of our reflections in Chapter 5 is twofold for relaxing the dichotomy between technical challenges and ethical concerns. On the one hand, we want to stimulate discussion on the definition of automatic and autonomous systems. On the other hand, we work past technical challenges and undertake the task of establishing a foundation for an interdisciplinary framework for defining and telling automatic and autonomous systems around us. In our view, this critical study can be applied both within and beyond scientific endeavors. The reflections in Chapter 5 prompt us to retrospectively reconsider the role of preprogrammed control (Chapter 2), energy harvesting and management (Chapter 3), and emergent behavior (Chapter 4) in relation to automatic and autonomous systems. Through this process, we place under scrutiny commonly accepted, yet sometimes ill-posed, definitions that are widespread within the (soft) robotics community, with the long-term aim of addressing them more critically in future work.

### 6.3.4 Future directions for mechanical adaptability and soft robotics

In this thesis, we argue that mechanical adaptability is instrumental for implementing behavior and improving performance in robotic systems. To support this statement, we consider examples from the literature where we envision that mechanical adaptability and soft robotics can expand operational potential beyond the currently available technological options.

We assert that integrating stimulus-responsive strategies into robotic designs has the potential to influence behaviors and facilitate changes in behaviors, as illustrated by the control strategies dictated by interactions with other sub-systems (Chapter 2 and Chapter 4) or driven by environmental changes (Chapter 3). In our works on control strategies and energy harvesting, we have demonstrated that different behaviors can be obtained as a response to fluid pressure and flows to enable mechanically adaptive responses. We believe a plethora of different systems, ranging from artificial organs to moving façades, can benefit from such an approach as it simplifies the control schemes, enhances their robustness, and reduces maintenance costs.

#### Mechanical adaptability through fluid-structure interaction

To support this statement in the architectural domain, we consider two examples in the context of kirigami structures used to control and redirect air flows. On the one hand, it has been shown that controlling air circulation in so-called *urban canyon* environments can improve air exchange rate, thus increasing air quality in urban environments by using kirigami structures [258]. On the other hand,

airflows on kirigami structures can drive shape morphing, e.g., turning symmetric structures into asymmetric ones and enabling oscillatory behavior [259]. Such structural shape morphing could operate as a positive or negative feedback to the kirigami system to enhance or reduce the influence of environmental flows on desired spaces. For both cases, considering how mechanically adaptive solutions can affect the interplay between systems and their surroundings is crucial to identifying their potential for applications and reliability.

Furthermore, we believe that mechanical adaptability can be used not only to drive changes in shape-morphing structures, but also as a safety mechanism that could cooperate with already available systems as protection in case of failure. Pressure safety valves, electrical fuses, and bimetallic strips are notable examples of systems that already operate by manifesting a response only when a critical threshold value in input is exceeded, just like the case of the *If* statement we introduce in Chapter 2. In these cases, mechanically adaptive behaviors are achieved through the design of non-linear responses and their associated energy landscapes to meet application-specific requirements in, e.g., timescales of responses and power conversion. For architectural purposes, in the presence of moving components such as the ones we described in our demonstrator in Figure 1.5, we believe architects can capitalize on similar intuitions from mechanical adaptability. As a practical example, we consider the technical and environmental challenge of having active shading elements embedded in building façades, where wind gusts can have detrimental effects and cause damage to the architecture in urban environments [260]. By embedding programmable, mechanically adaptive responses in the designs, moving parts in façades could enter protection to withstand impulsive forces and oscillations caused by wind gusts, or execute preprogrammed sequences of actuation following user inputs [261] and requests.

Similar strategies and fluidic logic principles can be applied in the context of artificial organs, such as total artificial heart prosthetics. Mechanical adaptability can be integrated into future designs to leverage the coupling between fluid and soft structures, allowing for the variation of amplitudes or frequencies of pulsation based on external cues and patient needs.

Therefore, through a comprehensive examination of these systems, alongside similar methodologies from the domain of non-linear dynamics and soft robotics, we propose that the mechanically adaptive solutions detailed in Chapter 2, Chapter 3, and Chapter 4 possess the potential to integrate such functionalities through hardware-based solutions.

# Contributions

## Published

- *Regulating airflow using hybrid LCN for soft pneumatic circuits*, Kurt, E., Golestani, Y. M., Barmpoutsis, E., Picella S., Selinger, R. L. B., Overvelde, J.T.B., Liu, D., *Advanced Intelligent Systems*, 2025

- *Pneumatic coding blocks enable programmability of elecrtonics-free fluidic soft*, Picella, S., van Riet, C.M., Overvelde, J.T.B., *Science Advances*, 2024

- *A retrofit sensing strategy for soft fluidic robots*, Zou, S., Picella, S., de Vries, J. Kortman, V.G., Sakes, A., Overvelde, *Nature Communications*, 2024

- *Robust phototaxis by harnessing implicit communication in modular soft robotic systems*, Schomaker, H.A.H., Picella, S., Kung Garcia, A., van Laake, L.C., Overvelde, J.T.B., *Advanced Functional Materials*, 2024

## In preparation

- *Harvesting environmental circadian oscillations for energy autonomy of soft robots*, Picella, S., Comoretto, A., Vaarkamp, O., Overvelde, J.T.B.

- *Proficient without training: on the design of automatic and autonomous systems*, Picella, S., Steur, E., Overvelde, J.T.B.

- *Reprogrammable metamaterials through non-linearities in mechanical structures and liquid crystal elastomers*, Kurt, E., Ducarme, P., Picella, S., Overvelde, J.T.B.

- *Symmetry breaking in $N = 2$ Kuramoto-inspired oscillators: excitability and frustration for soft robotics applications*, Picella, S., Steur, E., Overvelde, J.T.B.

- *A Pneumatic, Electronics-free Toolkit for Automated Sound Design*, van Riet, C.M., Di Maggio, F., Picella, S., Overvelde, J.T.B.

# Demonstrators

- *Soft Robotic Symphony*, 3rd place at Art Exibit - Robosoft 2025 (Lausanne, CH), van Riet, C.M., Picella, S.

- *Sombra*, Biennale di Architettura 2025 (Venice, IT), MVRDV, Metadecor, Airshade Technologies, AMOLF, Alumet, Arup, Kersten Europe, Van Rossum Raadgevend Ingenieurs
- *Haptic feedback enabled by proprioperception in pneumatic grippers* - Dutch Soft Robotic Meeting 2023 (Twente, NL), Zou, S., Picella, S., van Beek, F., Sadeghi, A.
- *Robotic Gripper Competition* - Robosoft 2022 (Edinburgh, GB), de Vries, J., Zou, S., Picella, S., Commandeur, N.

# Bibliography


[1] J. A. Brandon, W. Jones, M. D. Ohman, Multidecadal increase in plastic particles in coastal ocean sediments, *Science Advances* **5** (2019).

[2] M. Cho, P. Neubauer, C. Fahrenson, I. Rechenberg, An observational study of ballooning in large spiders: Nanoscale multi-fibers enable large spiders' soaring flight, *PLOS Biology* (2017).

[3] R. D. Lorenz, *et al.*, Lander and rover histories of dust accumulation on and removal from solar arrays on mars, *Planetary and Space Science* **207**, 105337 (2021).

[4] O. Tackenberg, P. Poschlod, S. Kahmen, Dandelion seed dispersal: The horizontal wind speed does not matter for long-distance dispersal - it is updraft!, *Plant Biology* **5**, 451–454 (2003).

[5] B. Mazzolai, C. Laschi, A vision for future bioinspired and biohybrid robots, *Science Robotics* **5** (2020).

[6] D. Luo, *et al.*, Autonomous self-burying seed carriers for aerial seeding, *Nature* **614**, 463–470 (2023).

[7] R. Niiyama, *et al.*, Pouch motors: Printable soft actuators integrated with computational design, *Soft Robotics* **2**, 59–70 (2015).

[8] MVRDV, Sombra, https://www.mvrdv.com/projects/1223/sombra (2025). Accessed: 2025-12-08.

[9] J. Byun, A. Pal, J. Ko, M. Sitti, Integrated mechanical computing for autonomous soft machines, *Nature Communications* **15** (2024).

[10] L. J. Kwakernaak, M. van Hecke, Counting and sequential information processing in mechanical metamaterials, *Physical Review Letters* **130** (2023).

[11] J. Ding, M. van Hecke, Sequential snapping and pathways in a mechanical metamaterial, *The Journal of Chemical Physics* **156** (2022).

[12] G. Mao, *et al.*, Ultrafast small-scale soft electromagnetic robots, *Nature Communications* **13** (2022).

[13] N. S. Usevitch, *et al.*, An untethered isoperimetric soft robot, *Science Robotics* **5** (2020).

[14] T. Godden, B. W. Mulvey, E. Redgrave, T. Nanayakkara, Pats-wheel: A passively-transformable single-part wheel for mobile robot navigation on unstructured terrain, *IEEE Robotics and Automation Letters* **9**, 5512–5519 (2024).

[15] E. W. Hawkes, L. H. Blumenschein, J. D. Greer, A. M. Okamura, A soft robot that navigates its environment through growth, *Science Robotics* **2** (2017).

[16] R. F. Shepherd, *et al.*, Multigait soft robot, *Proceedings of the National Academy of Sciences* **108**, 20400–20403 (2011).

[17] S. Hoang, K. Karydis, P. Brisk, W. H. Grover, A pneumatic random-access memory for controlling soft robots, *PLOS ONE* **16**, e0254524 (2021).

[18] H. T. Tazwar, M. F. Antora, I. Nowroj, A. B. Rashid, Conductive polymer composites in soft robotics, flexible sensors and energy storage: Fabrication, applications and challenges, *Biosensors and Bioelectronics: X* **24**, 100597 (2025).

[19] S. Chen, H.-Z. Wang, T.-Y. Liu, J. Liu, Liquid metal smart materials toward soft robotics, *Advanced Intelligent Systems* **5** (2023).

[20] G. Librandi, E. Tubaldi, K. Bertoldi, Programming nonreciprocity and reversibility in multistable mechanical metamaterials, *Nature Communications* **12** (2021).

[21] C. Chen, *et al.*, Advancing physical intelligence for autonomous soft robots, *Science Robotics* **10** (2025).

[22] Y. Yang, *et al.*, Complex deformation in soft cylindrical structures via programmable sequential instabilities, *Advanced Materials* **36** (2024).

[23] S. Zou, *et al.*, A retrofit sensing strategy for soft fluidic robots, *Nature Communications* **15** (2024).

[24] M. Gomez, D. E. Moulton, D. Vella, Dynamics of viscoelastic snap-through, *Journal of the Mechanics and Physics of Solids* **124**, 781–813 (2019).

[25] H. Zhang, H. Zeng, A. Priimagi, O. Ikkala, Viewpoint: Pavlovian materials—functional biomimetics inspired by classical conditioning, *Advanced Materials* **32** (2020).

[26] R. C. Arkin, *Behavior-based robotics*, Intelligent Robotics and Autonomous Agents series (Bradford Books, Cambridge, MA, 1998).

[27] O. Holland, The first biologically inspired robots, *Robotica* **21**, 351–363 (2003).

[28] D. C. Dennett, V. Braitenberg, Vehicles: Experiments in synthetic psychology., *The Philosophical Review* **95**, 137 (1986).

[29] R. A. Brooks, Intelligence without reason, *Tech. rep.*, Massachusetts Institute of Technology, Artificial Intelligence Laboratory, USA (1991).

[30] R. A. Brooks, Intelligence without representation, *Artificial Intelligence* **47**, 139–159 (1991).

[31] R. A. Brooks, Elephants don't play chess, *Robotics and Autonomous Systems* **6**, 3–15 (1990).

[32] R. Bastien, T. Bohr, B. Moulia, S. Douady, Unifying model of shoot gravitropism reveals proprioception as a central feature of posture control in plants, *Proceedings of the National Academy of Sciences* **110**, 755–760 (2012).

[33] J. C. Tuthill, E. Azim, Proprioception, *Current Biology* **28**, R194–R203 (2018).

[34] J. Danaher, Welcoming robots into the moral circle: A defence of ethical behaviourism, *Science and Engineering Ethics* **26**, 2023–2049 (2019).

[35] K. Mamak, K. Kowalczewska, Military robots should not look like a humans, *Ethics and Information Technology* **25** (2023).

[36] A. G. A. G. Drachmann, *Ktesibios, Philon and Heron, a study in ancient pneumatics.*, Acta historica scientiarum naturalium et medicinalium, v. 4 (E. Munksgaard, Copenhagen, 1948).

[37] A. Marsh, Elektro the *moto/man* had the biggest brain at the 1939 world's fair, https://spectrum.ieee.org/elektro-the-motoman-had-the-biggest-brain-at-the-1939-worlds-fair (2018). "Past Forward" technology-history column.

[38] S. Dafarra, *et al.*, *Proceedings of the 2020 IEEE/RSJ International Conference on Intelligent Robots and Systems (IROS)* (Las Vegas, NV, USA, 2020), pp. 3884–3891.

[39] J. He, F. Gao, Mechanism, actuation, perception, and control of highly dynamic multilegged robots: A review, *Chinese Journal of Mechanical Engineering* **33** (2020).

[40] S. Ahrar, M. Raje, I. C. Lee, E. E. Hui, Pneumatic computers for embedded control of microfluidics, *Science Advances* **9** (2023).

[41] A. Rajappan, *et al.*, Logic-enabled textiles, *Proceedings of the National Academy of Sciences* **119** (2022).

[42] T. R. Young, M. S. Xavier, Y. K. Yong, A. J. Fleming, *2021 IEEE/RSJ International Conference on Intelligent Robots and Systems (IROS)* (IEEE, 2021), p. 2822–2829.

[43] W.-K. Lee, *et al.*, A buckling-sheet ring oscillator for electronics-free, multimodal locomotion, *Science Robotics* **7** (2022).

[44] B. V. Raemdonck, E. Milana, M. D. Volder, D. Reynaerts, B. Gorissen, Nonlinear inflatable actuators for distributed control in soft robots, *Advanced Materials* (2023).

[45] A. J. Ijspeert, Central pattern generators for locomotion control in animals and robots: A review, *Neural Networks* **21**, 642–653 (2008).

[46] P. Baconnier, *et al.*, Selective and collective actuation in active solids, *Nature Physics* **18**, 1234–1239 (2022).

[47] H. A. H. Schomaker, S. Picella, A. Küng Garcia, L. C. van Laake, J. T. B. Overvelde, Robust phototaxis by harnessing implicit communication in modular soft robotic systems, *Advanced Functional Materials* **34** (2024).

[48] V. Lobato-Rios, *et al.*, Neuromechfly, a neuromechanical model of adult drosophila melanogaster, *Nature Methods* **19**, 620–627 (2022).

[49] Z. Song, J. Zhu, J. Xu, Gaits generation of quadruped locomotion for the cpg controller by the delay-coupled vdp oscillators, *Nonlinear Dynamics* **111**, 18461–18479 (2023).

[50] E. Navas, R. Fernández, D. Sepúlveda, M. Armada, P. Gonzalez-de Santos, *2021 IEEE International Conference on Autonomous Robot Systems and Competitions (ICARSC)* (2021), pp. 167–172.

[51] M. Arfaee, A. Vis, J. Kluin, Future technologies in total artificial heart development: can a robot become as good as a donor heart?, *European Heart Journal* **43**, 4970 (2022).

[52] S. Jadhav, V. Kannanda, B. Kang, M. T. Tolley, J. P. Schulze, Soft robotic glove for kinesthetic haptic feedback in virtual reality environments, *Electronic Imaging* **29**, 19 (2017).

[53] Y. Yim, Y. Noguchi, F. Tanaka, A wearable soft robot that can alleviate the pain and fear of the wearer, *Scientific Reports* **12** (2022).

[54] D. S. Shah, *et al.*, A soft robot that adapts to environments through shape change, *Nature Machine Intelligence* **3**, 51–59 (2020).

[55] Y. Zhang, *et al.*, Progress, challenges, and prospects of soft robotics for space applications, *Advanced Intelligent Systems* **5** (2022).

[56] C. Lee, *et al.*, Soft robot review, *International Journal of Control, Automation and Systems* **15**, 3–15 (2017).

[57] M. Cianchetti, C. Laschi, A. Menciassi, P. Dario, Biomedical applications of soft robotics, *Nature Reviews Materials* **3**, 143–153 (2018).

[58] M. Hassani, MINE KAFON LAB, Mine Kafon Ball, https://minekafon.org/index.php/mine-kafon-ball/ (2025). Accessed: 2025-07-15.

[59] S. T. Mahon, A. Buchoux, M. E. Sayed, L. Teng, A. A. Stokes, *2019 2nd IEEE International Conference on Soft Robotics (RoboSoft)* (2019), pp. 782–787.

[60] S. Song, S. Joshi, J. Paik, CMOS-inspired complementary fluidic circuits for soft robots, *Advanced Science* **8**, 2100924 (2021).

[61] Y. Masuda, M. Ishikawa, Review of electronics-free robotics: Toward a highly decentralized control architecture, *Journal of Robotics and Mechatronics* **34**, 202–211 (2022).

[62] D. J. Preston, *et al.*, Digital logic for soft devices, *Proceedings of the National Academy of Sciences* **116**, 7750 (2019).

[63] J. T. B. Overvelde, T. Kloek, J. J. A. D'haen, K. Bertoldi, Amplifying the response of soft actuators by harnessing snap-through instabilities, *Proceedings of the National Academy of Sciences* **112**, 10863–10868 (2015).

[64] B. Gorissen, *et al.*, Hardware sequencing of inflatable nonlinear actuators for autonomous soft robots, *Advanced Materials* **31**, 1804598 (2018).

[65] N. Vasios, A. J. Gross, S. Soifer, J. T. Overvelde, K. Bertoldi, Harnessing viscous flow to simplify the actuation of fluidic soft robots, *Soft Robotics* **7**, 1 (2020).

[66] Y. Chi, *et al.*, Bistable and multistable actuators for soft robots: Structures, materials, and functionalities, *Advanced Materials* **34**, 2110384 (2022).

[67] Z. Jiao, *et al.*, Reprogrammable, intelligent soft origami lego coupling actuation, computation, and sensing, *The Innovation* **5**, 100549 (2024).

[68] W. W. Peterson, T. Kasami, N. Tokura, On the capabilities of while, repeat, and exit statements, *Communications of the ACM* **16**, 503 (1973).

[69] L. C. van Laake, J. de Vries, S. Malek Kani, J. T. Overvelde, A fluidic relaxation oscillator for reprogrammable sequential actuation in soft robots, *Matter* **5**, 2898–2917 (2022).

[70] M. A. Unger, H.-P. Chou, T. Thorsen, A. Scherer, S. R. Quake, Monolithic microfabricated valves and pumps by multilayer soft lithography, *Science* **288**, 113 (2000).

[71] B. Jumet, *et al.*, Fluidically programmed wearable haptic textiles, *Device* p. 100059 (2023).

[72] S. V. Kendre, *et al.*, The soft compiler: A web-based tool for the design of modular pneumatic circuits for soft robots, *IEEE Robotics and Automation Letters* **7**, 6060 (2022).

[73] K. A. Gopinathan, A. Mishra, B. R. Mutlu, J. F. Edd, M. Toner, A microfluidic transistor for automatic control of liquids, *Nature* **622**, 735 (2023).

[74] C. J. Decker, *et al.*, Programmable soft valves for digital and analog control, *Proceedings of the National Academy of Sciences* **119** (2022).

[75] E. Gallardo Hevia, *et al.*, High-gain microfluidic amplifiers: The bridge between microfluidic controllers and fluidic soft actuators, *Advanced Intelligent Systems* **4** (2022).

[76] P. Polygerinos, *et al.*, Soft robotic glove for hand rehabilitation and task specific training, *2015 IEEE International Conference on Robotics and Automation (ICRA)* (2015).

[77] R. A. Shveda, *et al.*, A wearable textile-based pneumatic energy harvesting system for assistive robotics, *Science Advances* **8** (2022).

[78] L. Paternò, L. Lorenzon, Soft robotics in wearable and implantable medical applications: Translational challenges and future outlooks, *Frontiers in Robotics and AI* **10** (2023).

[79] K. Ikuta, Y. Matsuda, D. Yajima, Y. Ota, Pressure pulse drive: A control method for the precise bending of hydraulic active catheters, *IEEE/ASME Transactions on Mechatronics* **17** (2012).

[80] N. Oh, H. Rodrigue, Toward the development of large-scale inflatable robotic arms using hot air welding, *Soft Robotics* **10** (2023).

[81] Y. Zhang, *et al.*, Miniature pneumatic actuators for soft robots by high resolution multimaterial 3d printing, *Advanced Materials Technologies* **4** (2019).

[82] A. Pal, D. Goswami, R. V. Martinez, Elastic energy storage enables rapid and programmable actuation in soft machines, *Advanced Functional Materials* **30** (2019).

[83] A. C. Glavan, *et al.*, Rapid fabrication of pressure-driven open-channel microfluidic devices in omniphobic rf paper, *Lab on a Chip* **13**, 2922 (2013).

[84] Q. Zhang, *et al.*, Logic digital fluidic in miniaturized functional devices: Perspective to the next generation of microfluidic lab on chips, *ELECTROPHORESIS* **38** (2017).

[85] I. A. Loe, T. Zheng, K. Kotani, Y. Jimbo, Controlling fluidic oscillator flow dynamics by elastic structure vibration, *Scientific Reports* **13** (2023).

[86] M. S. Imtiaz, *Advances in Experimental Medicine and Biology* (Springer Netherlands, 2012), pp. 511–520.

[87] G. M. Durak, *et al.*, Smooth or with a snap! biomechanics of trap reopening in the venus flytrap (dionaea muscipula), *Advanced Science* **9**, 2201362 (2022).

[88] F. J. Tauber, V. Slesarenko, Early career scientists converse on the future of soft robotics, *Frontiers in Robotics and AI* **10** (2023).

[89] M. Arfaee, J. Kluin, J. T. Overvelde, *2023 IEEE International Conference on Soft Robotics (RoboSoft)* (IEEE, 2023).

[90] J. de Vries, Energy efficiency of soft pneumatic extension actuators, Msc thesis, Delft University of Technology (2021).

[91] L. C. van Laake, A. Comoretto, J. T. Overvelde, On the coexistence of pressure regulation and oscillation modes in soft hysteretic valves, *Journal of Fluids and Structures* **126**, 104090 (2024).

[92] K.-J. Cho, *2019 14th ACM/IEEE International Conference on Human-Robot Interaction (HRI)* (IEEE, 2019).

[93] F. Stella, J. Hughes, The science of soft robot design: A review of motivations, methods and enabling technologies, *Frontiers in Robotics and AI* **9** (2023).

[94] E. W. Hawkes, L. H. Blumenschein, J. D. Greer, A. M. Okamura, A soft robot that navigates its environment through growth, *Science Robotics* **2** (2017).

[95] Z. Wang, S. Hirai, S. Kawamura, Challenges and opportunities in robotic food handling: A review, *Frontiers in Robotics and AI* **8** (2022).

[96] Y. Liu, J. Hou, C. Li, X. Wang, Intelligent soft robotic grippers for agricultural and food product handling: A brief review with a focus on design and control, *Advanced Intelligent Systems* **5** (2023).

[97] A. Rajappan, *et al.*, Logic-enabled textiles, *Proceedings of the National Academy of Sciences* **119** (2022).

[98] D. K. Patel, *et al.*, Highly dynamic bistable soft actuator for reconfigurable multimodal soft robots, *Advanced Materials Technologies* **8** (2022).

[99] T. Wang, *et al.*, Mechanical intelligence simplifies control in terrestrial limbless locomotion, *Science Robotics* **8** (2023).

[100] G. Oliveri, L. C. van Laake, C. Carissimo, C. Miette, J. T. B. Overvelde, Continuous learning of emergent behavior in robotic matter, *Proceedings of the National Academy of Sciences* **118** (2021).

[101] Y. Tang, *et al.*, Leveraging elastic instabilities for amplified performance: Spine-inspired high-speed and high-force soft robots, *Science Advances* **6** (2020).

[102] D. S. Shah, *et al.*, A soft robot that adapts to environments through shape change, *Nature Machine Intelligence* **3**, 51–59 (2020).

[103] R. Baines, *et al.*, Multi-environment robotic transitions through adaptive morphogenesis, *Nature* **610**, 283–289 (2022).

[104] Y. Zhao, *et al.*, Sunlight-powered self-excited oscillators for sustainable autonomous soft robotics, *Science Robotics* **8** (2023).

[105] W. Hu, G. Z. Lum, M. Mastrangeli, M. Sitti, Small-scale soft-bodied robot with multimodal locomotion, *Nature* **554**, 81–85 (2018).

[106] M. Kaynak, A. Dolev, M. S. Sakar, 3d printed acoustically programmable soft microactuators, *Soft Robotics* **10**, 246 (2023). PMID: 35704862.

[107] V. Sanchez, *et al.*, Smart thermally actuating textiles, *Advanced Materials Technologies* **5** (2020).

[108] D. Drotman, S. Jadhav, D. Sharp, C. Chan, M. T. Tolley, Electronics-free pneumatic circuits for controlling soft-legged robots, *Science Robotics* **6** (2021).

[109] G. Fusi, D. Del Giudice, O. Skarsetz, S. Di Stefano, A. Walther, Autonomous soft robots empowered by chemical reaction networks, *Advanced Materials* **35** (2022).

[110] M. Kaynak, A. Dolev, M. S. Sakar, 3d printed acoustically programmable soft microactuators, *Soft Robotics* **10**, 246 (2023). PMID: 35704862.

[111] L. X. Lyu, *et al.*, Bio-inspired untethered fully soft robots in liquid actuated by induced energy gradients, *National Science Review* **6**, 970–981 (2019).

[112] C. A. Aubin, *et al.*, Towards enduring autonomous robots via embodied energy, *Nature* **602**, 393–402 (2022).

[113] R. Louis, K. Shea, Solar-powered thermo-pneumatic actuators for passively controlled adaptive shading, *Smart Materials and Structures* **33**, 125034 (2024).

[114] M. Sogabe, F. C. Uetrecht, T. Kanno, T. Miyazaki, K. Kawashima, A quick response soft actuator by miniaturized liquid-to-gas phase change mechanism with environmental thermal source, *Sensors and Actuators A: Physical* **361**, 114587 (2023).

[115] J. W. Boley, *et al.*, Shape-shifting structured lattices via multimaterial 4d printing, *Proceedings of the National Academy of Sciences* **116**, 20856–20862 (2019).

[116] H. Y. Jeong, E. Lee, S. Ha, N. Kim, Y. C. Jun, Multistable thermal actuators via multimaterial 4d printing, *Advanced Materials Technologies* **4** (2018).

[117] Y. Zhao, *et al.*, Twisting for soft intelligent autonomous robot in unstructured environments, *Proceedings of the National Academy of Sciences* **119** (2022).

[118] Y. Chi, Y. Hong, Y. Zhao, Y. Li, J. Yin, Snapping for high-speed and high-efficient butterfly stroke–like soft swimmer, *Science Advances* **8** (2022).

[119] B. Jumet, M. D. Bell, V. Sanchez, D. J. Preston, A data-driven review of soft robotics, *Advanced Intelligent Systems* **4** (2021).

[120] Q. Lu, *et al.*, *Proceedings of the 36th Annual ACM Symposium on User Interface Software and Technology*, UIST '23 (ACM, 2023).

[121] H.-T. D. Chun, N. K. Taylor, A. A. Stokes, Energy-based abstraction for soft robotic system development, *Advanced Intelligent Systems* **5** (2021).

[122] R. Louis, K. Shea, Solar-powered thermo-pneumatic actuators for passively controlled adaptive shading, *Smart Materials and Structures* **33**, 125034 (2024).

[123] K. Nakahara, K. Narumi, R. Niiyama, Y. Kawahara, *2017 IEEE International Conference on Robotics and Automation (ICRA)* (IEEE, 2017).

[124] T. Exley, *et al.*, Agonist-antagonist pouch motors: Bidirectional soft actuators enhanced by thermally responsive peltier elements (2024).

[125] R. Uramune, *et al.*, Hapouch: A miniaturized, soft, and wearable haptic display device using a liquid-to-gas phase change actuator, *IEEE Access* **10**, 16830–16842 (2022).

[126] M. Garrad, G. Soter, A. T. Conn, H. Hauser, J. Rossiter, *2019 2nd IEEE International Conference on Soft Robotics (RoboSoft)* (IEEE, 2019).

[127] Y. Nishikawa, M. Matsumoto, A design of fully soft robot actuated by gas–liquid phase change, *Advanced Robotics* **33**, 567–575 (2019).

[128] E. Shahabi, M. Shabani, F. Meder, B. Mazzolai, Solar spectrum light-driven silicone-based fluidic actuators, *Advanced Physics Research* (2024).

[129] S. Hirai, *et al.*, Micro elastic pouch motors: Elastically deformable and miniaturized soft actuators using liquid-to-gas phase change, *IEEE Robotics and Automation Letters* **6**, 5373–5380 (2021).

[130] D. J. Kang, S. An, A. L. Yarin, S. Anand, Programmable soft robotics based on nano-textured thermo-responsive actuators, *Nanoscale* **11**, 2065–2070 (2019).

[131] B. Hao, *et al.*, Focused ultrasound enables selective actuation and newton-level force output of untethered soft robots, *Nature Communications* **15** (2024).

[132] Y. I. Kim, S. W. Kim, S. An, A. L. Yarin, S. S. Yoon, Untethered nanotextured thermopneumatic soft actuators operable with different stimuli: Thermal blowing, infrared light, and electromagnetic field, *International Journal of Energy Research* **2023**, 1–12 (2023).

[133] S. Deglurkar, C. Xiao, L. Gockowski, M. T. Valentine, E. W. Hawkes, A light- and heat-seeking vine-inspired robot with material-level responsiveness, *IEEE Robotics and Automation Letters* **9**, 1–8 (2024).

[134] A. M. R. Abolhosen, *et al.*, Functional soft robotic composites based on organic photovoltaic and dielectric elastomer actuator, *Scientific Reports* **14** (2024).

[135] E. Galloni, G. Fontana, S. Staccone, Design and experimental analysis of a mini orc (organic rankine cycle) power plant based on r245fa working fluid, *Energy* **90**, 768–775 (2015).

[136] A. Comoretto, H. A. H. Schomaker, J. T. B. Overvelde, Physical synchronization of soft self-oscillating limbs for fast and autonomous locomotion, *Science* **388**, 610 (2025).

[137] J. Liu, P. Li, Z. Huang, H. Liu, T. Huang, Earthworm-inspired multimodal pneumatic continuous soft robot enhanced by winding transmission, *Cyborg and Bionic Systems* **6** (2025).

[138] A. Kandhari, Y. Wang, H. J. Chiel, R. D. Quinn, K. A. Daltorio, An analysis of peristaltic locomotion for maximizing velocity or minimizing cost of transport of earthworm-like robots, *Soft Robotics* **8**, 485–505 (2021).

[139] A. Sakes, *et al.*, Shooting mechanisms in nature: A systematic review, *PLOS ONE* **11** (2016).

[140] J. Kohlmeyer, B. Volkmann-Kohlmeyer, Fungi on juncus roemerianus. 6. glomerobolus gen. nov., the first ballistic member of agonomycetales, *Mycologia* **88**, 328–337 (1996).

[141] S. Li, Y. Zhang, J. Liu, Seed ejection mechanism in an oxalis species, *Scientific Reports* **10** (2020).

[142] S. M. Deban, J. C. O'Reilly, U. Dicke, J. L. van Leeuwen, Extremely high-power tongue projection in plethodontid salamanders, *J. Exp. Biol.* **210**, 655 (2007).

[143] A. Karabulut, *et al.*, The architecture and operating mechanism of a cnidarian stinging organelle, *Nature Communications* **13** (2022).

[144] B. An, *et al.*, *Proceedings of the 2018 CHI Conference on Human Factors in Computing Systems*, CHI '18 (ACM, 2018).

[145] L. Born, Flectofold und flectoline - entwicklung adaptiver fassadenbauteile aus faserverbundkunststoff, *AG Textile Techniken* (2023).

[146] W. Yan, *et al.*, Self-sustained, continuous jumping of a light-driven electronics-free insect-scale soft robot, *Advanced Materials* (2025).

[147] A. H. Gelebart, *et al.*, Making waves in a photoactive polymer film, *Nature* **546**, 632–636 (2017).

[148] C. Zheng, S. Jia, Bioinspired photoresponsive soft robotic lens, *Science Robotics* **10** (2025).

[149] T. Cheng, *et al.*, Weather-responsive adaptive shading through biobased and bioinspired hygromorphic 4d-printing, *Nature Communications* **15** (2024).

[150] S. Picella, C. M. van Riet, J. T. B. Overvelde, Pneumatic coding blocks enable programmability of electronics-free fluidic soft robots, *Science Advances* **10** (2024).

[151] A. C. Robin, Paper bag problem, *Bulletin of the Institute of Mathematics and its Applications* **40**, 104–107 (2004).

[152] R. F. Shepherd, *et al.*, Using explosions to power a soft robot, *Angewandte Chemie International Edition* **52**, 2892–2896 (2013).

[153] C. A. Aubin, *et al.*, Powerful, soft combustion actuators for insect-scale robots, *Science* **381**, 1212–1217 (2023).

[154] M. A. Bell, B. Gorissen, K. Bertoldi, J. C. Weaver, R. J. Wood, A modular and self-contained fluidic engine for soft actuators, *Advanced Intelligent Systems* **4** (2021).

[155] S. D. Gollob, *et al.*, *2025 IEEE 8th International Conference on Soft Robotics (RoboSoft)* (IEEE, 2025), p. 1–8.

[156] D. Fonseca, P. Neto, Electrically-driven phase transition actuators to power soft robot designs, *Nature Communications* **16** (2025).

[157] M. Adami, A. Seibel, On-board pneumatic pressure generation methods for soft robotics applications, *Actuators* **8**, 2 (2018).

[158] J. Wang, *et al.*, Hybrid films with excellent oxygen and water vapor barrier properties as efficient anticorrosive coatings, *RSC Advances* **8**, 21651–21657 (2018).

[159] A. Liga, *et al.*, Study on heat transfer coefficients during cooling of pet bottles for food beverages, *Heat and Mass Transfer* **52**, 1479–1488 (2015).

[160] B. Saggin, *et al.*, Non-contact measurement of the temperature profile of pet preforms, *Measurement* **133**, 412–420 (2019).

[161] D. Meng, *et al.*, Polyethylene terephthalate-based colored emitters for efficient daytime radiative cooling, *Results in Physics* **46**, 106254 (2023).

[162] J. C. Wyngaard, Book review: Atmospheric turbulence. models and methods for engineering applications by hans a. panofsky and john a. dutton, *AIAA Journal* **23**, 2008–2009 (1985).

[163] Y. A. Cengel, M. A. Boles, *Thermodynamics: An Engineering Approach* (McGraw-Hill Professional, New York, NY, 2014), 8th edn.

[164] A. L. Hodgkin, A. F. Huxley, A quantitative description of membrane current and its application to conduction and excitation in nerve, *The Journal of Physiology* **117**, 500–544 (1952).

[165] D. Cebrián-Lacasa, P. Parra-Rivas, D. Ruiz-Reynés, L. Gelens, Six decades of the fitzhugh–nagumo model: A guide through its spatio-temporal dynamics and influence across disciplines, *Physics Reports* **1096**, 1–39 (2024).

[166] J. L. Hindmarsh, R. M. Rose, A model of neuronal bursting using three coupled first order differential equations, *Proceedings of the Royal Society of London. Series B. Biological Sciences* **221**, 87–102 (1984).

[167] B. Ermentrout, Type i membranes, phase resetting curves, and synchrony, *Neural Computation* **8**, 979–1001 (1996).

[168] C. Morris, H. Lecar, Voltage oscillations in the barnacle giant muscle fiber, *Biophysical Journal* **35**, 193–213 (1981).

[169] K. P. O'Keeffe, S. H. Strogatz, Dynamics of a population of oscillatory and excitable elements, *Physical Review E* **93** (2016).

[170] J. A. Acebrón, L. L. Bonilla, C. J. Pérez Vicente, F. Ritort, R. Spigler, The kuramoto model: A simple paradigm for synchronization phenomena, *Reviews of Modern Physics* **77**, 137–185 (2005).

[171] M. Breakspear, S. Heitmann, A. Daffertshofer, Generative Models of Cortical Oscillations: Neurobiological Implications of the Kuramoto Model, *Frontiers in Human Neuroscience* **4** (2010).

[172] T. Po, E. Kanso, M. J. McHenry, Cooperative transport in sea star locomotion, *Current Biology* **34**, 2551 (2024).

[173] F. C. Hoppensteadt, E. M. Izhikevich, *Weakly Connected Neural Networks* (Springer New York, 1997).

[174] D. J. Preston, *et al.*, A soft ring oscillator, *Science Robotics* **4** (2019).

[175] M. Mousa, A. Rezanejad, B. Gorissen, A. E. Forte, Frequency-controlled fluidic oscillators for soft robots, *Advanced Science* **11** (2024).

[176] A. Jenkins, Self-oscillation, *Physics Reports* **525**, 167–222 (2013).

[177] Y. Kuramoto, Collective synchronization of pulse-coupled oscillators and excitable units, *Physica D: Nonlinear Phenomena* **50**, 15–30 (1991).

[178] N. Vasios, A. J. Gross, S. Soifer, J. T. Overvelde, K. Bertoldi, Harnessing viscous flow to simplify the actuation of fluidic soft robots, *Soft Robotics* **7**, 1–9 (2020).

[179] B. van der Pol, J. van der Mark, Lxxii.the heartbeat considered as a relaxation oscillation, and an electrical model of the heart, *The London, Edinburgh, and Dublin Philosophical Magazine and Journal of Science* **6**, 763–775 (1928).

[180] V. Flovik, F. Macià, E. Wahlström, Describing synchronization and topological excitations in arrays of magnetic spin torque oscillators through the Kuramoto model, *Scientific Reports* **6** (2016).

[181] G. Elisha, *et al.*, A mechanics-based perspective on the pressure-cross-sectional area loop within the esophageal body, *Frontiers in Physiology* **13** (2023).

[182] B. C. Daniels, S. T. M. Dissanayake, B. R. Trees, Synchronization of coupled rotators: Josephson junction ladders and the locally coupled kuramoto model, *Physical Review E* **67** (2003).

[183] H. Sakaguchi, Y. Kuramoto, A soluble active rotator model showing phase transitions via mutual entrainment, *Progress of Theoretical Physics* **76**, 576–581 (1986).

[184] S. Dutta, *et al.*, Programmable coupled oscillators for synchronized locomotion, *Nature Communications* **10** (2019).

[185] L. Righetti, A. J. Ijspeert, *2008 IEEE International Conference on Robotics and Automation* (IEEE, 2008), p. 819–824.

[186] A. Crespi, A. Badertscher, A. Guignard, A. Ijspeert, *Proceedings of the 2005 IEEE International Conference on Robotics and Automation* (IEEE, 2005), pp. 3024–3028.

[187] A. J. Ijspeert, A connectionist central pattern generator for the aquatic and terrestrial gaits of a simulated salamander, *Biological Cybernetics* **84**, 331–348 (2001).

[188] A. J. Ijspeert, A. Crespi, D. Ryczko, J.-M. Cabelguen, From swimming to walking with a salamander robot driven by a spinal cord model, *Science* **315**, 1416–1420 (2007).

[189] K. Yasui, *et al.*, Multisensory feedback makes swimming circuits robust against spinal transection and enables terrestrial crawling in elongate fish, *Proceedings of the National Academy of Sciences* **122** (2025).

[190] A. J. Ijspeert, Central pattern generators for locomotion control in animals and robots: A review, *Neural Networks* **21**, 642–653 (2008).

[191] A. J. Ijspeert, M. A. Daley, Integration of feedforward and feedback control in the neuromechanics of vertebrate locomotion: a review of experimental, simulation and robotic studies, *Journal of Experimental Biology* **226** (2023).

[192] A. Badri-Spröwitz, A. Aghamaleki Sarvestani, M. Sitti, M. A. Daley, Birdbot achieves energy-efficient gait with minimal control using avian-inspired leg clutching, *Science Robotics* **7** (2022).

[193] B. Li, K. Y. M. Wong, Optimizing synchronization stability of the kuramoto model in complex networks and power grids, *Physical Review E* **95** (2017).

[194] T. Iwasaki, M. Zheng, Sensory feedback mechanism underlying entrainment of central pattern generator to mechanical resonance, *Biological Cybernetics* **94**, 245–261 (2006).

[195] G. Bellegarda, A. Ijspeert, Cpg-rl: Learning central pattern generators for quadruped locomotion, *IEEE Robotics and Automation Letters* **7**, 12547–12554 (2022).

[196] A. Szorkovszky, F. Veenstra, K. Glette, Central pattern generators evolved for real-time adaptation to rhythmic stimuli, *Bioinspiration and Biomimetics* **18**, 046020 (2023).

[197] R. Taylor, Finding Non-Zero Stable Fixed Points of the Weighted Kuramoto model is NP-hard (2015).

[198] E. Ott, T. M. Antonsen, Low dimensional behavior of large systems of globally coupled oscillators, *Chaos: An Interdisciplinary Journal of Nonlinear Science* **18** (2008).

[199] J. L. van Hemmen, W. F. Wreszinski, Lyapunov function for the kuramoto model of nonlinearly coupled oscillators, *Journal of Statistical Physics* **72**, 145–166 (1993).

[200] Y. Pomeau, P. Manneville, Intermittent transition to turbulence in dissipative dynamical systems, *Communications in Mathematical Physics* **74**, 189–197 (1980).

[201] E. Izhikevich, Y. Kuramoto, *Weakly Coupled Oscillators* (Elsevier, 2006), p. 448–453.

[202] S. R. Jammalamadaka, A. SenGupta, *Topics in Circular Statistics* (WORLD SCIENTIFIC, 2001).

[203] A. Spröwitz, *et al.*, Towards dynamic trot gait locomotion: Design, control, and experiments with cheetah-cub, a compliant quadruped robot, *The International Journal of Robotics Research* **32**, 932–950 (2013).

[204] M. Arfaee, *et al.*, A soft robotic total artificial hybrid heart, *Nature Communications* **16** (2025).

[205] M. K. Friedberg, A. N. Redington, Right versus left ventricular failure: Differences, similarities, and interactions, *Circulation* **129**, 1033–1044 (2014).

[206] T. Bombardini, *et al.*, Diastolic time – frequency relation in the stress echo lab: filling timing and flow at different heart rates, *Cardiovascular Ultrasound* **6** (2008).

[207] B. Ottino-Löffler, S. H. Strogatz, Kuramoto model with uniformly spaced frequencies: Finite-n asymptotics of the locking threshold, *Physical Review E* **93** (2016).

[208] A. Comoretto, H. A. H. Schomaker, J. T. B. Overvelde, Physical synchronization of soft self-oscillating limbs for fast and autonomous locomotion, *Science* **388**, 610–615 (2025).

[209] F. M. White, *Fluid Mechanics* (McGraw Hill Higher Education, Maidenhead, England, 2010), 7th edn.

[210] T. Insperger, On the Approximation of Delayed Systems by Taylor Series Expansion, *Journal of Computational and Nonlinear Dynamics* **10** (2015).

[211] J. Veenstra, *et al.*, Non-reciprocal topological solitons in active metamaterials, *Nature* **627**, 528–533 (2024).

[212] B. Herrmann, P. Oswald, R. Semaan, S. L. Brunton, Modeling synchronization in forced turbulent oscillator flows, *Communications Physics* **3** (2020).

[213] M. Arfaee, *et al.*, Toward developing a compact total artificial heart using a soft robotic fluidic transmission system, *Science Advances* **11** (2025).

[214] D. Owaki, M. Goda, S. Miyazawa, A. Ishiguro, A minimal model describing hexapedal interlimb coordination: The tegotae-based approach, *Frontiers in Neurorobotics* **11** (2017).

[215] C. L. Kelly, *et al.*, Synthetic negative feedback circuits using engineered small rnas, *Nucleic Acids Research* **46**, 9875–9889 (2018).

[216] R. Pfeifer, C. Scheier, *Understanding Intelligence*, A Bradford Book (Bradford Books, Cambridge, MA, 2001).

[217] K. Capek, C. Novack, *R.U.R. (Rossum's Universal Robots)* (Penguin, New York, NY, 2004).

[218] Q. He, Z. Wang, K. Li, Y. Zhang, M. Li, Research on autonomous navigation of mobile robots based on IA-DWA algorithm, *Sci. Rep.* **15**, 2099 (2025).

[219] R. Baines, *et al.*, Multi-environment robotic transitions through adaptive morphogenesis, *Nature* **610**, 283–289 (2022).

[220] P. Wang, On defining artificial intelligence, *Journal of Artificial General Intelligence* **10**, 1–37 (2019).

[221] F. Emmert-Streib, O. Yli-Harja, M. Dehmer, Artificial intelligence: A clarification of misconceptions, myths and desired status, *Frontiers in Artificial Intelligence* **3** (2020).

[222] S. Legg, M. Hutter, Universal intelligence: A definition of machine intelligence, *arXiv* (2007).

[223] S. Chen, *et al.*, A taxonomy for autonomous vehicles considering ambient road infrastructure, *Sustainability* **15**, 11258 (2023).

[224] R. Pfeifer, Design principles for autonomous agents: A case study of classification, *Artificial Life and Robotics* **1**, 43–46 (1997).

[225] C. Castelfranchi, R. Falcone, *From Automaticity to Autonomy: The Frontier of Artificial Agents* (Springer US, 2003), p. 103–136.

[226] S. Kim, J. R. Anthis, S. Sebo, *Proceedings of the 2024 ACM/IEEE International Conference on Human-Robot Interaction*, HRI '24 (ACM, 2024), p. 381–393.

[227] L. C. van Laake, J. T. B. Overvelde, Bio-inspired autonomy in soft robots, *Communications Materials* **5** (2024).

[228] W. F. Haselager, Robotics, philosophy and the problems of autonomy, *Pragmatics and Cognition* **13**, 515–532 (2005).

[229] F. Stella, J. Hughes, The science of soft robot design: A review of motivations, methods and enabling technologies, *Frontiers in Robotics and AI* **9** (2023).

[230] V. G. Kortman, B. Mazzolai, A. Sakes, J. Jovanova, Perspectives on intelligence in soft robotics, *Advanced Intelligent Systems* (2024).

[231] G. G. Rigatos, *Advanced Models of Neural Networks* (Springer Berlin Heidelberg, 2015).

[232] J. N. Reddy, *Theory and Analysis of Elastic Plates and Shells* (CRC Press, 2006).

[233] B. Saintyves, M. Spenko, H. M. Jaeger, A self-organizing robotic aggregate using solid and liquid-like collective states, *Science Robotics* **9** (2024).

[234] T. Smithers, Autonomy in robots and other agents, *Brain and Cognition* **34**, 88–106 (1997).

[235] E. J. Peterson, T. D. Verstynen, Embracing curiosity eliminates the exploration-exploitation dilemma, *bioRXiv* (2019).

[236] C. Bartneck, T. Kanda, O. Mubin, A. Al Mahmud, Does the design of a robot influence its animacy and perceived intelligence?, *International Journal of Social Robotics* **1**, 195–204 (2009).

[237] Y. Zhao, *et al.*, Sunlight-powered self-excited oscillators for sustainable autonomous soft robotics, *Science Robotics* **8** (2023).

[238] Y. Xi, T. Marzin, R. B. Huang, T. J. Jones, P.-T. Brun, Emergent behaviors of buckling-driven elasto-active structures, *Proceedings of the National Academy of Sciences* **121** (2024).

[239] K. Narumi, *et al.*, Liquid pouch motors: Printable planar actuators driven by liquid-to-gas phase change for shape-changing interfaces, *IEEE Robotics and Automation Letters* **5**, 3915–3922 (2020).

[240] J. Werfel, K. Petersen, R. Nagpal, Designing collective behavior in a termite-inspired robot construction team, *Science* **343**, 754–758 (2014).

[241] H. Suda, *et al.*, Calcium dynamics during trap closure visualized in transgenic venus flytrap, *Nature Plants* **6**, 1219 (2020).

[242] F. Stella, Q. Guan, J. Leng, C. Della Santina, J. Hughes, Piecewise affine curvature model: a reduced-order model for soft robot-environment interaction beyond pcc (2022).

[243] A. Kazemipour, O. Fischer, Y. Toshimitsu, K. W. Wong, R. K. Katzschmann, *2022 International Conference on Robotics and Automation (ICRA)* (IEEE, 2022), p. 3259–3265.

[244] M. Trumic, C. della Santina, K. Jovanovic, A. Fagiolini, *2021 American Control Conference (ACC)* (IEEE, 2021), p. 4991–4996.

[245] J. von Uexküll, *Umwelt und Innenwelt der Tiere* (Springer Berlin Heidelberg, 1921).

[246] M. Polzin, Q. Guan, J. Hughes, Robotic locomotion through active and passive morphological adaptation in extreme outdoor environments, *Science Robotics* **10** (2025).

[247] The Levin Lab, https://drmichaellevin.org/resources/. Accessed: 2025-09-20.

[248] L. M. Kamp, *et al.*, Reprogrammable sequencing for physically intelligent underactuated robots, *Proceedings of the National Academy of Sciences* **122** (2025).

[249] I. Rañó, Biologically inspired navigation primitives, *Robotics and Autonomous Systems* **62**, 1361–1370 (2014).

[250] R. Pfeifer, F. Iida, *Embodied Artificial Intelligence*, Lecture notes in computer science (Springer Berlin Heidelberg, Berlin, Heidelberg, 2004), pp. 1–26.

[251] B. Hochner, An embodied view of octopus neurobiology, *Current Biology* **22**, R887–R892 (2012).

[252] H. Stuart, S. Wang, O. Khatib, M. R. Cutkosky, The ocean one hands: An adaptive design for robust marine manipulation, *The International Journal of Robotics Research* **36**, 150 (2017).

[253] K. Rushdi, D. Koop, C. Q. Wu, Experimental studies on passive dynamic bipedal walking, *Robotics and Autonomous Systems* **62**, 446–455 (2014).

[254] M. Trumic, C. della Santina, K. Jovanovic, A. Fagiolini, *2021 American Control Conference (ACC)* (IEEE, 2021).

[255] C. Della Santina, R. K. Katzschmann, A. Bicchi, D. Rus, Model-based dynamic feedback control of a planar soft robot: trajectory tracking and interaction with the environment, *The International Journal of Robotics Research* **39**, 490–513 (2020).

[256] K. Barvenik, Z. Coogan, G. Librandi, M. Pezzulla, E. Tubaldi, Tactile sensing and grasping through thin-shell buckling, *Advanced Intelligent Systems* **6** (2024).

[257] Editorial, Ai will transform science - now researchers must learn to tame it, *Nature* **621**, 658–658 (2023).

[258] L. Stein-Montalvo, L. Ding, M. Hultmark, S. Adriaenssens, E. Bou-Zeid, Kirigami-inspired wind steering for natural ventilation, *Journal of Wind Engineering and Industrial Aerodynamics* **246**, 105667 (2024).

[259] T. Marzin, K. Le Hay, E. de Langre, S. Ramananarivo, Flow-induced deformation of kirigami sheets, *Physical Review Fluids* **7** (2022).

[260] O. Metwally, H. A. Ibrahim, A. Elawady, I. Zisis, A. G. Chowdhury, Wind load impact on tall building facades: damage observations during severe wind events and wind tunnel testing, *Frontiers in Built Environment* **10** (2025).

[261] M. Architecture, HypoSurface, https://parametrichouse.com/hyposurface-mit/ (2025). Accessed: 2025-07-11.

# About the Author

Sergio Picella is a PhD working in the Soft Robotic Matter Group at AMOLF and the Dynamics and Control section at TU/e (Eindhoven University of Technology). He completed his Bachelor in Physics at Università degli Studi "Aldo Moro" di Bari and his Master of Science at Utrecht University in Experimental Physics, focusing on Complex Systems.

During his PhD, he investigated the encoding of behaviors within soft robotic systems. His research explored the interplay between fluidic and mechanical non-linearities, primarily focusing on establishing design principles to embed adaptability into electronics-free systems. For his work, he employed experimental and modeling approaches to expand both the functional capabilities and the adaptive features of soft robotics.

Present projects include architectural design, with a particular emphasis on the development of self-regulating façades and demonstrators. These efforts aim to translate findings from laboratory settings into real-world applications.

Outside the lab, and whenever the weather allows, Sergio is most often sailing or running. On Wednesday evening, he hosts a Language Café in Utrecht.

# Acknowledgements

I have always appreciated taking the time and space to thank those around me. However, page and time constraints compel me to be brief. I will do my best to comply with these boundary conditions, but I am going, at least, to soften them a bit.

I would have never been able to do this alone. This holds for what concerns not only academic ideas but, most importantly for me, the energies I gathered by interacting with you all. I have been fortunate over these years to have had so many safe harbours in each and every one of you. I feel protected, supported, and cared for. I hope I will be able to express my gratitude to you all, if not in these few (?) lines, at least with a word, a letter, a hug, or a gesture of appreciation.

Dear Bas, words cannot express the (positive!) impact you had on me. You are living proof that one can be serious and professional without being dull, knowledgeable without being pedantic, and goal-orientated while being empathetic. I enjoyed working and learning with/from you and thanks for always pushing me an extra mile. Thank you for creating a strong foundation to bring exceptional people together while allowing and encouraging *playful fruitful randomness* in the lab. Thanks for bringing to the table new challenges and toys to study for inspiring conversations and understanding. Thanks for providing me with the time, space, and resources to succeed, as well as for allowing me to make mistakes when I needed to. It has been a great pleasure working with you, and I really look forward to finishing our works together and keeping in touch with you.

Dear Erik, your support during my very non-linear research trajectories in these years has been fundamental to overcoming many obstacles and conceptual dead-ends. I will always cherish the good memories of our meetings, despite their irregular cadence and the sensation of sweet frustration when you accurately pointed out internal inconsistencies in terminology and approach. Your attention, accuracy, and precision have taught me a great deal over the years. I want to thank you for consistently providing a good reference and book to share with me. Thank you for guiding me in the various research projects and for bringing me back to reality, encouraging me to refocus through your Dutch-styled comments. I have learnt a great deal from you and the entire TUe system.

From my shy initial draft to the completed work you see here, your input on content, format, and style has significantly improved this thesis, following the feedback, comments, and observations from all of you working together as a committee. Thank you, Perla, Jonathan, Florian, Nathan, and Ali, for thoroughly

reading my thesis. I am grateful to all of you for sharing your perspectives and honest opinions on my work.

I wish for all of you reading this to have such a combination of friends and colleagues in your life, embodied in such peculiar human beings. To Rodolfo and Paul. You have never withdrawn from random talk, jumping into the lab, sharing a nice joke/meme, cooking weird fishes, being a rubber duck for self-reflections, and sailing through mental, academic and personal storms. I wish you all could have such great and inspiring colleagues, ready to keep you upright, push you forward, hold you back, and party hard when it is time to. Many ideas in this thesis have been inspired and/or polished after the timeless discussions we had. I am honoured by how much you have cared about me in these years and for your invaluable friendships. Rodolfo, sharing with you this full Dutch experience from day zero up to now, it has been a wonderful ride. Hope to keep on perculating with you as long as I can. Paul(o), you are a bright mind and a master of many domains (from chess to monocyle, from CAD to Veritasium, from magician to football prodigy), as you are not afraid to recall us. No jokes here. You are an amazing person, and I feel so lucky to have shared so many Amolf and not Amolf hours with you. You are a generous human being and a kind researcher, even people have formatting styles you don't really approve.

To all the people who have been around me during these Dutch years: I am grateful to have shared life paths with you and look forward to keeping in touch for our respective following steps in life.

To the JacksonMartinez crowd. The infinite amount of gourmet food, improv dinner, Munchkin, random nights, drinks and laughs. Without you, my life would have been significantly flatter in these flatlands. In these years, I have deeply valued our connexions, spontaneous interactions, and the desire to reconvene at the end of the week to spend time together, from puzzles to boat outings and impressive dinners. You all provided great solidity and shelter, and I could not hope for a better mixture of family-friends to have had close to me to rejoice of good times as well as to fight PhD, weather and life stresses. You have been a constant in my life in these years, and I hope we manage to be in touch for our respective upcoming futures.

To Fracucci, for the conversations, help and for bringing me out of my shell in these years. Your presence has helped me a great deal. To AnnaP (and Vanda), for always being there for me. I love the way you balanced your life (even if you don't think so), you are a great inspiration to me. To Claudio, for his calming aura, lessons on how to enjoy and slow down, to the greenwashing talks and paper companies ideas, your broad specificity of focuses in crafts, and boat repair skills. To Leo and Leo (you decide who is first): I enjoyed all the conversations we had, and witnessing the arguments between the two of you has been the greatest lesson in dialectics ever. To Alicia, for always being careful and attentive to all

of us. You are a kind human being. Thanks to Enrico for the graphical arts that made the cover of this thesis good-looking, bringing my lump of ideas into such a beautiful output. To Luca, for the improv culinary life-lessons and your self-criticisms during the various cooking sessions (and to be a winning cleric together with me in Munchkin!). To Karina for her energy and enthusiasm.

To Manfra for being a wonderful first housemate in NL. To Giuditta for bringing and literally being a Sun to us every time she visited. To Millo and his absolute care for the underlying understanding. To Jack for guiding me through topological mental strolls at late hours during parties. To Lois for encouraging me to go the extra mile for Sombra. To Becca for sharing her stream of consciousness and ideas while debating microfluidic sensing. To Lotta and Jos for their friendship and exquisite cuisine.

To that little jewel in fibreglass, spiderwebs, love, and improvised haute cuisine of the SantaNicola. Thank you for keeping us afloat during the warmer times in the NL. To my fellow co-capitains Claudio, Francesca, Rudy and Simo. I cherished every moment we spent together over these years, but the memories of our time on the boat hold a special place for me: sharing sails with you has been a true blessing. Most importantly, I extend my gratitude to all the crew members who have stepped onto that boat for entrusting their lives to us.

To Raquel, my Galician sister, to your big heart, improv plans, listening skills great food, even better wines and laughs. To Joaquin and Sofi, to the laughs, Spanish-Italian-Greek high-frequency conversations, for sharing our respective food delicacies after 'holiday time refills'. To Huy and his impeccable style. To my supplì mastri, Simo and Gabri, for their enthusiasm and big up for their dreams to become true. For the preparation nights and opening my eyes and ears to great Italian/Roman rap music. Thank you, Gabri, for also sharing regatta dreams with me: one day we will reach the top of the rankings in Loosdrecht.

To Nikola, for allowing me to embark on a journey through architecture and beyond during my PhD. To the 100+ pouches we fabricated in 2 days, to Sombra and its potential future in other shapes.

To Alessia and Marta. To be great friends and clear mental fog during difficult times. To the suggestions we provided to each other and our life choices. To Arianna, Davide and Amelia (ci vedremo di più quando sarà tempo di tabelline spero). To Nico, Magda, Andrea, Miriam, Alessandro, Maristella, Eleonora and Roberto. To the friends I always go back as soon as I reach my hometown: Vittorio, Andrea, Davada, Mauro, Dario, Mincu, Giorgio and Claudio. To Angela to be a great long-lost friend from the past. To the sense of protection, randomness, and levity, irrespective of what life shoots at us over the years.

If I were ever able to learn and produce anything from the lab experience, it's because I have had a very functional, clean, and organised lab. Thank you, Niels, for holding ground to my attitude and requests on apparatuses and for

experimenting together ideas for fabrications. It has been a pleasure to learn from you on a daily basis, and I am glad you have an Italian car again. To the master of memes, king of the SoromaVibes playlist on Spotify (highly recommended!), fellow French-electropop listener, and sagacious artist, Bob: thank you for breaking me with a laugh during the long lab hours we spent together. To Katrien, the person with whom I shared (too?) many neurons with, choir director, flying robot designer, open-access master and Utrecht-Amolf commute companion. To Nienke, bright young mind, for your moral compass and listening capabilities. To Elif, to the students we supervised together, to the deep conversations, and to the Mediterranean sea nostalgia we shared. To Mannus, for the topics that aligned us, the random chats, and your intuition in sensing where interesting results were. Your persistence and patience in both simulations and experiments have been a great inspiration to me. To Alberto, for the laughs, for the conferences we attended together, for the things we have learnt from each other, and for the lessons we still have to learn. To Maziar, for your persistence, kindness, comforting conversations, and incredible aplomb. To Luuk, for being an excellent first office mate at AMOLF, for your shared stream of academic consciousness and ideas, and for being a great foosball player. To Jelle, for teaching me the ropes in fluidic setup, fabrication, and Dutch humour. To Shibo, for your boundless enthusiasm and care, for your attention to detail, for our rocambolesque adventures with the robotic arm, and for your capability to convert any random thought into feasible good ideas. To Sumit, for your humour, determination, sense of justice, and capability to stand up for others. To Stijn, for the deep conversations, the honesty in asking simple questions and not being satisfied with approximate answers, for your precision, and for showing me that counterintuitive starting (e.g. crossed arms on a boulder or in life) can sometimes be a very good strategy. To Ze, for his jokes and laughter, curiosity, kindness, and food treats. To Lio, for her kindness, *determination aura*, and book suggestions. To Olivier and Luca, for following me down my rabbit holes of academic curiosities and for bringing valuable original ideas to the table. To Dennis, Tanaya, Louise, Zak, Arthur, Charlotte, Erwin, Laura, Yorick to bring intense bursts of novelties and curiosities to the lab.

For Amolf, as a wonderful working environment: to Paula and Huib for supporting and encouraging such a pleasant working environment for all of us. Thanks for making me feel at home even in my working environment. 'I wish you all a great working day' echoes in my mind every time I finish a coffee now. I will never forget the random coffee breaks, yoga classes, *cafternoons*, and outings. To all the activities of PV and the amazing parties, always walking extra miles to organise great gatherings for all of us. To ME, EE, IT, and Mechanical workshop departments, as well as the Secretarial office and HR, in particular, Sofjia, Remco, Henk-Jan, Jan, Max, Bob, Remco, Richard, Rutger, and Kallinikos. To Petra, for her enthusiasm in the Science Day/Wetenschapsdag organisations.

To Martin, Marc, Kristina, Wim, and Jeroen for organising interdisciplinary meetings and activities to bring together all various expertises from Amolf. Modern Mechanics and Autonomous Matter meetings have facilitated an in-depth approach to identifying common denominators in diverse topics. I am convinced that this skill is as fundamental as in-depth technical knowledge in a specific topic.

Jack, Dhawal, Parisa, Finn, and Phil: I enjoyed all the random interactions, laughs, and venting-out sessions we had while crossing paths from the lab to the coffee corners and offices.

For the TUe DC and Robotics colleagues and friends: Farhad, Philip, Benn, Krishna. To Femke and Brett for their calm and enthusiasm. To Henk, to the concepts we agree on, and those we disagree about.

To Anouar (Ettore) and Paul: to the projects, laughs, and times we have shared over these years.

To the Language Cafè Utrecht hosts and crowd. Marieke, Luka, Sarah, Rachid (and their birthday parties), Nikos, Joris, and all the wonderful human beings I have met on Wednesdays during these 6 years of life in Utrecht. Although I am likely to forget many faces and names, I can never forget the environment we created and the randomness of interaction in Cafè Marktzicht. Having another safe harbour in you on Wednesday nights set a clear schedule in my mind, made me a slow-starting machine on Thursday mornings, and made me realise the joy in being a welcoming person. Thanks to all the names and faces I never managed to memorise in these years: I still feel a strong connection with you all.

Alla mia famiglia, Francesco, MariaPaola, e Tommaso. Se sono capace di partire, è solo perché ho solido porto in cui tornare. Siete voi le mie basi. Con amore e forza, alla nostra bellezza, ai nostri percorsi, alle nostre passioni, nonostante le incongruenze, le incomprensioni e le distanze.

To Anna, for the distances we travelled together and the ones we covered towards each other. To the steps, trains, planes, boats, and times we have shared over these years. It has been a rough ride, but it holds infinite value for me. Thank you for teaching me the value of speaking one's mind and expressing emotions. Thank you for your infinite support and care. I am a better person thanks to you.